UNIVERSITÉ DE STRASBOURG

Université de Strasbourg

msii ÉCOLE DOCTORALE

ÉCOLE DOCTORALE Mathématiques, Science de l'information et de l'ingénieur

UMR 7357

THÈSE présentée par :

Romain VOLLONDAT

soutenue le : **13 Décembre 2022**

pour obtenir le grade de : **Docteur de l'université de Strasbourg**

Discipline/ Spécialité : Physique de la matière condensée

Synthesis and Characterization of Silicon Clathrates Films for Photovoltaic Applications

---

RAPPORTEURS :
 Mme KAMINSKI-CACHOPO Anne   Professeur, IMEP-LAHC, CNRS - Grenoble INP
 M. ROCA i CABARROCAS Pere   Directeur de recherche, LPICM, Institut Polytechnique de Paris

---

AUTRES MEMBRES DU JURY :
 Mme BEGIN Sylvie   Professeur, IPCMS, CNRS-Université de Strasbourg
 M. POORTMANS Jef   Directeur de recherche, IMEC, Leuven, Belgium

---

THÈSE dirigée par :
 M. FIX Thomas   Chargé de recherche, ICube, CNRS- Université de Strasbourg
 M. SLAOUI Abdelilah   Directeur de recherche, ICube, CNRS-Université de Strasbourg

Acknowledgements

First of all, I would like to warmly thank my thesis supervisors, Thomas Fix and Abdelilah Slaoui, for giving me the opportunity to work on this subject. I am grateful for their continuous support and their valuable advice. This work has been enhanced thanks to their counseling and would not have been possible without them.

I would like to express my gratitude to the members of the jury, Anne Kaminksi-Cachopo, Pere Roca i Cabarrocas, Sylvie Bégin and Jef Poortmans for agreeing to examine this work, their benevolence during the defense and their helpful insightful comments and advice on this work.

Once more, I thank Thomas Fix for always keeping an eye on my work and for providing me with valuable ideas that allowed me to make significant breakthroughs. Thomas was always here with a smile to help me, from evolving and working in the lab to helping me grow as a beginner scientist. I owe him for all the time and dedication he gave me these three years.

I should thank Aziz Dinia for providing me with the opportunity to work independently at the IPCMS laboratory without whom my work would have been greatly hampered.

I am deeply grateful to Stéphane Roques for all the help he provided with experiments and resolving in a flash every issue we encountered. Without him, nothing would have been possible.

I warmly thank Jean-Luc Rehspsringer for his assistance in setting up the experiment and for his constant reassuring mood.

A big thanks to Céline Chevalier for allowing and performing the beneficial annealing under mechanical pressure of our samples at the Institut des Nanotechnologies de Lyon.

A huge thanks to Daniel Stoeffler for his precious DFT calculations of our various complex structures on his time. Another big thanks should belong to Daniele Preziosi for the resistance versus temperature measurements on our needy samples.

A special thanks to Dominique Muller and Yann Le Gall for ionic implantation of the samples, RBS measurements and their positive moods.

I'm much obliged to all the people who helped me make this work possible, Marc Lenertz, Jacques Faerber, Cedric Leuvrey, Corinne Bouillet, Guy Schmerber, Nicolas Zimmerman, Florent Dietrich, Marina Urban, Jérémy Bartringer, Nicolas Collin, Florian Mugler, Stéphane Roques, and all the people who helped me during this thesis.

I would like to acknowledge the constant and vital help of Stéphane Roques, Florian Mugler and Jérémy Bartringer. They were always here and ready to help with setting up experiments and solving issues.

Again a special mention to Stéphane Roques for his bright mood. The laboratory felt like home during the three years he spent there because of his sympathy and support.

In addition, I would like to thank all the students present in the lab, from PhD to master's to post-doc. In particular, I would like to thank Nacer Boubiche for his valuable advice along with Chithira Venugoplan Kartha and Yahya Zakaria for their support. I also have to mention my friends in Strasbourg for making my life easier and for their huge support.

Table of contents

General Introduction

In a world with growing widespread access to electricity and with evermore consuming economies, energy consumption has been in constant growth with an astounding 84% rise of the demand in between 2000 (14954 TWh) and 2021 (27450 TWh)[1]. This electricity generation is still largely dominated by a production from limited fossil fuels originating mainly from coal and fossil gas. Not only are these sources limited, but their life-cycle impacts are massive stretching from global pollution, ecosystems destruction to heavy greenhouse gases emissions.

To deal with pressing climate change while satisfying electricity demands, a shift toward efficient and clean renewable energy is crucial. As of today, cumulative wind and solar, which are the renewable energy with the biggest growth potential in energy output, electricity generation are reaching a little more than 10% of the world electricity mix[1].
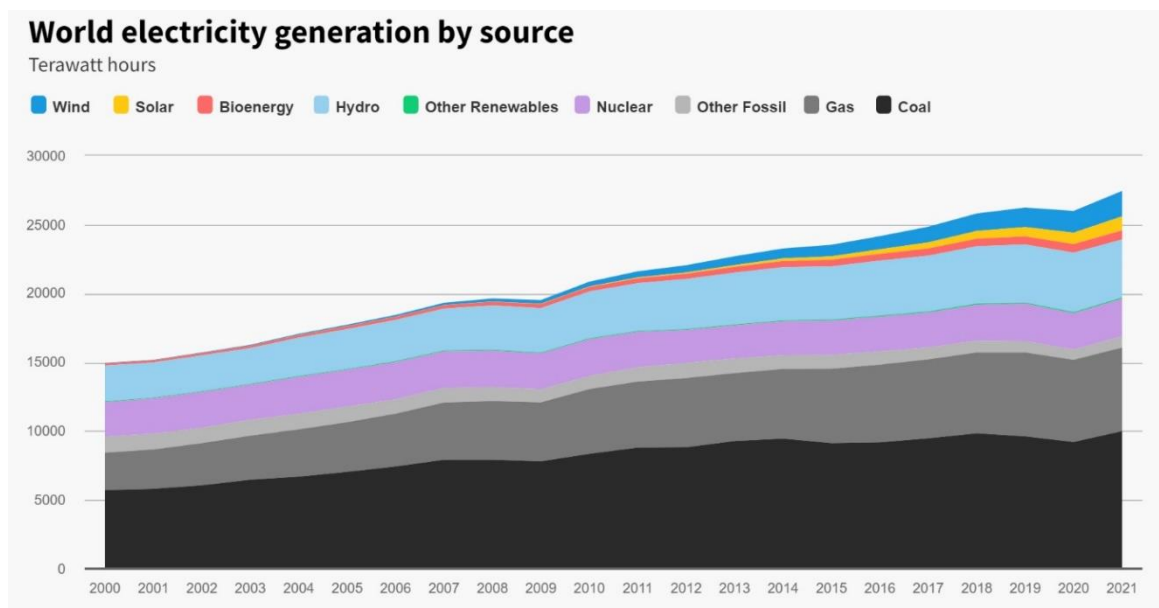
Thanks to satellite measurements, the average solar irradiance reaching the top of the atmosphere directly facing the sun is around 1.36kW/m^2.This means that, in theory, close to 175 PW are received from the sun by the earth atmosphere. To give an idea of this amount, it's about four orders of magnitude higher than the total human energy consumption, highlighting the potential of solar energy. Undoubtedly, the situation is diverse around the globe, depending not only on the effective solar energy harvestable

---

[1] From ember-climate.org and the Ember Global Electricity Review 2022 report

at a specific location but also the physical and technical constraints along with specific socio-economic indicators. Study of this photovoltaic power potential around the world is a helpful indicator on the extent to which each region could install efficient solar panels[2].
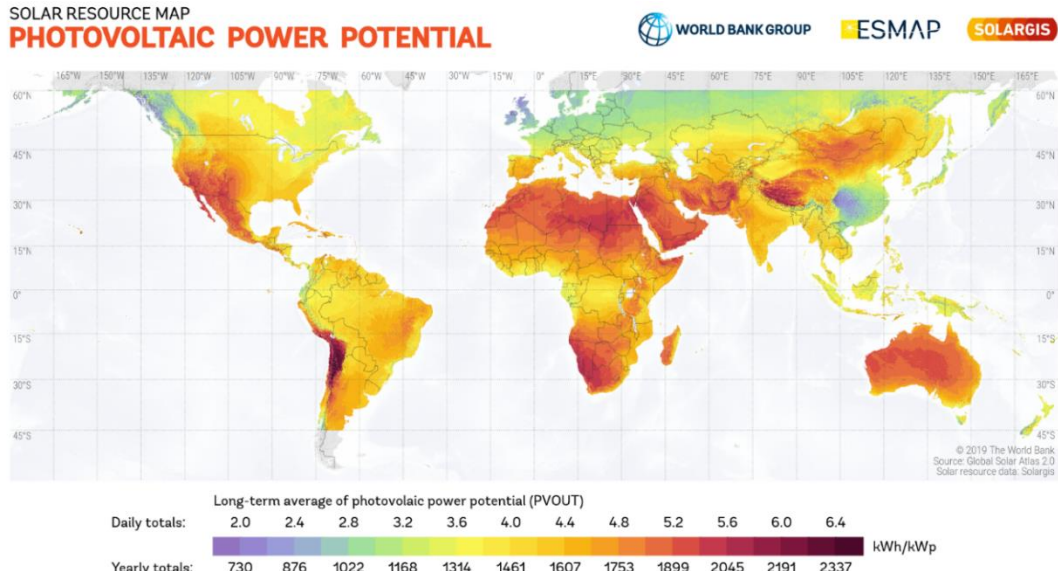
Since half a century, solar energy production is undergoing an explosive growth[3] and to sustain this trend, solar panel with enhanced efficiencies, long term of life with reduced cost both in term of cost and materials usage are necessary along with the development of clean and efficient ways of energy conversion and storage.
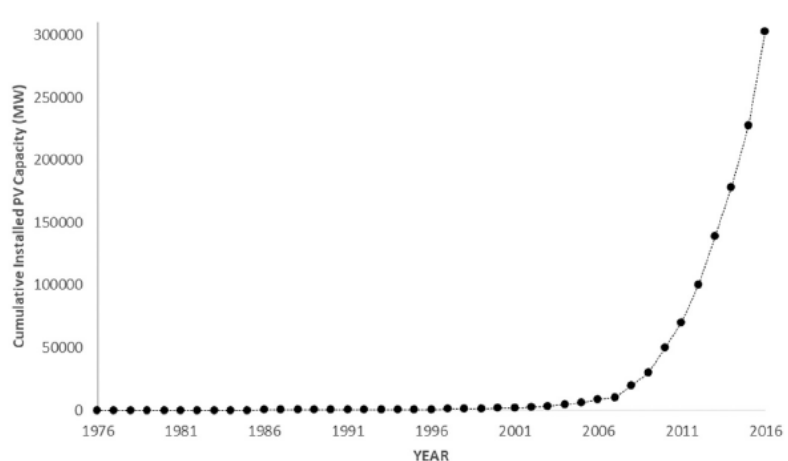
To reach these goals, finding materials with appropriate optical and electrical properties, readily available and easy to produce would be a convenient way.

The huge usage of crystalline silicon in photovoltaic industry while its optoelectronic properties are not the optimal ones (indirect bandgap, low light absorption,...) is explained by its large availability as a raw material for all electronic devices, its non-

---

[2] 2020 The World Bank, Source: Global Solar Atlas 2.0, Solar resource data: Solargis.
[3] H. Ritchie, M. Roster, Renewable Energy, Published online at ourworldindata.org, 2020

chemical toxicity as well as its thermal stability. Taking advantage of this availability and the accumulated knowledge, it would be convenient to find crystallographic phases with equal alluring properties by exploring the vast allotropy of the silicon. The low-density allotropes of silicon are all characterized by a beneficial direct bandgap. Among them are the specific guest-free silicon clathrates of type I, Si_{46}, and type II, Si_{136}.

Silicon clathrates are guest-host structures characterized by a silicon framework of polyhedral cages which can host guest atoms, usually alkali metals. The properties of these structures depend on the cages' arrangements and their occupation in guest atoms. For some structure, these atoms can be reversibly inserted or removed leading to structures ranging from $Na_{0<x<32}Si_{136}$ leading to the desired Si_{136} silicon allotrope.

In Chapter 1, the focus is on the allotropy of silicon and especially on the Silicon Clathrates. The specific structures of the clathrate compounds will be detailed before focusing on the silicon clathrates properties, synthesis and applications.

Chapter 2 gives details on the synthesis and characterizations of the silicon clathrates films. The two-step thermal decomposition process used is described and the effects of the experimental parameters on the obtained films are reported. The properties of the synthesized pure type I, Na_8Si_{46} on one hand and type II, Na_xSi_{136}, films on the other hand are detailed. Annealing under mechanical pressure is proposed as an efficient way to compact the silicon clathrates layer and smooth their surfaces.

In Chapter 3, the effects on the silicon clathrates films properties of various post-synthesis' treatments are presented. In particular, the insertion of additional sodium or its removal in type II silicon clathrates films are investigated and the consequences on the properties of the resulting films are presented and discussed. These processes allowed the obtention of chemical composition ranging from $Na_{0.1}Si_{136}$, almost guest-free structure, up to $Na_{23}Si_{136}$, close to full occupation. DFT calculations were carried out to sustain the experimental observation versus the sodium content within the cages. The transition from metallic to semiconductor character of the films is also demonstrated. Finally, feasibility of the doping of the silicon clathrate films is explored using arsenide ionic implantation and thermal annealing. Doped Si clathrate films showed a slight improvement of their photovoltaic response and tentative explanation are given.

The manuscript end with a summary of the carried work and with perspectives.

Chapter 1: Context and state of the art

1.1 Introduction

Taking advantage of the photovoltaic effect has enabled humankind to harvest some fraction of the solar power reaching the earth surface by converting it into electricity. Using a classic p-n junction solar cell, light is absorbed, generating electrons and holes inducing a current as electrons exit the cell. Thanks to extensive research on the topic, criteria to choose materials fitted for large deployment of photovoltaic are established[1]:

- The materials should efficiently absorb photons in the visible light range, meaning high absorption coefficient and a direct band gap, or failing that, an indirect with a value in the optimal range of 1.1 to 1.3 eV[2].

- The material comprehensive understanding of its chemistry, metallurgy to physics, allowing a steady production flow of devices.

- The material durability should at least allow a several decades-long time of service of the device.

- The material must be proven harmless, in a short or long time, to the environment in which he is set-up, even upon eventual breakdown.

- The material should be easily collected, refined, and shaped with minimal infrastructural, ecological and production costs.

Indeed, even if other semiconductive materials have shown more favourable optoelectronics properties than silicon resulting in solar cells of higher efficiency[3,4], their toxicity, rapid degradation and/or high cost prevent them from being used for industrial production. As of today, silicon represents the best compromise between all these criteria. In the era of silicon, this material is by far the more exhaustively studied and understood semiconductor and this despite the ecological impact of its refinement emitting large amount of CO_2. But due to its wide abundance, steadily decreasing prices[6] and durability reaching up to forty years, Silicon is the best candidates until now.

In this chapter, the growth or deposition of silicon will be briefly introduced along with the crystallographic structures of obtained silicon. We will focus on the exotic allotropy

of silicon, from high-pressure phases to low density ones. Then we will review the clathrates structure in general, with a focus on silicon clathrates. Finally, we will report synthesis pathways of such structure before detailing their possible applications.

1.2 Silicon and its allotropy

1.2.1 Silicon allotropy at ambient conditions

Silicon, second most abundant element in the earth crust, is extracted from SiO_2 oxide, or silica, predominantly under the form of quartz mineral[7]. Quartz contains various amount and nature of impurities depending on their extraction location. Obviously, for technological applications, this quartz has to be picked with the lowest concentration of impurities, even more if these impurities are of metallic nature such as iron or aluminium among others. In order to obtain silicon in its elemental form, the SiO_2 has to be reduced, meaning the breaking of the Si-O bonds. The most widely used process is the carbothermal reduction[8] of silica using graphitic carbon in energy intensive electrical arc furnaces at temperature around 2000°C[9]. These conditions favour the transfer of the oxygen atoms from the silicon to the carbon atoms, resulting in the production of elemental silicon while releasing carbon dioxide. The silicon obtained this way is called metallurgical grade silicon[10], or MG-Si, with purity around 98% which is far from sufficient to be usable by the semiconductor or photovoltaic industry. These impurities are mainly due to carbon, alkaline-earth elements or transition metals along with ppm in mass of phosphorus and boron.

To reach electronic grade silicon or EG-Si, further purification is needed and obtained through the so-called Siemens process[10]. Thus, powdery MG-Si is introduced in anhydrous chloric acid heated at 300°C to obtain $SiHCl_3$ and to induce the chlorination of the various impurities. The discrimination of $SiHCl_3$ from the other chlorides is then performed thanks to its low boiling point. Due to this separation step, the $SiHCl_3$ is obtained with traces of electrically active impurities below the ppb. Silicon is retrieved by reacting the $SiHCl_3$ with hydrogen at 1100°C and is then disposed in the tens of centimetre-wide cylinder which will be the base material for the various process of crystalline growth. This process is again very energy consuming and additionally

produces toxic waste[6]. In an attempt to reduce the overall cost necessary to obtain EG-Si and as photovoltaics applications don't need such purity levels, solar grade silicon[11] or SOG-Si, also exists in the market in minor shares.

In the prospect of heavy silicon solar cell production able to reach the need of human electricity needs, new "Sand-to-Si" processes[1] are beginning to be developed relying on the use of even impure quartz stock and using new chemical approaches which results in lower energy consumption and better CO_2 remediation.

Figure 1.1 (extracted from Saga[12]) depicts the most deployed routes to fabricate silicon cells used for modules fabrication: the Czochralski crystallisation method that results into monocrystalline silicon (Cz-Si) and cast crystallization method that conduct to multicrystalline silicon (mc-Si). Yet, the late obtained in large ingot block directly from the casting of silicon feedstock along with the waste produced by the Cz-Si production resulting in simpler, quicker and less energy consuming process while keeping most of silicon advantages thanks to passivation techniques[13].
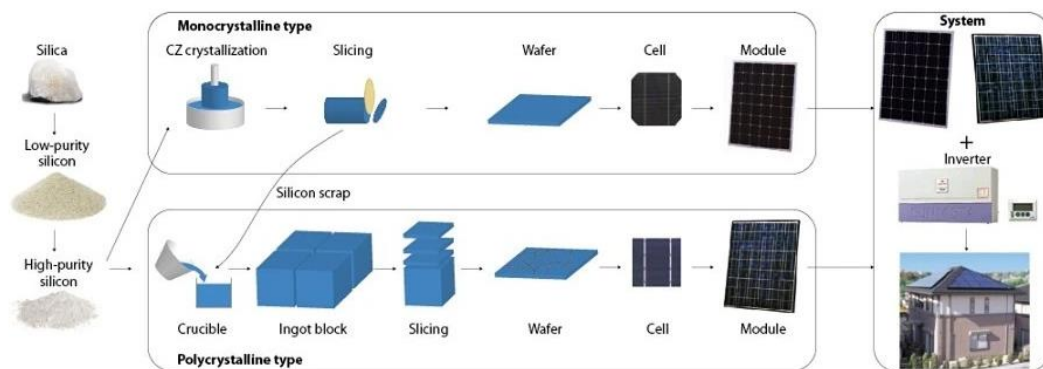
Figure 1.1 Production process of common commercial crystalline solar cells extracted from Saga[12]

At ambient conditions of temperature and pressure, silicon is properly stable in two forms: crystalline diamond silicon and amorphous silicon. Diamond crystalline silicon (Si-I, $Fd\bar{3}m$) is the widely known form of silicon crystallizing in the same arrangement than diamond carbon. It is a semi-conductive material with a wide direct band gap of 3.4 eV and an indirect gap of 1.12 eV[14] limiting its light absorption[15]. Additional structural information about Si-I is reported in **Table 1.1**.

Table 1.2 Diamond silicon structural properties[12]

Diamond silicon, Si-I		
Space group		$Fd\overline{3}m$
Lattice parameter (Å)		5.4309
Volume of the cell (Å³)		160.18
Density (g.cm⁻³)		2.329
Band gap	Direct (eV)	1.1
	Indirect (eV)	3.4

As a crystalline semi-conductive material, its properties can be altered as its crystallinity changes. Thus, different type of Si-I materials can be defined depending on the dimension of the grains[16] as visible in the **Table 1.2** along with their most common synthetic route.

Table 1.1 Silicon terminology depending on the material grain size from Basore[16]

Terminology	Symbol	Grain Size	Usual Growth technique
Single crystal	sc-Si	>10 cm	Czochralski (CZ) / Float Zone (FZ)
Multicrystaline	mc-Si	1 mm to 10 cm	Cast, sheet, ribbon
Polycrystalline	pc-Si	1 µm to 1 mm	Chemical Vapor deposition
Microcrystalline	µc-Si	<1 µm	Plasma deposition
nanocrystalline	nc-Si	<10 nm	Plasma deposition
Amorphous silicon	a-Si	-	Plasma deposition

Yet, both growth techniques used for the synthesis of large crystalline silicon are not satisfying in terms of cost and energy consumption while inducing consequent amount of silicon waste.

In order to reduce the silicon fabrication cost (material reduction) and to enlarge the possible applications (windows, roofs…), thin silicon films deposited on glass or metal substrates were developed. The crystallographic properties of the obtained silicon film depend strongly on the deposition method used and the temperature and pressure

during the growth. The average grain sizes of the crystallite can thus be varied from few nanometers[17] (nc-Si) to several micrometers[18] (μc-Si). Larger grains up to several millimeters can be reached by post-treatment of amorphous silicon using ion, lamp or laser beams[19].

Finally, amorphous silicon (or a-Si) has been widely produced and studied as its growth conditions are strongly relaxed. Its dangling bonds can easily be passivated by hydrogen resulting in hydrogenated amorphous silicon, a-Si:H. In comparison to Si-I, a-Si:H exhibits a direct band gap in the 1.5-2.0 eV range[20], almost forty times higher absorption coefficient, lower energetic production' cost and the possibility to be deposited on large surface (m²) in one run and on a diversity of substrates[21].

- *Silicon based solar cells*

Ever since the commercial production of solar cells, silicon has been the material with the most dominant presence on the market and as of 2022, silicon in its classical crystalline form, represents close to 95% of the photovoltaic production share[22]. Various technologies and approaches were developed and optimized to take advantage of the various forms of silicon mentioned above, which can be mainly divided in two categories:

- First generation or wafer branch, relies on the use of thick silicon substrates inherent to the indirect bandgap of Si-I. Both mono and multicrystalline solar cells used widely in commercial applications and are competing the leadership in the market share continuously influenced by the state of the research and obviously by the silicon price and availability. In June 2022, single crystal silicon solar cell is at a 26.7 % efficiency[23] while multicrystalline is a bit lower at 24.4 % by Jinko Solar[24].

- Second generation or thin-film branch, using materials with better light absorption coefficients resulting in reduced thickness. Silicon in this case in its amorphous form and due to its more efficient light absorption than Si-I resulting in active layer thickness reduced by more than two order of magnitude[21]. The main drawback of a-Si:H is the formation of silicon dangling bonds upon light

exposure[25], resulting in higher density of states and thus reduced efficiencies. As of June 2020, top a-Si:H single junction reach efficiency of 10.2 %[26]

In the state-of-the-art research, silicon solar cells are quite close to reach the theoretical Shockley maximum value of efficiency of 29 % as shown on **Figure 1.2**, meaning that to continue reaching higher efficiencies, novel concepts or materials are necessary.

Regarding photovoltaic applications, Silicon is right now the most convenient material, which explains its continued predominance in the industry for the past decades. However, to answer modern challenges, solar cells with higher efficiencies and reduced material cost will be necessary. Emergent approaches, resulting in so-called third generation solar cells[27], are under way in order to use thin-film solar cells with long term stability and high efficiencies. As far as silicon is concerned, the early investigations concern several approaches such as: silicon band-gap and light absorption engineering by strain constraint[28,29], or photonic designs, use of silicon nanoparticles[30,31] or quantum dots and quantum well structures[32,33]. Since the 2000s, innovative studies on the potential of silicon metastable allotropes[34] bring novel perspectives from the fundamental point of view as well as for applications.
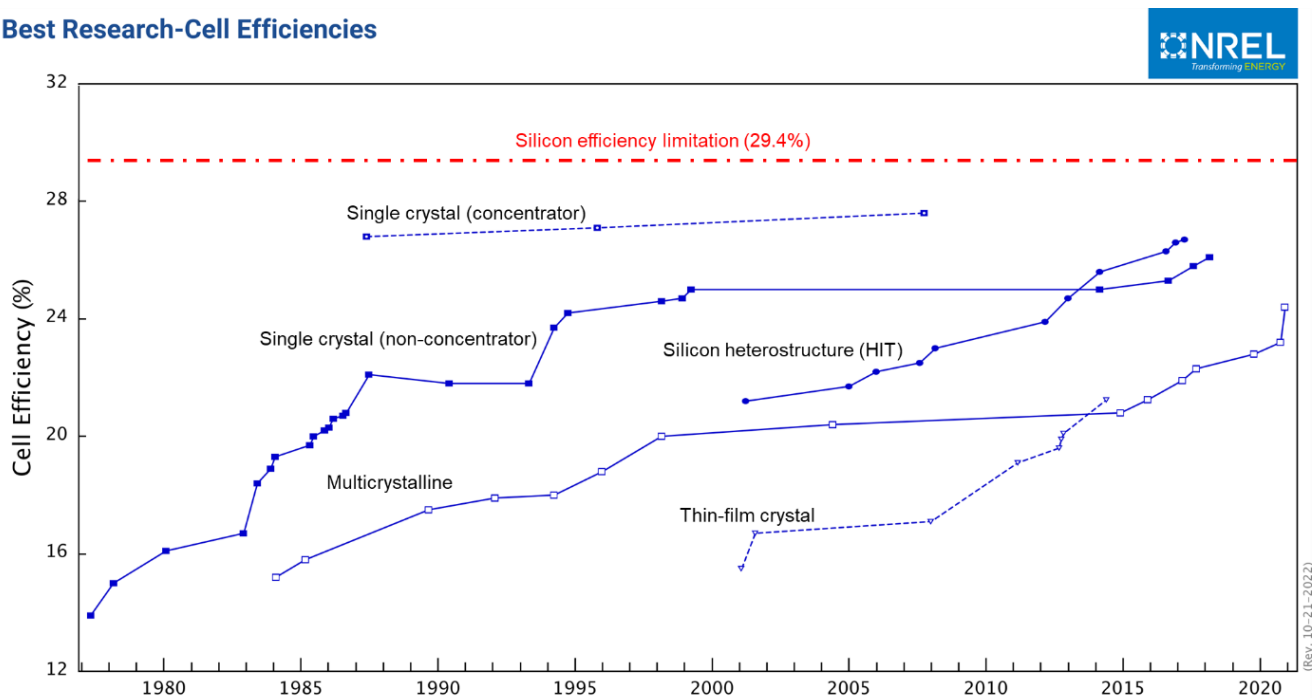
Figure 1.2 Best crystalline silicon solar cells efficiencies reported by NREL in 2021

An extensive exploration of the variety of silicon allotropy in search of alluring metastable form is crucial. A large number of semiconducting phases of silicon other than Si-I have already been identified[35], but there is little knowledge about their specific physics and chemistry. In the next section, an overview of the diverse allotropy of silicon is displayed, along with their conditions of existence and properties.

1.2.2 « Exotic » allotropy of Silicon

Silicon benefits of an energy landscape containing a multitude of local minima at the origin of its rich polymorphism depending on temperature and pressure conditions. Upon the used conditions, several silicon phases (allotropes) are possible as shown in **Figure 1.3**[36], Due to elevated kinetic barrier, a considerable amount of silicon allotropes is in fact metastable at ambient conditions and could exhibit properties more favourable toward optoelectronic applications than diamond silicon, Si-I.
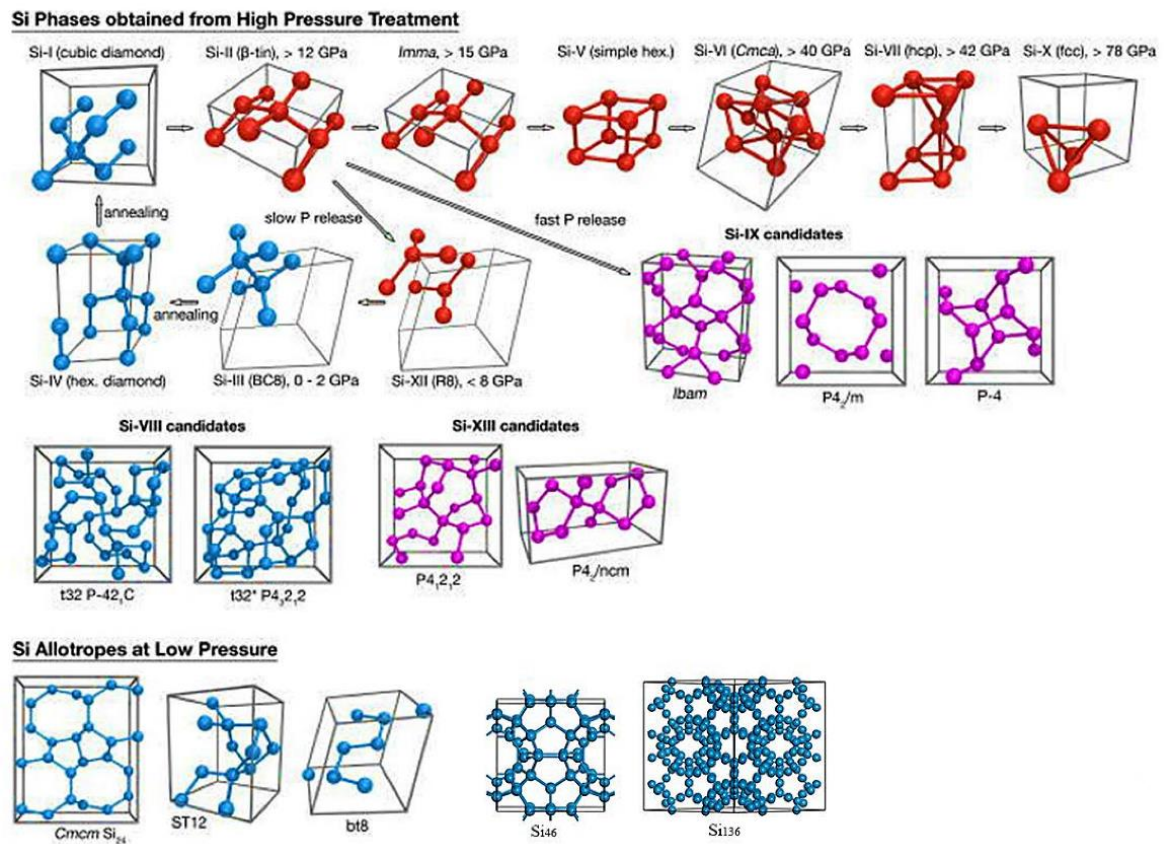
Figure 1.3 Structures of the known silicon allotropes. Structure in blue are metastable at ambient conditions. Structure of phases stable only at high pressure are in red. Structure in purple depicts proposal for less known phases[36].

In the following, conditions to reach high-pressure allotropes of silicon will be detailed followed by the description of low-density allotropy of silicon.

A. High pressure Silicon allotropes

To produce silicon allotropy at high pressure, diamond or amorphous silicon are subject to elevated compression by using a Diamond Anvil Cell (DAC). DAC are compression device made of two diamond anvils allowing to submit small volume of material (around the thousandth of mm^3) held in a dedicated gasket. Resulting structures are routinely characterized using in situ XRD and in situ infrared, Raman, or Brillouin spectroscopy.

A gradual metallization of silicon is observed with the pressure, as the coordination number goes from four, for the Si-I, up to twelve for the allotropes obtained at the most elevated pressure. All these metallic phases are unstable upon decompression and not observed at ambient conditions. Transition between metallic phases are reversible at 300 K under linear decompression[37].

However it is not the case of the semiconductor-metal transition between Si-I and the first metallic allotrope Si-II due to high kinetic barrier[38] . During the release of pressure, Si-II gives way to various metastable structures of 4-fold coordination depending mainly on the rate of the decompression.

Under linear decompression, the rhombohedral Si-XII[39] (R8-Si,$R\overline{3}$) appears when the pressure is below 8 GPa as displayed on **Figure 1.3**. Then between 2 GPa and atmospheric pressure, Si-XII turns into the centred cubic Si-III[40] (BC8,$Ia\overline{3}$) and is metastable due to the indefinite kinetic of its degradation[41]. Si-III was first identified as a semi-metal[42] before being characterized as 20 meV narrow band gap semiconductor[43]. When annealed at 200°C, Si-III undergoes a rearrangement into lonsdaleite / hexagonal diamond Si-IV[41] (HD-Si,$P6_3/mmc$). Si-IV has substantially the same bond angles and length than Si-I and they thus share very close density. Due to these similarities, Si-IV can be turned into Si-I using annealing at sufficient temperature allowing the following pathway to recover diamond silicon: Si-II $\rightarrow$ Si-XII $\rightarrow$ Si-III $\rightarrow$ Si-IV $\rightarrow$ Si-I.

Si-XIII was isolated by submitting a Si-III / Si-XII mixture to annealing at 100°C[44]. Its degradation into Si-IV starts at 200°C to finally disappear at 240°C[45], then Si-I is the only phase left at 255°C[46]. Two structures are currently proposed to describe the Si-XIII phase: $P4_2/ncm$ [47] et $P4_12_12$ [48]. All these phases are summarized in **Table 1.3**.

Table 1.3 Summary of the information on the silicon allotropes obtained upon Si-II linear decompression[48-50,52,56,57].

arrangement	Si-XII / R8-Si	Si-III / BC8-Si	Si-IV / HD-Si	Si-XIII
Structure	Rhombohedral	Centred cubic	Hexagonal diamond	Tetragonal
Space group	$R\bar{3}$	$Ia\bar{3}$	$P6_3/mmc$	$P4_2/ncm$ or $P4_12_12$
Nature	Direct band gap semiconductor (1.2 eV)	Narrow band gap semiconductor (20 meV)	Direct band gap semiconductor (1.6 eV)	Direct band gap semiconductor (1.4 eV)

For fast pressure release, meaning decompression to atmospheric pressure in a hundred of ms, two additional tetragonal phases have been obtained according to the starting pressure and are reported in **Table 1.4**. From 15 GPa and 12 GPa, the phases Si-VIII and Si-IX[49] are respectively recovered. Si-VIII phase can be described by the two almost identical structures : t32 ($P\bar{4}2_1C$) and t32* ($P\bar{4}2_1C$) and is predicted to be an alluring semiconductor due its direct band gap of 1.28 eV[50]. Regarding Si-IX, three structures are proposed for now: $Ibam$ [51], $P4_2/m$ and $P\bar{4}$ [52] and is predicted to either be a semi-metal or a narrow band semiconductor[51].

Table 1.4 Information on the silicon allotropes obtained upon Si-II fast decompression[59-61].

Denomination	Si-VIII	Si-IX
Structure	Tetragonal	Orthorhombic or tetragonal
Space group	$P\bar{4}2_1C$ / $P4_32_12$	$Ibam$ / $P4_2/m$ / $P\bar{4}$
Nature	Quasi-direct band gap semiconductor (1.28 eV)	Semimetal or narrow band semiconductor

B. Low-density Silicon allotropes

By convention, low-density allotropy of silicon is used to identify allotropes with a volume per atom lower than in a diamond silicon structure. In contrast to the previously mentioned allotropes, these low-density structures are all direct band gap semiconductors[34,53] and thus are promising for optoelectronics applications.

Such structures are in fact the silicon framework of host-guest inclusion compounds from which all the guest species have been removed[54–56]. For example, the Si_{136} allotrope is obtained from the Na_xSi_{136} type II clathrate structure by removing the sodium atoms contained in the host framework as depicted in **Figure 1.4**. These inclusion compounds with open framework are either silicon clathrate compounds with composition as Na_8Si_{46} and Na_xSi_{136} or the zeolite type Na_4Si_{24}. The guest removal can be performed using chemical, electrochemical and/or diffusive routes. The emptied framework of these structures results in the Si_{46}, Si_{136} and Si_{24} compounds, which are the true low-density silicon allotropes and defined in **Table 1.5**.
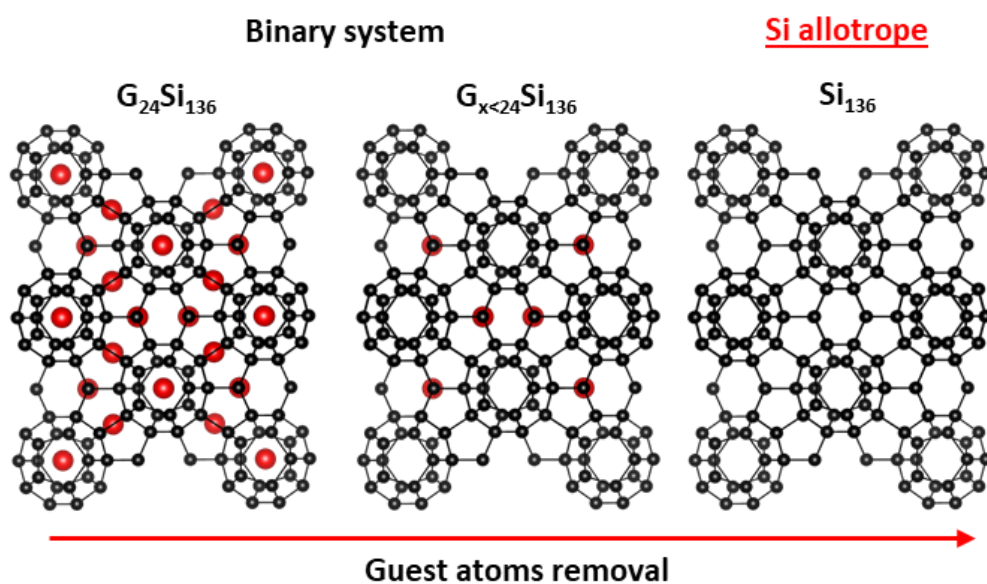
Figure 1.4 Schematic pathway to obtain a pure elemental silicon allotrope from the removal of guest atoms from an inclusion compound with a silicon framework.

Table 1.5 Summary of the low-density silicon allotropes[65-67].

Phase	Si_{46}	Si_{136}	Si_{24}
Structure	Cubic	Cubic	Orthorhombic
Space group	$Fd\bar{3}m$	$Pm\bar{3}n$	$Cmcm$
Direct band gap (eV)	1.3-1.9 (theory)	1.8	1.3

Due to the channel cavities running through its structure, the removal of guest is easily performed by thermal degassing. The resulting Si_{24} is stable up to 450°C and exhibits the very proficient quasi-direct band gap of 1.3 eV. However, similarly to all phases which need high pressure[57], its synthesis scalability is reduced and thus limits its potential for future applications. Clathrate compounds can be synthesized using different techniques. Thus, a special attention will be brought to these compounds in the next section.

1.3 Silicon Clathrates

1.3.1 Introduction to the clathrate structures

As mentioned earlier, Clathrates is a specific class of guest-host structure inclusion compound defined by an open host lattice made of tetrahedral cages able to enclose guest atoms as introduced by Powell[58] in 1948. They are additionally characterized by the following features:

- an highly symmetrical lattices with large lattice parameters that are mainly impacted by the nature of the host species[59].
- the host lattice can be considered as a metastable phase of the host species stabilized by the guest' atoms presence which decomposes into its stable form under annealing at sufficient temperature[60].
- the interaction between the guest and the host lattice is relying on weak interactions and there is no covalent bonding between the host and the guest.

Clathrates exist in a broad range of materials divided into two mains families: organic and inorganic clathrates according to the nature of the host framework. Organic clathrates have been found to occur naturally whenever the pressure and temperature conditions allow their formation.

To ease the identification of these clathrate structures, they are defined as type "Y" clathrates[59]. The structure found mainly in liquid hydrates, resulting in a $L_{x<24}\cdot(H_2O)_{136}$ formula with a cubic $Fd\overline{3}m$ space group is referred to as type II Clathrates. For the gas hydrates structures, the most common with a $G_{x=6 \text{ or } 8}\cdot(H_2O)_{46}$ formula in a cubic $Pm\overline{3}n$ structure while the structure with three type of cages results in the hexagonal $P6/mmm$ $G_6\cdot(H_2O)_{36}$ lattice. **Figure 1.5**[61] depicts these three structures.
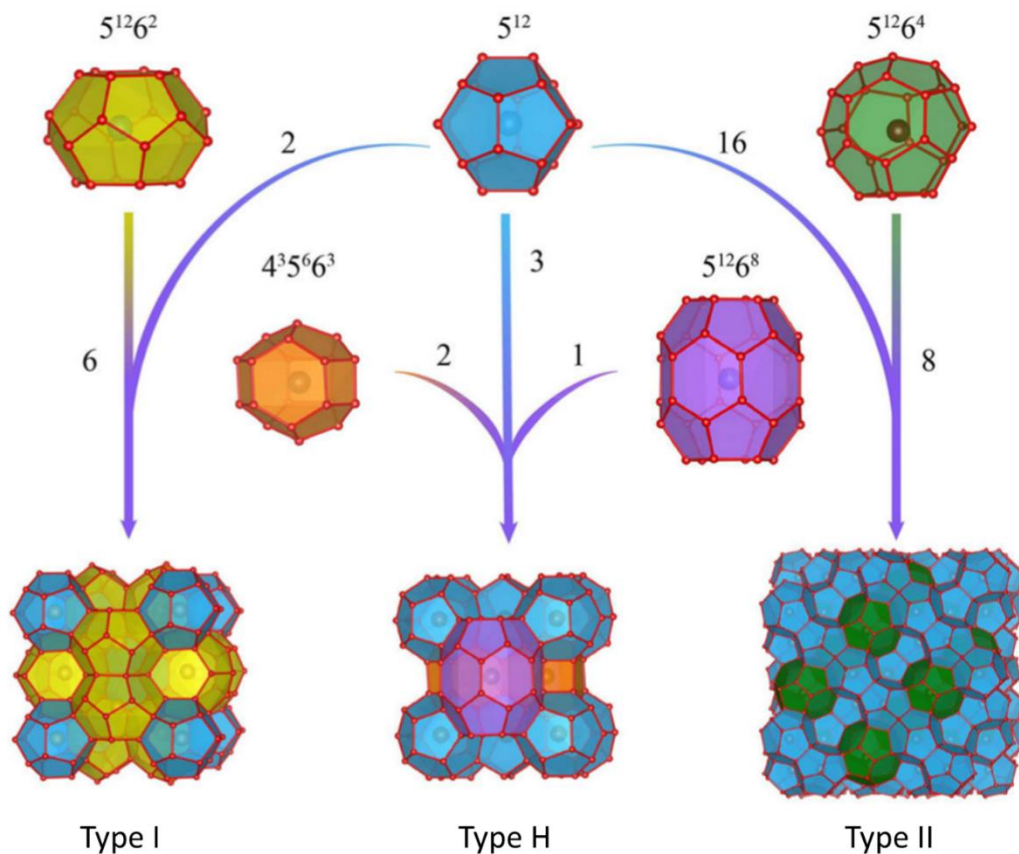
Figure 1.5 Structure of the Type I, H and II hydrates. For each of them, their unique composition in term of polyhedrons is reported. Adapted from Liu et al.[61].

Extensive investigations on hydrates allowed to evidence the fact that clathrates specifically decompose into their components hinted that the various species forming the clathrates are in molecular state as close as possible to the ones of their free states[60]. The organic clathrates also highlighted that the main criterion in the

occupation of the cages is the size of guest species in comparison to the size of the polyhedral cages, resulting in various structures and cages occupations[62].

The first synthesis and identification of inorganic clathrates was reported in 1965[63] about the intermetallic silicon clathrates, initiating the obtention of clathrates framework from diverse elements, most of them within the groups XI to XV of the periodic table. This large possibilities in elements combination[64], visible on **Figure 1.6**, led to the composition of simple binary clathrates, meaning two different species, up to quinary clathrates due to various guests in the cages and alloyed host framework. Thanks to this diversity of chemical composition and related properties, inorganic clathrates are attractive for a multitude of applications such as: thermoelectricity, superconductivity, batteries, hydrogen storage, and photovoltaics[65].
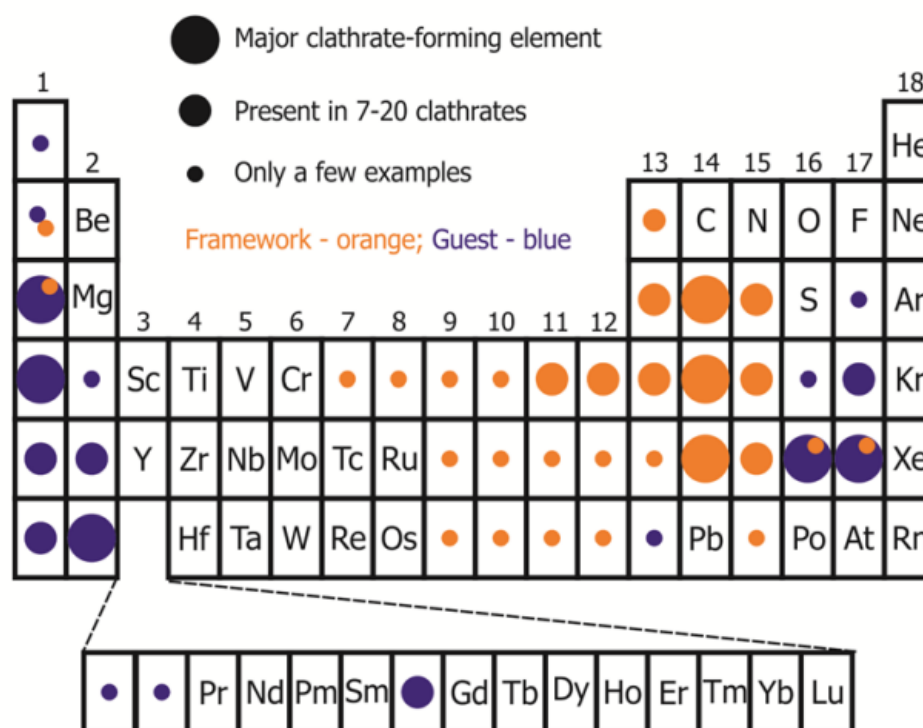
Figure 1.6 Representation of the periodic table according to their role either as guest and/or as host elements in inorganic clathrates. Size of the circle represents the relative frequency of each element in each role among inorganic clathrates compounds[64].

To discriminate among these inorganic clathrates, a classification according to the formal charges is commonly used, namely anionic, neutral and cationic clathrates[66]. The overly predominant category is the anionic one containing all clathrates which has a framework bearing a formal negative charge often due to the electrons given by their cationic guests of metallic alkali, alkaline earth and sometimes rare earths. The less likely cationic, or reverse, clathrates are found to host halides and chalcogenide

cations. Finally, the neutral clathrates are synonyms of guest-free clathrates so far obtained only for clathrates of silicon or germanium framework[67].

With hundreds of inorganic clathrates with singular properties, an extensive review[64,68–70] of these structures will not be performed here. In the following sections, we will focus on the Silicon Clathrates and their properties.

Silicon clathrates in their binary type I Na_8Si_{46} and type II Na_xSi_{136} were the very first inorganic clathrates to be synthesised. The two structures were obtained through the use of the highly reactive sodium silicide Na_4Si_4 phase precursor. Na_4Si_4 is part of the Zintl phases[63]. Zintl phases are stoichiometric intermetallic compounds[71] exhibiting simultaneously covalent and ionic bonds due to the presence of polyanions from group 13 to 16 and cations of alkali / alkaline-earth metals resulting in A_xB_y formula as shown in **Figure 1.7**. Other Zintl phase such as M_4Si_4 and M_4Ge_4, with M = Na, K, Rb or Cs, are known to also allow the obtention of silicon and germanium clathrates upon thermal decomposition[72].
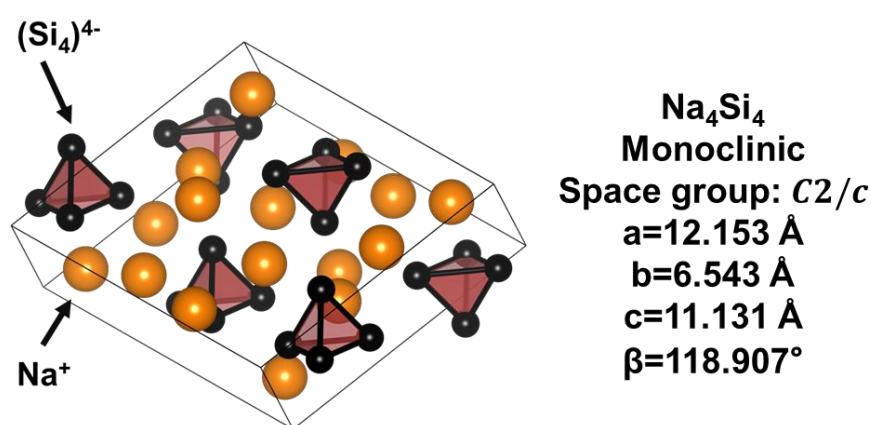
Figure 1.7 Crystallographic structure of the Na_4Si_4 zintl phase made with Vesta along with its space group and lattice parameters and angles.

Silicon clathrate cages can be filled with alkaline-earth metals and sometimes even with rare-earth[73]. Silicon clathrates with alloyed framework are also reported such as other Group 14 ones[74] along Group 13[75], pnictogens[76] and transitions metals[77].

Silicon clathrates are the most represented family in the inorganic clathrate compounds, with properties ranging from superconductivity[78], semi-conductivity[53] and phonon-glass electron-crystal (PGEC) for thermoelectric[79]. To these properties must

be added the specific polyhedral cage open framework structure, alluring for both batteries[80] and hydrogen storage applications[81].

In this work, the attention is specifically drawn on silicon clathrates of the binary Na-Si system. In this case, silicon clathrates are mainly present in two type of clathrates structures: Type I and Type II silicon clathrates. As long as silicon clathrates are filled with sodium atoms, they are anionic clathrates since the sodium atoms will act as a donor that will give electrons to the framework.

This results, similarly to most anionic clathrates, in an excess of electrons in the structure causing the metallic or semiconductive materials to have their electrical conduction controlled by negative charge carriers. Depending on each structure and the occupations of their cages, the silicon clathrates properties are drastically different.

1.3.2 Type I Silicon

Type I silicon clathrates Na_8Si_{46}, pictured in **Figure 1.8,** under most synthesis parameters, exhibits a full occupancy of the cages due to the small covalent radius of the sodium atoms (r_{Na} = 0.154 nm) compared to the free radii of the two small Si_{20}, $r_I(Si_{20})$ = 0.204 nm, and the six larger Si_{24}, $r_I(Si_{24})$ = 0.223 nm[69]. Na_8Si_{46} crystallizes in a cubic $Pm\bar{3}n$ structure with a lattice parameter of 10.2 Å[63]. The structural parameters of type I silicon clathrate are given on **Table 1.6**.
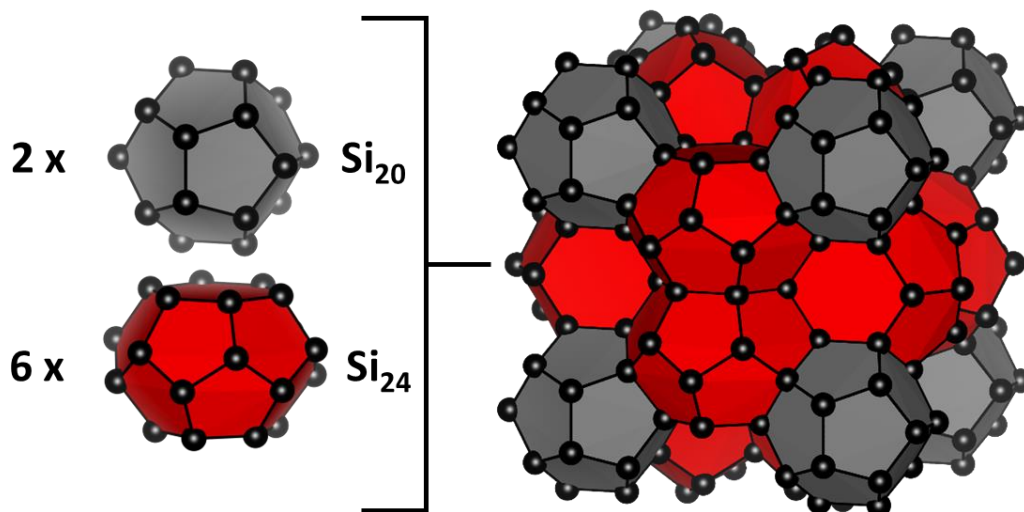
Figure 1.8 Crystallographic structure of the Type I Silicon clathrate made with Vesta

Table 1.6 Structural properties and atomic positions of the Type I silicon clathrates Na$_8$Si$_{46}$[89]

Na$_8$Si$_{46}$[63]	
Structure	Cubic
Space Group	$Pm\bar{3}n$
Atomic positions — Si	6 Si1 in 6(c)
	16 Si2 in 16(i)
	24 Si3 in 24(k)
Na	2 Na1 in 2(a)
	6 Na2 in 6(d)
Lattice parameters (Å)	10.1945
Cell volume (Å^3)	1059.5
Density (g·cm^{-3})	2.313

Na$_8$Si$_{46}$ exhibits a metallic behaviour in all of its stable temperature range as expected from the excess of electrons donated by the sodium guest. Estimation on single-crystal sample indicates a 9.8x10^{-5} Ω·cm resistivity at room temperature for a carrier concentration of 5.7x10^{21} cm^{-3} and a 11.2 cm^{2}V^{-1}s^{-1} electron mobility[82]. Type is an evidenced metallic phase as demonstrated in **Figure 1.9**[82].
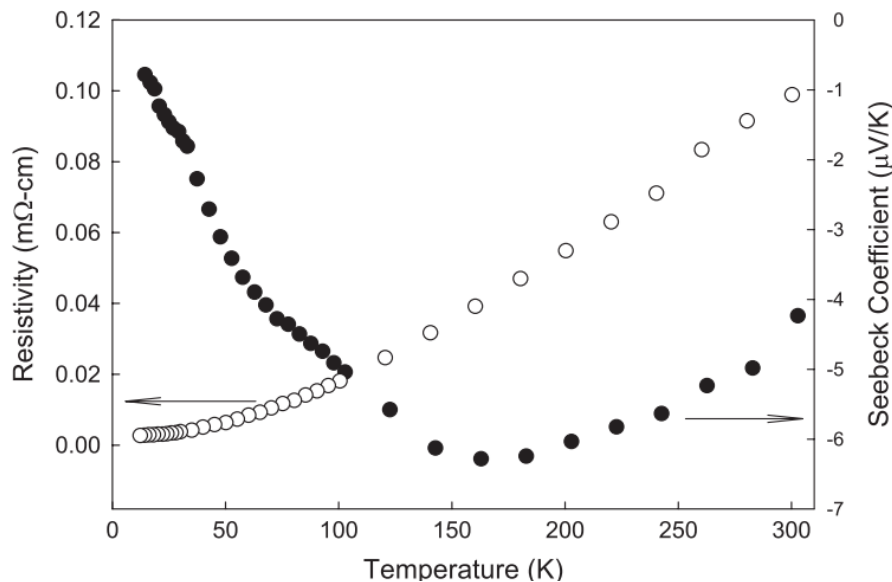
Figure 1.9 Temperature dependent resistivity and Seebeck coefficient of Na$_8$Si$_{46}$ single crystals[82]

At the same time, low thermal conductivity is observed in this type I silicon clathrates as visible in **Figure 1.10**[82]. This duality is thanks to a PGEC behaviour as an efficient electrical conduction is performed by the silicon framework filling the "electron crystal" part. The phonon conduction is hindered by the rattling of the sodium atoms inside cages which act as scattering centres resulting in a "phonon glass"[83].
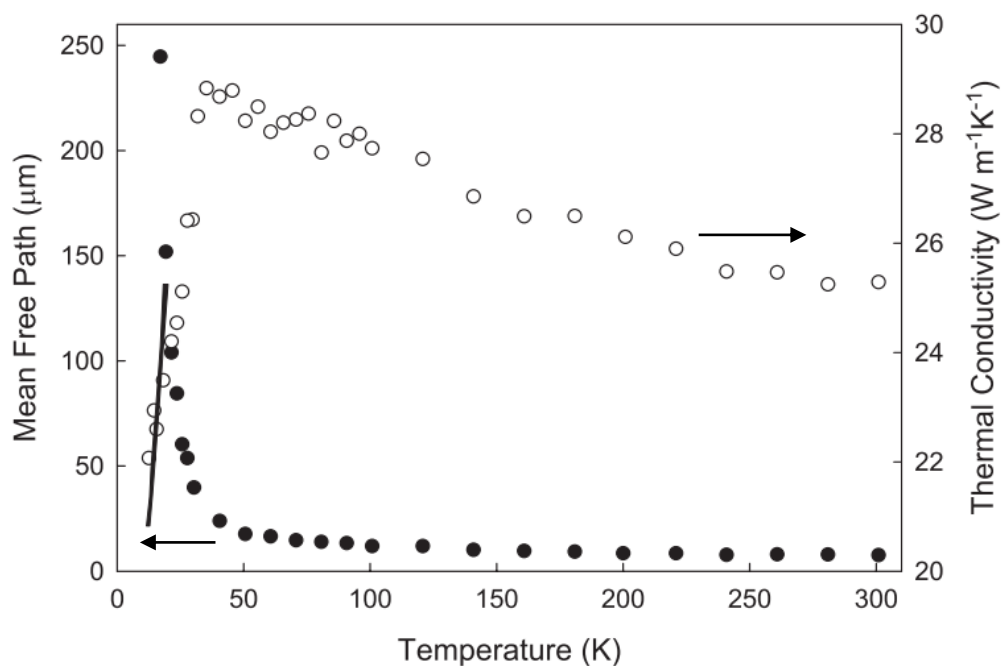
Figure 1.10 Temperature dependent mean free path and thermal conductivity of Na$_8$Si$_{46}$ single crystals[82]

Theoretically, deprived of its sodium guest atoms, the resulting neutral or guest-free Si$_{46}$ silicon clathrates is expected to have a direct-band gap around 1.3 to 1.9 eV[84,85] depending on the calculations, as suggested from **Figure 1.11,** such structured material is exhibiting better light absorption coefficients in the from the near-infrared (NIR) up to the visible range of light than diamond silicon.
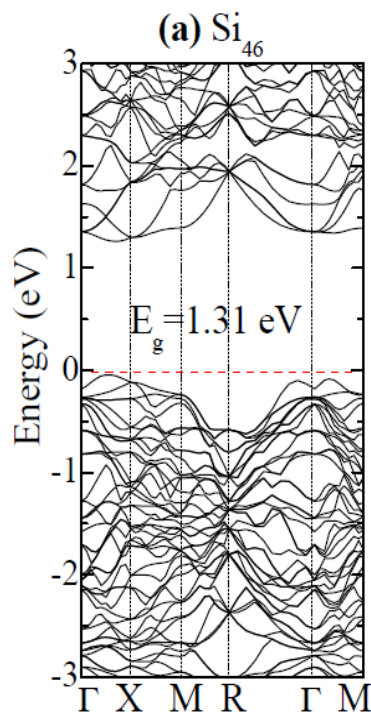
Figure 1.11 Band structure of the theoretical guest-free Si_{46}[84]

All these variations in the type I structure properties happen with barely any change in its lattice parameter with the temperature as shown on **Figure 1.12**[86]. However, Type I structure does not allow the removal of guest atoms from the structure without its decomposition. As of now, the only way to reach guest free Si_{46} is to react the Na_4Si_4 sodium silicide with an ionic liquid to allow an Hoffman-type elimination-oxidation reaction[87] to happen leading yet to the conversion of small quantities, around 20 mg, of neutral Si_{46}.
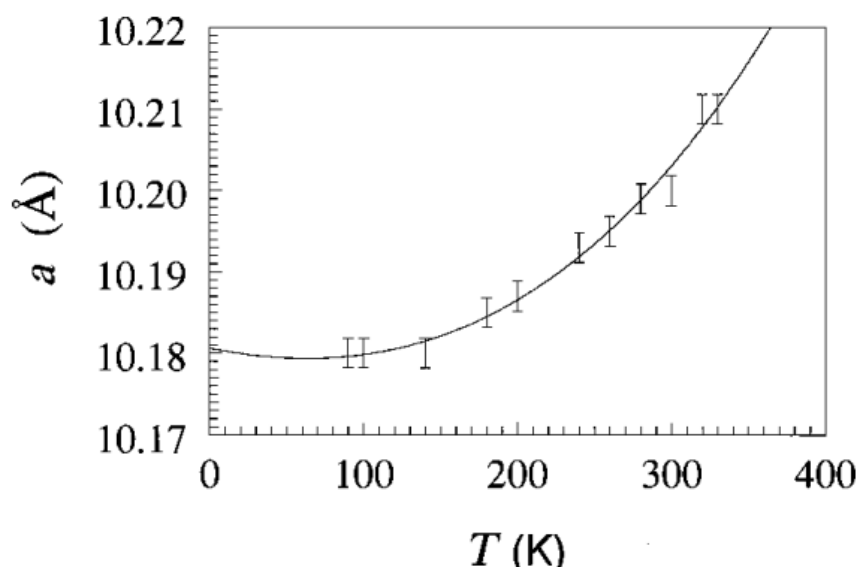
Figure 1.12 Temperature dependent lattice parameter of Na_8Si_{46} single crystals[86]

1.3.3 Type II Silicon Clathrates, $Na_{x \leq 32}Si_{136}$

Among the types of inorganic clathrate structures, Type II structure is the only one that allows both the removal and the insertion of guest atoms post-synthesis without degradation of the structure. Due to this unique property, the Type II silicon clathrate is a non-stoichiometric phase whose composition is ranging from guest-free Si_{136} to $Na_{24}Si_{136}$ and can even reach $Na_{32}Si_{136}$ as the eight large Si_{28} cages are able to host sodium dimers when submitted to high-pressure. Regarding the cages, the sixteen Si_{20} have a free radius $r_{II}(Si_{20}) = 0.198$ nm while the eight Si_{28} measure $r_{II}(Si_{28}) = 0.268$ nm[63]. $Na_{x \leq 32}Si_{136}$ is a cubic $Fd\bar{3}m$ with lattice parameters ranging from 14.62 to 14.79 Å depending on the sodium occupation. Its crystallographic structure is shown in **Figure 1.13** along with structural parameters given in **Table 1.7**. Sodium atoms can be removed or inserted in the cages by chemical[67], electrochemical[88] and diffusion process[89].
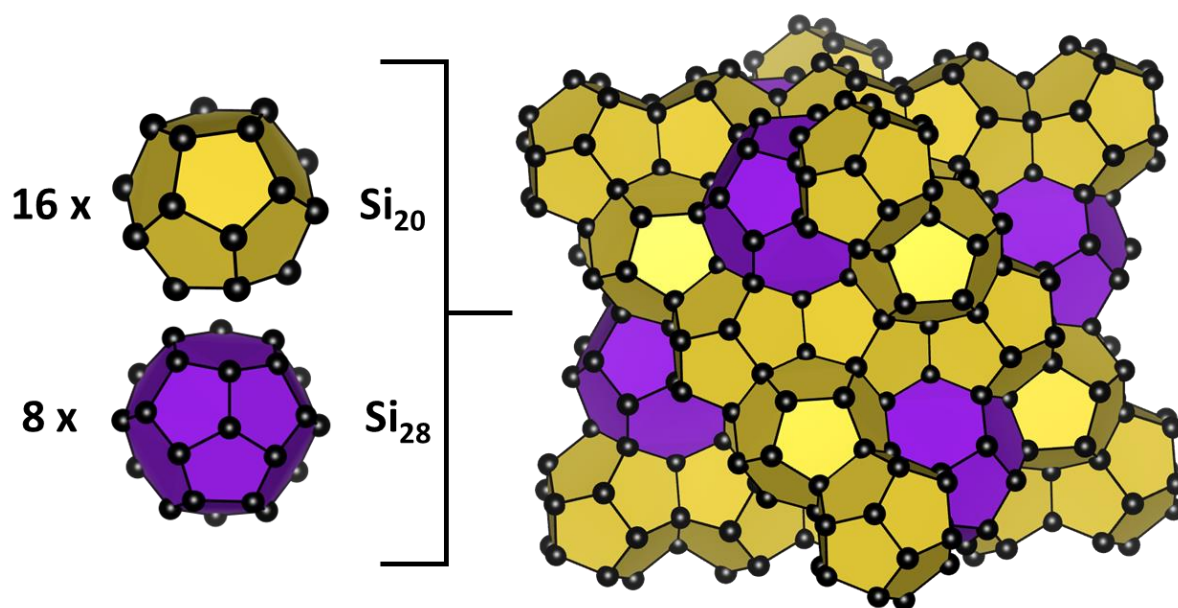
Figure 1.13 Crystallographic structure of the Type II Silicon clathrates made with Vesta

Table 1.7 Structural properties and atomic positions of the Type II Silicon clathrates Na_xSi_{46} with x from 0 to 32[89,99,124]

Na_xSi_{136} with x from 0 to 32[63,67,89]		
Structure		Cubic
Space Group		$Pm\bar{3}n$
Atomic positions	Si	8 Si1 in 8(a),
		32 Si2 in 32(e),
		96 Si3 in 96(g)
	Na	16α Na1 in 16(c)
		8β Na2 in 8(b)
		with α=0 to 1and β = 0 to 2
Lattice parameters (Å)		14.62 to 14.79
Cell volume (Å³)		3124.9 to 3228.7
Density (g.cm⁻³)		2.03 to 2.33

Counterintuitively, when submitted to sodium vapor, the first cage to be filled are the eight largest ones and the small cages are only going to be filled once it is done for all the eight large cages[90]. This phenomenon is due to a conjoined effect originating from better stabilization of the sodium atoms in the large cages due to their slightly off-centre position as they interact with sodium atoms inside of the neighbouring ($5^{12}6^4$) cages and from a lower energy barrier to enter the cages by the wider hexagonal faces. Another unexpected feature is that the evolution of the lattice parameters is not linearly increasing with the sodium concentration, a slight increase in the lattice parameters has been observed for low occupation resulting in a minimum lattice parameter usually reached for x between 6 and 8[91]. The cage occupation and lattice parameter trends are depicted in **Figure 1.14**[90].
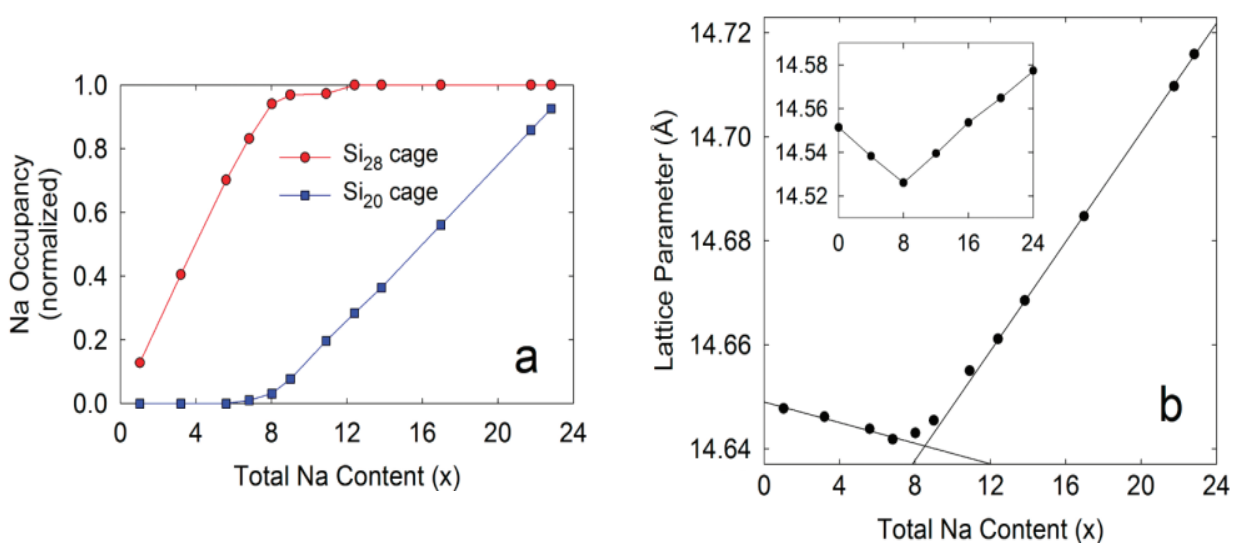
Figure 1.14 a) Occupation of the two different cages of the type II Silicon clathrates depending on the sodium occupation. b) Variations of the lattice parameters of the type II Silicon Clathrates depending on the sodium occupation[90].

Obviously, the sodium amount not only affects the structure of the type II silicon clathrates, but also impacts its properties and stability as it can be seen in **Figure 1.15**[69]. Type II silicon clathrates is a metallic phase for occupation above x = 8 with increasing electrical conductivity as sodium occupation increases. While keeping its metallic behaviour, when the large cages are being filled with two sodium atoms simultaneously, a specific positive temperature-dependent Pauli paramagnetism is observed as the Na-Na pairs are shifting from a disordered to ordered state at temperature below 90 K[89].
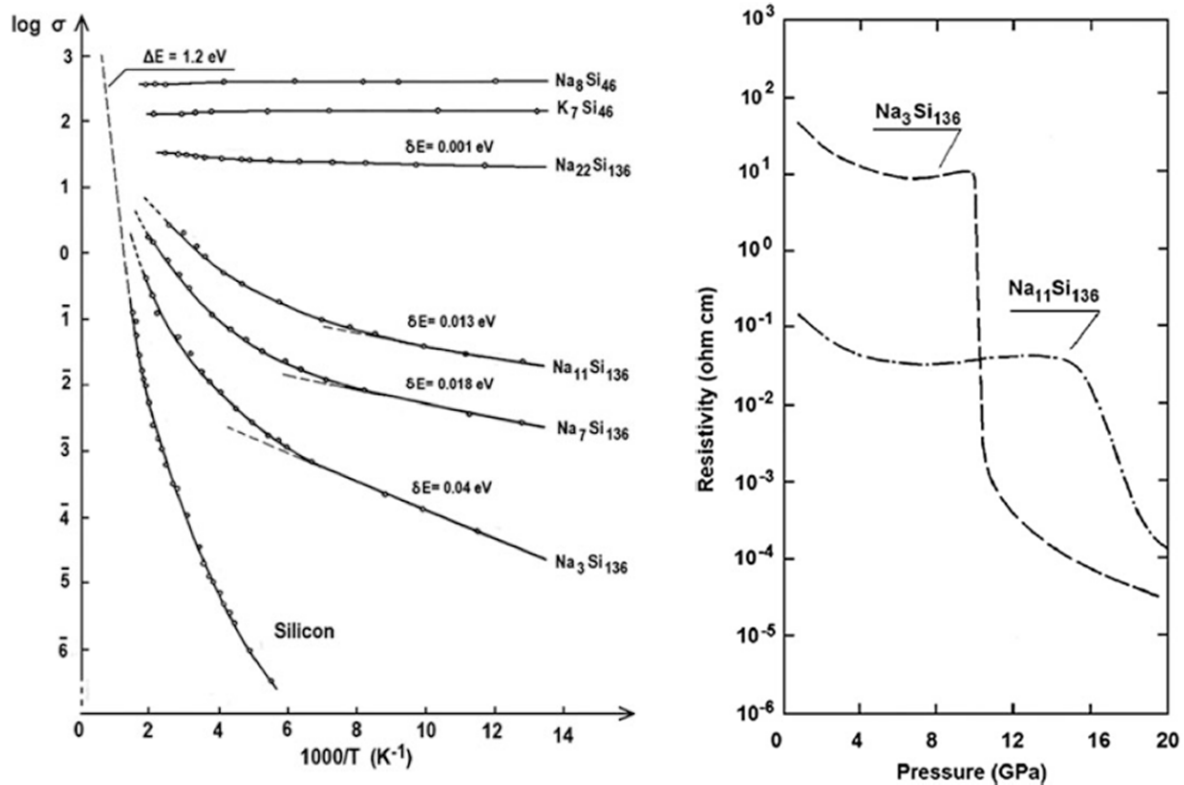
Figure 1.15 Left: Electrical conductivity versus reciprocal temperature behaviour depending on the Silicon Clathrates composition. Right: Resistivity variation as pressure is applied depending on Type II silicon clathrates composition[69].

However, when the occupation is reduced to x < 8 (**Figure 1.16**[92]) the type II silicon clathrate becomes a n-type semiconductor with a large energy bandgap given around 1.7 to 2.1 eV by calculations[93–95] and confirmed experimentally[96] with better adsorption coefficient in the NIR and visible range as compared to diamond silicon. These observations are similar to the one done on empty Si$_{46}$ with the major difference that type II Silicon clathrates has flexible and easily tuneable sodium guest occupations.
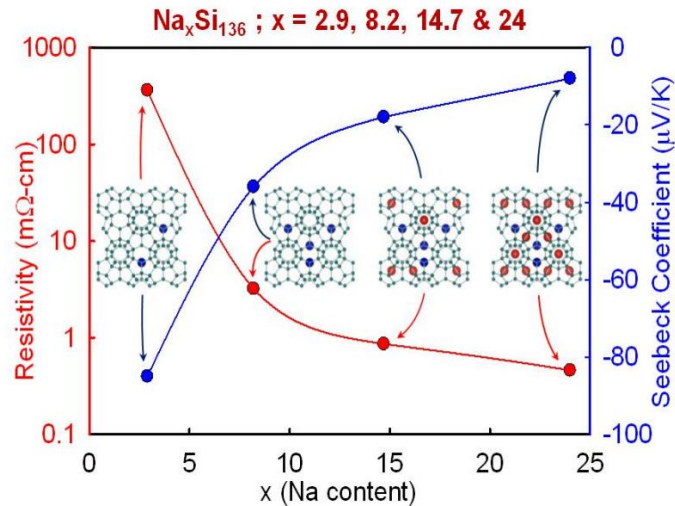
Figure 1.16 Room temperature Seebeck coefficient and resistivity versus sodium occupation of the type II structure[92].

Experiments on powdery samples allowed to witness the slight energy bandgap variation as the occupation is lowered, shown in **Figure 1.17**[97], emphasizing on the pathway to truly guest-free silicon clathrates in order to reach a slightly reduced and more favourable band gap. Additionally, this ability to accept and release guest atoms without significant change in the lattice parameters value is promising for its cycling durability in batteries. Finally, thermal conductivity of the type II silicon clathrates is logically increasing with the sodium content as visible in **Figure 1.18**[92].
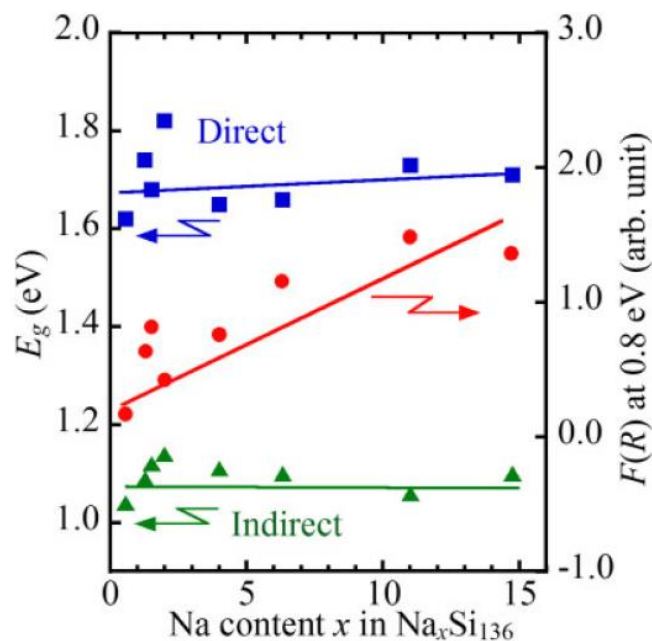
Figure 1.17 Value of the direct and indirect band gap versus the sodium concentration[97].
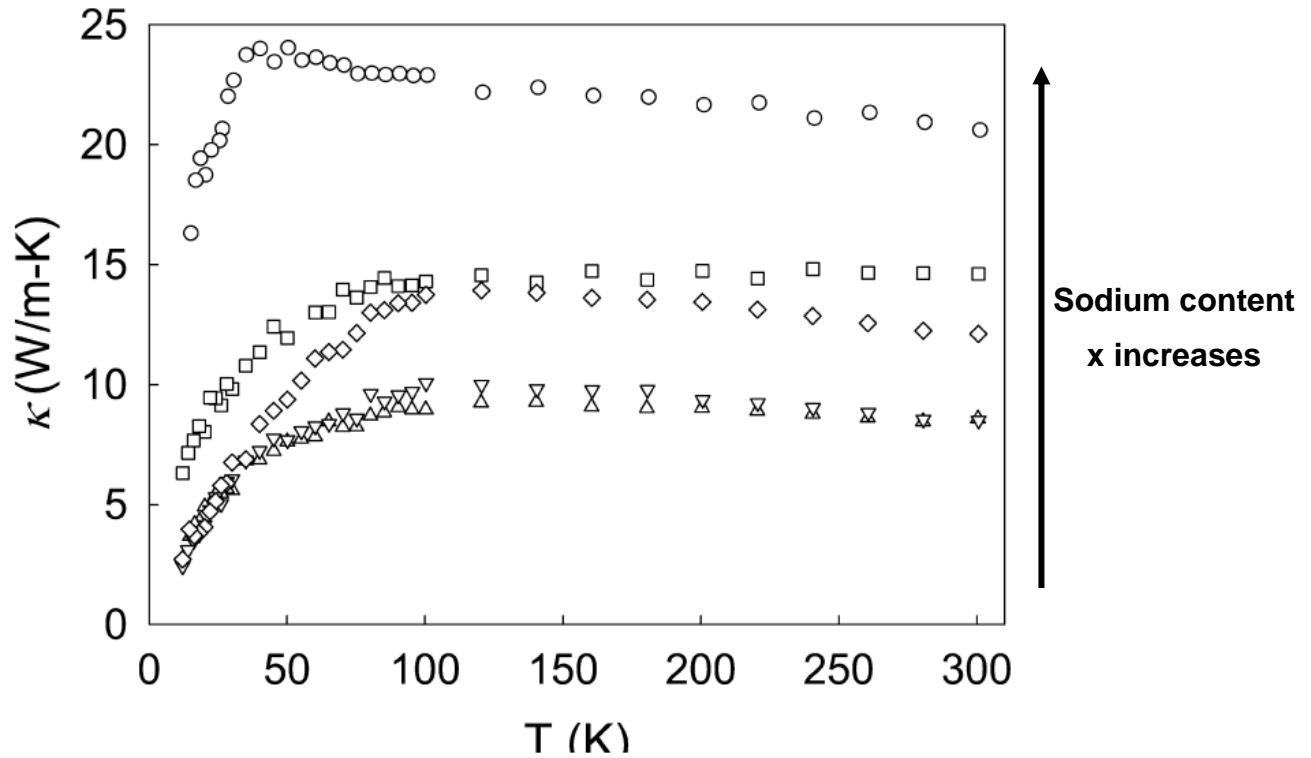
Figure 1.18 Thermal conductivity as function of temperature for Na_xSi_{136} for x =2.9, 5.1, 8.2, 14.7 and 24[92].

1.4 Synthesis of Silicon Clathrates

The type I and type II silicon clathrates of the Na-Si systems are alluring from thermoelectric, optoelectronics, batteries, and hydrogen storage. This diversity of applications implies the need to shape these materials under various forms, from polycrystalline powders to large single crystals along with silicon clathrates films and ultra-thin films. In this section, the wide diversity of synthetic routes according to the wished shape are enlightened.

1.4.1 Thermal decomposition

Among all the techniques, the first to be described is the thermal decomposition of Zintl phases[63] from which the discovery of silicon, and more generally inorganic clathrates originate. Thermal decomposition relies on the removal of the alkali cations from powdery A_xB_y zintl phases precursor[98], here Na_4Si_4, described in 1.3.2. when heated

under vacuum inducing the rearrangement into clathrates of the species from the polyanionic clusters hosting the remaining alkali metals as shown on **Figure 1.19**[99].
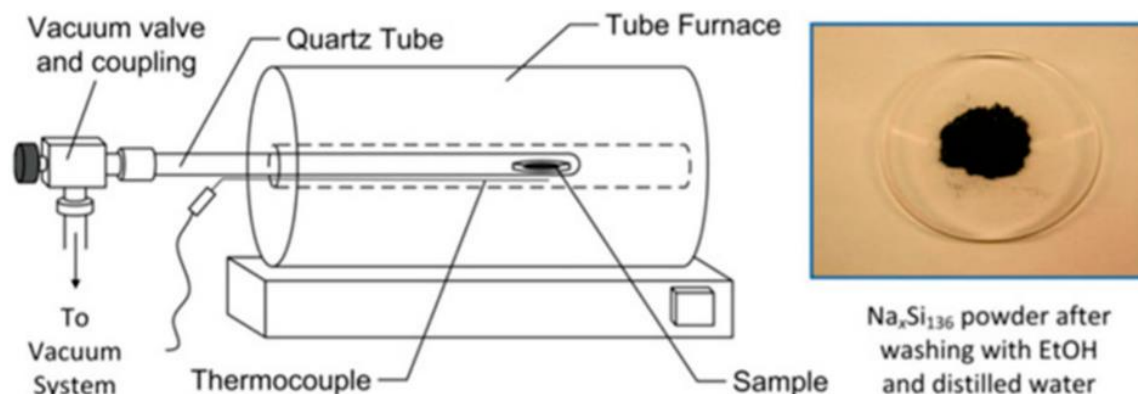
Figure 1.19 Schematic of the thermal decomposition setup used for the synthesis of silicon clathrates[99].

The most crucial parameters of the thermal decomposition are the temperature, the amount of the vapor pressure of the alkali metal[100]. For minimized sodium vapor pressure, the formation of silicon clathrates occurs around 400 to 430°C with almost no diamond silicon impurities, whereas presence of sodium vapor imposes higher temperature leading to the partial decomposition of the silicon clathrates into Si-I[91]. In order to reduce the sodium vapor, dynamic vacuum system equipped with a cold plate[101] inducing the condensation of sodium at its surface and showed that in this case selective type II silicon clathrates is reached. An other important point is the high reactivity of the Na_4Si_4 phase[99] with any trace of humidity motivating the use of setup installed in inert glove-box and the choice of the crucible material which should not be reactive with sodium such as tungsten or stainless steel.

The resulting silicon clathrate powders usually have crystallites in the micron range and exhibit large amounts of defects due to the sudden phase rearrangement from the zintl to the clathrate phase[102]. Additionally, thermal decomposition shows some limitations in terms of phase selectivity and reproducibility of the experimental parameters[103].

Production of single crystals is also possible using a modified setup, shown in **Figure 1.20**[104], in which the Na_4Si_4 precursor is placed in a closed volume under uniaxial pressure along with graphite to trap any amount of sodium vapour. The precursor and

the graphite are separated using a NaCl layer in order to allow the sodium diffusion while preventing direct reaction between Na_4Si_4 and the graphite.
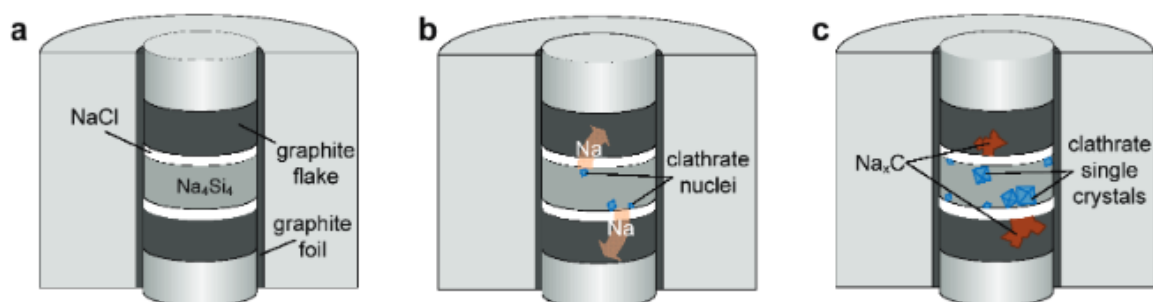
Figure 1.20 Schematic of the custom setup for crystal growth using thermal decomposition during a) the initial configuration b) Beginning of the local composition change and nucleation of the clathrates phase c) Formation of silicon clathrates crystals and sodium intercalated graphite[104].

Performing thermal decomposition in this setup allow the removal of sodium atoms from the precursor and their quick reaction with the graphite inducing the rearrangement into silicon clathrates and the intercalation of sodium in the graphite. Na_8Si_{46} and $Na_{24}Si_{136}$ single crystals of several hundreds of microns are obtained after 8h of thermal decomposition at 585°C and 665°C respectively.

Finally, aiming to the synthesis of silicon clathrates films and thin-films, two different ways to adapt the thermal decomposition reaction are reported.

First report of tuned thermal decomposition consists in using a diamond silicon substrate which will be successively covered by first an n-type diamond silicon layer and then a sodium metal layer. Then the covered silicon substrate is heated at temperature from 500 to 600°C in inert atmosphere or in vacuum resulting on the formation of a Na_4Si_4 film at the sodium/silicon interface. The thermal decomposition of the Zintl precursor is performed in dynamic vacuum allowing to obtain Na_8Si_{46} and $Na_{x<10}Si_{136}$ clathrates polycrystalline film after the cleaning of the leftover sodium layer in ethanol and distilled water[105]. The concept of the two-step decomposition process is based on the use of a silicon substrate and a silicon layer to transform it into Na_4Si_4 precursor. The precursor is then decomposed into the desired clathrates.

Later, this concept is at the origin of a related method to get silicon clathrate films and thin films. The two steps are the same: formation of the Zintl precursor and its thermal decomposition, except that the Zintl precursor here is obtained by the reaction of a silicon wafer with sodium vapor originating from a metallic sodium source under argon atmosphere[106]. This is a done by inserting a piece of sodium at the bottom of a tantalum

or stainless-steal boat which will be fully covered by the diamond silicon substrate or layer on a sapphire as depicted on **Figure 1.21**.
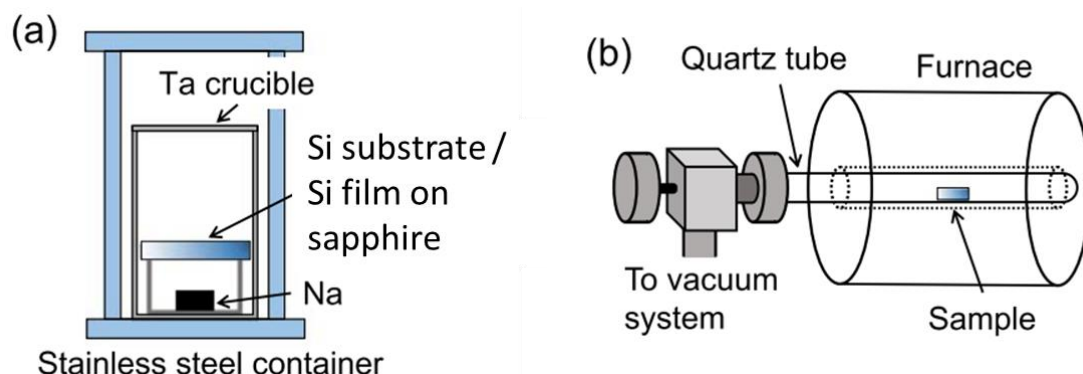
Figure 1.21 Schematic of an experimental two-step thermal decomposition setup for the a) formation of the precursor step b) thermal decomposition step[106].

This system is then inserted in a stainless-steal vessel and heated to create the zintl precursor film. In some setups, the system is first inserted in a tantalum crucible that will be put in the vessel to catch any trace of leftover humidity[107]. Once the precursor film obtained, the sample is transferred to a furnace under dynamic vacuum to perform the thermal decomposition into silicon clathrates. To prevent any exposure of the diamond silicon substrate, the sodium and the subsequent Na_4Si_4 film to either O_2 or ambient humidity during loading and transfers, these steps are usually performed using a dedicated glovebox of inert atmosphere. Using such setup, thick films of several microns are commonly obtained using a silicon substrate as the silicon source[106,107], while 700 nm films was obtained using silicon layer deposited on a sapphire substrate[95]. A study also hints toward a phase selectivity according to the silicon substrate orientation, with type I and type II preferentially obtained using diamond Si (1 0 0) and (1 1 1) respectively[108].

Recently, a refreshing technique was developed for germanium clathrate films based simultaneously on a portable vacuum evaporation and annealing system (pVEAS) and on an amorphous germanium covered sapphire substrate[109]. The amorphous germanium sample is first inserted in the mobile chamber in a glove box and a piece of sodium is placed on an underneath tungsten basket. The chamber is then attached to a vacuum system and an infrared lamp allowing the evaporation of the sodium from the tungsten basket and is condensation of the amorphous germanium layer under high vacuum below 10^{-3} Pa. Once the sodium evaporated, the sapphire substrate is heated using a graphite sheet illuminated by the infrared lamp at vacuum below 10^{-4}

Pa allowing the thermal decomposition of the Na_4Ge_4 into germanium clathrate. The working principle is summarized on **Figure 1.22**. High quality type II germanium clathrates thin films are obtained this way and thus it represents a very promising technique for a future efficient production of silicon clathrate thin films.
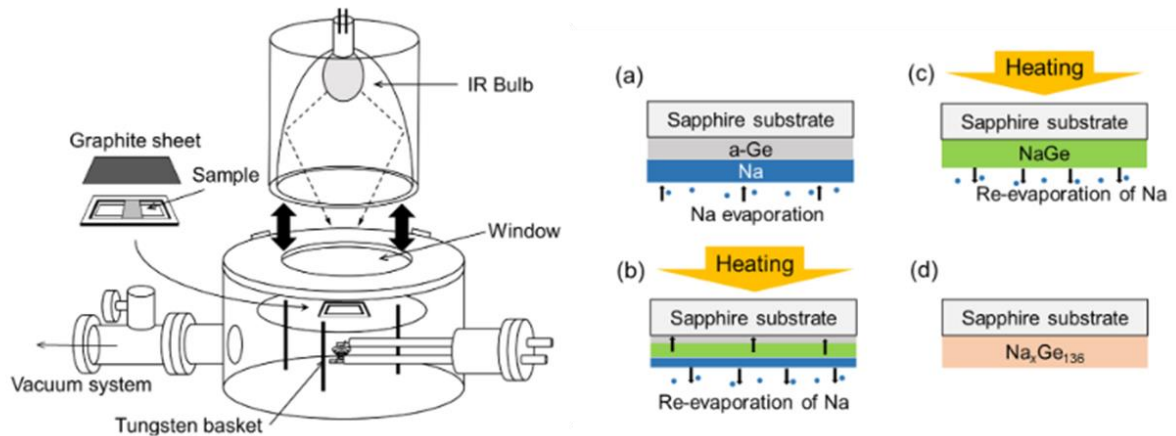
Figure 1.22 On the left, schematic of the pVEAS setup. On the right, the suspected formation of the germanium clathrate film using the pVEAS[109].

1.4.2 Flux synthesis

In order to synthesize single crystal of non-congruently melting silicon clathrates, alternative methods are required and depicted in **Figure 1.23**[110]. Flux growth is one of them, allowing the reaction of the reagents dissolved in a flux, a high temperature solvent with single crystal reaching easily the centimetres scale. The salt or molten metal solvent is carefully selected according to its properties and its interaction with the reagents and the products.
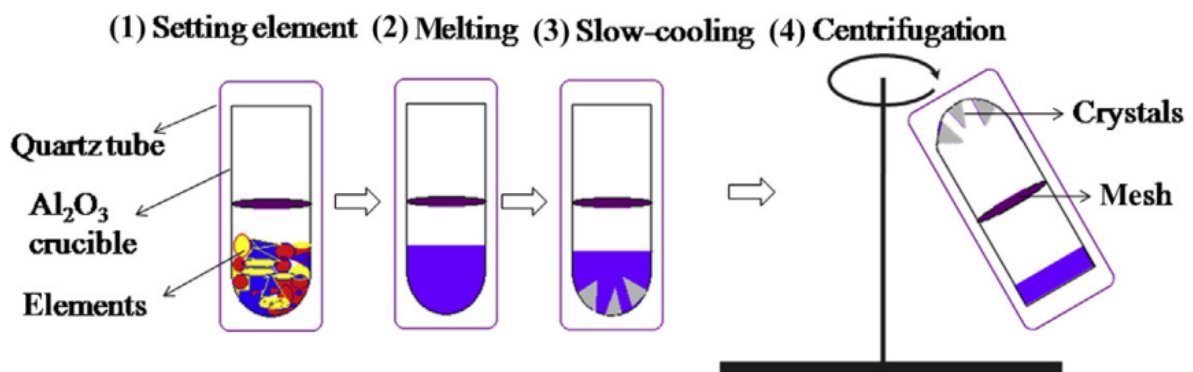
Figure 1.23 Schematic self-flux method[110].

Interestingly, intermetallic clathrates usually contain elements which can be used as a part of the molten solvents[111]. The use of such reactive solvents with lower melting temperature than silicon is the pathway generally used for the growth of inorganic clathrates. A good example is the use of aluminium as a solvent for the synthesis of $Ba_8Al_xSi_{46-x}$ clathrates[112]. A mixed salt and metal flux consisting of alkali halide and aluminium was used to obtain $A_8Al_8Si_{38}$ clathrates, with A = K, Rb, Cs[113] an quaternary type I Na-Sr-Si-Ga clathrates were reported using a Na–Sr–Ga–Si–Sn flux[114].

For Na-Si silicon clathrates, both type I and fully occupied type II structures have been obtained using a Na-Sn flux at 823 K for 12 h in which Na_4Si_4 is dissolved allowing the growth of single-crystal of around 1 mm in size. The seeded growth of these single-crystals using the same flux with addition sodium silicide was demonstrated and shown on **Figure 1.24**[115].
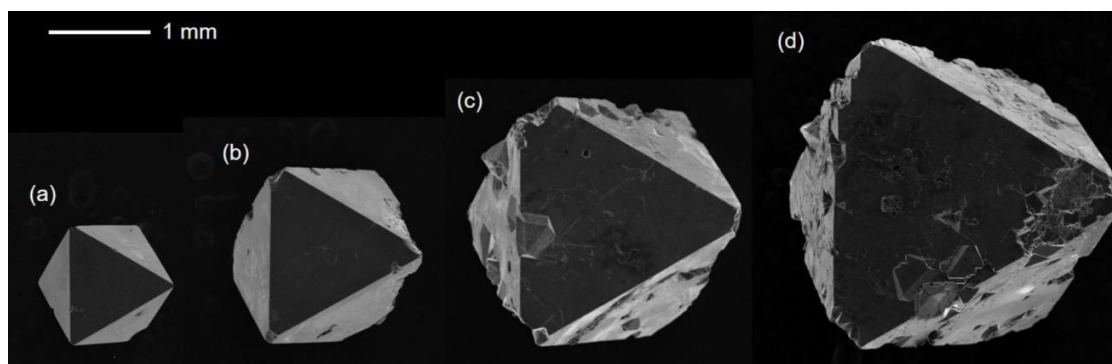
Figure 1.24 SEM images of a) seed crystal grown by Na-Sn flux and seeded grown crystals obtained after b) 12 hours c) 24 hours and d) 36 hours[115].

1.4.3 Other alternative synthesis

A. Crystallization from the melts

Crystallization from the melts is a classic process toward the acquisition of large and pure single crystal of the wished compounds. Most famous methods of such crystallization are the Czochralski (CZ) and the Floating Zone (FZ), visible in **Figure 1.25**[116]. One of a major difficulty of such methods for inorganic clathrates is the need of congruently melting compounds.
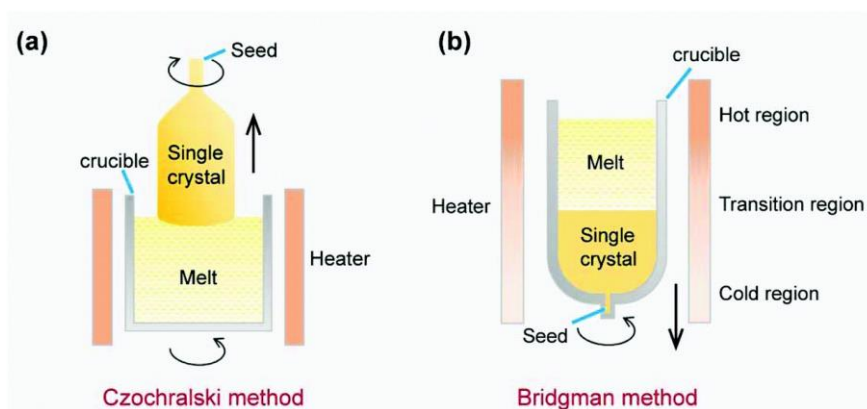
Figure 1.25 Schematic of the typical methods of single-crystal growth based on the solid-liquid transition[116].

The CZ method consists in the growth of single crystals by the progressive pulling of a starting seed crystal from the melt. Due to the dependence on the method on the reaction atmosphere, only silicon clathrates with low vapour pressures such as $Ba_8Al_xSi_{46-x}$ are grown into single crystal reaching up to 30 mm-length and 10 mm-diameter[117].

The FZ technique uses a mobile heater to induce locally the crystallization on a rotating polycrystal under into a single crystal. Rare-earth doped silicon clathrates single crystals such as the $Ba_7Ce_1Au_xSi_{46-x}$[118] with enhanced thermopower were obtained by this method. Moreover, ternary $Sr_8Ga_xSi_{46-x}$ silicon clathrates are also grown to dimension comparable to the one made using the CZ method[119].

B. Redox reaction

Redox reaction in soft condition is an alternative way to transform solid precursor into metastable clathrates unreachable at any temperature of pressure conditions at low temperatures while reaching high phase selectivity. These precursors are converted into clathrates using ionic liquids inside a sealed ampoule at temperature below 400 K[69]. High purity is usually obtained from the precise control of the reaction conditions and from the generally water-soluble side products. However, some reports of decomposition of the ionic liquid during the reaction led to the product's irreversible pollution. To solve this issue, redox reaction are gradually using more and more gaseous oxider such as HCl or organic halides rather than ionic liquids[120]. The two different methods to perform redox reaction are shown in **Figure 1.26**[121].
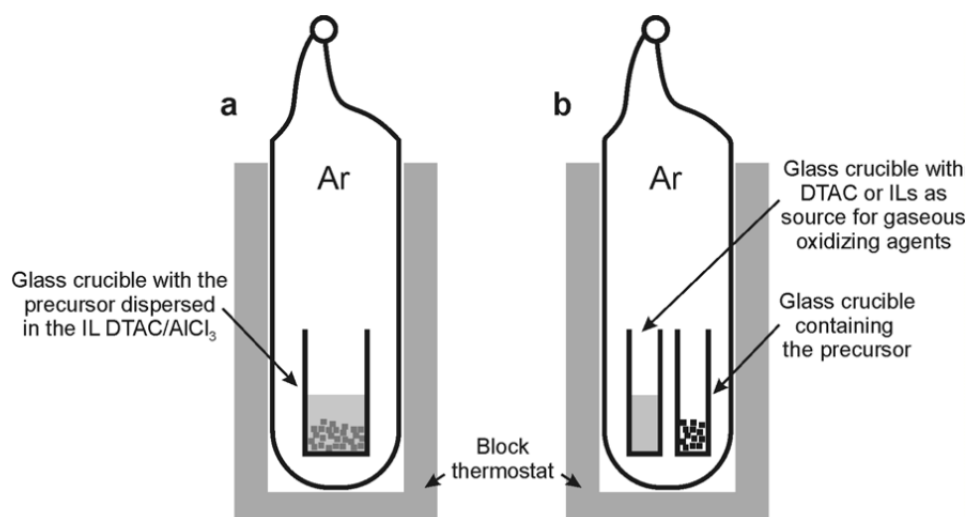
Figure 1.26 Schematic of redox reaction using a) liquid-solid reaction b) gas-solid reaction[121].

Zintl precursors used in thermal decomposition are also transformed into clathrates by either liquid-solid or gas-solid redox reaction, resulting for example in the synthesis of $Na_2Ba_6Si_{46}$[122] along with Na-Si, K-Si and Ba-Si clathrates[120,123] of type I and II with high phase selectivity.

Redox reactions are also of interest for the synthesis of guest-free clathrates. For example, transformation of the Zintl phase $Na_{12}Ge_{17}$ by reacting it in $DTAL/AlCl_3$ ionic liquid allowing synthesis of Na_xGe_{136} for x ranging from 0 to 24[124] or from Na_4Ge_9 in the same ionic liquid for direct conversion into the neutral clathrate Ge_{136}[125]. More recently, the previously mentioned Si_{46} synthesis from Na_4Si_4 in alkylammonium-$AlCl_3$ ionic liquid, through Hofmann elimination-oxidation reaction similar to the Ge_{136} pathway, was reported[87].

C. Spark-plasma sintering

Spark-plasma sintering (SPS) is known for being a compaction technique turning microcrystalline powders into polycrystalline pellets by combining high pressure and high temperature condition in inert atmosphere or vacuum. Thanks to the reached temperature, SPS is also an interesting technique for crystal growth of intermetallics.

Regarding silicon clathrates, SPS can be used in the crystal growth of simple binary system to much more complex ones such as the rare-earth doped quinary clathrate $Ba_6E_2AuGa_xSi_{45-x}$ with E= Sr, Eu[126]. SPS was also the first step toward type I and type II Na-SI clathrates single-crystals, deepening the knowledge about these phases' properties[127]. Na_8Si_{46} and $Na_{24}Si_{136}$ were obtained at 450°C and 600°C respectively and the shape could be selected from powders at 60 MPa to single-crystals at 100 MPa[128] using the setup visible on **Figure 1.27**[127].
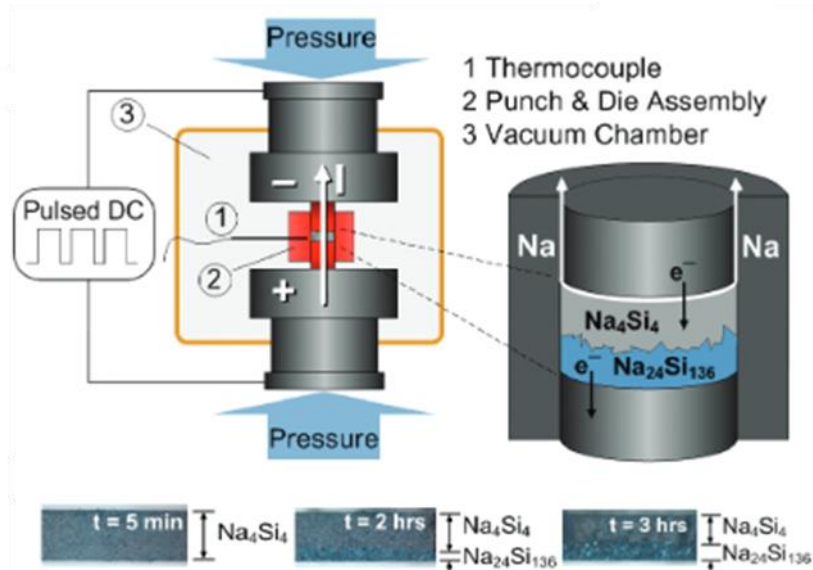
Figure 1.27 Top: SPS synthesis setup for Silicon Clathrates growth. Bottom: Cross-section of the samples for SPS at 600°C and 100 MPa[127].

1.5 Applications of Silicon Clathrates

While the Na-Si Silicon clathrates have less interest than other ternary or quaternary silicon clathrates for thermoelectric applications, they are promising candidates for applications such as hydrogen storage, batteries and photovoltaics[64] which required their production as films.

1.5.1 Hydrogen storage and batteries

Organic clathrates are known since their discovery for being able to entrap gaseous species such as methane, CO_2 or H_2 among others thanks to steric barrier effect and hydrogen bonds. In comparison the host-guest stability in inorganic clathrates mainly relies on electrostatic interaction which make difficult the insertion of such gaseous species, still encapsulation of hydrogen in the large ($5^{12}6^2$) cages of the type I Na-Si clathrates was observed. This encapsulation led to compound with the formula $Na_{5.5}(H_2)_{2.15}Si_{46}$ where the hydrogen is very mobile and not bound in any way to the silicon framework. The drawback of using Na-Si as such is the high desorption temperature of 400°C[129], which make it unusable for most practical applications. However, DFT calculations showed that small inclusion of aluminium or carbon atoms in the silicon framework could lead to room temperature desorption with possible storage up to 10 wt.% with only a minor expansion of the lattice[81].

This ability of silicon clathrates to let species enter and leave their framework without consequent lattice expansion is also a massive advantage for lithium and sodium batteries applications as anode materials. Diamond silicon for example exhibits a very high specific capacity 4200 mAh/g in comparison to the 372 mAh/g graphite commonly used but is rejected due to the significant volume change during the lithiation / delithiation of 300%.

Experiments of lithiation on fully occupied type II silicon clathrates showed that the specific capacity was of 2400 mAh/g but is quickly reducing as the phase is undergoing gradual amorphization[130] while study on Na_1Si_{136} show the preservation of the structure for a specific capacity of 1600 mAh/g[131]. Type II silicon clathrates appears more promising for sodium ion applications but still need some more understanding on the sodium circulation in the structure during the cycling[132].

Regarding Type I silicon clathrates, the purposedly emptied Si_{46} structure has been demonstrated to exhibit initial specific capacity of around 700 mAh/g going up to 800 mAh/g at the 50th cycle to finally be reduced to 550 mAh/g after 1000 cycles. A 99% coulombic efficiency was maintained during the vast majority of the cycles as seen on **Figure 1.28**[87]. These values are in agreement with calculations hinting toward the insertion of a total of 48 lithium atoms[133] in the structure and the observed expansion

of the lattice was quite low (less than 40%). Such Si_{46} anode materials with elevated specific capacity and long-term cycling durability are alluring for lithium-ion batteries.
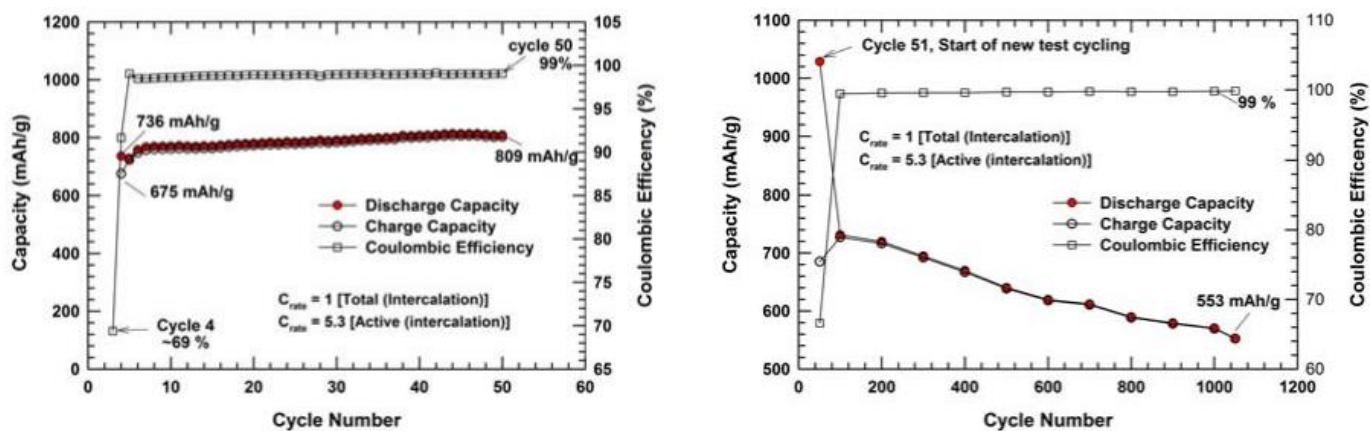
Figure 1.28 Specific capacity and coulombic efficiency of Si_{46} electrode during the a)4th to the 50th cycle b) 51st to the 1000th cycle[87].

1.5.2 Solar cells

As forementioned in the introduction, diamond silicon with its indirect band gap is an inefficient light absorber material requiring consequent layer of tens of microns to harvest successfully more than 95 % of the incoming light. Ideally, semiconducting allotrope of silicon with direct band gap such as the predicted guest-free Si_{46} and Si_{136} are promising candidates toward novel all silicon solar cells[84,85,93]. Extended calculations of alternative silicon clathrate structures using unusual polyhedral cages predicted more than forty metastable structures, including eleven among them even have a direct or quasi-direct bandgap in the 1.0 to 1.8 eV range and thus are alluring for photovoltaics applications[34,35].

In addition to these calculations, characterization of the silicon clathrate properties and especially the evidence of its quasi-direct band gap of the Na_xSi_{136} clathrates[134] when x is below 8 stimulated the synthesis of silicon clathrate films described in the section 1.4.1. As expected, both silicon clathrates exhibits higher absorption coefficients than diamond silicon in the NIR and visible range of light as shown on **figure 1.29**[135]. For example, a 2 to 3 micrometer film of semiconducting type II Na-Si clathrate would be able to absorb more than 95 % of the incoming light[95] resulting in thinner layers than the one currently needed for diamond silicon.
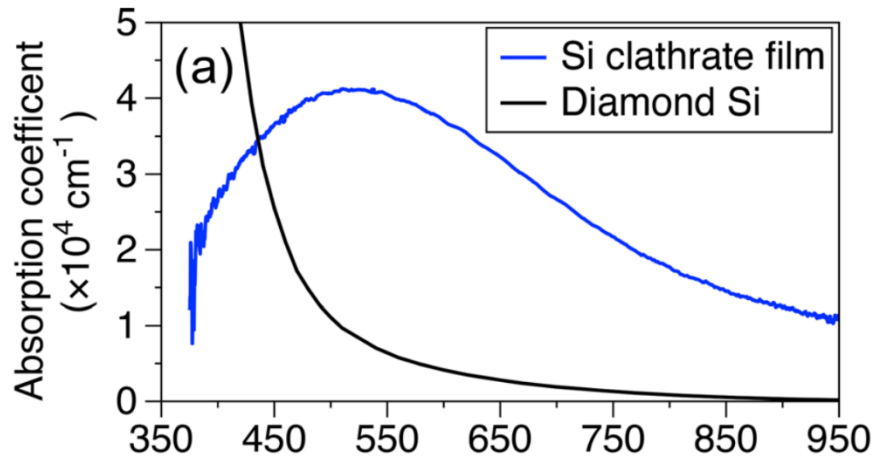
Figure 1.29 Absorption coefficient of a 700 nm thick $Na_{x<8}Si_{136}$ film in blue, of diamond silicon in black[135].

Moreover, calculations and experiments on type II silicon-germanium clathrates showed that the bandgap would be tuneable in the 0.8 (Ge_{136} band gap) to 1.7 (Si_{136} band gap) according to the Si/Ge ratio[94] as shown on **Figure 1.30**[136]. The synthesis of such thin films would allow the conception of a material with the ideal 1.3 eV direct band gap by controlling accurately this type II SiGe clathrate composition.
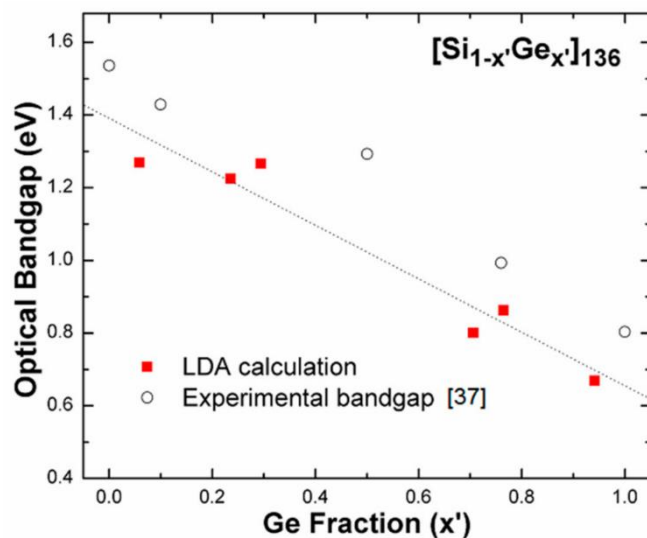
Figure 1.30 Theoretical and experimental optical band gap value according to the Ge fraction of the type II SiGe clathrate[136].

Early basic solar device have been reported, using a n-type Si_{136} clathrates grown on a p-doped diamond silicon substrate[108]. The resulting device successfully showed a downward shift under AM1.5 light exposure as shown on **Figure 1.31**[108]. A low short-circuit current of 9.2 nA was measured on this basic device, along with a 0.036 open-circuit voltage and an efficiency of 10^{-5} %. Despite an especially low efficiency, this simple device demonstrates the photoresponse of Si_{136} silicon clathrate..
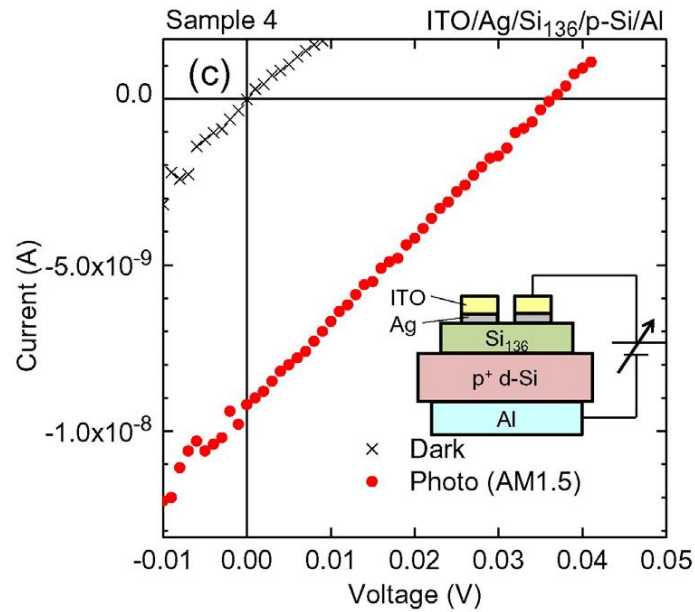
Figure 1.31 I-V of the early Si_{136}/p-doped diamond silicon device in the dark and under AM1.5 exposure[108].

The low efficiency is suspected to originate mainly from the poor overall quality of the polycrystalline films that usually contains extensive amount of defects due to the nature of the thermal decomposition reaction along with the low adhesion on the underlying diamond silicon substrate since no epitaxy is obtained[97]. To reach higher efficiency values, a deeper understanding of the silicon clathrates materials and of the thermal decomposition is required. It is exactly the purpose of this thesis work.

1.6 Summary of Chapter 1

In this introducing chapter, the wide diversity of the silicon allotropy has been exposed and the low-density allotropes of silicon have been highlighted due to their alluring properties for photovoltaic application. The focus was mainly put on the unique guest-host compounds that are the silicon clathrates, in particular those called of type I, (Na_8Si_{46}) and type II (Na_xSi_{136}.). Their specific clathrate structures made of a silicon framework of interconnected polyhedral cages filled by sodium guest atoms and their consequent properties as guest-host structures have been defined.

While easily obtained under the form of powders or single crystals by various detailed methods, the synthesis of silicon clathrates as films and thin films remains a challenge. The two-step thermal decomposition process is so far the only reliable way to obtain silicon clathrates films in addition to be partially understood. As silicon clathrates films became feasible, they started to be considered as possible candidates for applications ranging from batteries, hydrogen storage to photovoltaics.

The upcoming Chapter 2 is dedicated to the synthesis and characterizations of the silicon clathrates films. The description of the setup used for the two-step thermal decomposition process will be given. The various parameters of the reaction and their effects on the obtained films will then be investigated in order to reach efficient and selective synthesis of either type I or II of silicon clathrates. A thorough characterisation of both type I and II silicon clathrates will be performed and shouldered by DFT calculations.

References of Chapter 1

(1)   Maldonado, S. The Importance of New "Sand-to-Silicon" Processes for the Rapid Future Increase of Photovoltaics. *ACS Energy Lett.* **2020**, *5* (11), 3628–3632. https://doi.org/10.1021/acsenergylett.0c02100.

(2)   Shockley, W.; Queisser, H. J. Detailed Balance Limit of Efficiency of P-n Junction Solar Cells. *Journal of Applied Physics* **1961**, *32* (3), 510–519. https://doi.org/10.1063/1.1736034.

(3)   Repins, I.; Contreras, M. A.; Egaas, B.; DeHart, C.; Scharf, J.; Perkins, C. L.; To, B.; Noufi, R. 19·9%-Efficient ZnO/CdS/CuInGaSe ^{2} Solar Cell with 81·2% Fill Factor: 19·9% EFFICIENT Cu(In, Ga)Se ^{2} -BASED THIN-FILM SOLAR CELLS. *Prog. Photovolt: Res. Appl.* **2008**, *16* (3), 235–239. https://doi.org/10.1002/pip.822.

(4)   Rau, U.; Schock, H. W. Electronic Properties of Cu(In,Ga)Se2 Heterojunction Solar Cells–Recent Achievements, Current Understanding, and Future Challenges. *Appl Phys A* **1999**, *69* (2), 131–147. https://doi.org/10.1007/s003390050984.

(5)   *Properties of Crystalline Silicon*; Hull, R., Institution of Electrical Engineers, Eds.; EMIS datareviews series; INSPEC: London, 1999.

(6)   Goodrich, A.; Hacke, P.; Wang, Q.; Sopori, B.; Margolis, R.; James, T. L.; Woodhouse, M. A Wafer-Based Monocrystalline Silicon Photovoltaics Road Map: Utilizing Known Technology Improvement Opportunities for Further Reductions in Manufacturing Costs. *Solar Energy Materials and Solar Cells* **2013**, *114*, 110–135. https://doi.org/10.1016/j.solmat.2013.01.030.

(7)   Kuhlmann, A. M. The Second Most Abundant Element in the Earth's Crust. *JOM* **1963**, *15* (7), 502–505. https://doi.org/10.1007/BF03378936.

(8)   Furgal, J. C.; Lenora, C. U. Green Routes to Silicon-Based Materials and Their Environmental Implications. *Physical Sciences Reviews* **2020**, *5* (1), 20190024. https://doi.org/10.1515/psr-2019-0024.

(9)   Eriksson, G.; Hack, K. IV.7 - Production of Metallurgical-Grade Silicon in an Electric Arc Furnace. In *The SGTE Casebook (Second Edition)*; Hack, K., Ed.; Woodhead Publishing Series in Metals and Surface Engineering; Woodhead Publishing, 2008; pp 415–424. https://doi.org/10.1533/9781845693954.4.415.

(10)   Maurits, J. E. A. Chapter 2.6 - Silicon Production. In *Treatise on Process Metallurgy*; Seetharaman, S., Ed.; Elsevier: Boston, 2014; pp 919–948. https://doi.org/10.1016/B978-0-08-096988-6.00022-5.

(11)   Bye, G.; Ceccaroli, B. Solar Grade Silicon: Technology Status and Industrial Trends. *Solar Energy Materials and Solar Cells* **2014**, *130*, 634–646. https://doi.org/10.1016/j.solmat.2014.06.019.

(12)   Saga, T. Advances in Crystalline Silicon Solar Cell Technology for Industrial Mass Production. *NPG Asia Mater* **2010**, *2* (3), 96–102. https://doi.org/10.1038/asiamat.2010.82.

(13)   Budhraja, V.; Misra, D.; Ravindra, N. M. Advancements in PV Multicrystalline Silicon Solar Cells from 1980 to 2010 - An Overview. In *2011 37th IEEE Photovoltaic Specialists Conference*; IEEE: Seattle, WA, USA, 2011; pp 001032–001037. https://doi.org/10.1109/PVSC.2011.6186128.

(14)   Hull, R. *Properties of Crystalline Silicon*; IET, 1999.

(15)   Little, R. G.; Nowlan, M. J. Crystalline Silicon Photovoltaics: The Hurdle for Thin Films. *Progress in Photovoltaics: Research and Applications* **1997**, *5* (5), 309–315. https://doi.org/10.1002/(SICI)1099-159X(199709/10)5:5<309::AID-PIP180>3.0.CO;2-X.

(16)   Basore, P. A. Defining Terms for Crystalline Silicon Solar Cells. *Prog. Photovolt: Res. Appl.* **1994**, *2* (2), 177–179. https://doi.org/10.1002/pip.4670020213.

(17)   Sharma, M.; Panigrahi, J.; Komarala, V. K. Nanocrystalline Silicon Thin Film Growth and Application for Silicon Heterojunction Solar Cells: A Short Review. *Nanoscale Adv.* **2021**, *3* (12), 3373–3383. https://doi.org/10.1039/D0NA00791A.

(18)   Matsuda, A. Microcrystalline Silicon.: Growth and Device Application. *Journal of Non-Crystalline Solids* **2004**, *338–340*, 1–12. https://doi.org/10.1016/j.jnoncrysol.2004.02.012.

(19)   Franz, Y.; Runge, A. F. J.; Oo, S. Z.; Jimenez-Martinez, G.; Healy, N.; Khokhar, A.; Tarazona, A.; Chong, H. M. H.; Mailis, S.; Peacock, A. C. Laser Crystallized Low-Loss Polycrystalline Silicon Waveguides. *Opt. Express, OE* **2019**, *27* (4), 4462–4470. https://doi.org/10.1364/OE.27.004462.

(20)   Zhu, F.; Singh, J. Approach to Study the Relation between Optical Energy Gap and Hydrogen Concentration in Hydrogenated Amorphous Silicon Thin Films. *Journal of Applied Physics - J APPL PHYS* **1993**, *73*, 4709–4711. https://doi.org/10.1063/1.352742.

(21) Gaspari, F.; Quaranta, S. 2.5 PV Materials. In *Comprehensive Energy Systems*; Dincer, I., Ed.; Elsevier: Oxford, 2018; pp 117–149. https://doi.org/10.1016/B978-0-12-809597-3.00215-7.

(22) Glunz, S. W.; Preu, R. 1.14 - Crystalline Silicon Solar Cells – State-of-the-Art and Future Developments☆. In *Comprehensive Renewable Energy (Second Edition)*; Letcher, T. M., Ed.; Elsevier: Oxford, 2022; pp 293–324. https://doi.org/10.1016/B978-0-12-819727-1.00129-1.

(23) Yoshikawa, K.; Kawasaki, H.; Yoshida, W.; Irie, T.; Konishi, K.; Nakano, K.; Uto, T.; Adachi, D.; Kanematsu, M.; Uzu, H.; Yamamoto, K. Silicon Heterojunction Solar Cell with Interdigitated Back Contacts for a Photoconversion Efficiency over 26%. *Nat Energy* **2017**, *2* (5), 1–8. https://doi.org/10.1038/nenergy.2017.32.

(24) Green, M. A.; Dunlop, E. D.; Hohl-Ebinger, J.; Yoshita, M.; Kopidakis, N.; Bothe, K.; Hinken, D.; Rauer, M.; Hao, X. Solar Cell Efficiency Tables (Version 60). *Progress in Photovoltaics: Research and Applications* **2022**, *30* (7), 687–701. https://doi.org/10.1002/pip.3595.

(25) Staebler, D. L.; Wronski, C. R. Reversible Conductivity Changes in Discharge-produced Amorphous Si. *Appl. Phys. Lett.* **1977**, *31* (4), 292–294. https://doi.org/10.1063/1.89674.

(26) Matsui, T.; Bidiville, A.; Maejima, K.; Sai, H.; Koida, T.; Suezaki, T.; Matsumoto, M.; Saito, K.; Yoshida, I.; Kondo, M. High-Efficiency Amorphous Silicon Solar Cells: Impact of Deposition Rate on Metastability. *Appl. Phys. Lett.* **2015**, *106* (5), 053901. https://doi.org/10.1063/1.4907001.

(27) Conibeer, G. Third-Generation Photovoltaics. *Materials Today* **2007**, *10* (11), 42–50. https://doi.org/10.1016/S1369-7021(07)70278-X.

(28) Karazhanov, S. Zh.; Davletova, A.; Ulyashin, A. Strain-Induced Modulation of Band Structure of Silicon. *Journal of Applied Physics* **2008**, *104* (2), 024501. https://doi.org/10.1063/1.2940135.

(29) Rödl, C.; Sander, T.; Bechstedt, F.; Vidal, J.; Olsson, P.; Laribi, S.; Guillemoles, J.-F. Wurtzite Silicon as a Potential Absorber in Photovoltaics: Tailoring the Optical Absorption by Applying Strain. *Phys. Rev. B* **2015**, *92* (4), 045207. https://doi.org/10.1103/PhysRevB.92.045207.

(30) Hannah, D. C.; Yang, J.; Podsiadlo, P.; Chan, M. K. Y.; Demortière, A.; Gosztola, D. J.; Prakapenka, V. B.; Schatz, G. C.; Kortshagen, U.; Schaller, R. D. On the Origin of Photoluminescence in Silicon Nanocrystals: Pressure-Dependent Structural and Optical Studies. *Nano Lett.* **2012**, *12* (8), 4200–4205. https://doi.org/10.1021/nl301787g.

(31) Kovalev, D.; Heckler, H.; Polisski, G.; Koch, F. Optical Properties of Si Nanocrystals. *physica status solidi (b)* **1999**, *215* (2), 871–932. https://doi.org/10.1002/(SICI)1521-3951(199910)215:2<871::AID-PSSB871>3.0.CO;2-9.

(32) Le Bris, A.; Rodiere, J.; Colin, C.; Collin, S.; Pelouard, J.-L.; Esteban, R.; Laroche, M.; Greffet, J.-J.; Guillemoles, J.-F. Hot Carrier Solar Cells: Controlling Thermalization in Ultrathin Devices. *IEEE J. Photovoltaics* **2012**, *2* (4), 506–511. https://doi.org/10.1109/JPHOTOV.2012.2207376.

(33) Zhang, P.; Crespi, V. H.; Chang, E.; Louie, S. G.; Cohen, M. L. Computational Design of Direct-Bandgap Semiconductors That Lattice-Match Silicon. *Nature* **2001**, *409* (6816), 69–71. https://doi.org/10.1038/35051054.

(34) Botti, S.; Flores-Livas, J. A.; Amsler, M.; Goedecker, S.; Marques, M. A. L. Low-Energy Silicon Allotropes with Strong Absorption in the Visible for Photovoltaic Applications. *Phys. Rev. B* **2012**, *86* (12), 121204. https://doi.org/10.1103/PhysRevB.86.121204.

(35) Amsler, M.; Botti, S.; Marques, M. A. L.; Lenosky, T. J.; Goedecker, S. Low-Density Silicon Allotropes for Photovoltaic Applications. *Phys. Rev. B* **2015**, *92* (1), 014101. https://doi.org/10.1103/PhysRevB.92.014101.

(36) Fan, L.; Yang, D.; Li, D. A Review on Metastable Silicon Allotropes. *Materials* **2021**, *14* (14), 3964. https://doi.org/10.3390/ma14143964.

(37) Mujica, A.; Rubio, A.; Muñoz, A.; Needs, R. J. High-Pressure Phases of Group-IV, III–V, and II–VI Compounds. *Rev. Mod. Phys.* **2003**, *75* (3), 863–912. https://doi.org/10.1103/RevModPhys.75.863.

(38) Gaál-Nagy, K.; Strauch, D. Transition Pressures and Enthalpy Barriers for the Cubic Diamond → β -Tin Transition in Si and Ge under Nonhydrostatic Conditions. *Phys. Rev. B* **2006**, *73* (13), 134101. https://doi.org/10.1103/PhysRevB.73.134101.

(39) Piltz, R. O.; Maclean, J. R.; Clark, S. J.; Ackland, G. J.; Hatton, P. D.; Crain, J. Structure and Properties of Silicon XII: A Complex Tetrahedrally Bonded Phase. *Phys. Rev. B* **1995**, *52* (6), 4072–4085. https://doi.org/10.1103/PhysRevB.52.4072.

(40) Crain, J.; Ackland, G. J.; Maclean, J. R.; Piltz, R. O.; Hatton, P. D.; Pawley, G. S. Reversible Pressure-Induced Structural Transitions between Metastable Phases of Silicon. *Phys. Rev. B* **1994**, *50* (17), 13043–13046. https://doi.org/10.1103/PhysRevB.50.13043.

(41) Wentorf, R. H.; Kasper, J. S. Two New Forms of Silicon. *Science* **1963**. https://doi.org/10.1126/SCIENCE.139.3552.338-A.

(42) Besson, J. M.; Mokhtari, E. H.; Gonzalez, J.; Weill, G. Electrical Properties of Semimetallic Silicon III and Semiconductive Silicon IV at Ambient Pressure. *Phys. Rev. Lett.* **1987**, *59* (4), 473–476. https://doi.org/10.1103/PhysRevLett.59.473.

(43) Zhang, H.; Liu, H.; Wei, K.; Kurakevych, O. O.; Le Godec, Y.; Liu, Z.; Martin, J.; Guerrette, M.; Nolas, G. S.; Strobel, T. A. BC8 Silicon (Si-III) Is a Narrow-Gap Semiconductor. *Phys. Rev. Lett.* **2017**, *118* (14), 146601. https://doi.org/10.1103/PhysRevLett.118.146601.

(44) Ge, D.; Domnich, V.; Gogotsi, Y. Thermal Stability of Metastable Silicon Phases Produced by Nanoindentation. *Journal of Applied Physics* **2004**, *95* (5), 2725–2731. https://doi.org/10.1063/1.1642739.

(45) Wong, S.; Johnson, B. C.; Haberl, B.; Mujica, A.; McCallum, J. C.; Williams, J. S.; Bradby, J. E. Thermal Evolution of the Indentation-Induced Phases of Silicon. *J. Appl. Phys.* **2019**, *126* (10), 105901. https://doi.org/10.1063/1.5108751.

(46) Haberl, B.; Guthrie, M.; Sinogeikin, S. V.; Shen, G.; Williams, J. S.; Bradby, J. E. Thermal Evolution of the Metastable R8 and Bc8 Polymorphs of Silicon. *High Pressure Research* **2015**, *35* (2), 99–116. https://doi.org/10.1080/08957959.2014.1003555.

(47) Zhao, Z.; Tian, F.; Dong, X.; Li, Q.; Wang, Q.; Wang, H.; Zhong, X.; Xu, B.; Yu, D.; He, J.; Wang, H.-T.; Ma, Y.; Tian, Y. Tetragonal Allotrope of Group 14 Elements. *J. Am. Chem. Soc.* **2012**, *134* (30), 12362–12365. https://doi.org/10.1021/ja304380p.

(48) Mujica, A.; Pickard, C. J.; Needs, R. J. Low-Energy Tetrahedral Polymorphs of Carbon, Silicon, and Germanium. *Phys. Rev. B* **2015**, *91* (21), 214104. https://doi.org/10.1103/PhysRevB.91.214104.

(49) Zhao, Y.-X.; Buehler, F.; Sites, J. R.; Spain, I. L. New Metastable Phases of Silicon. *Solid State Communications* **1986**, *59* (10), 679–682. https://doi.org/10.1016/0038-1098(86)90372-8.

(50) Zhu, Q.; Oganov, A. R.; Lyakhov, A. O.; Yu, X. Generalized Evolutionary Metadynamics for Sampling the Energy Landscapes and Its Applications. *Phys. Rev. B* **2015**, *92* (2), 024106. https://doi.org/10.1103/PhysRevB.92.024106.

(51) Malone, B. D.; Cohen, M. L. Prediction of a Metastable Phase of Silicon in the *Ibam* Structure. *Phys. Rev. B* **2012**, *85* (2), 024116. https://doi.org/10.1103/PhysRevB.85.024116.

(52) Nguyen, M. C.; Zhao, X.; Wang, Y.; Wang, C.-Z.; Ho, K.-M. Genetic Algorithm Prediction of Crystal Structure of Metastable Si-IX Phase. *Solid State Communications* **2014**, *182*, 14–16. https://doi.org/10.1016/j.ssc.2013.12.005.

(53) Beekman, M.; Wei, K.; Nolas, G. S. Clathrates and beyond: Low-Density Allotropy in Crystalline Silicon. *Applied Physics Reviews* **2016**, *3* (4), 040804. https://doi.org/10.1063/1.4953165.

(54) McMillan, P. F. New Materials from High-Pressure Experiments. *Nature Mater* **2002**, *1* (1), 19–25. https://doi.org/10.1038/nmat716.

(55) Wilson, M.; McMillan, P. F. Crystal-Liquid Phase Relations in Silicon at Negative Pressure. *Phys. Rev. Lett.* **2003**, *90* (13), 135703. https://doi.org/10.1103/PhysRevLett.90.135703.

(56) Daisenberger, D.; McMillan, P. F.; Wilson, M. Crystal-Liquid Interfaces and Phase Relations in Stable and Metastable Silicon at Positive and Negative Pressure. *Phys. Rev. B* **2010**, *82* (21), 214101. https://doi.org/10.1103/PhysRevB.82.214101.

(57) Guerette, M.; Ward, M. D.; Lokshin, K. A.; Wong, A. T.; Zhang, H.; Stefanoski, S.; Kurakevych, O.; Le Godec, Y.; Juhl, S. J.; Alem, N.; Fei, Y.; Strobel, T. A. Synthesis and Properties of Single-Crystalline Na $_4$ Si $_{24}$. *Crystal Growth & Design* **2018**, *18* (12), 7410–7418. https://doi.org/10.1021/acs.cgd.8b01099.

(58) Powell, H. M. 15. The Structure of Molecular Compounds. Part IV. Clathrate Compounds. *J. Chem. Soc.* **1948**, 61. https://doi.org/10.1039/jr9480000061.

(59) Jeffrey, G. A. Hydrate Inclusion Compounds. *Journal of Inclusion Phenomena* **1984**, *1* (3), 211–222. https://doi.org/10.1007/BF00656757.

(60) Berthelot, M. Recherches Sur Les Relations Qui Existent Entre l'Oxyde de Carbone et l'Acide Formique. *Ann. Chem. Phys* **1856**, *3* (46), 477–491.

(61) Liu, J.; Xu, K.; Yang, L.; Lin, Y.; Li, T.; Gao, X.; Zhang, Z.; Wu, J. Fracture Mechanics of Methane Clathrate Hydrates. *Acta Mech. Sin.* **2021**, *37* (9), 1387–1394. https://doi.org/10.1007/s10409-021-01105-y.

(62) Pauling, L.; Marsh, R. E. The Structure of Chlorine Hydrate. *Proc Natl Acad Sci U S A* **1952**, *38* (2), 112–118. https://doi.org/10.1073/pnas.38.2.112.

(63) Kasper, J. S.; Hagenmuller, P.; Pouchard, M.; Cros, C. Clathrate Structure of Silicon Na $_8$ Si $_{46}$ and Na $_x$ Si $_{136}$ (x < 11). *Science* **1965**, *150* (3704), 1713–1714. https://doi.org/10.1126/science.150.3704.1713.

(64) Dolyniuk, J.-A.; Owens-Baird, B.; Wang, J.; Zaikina, J. V.; Kovnir, K. Clathrate Thermoelectrics. *Materials Science and Engineering: R: Reports* **2016**, *108*, 1–46. https://doi.org/10.1016/j.mser.2016.08.001.

(65) Beekman, M.; Nolas, G. S. Inorganic Clathrate-II Materials of Group 14: Synthetic Routes and Physical Properties. *J. Mater. Chem.* **2008**, *18* (8), 842–851. https://doi.org/10.1039/B706808E.

(66) Delgado-Friedrichs, O.; O'Keeffe, M. Identification of and Symmetry Computation for Crystal Nets. *Acta Crystallographica Section A* **2003**, *59* (4), 351–360. https://doi.org/10.1107/S0108767303012017.

(67) Ammar, A.; Cros, C.; Pouchard, M.; Jaussaud, N.; Bassat, J.-M.; Villeneuve, G.; Duttine, M.; Ménétrier, M.; Reny, E. On the Clathrate Form of Elemental Silicon, Si136: Preparation and Characterisation of NaxSi136 (X→0). *Solid State Sciences* **2004**, *6* (5), 393–400. https://doi.org/10.1016/j.solidstatesciences.2004.02.006.

(68) Krishna, L.; Koh, C. A. Inorganic and Methane Clathrates: Versatility of Guest–Host Compounds for Energy Harvesting. *MRS Energy & Sustainability* **2015**, *2* (1), 8. https://doi.org/10.1557/mre.2015.9.

(69) *The Physics and Chemistry of Inorganic Clathrates*; Nolas, G. S., Ed.; Springer Series in Materials Science; Springer Netherlands: Dordrecht, 2014; Vol. 199. https://doi.org/10.1007/978-94-017-9127-4.

(70) Pouchard, M.; Cros, C. The Early Development of Inorganic Clathrates. In *The Physics and Chemistry of Inorganic Clathrates*; Nolas, G. S., Ed.; Springer Series in Materials Science; Springer Netherlands: Dordrecht, 2014; pp 1–33. https://doi.org/10.1007/978-94-017-9127-4_1.

(71) Hohmann, E. Silicide und Germanide der Alkalimetalle. *Z. Anorg. Chem.* **1948**, *257* (1–3), 113–126. https://doi.org/10.1002/zaac.19482570113.

(72) Cros, C.; Pouchard, M. Sur Les Phases de Type Clathrate Du Silicium et Des Éléments Apparentés (C, Ge, Sn) : Une Approche Historique. *Comptes Rendus Chimie* **2009**, *12* (9), 1014–1056. https://doi.org/10.1016/j.crci.2009.05.004.

(73) Toulemonde, P.; Adessi, Ch.; Blase, X.; San Miguel, A.; Tholence, J. L. Superconductivity in the (Ba$_{1-x}$Sr$_x$)$_8$Si$_{46}$ Clathrates: Experimental and Ab Initio Investigation. *Phys. Rev. B* **2005**, *71* (9), 094504. https://doi.org/10.1103/PhysRevB.71.094504.

(74) Fukuoka, H.; Kiyoto, J.; Yamanaka, S. Superconductivity and Crystal Structure of the Solid Solutions of Ba8−Si46−Ge (0⩽x⩽23) with Type I Clathrate Structure. *Journal of Solid State Chemistry* **2003**, *175* (2), 237–244. https://doi.org/10.1016/S0022-4596(03)00253-6.

(75) Shimizu, H.; Takeuchi, Y.; Kume, T.; Sasaki, S.; Kishimoto, K.; Ikeda, N.; Koyanagi, T. Raman Spectroscopy of Type-I and Type-VIII Silicon Clathrate Alloys Sr8AlxGa16−xSi30. *Journal of Alloys and Compounds* **2009**, *487* (1), 47–51. https://doi.org/10.1016/j.jallcom.2009.08.048.

(76) Wang, J.; Lebedev, O. I.; Lee, K.; Dolyniuk, J.-A.; Klavins, P.; Bux, S.; Kovnir, K. High-Efficiency Thermoelectric Ba8Cu14Ge6P26: Bridging the Gap between Tetrel-Based and Tetrel-Free Clathrates. *Chem. Sci.* **2017**, *8* (12), 8030–8038. https://doi.org/10.1039/C7SC03482B.

(77) Yang, L.; Wang, Y.; Liu, T.; Hu, T. D.; Li, B. X.; Ståhl, K.; Chen, S. Y.; Li, M. Y.; Shen, P.; Lu, G. L.; Wang, Y. W.; Jiang, J. Z. Copper Position in Type-I Ba8Cu4Si42 Clathrate. *Journal of Solid State Chemistry* **2005**, *178* (6), 1773–1777. https://doi.org/10.1016/j.jssc.2005.03.015.

(78) Kawaji, H.; Horie, H.; Yamanaka, S.; Ishikawa, M. Superconductivity in the Silicon Clathrate Compound (Na,Ba) x S i 46. *Phys. Rev. Lett.* **1995**, *74* (8), 1427–1429. https://doi.org/10.1103/PhysRevLett.74.1427.

(79) Slack, G. A. Design Concepts for Improved Thermoelectric Materials. *MRS Online Proceedings Library (OPL)* **1997**, *478*. https://doi.org/10.1557/PROC-478-47.

(80) Warrier, P.; Koh, C. A. Silicon Clathrates for Lithium Ion Batteries: A Perspective. *Applied Physics Reviews* **2016**, *3* (4), 040805. https://doi.org/10.1063/1.4958711.

(81) Chan, K. S.; Miller, M. A.; Peng, X. First-Principles Computational Study of Hydrogen Storage in Silicon Clathrates. *Materials Research Letters* **2018**, *6* (1), 72–78. https://doi.org/10.1080/21663831.2017.1396261.

(82) Stefanoski, S.; Martin, J.; Nolas, G. S. Low Temperature Transport Properties and Heat Capacity of Single-Crystal Na8Si46. *J Phys Condens Matter* **2010**, *22* (48), 485404. https://doi.org/10.1088/0953-8984/22/48/485404.

(83) Iversen, B. B.; Palmqvist, A. E. C.; Cox, D. E.; Nolas, G. S.; Stucky, G. D.; Blake, N. P.; Metiu, H. Why Are Clathrates Good Candidates for Thermoelectric Materials? *Journal of Solid State Chemistry* **2000**, *149* (2), 455–458. https://doi.org/10.1006/jssc.1999.8534.

(84) Chan, K. Hybrid Carbon-Based Clathrates for Energy Storage. *C* **2018**, *4* (1), 7. https://doi.org/10.3390/c4010007.

(85) Saito, S.; Oshiyama, A. Electronic Structure of Si46 and Na2Ba6Si46. *Phys. Rev. B* **1995**, *51* (4), 2628–2631. https://doi.org/10.1103/PhysRevB.51.2628.

(86) Qiu, L.; White, M. A.; Li, Z.; Tse, J. S.; Ratcliffe, C. I.; Tulk, C. A.; Dong, J.; Sankey, O. F. Thermal and Lattice Dynamical Properties of Na8S46 Clathrate. *Phys. Rev. B* **2001**, *64* (2), 024303. https://doi.org/10.1103/PhysRevB.64.024303.

(87) Chan, K. S.; Miller, M. A.; Ellis-Terrell, C.; Chan, C. K. Synthesis and Characterization of Empty Silicon Clathrates for Anode Applications in Li-Ion Batteries. *MRS Advances* **2016**, *1* (45), 3043–3048. https://doi.org/10.1557/adv.2016.434.

(88) Iwasaki, S.; Morito, H.; Komine, T.; Morita, K.; Shibuya, T.; Nishii, J.; Fujioka, M. A Novel Technique for Controlling Anisotropic Ion Diffusion: Bulk Single-Crystalline Metallic Silicon Clathrate. *Advanced Materials* **2022**, *34* (9), 2106754. https://doi.org/10.1002/adma.202106754.

(89) Yamanaka, S.; Komatsu, M.; Tanaka, M.; Sawa, H.; Inumaru, K. High-Pressure Synthesis and Structural Characterization of the Type II Clathrate Compound Na $_{30.5}$ Si $_{136}$ Encapsulating Two Sodium Atoms in the Same Silicon Polyhedral Cages. *J. Am. Chem. Soc.* **2014**, *136* (21), 7717–7725. https://doi.org/10.1021/ja502733e.

(90) Beekman, M.; Nenghabi, E. N.; Biswas, K.; Myles, C. W.; Baitinger, M.; Grin, Y.; Nolas, G. S. Framework Contraction in Na-Stuffed Si(*CF* 136). *Inorg. Chem.* **2010**, *49* (12), 5338–5340. https://doi.org/10.1021/ic1005049.

(91) Ramachandran, G. K.; Dong, J.; Diefenbacher, J.; Gryko, J.; Marzke, R. F.; Sankey, O. F.; McMillan, P. F. Synthesis and X-Ray Characterization of Silicon Clathrates. *Journal of Solid State Chemistry* **1999**, *145* (2), 716–730. https://doi.org/10.1006/jssc.1999.8295.

(92) Stefanoski, S.; Malliakas, C. D.; Kanatzidis, M. G.; Nolas, G. S. Synthesis and Structural Characterization of Na $_x$ Si $_{136}$ (0 < *x* ≤ 24) Single Crystals and Low-Temperature Transport of Polycrystalline Specimens. *Inorg. Chem.* **2012**, *51* (16), 8686–8692. https://doi.org/10.1021/ic202199t.

(93) Connétable, D. Structural and Electronic Properties of p-Doped Silicon Clathrates. *Phys. Rev. B* **2007**, *75* (12), 125202. https://doi.org/10.1103/PhysRevB.75.125202.

(94) Baranowski, L. L.; Krishna, L.; Martinez, A. D.; Raharjo, T.; Stevanović, V.; Tamboli, A. C.; Toberer, E. S. Synthesis and Optical Band Gaps of Alloyed Si–Ge Type II Clathrates. *J. Mater. Chem. C* **2014**, *2* (17), 3231–3237. https://doi.org/10.1039/C3TC32102A.

(95) Martinez, A.; Krishna, L.; Baranowski, L.; Lusk, M.; Toberer, E.; Tamboli, A. Synthesis of Group IV Clathrates for Photovoltaics. *Photovoltaics, IEEE Journal of* **2013**, *3*, 1305–1310. https://doi.org/10.1109/JPHOTOV.2013.2276478.

(96) Krishna, L.; Martinez, A. D.; Baranowski, L. L.; Brawand, N. P.; Koh, C. A.; Stevanović, V.; Lusk, M. T.; Toberer, E. S.; Tamboli, A. C. Group IV Clathrates: Synthesis, Optoelectonic Properties, and Photovoltaic Applications. In *Physics, Simulation, and Photonic Engineering of Photovoltaic Devices III*; SPIE, 2014; Vol. 8981, pp 29–39. https://doi.org/10.1117/12.2040056.

(97) Kume, T.; Ohashi, F.; Nonomura, S. Group IV Clathrates for Photovoltaic Applications. *Jpn. J. Appl. Phys.* **2017**, *56* (5S1), 05DA05. https://doi.org/10.7567/JJAP.56.05DA05.

(98) Witte, J.; Schnering, H. G.; Klemm, W. Das Verhalten der Alkalimetalle zu Halbmetallen. XI. Die Kristallstruktur von NaSi und NaGe. *Z. Anorg. Allg. Chem.* **1964**, *327* (3–4), 260–273. https://doi.org/10.1002/zaac.19643270319.

(99) Beekman, M.; Kauzlarich, S.; Doherty, L.; Nolas, G. Zintl Phases as Reactive Precursors for Synthesis of Novel Silicon and Germanium-Based Materials. *Materials* **2019**, *12* (7), 1139. https://doi.org/10.3390/ma12071139.

(100) Cros, C.; Pouchard, M.; Hagenmuller, P. Sur une nouvelle famille de clathrates minéraux isotypes des hydrates de gaz et de liquides. Interprétation des résultats obtenus. *Journal of Solid State Chemistry* **1970**, *2* (4), 570–581. https://doi.org/10.1016/0022-4596(70)90053-8.

(101) Krishna, L.; Baranowski, L. L.; Martinez, A. D.; Koh, C. A.; Taylor, P. C.; Tamboli, A. C.; Toberer, E. S. Efficient Route to Phase Selective Synthesis of Type II Silicon Clathrates with Low Sodium Occupancy. *CrystEngComm* **2014**, *16* (19), 3940–3949. https://doi.org/10.1039/C3CE42626B.

(102) Baitinger, M.; Schnering, H. G. von; Chang, J.-H.; Peters, K.; Grin, Y. Crystal Structure of Sodium Barium Silicide (2:6:46), Na2Ba6Si46. *Zeitschrift für Kristallographie - New Crystal Structures* **2007**, *222* (2), 87–88. https://doi.org/10.1524/ncrs.2007.0035.

(103) Horie, H.; Kikudome, T.; Teramura, K.; Yamanaka, S. Controlled Thermal Decomposition of NaSi to Derive Silicon Clathrate Compounds. *Journal of Solid State Chemistry* **2009**, *182* (1), 129–135. https://doi.org/10.1016/j.jssc.2008.10.007.

(104) Stefanoski, S.; Beekman, M.; Wong-Ng, W.; Zavalij, P.; Nolas, G. S. Simple Approach for Selective Crystal Growth of Intermetallic Clathrates. *Chem. Mater.* **2011**, *23* (6), 1491–1495. https://doi.org/10.1021/cm103135k.

(105) Grigorian, L.; Eklund, P.; Fang, S. Clathrate Structure for Electronic and Electro-Optic Applications. US6103403A, August 15, 2000.

(106) Kume, T.; Iwai, Y.; Sugiyama, T.; Ohashi, F.; Ban, T.; Sasaki, S.; Nonomura, S. NaSi and Si Clathrate Prepared on Si Substrate. *physica status solidi (c)* **2013**, *10*. https://doi.org/10.1002/pssc.201300397.

(107) Ohashi, F.; Iwai, Y.; Noguchi, A.; Sugiyama, T.; Hattori, M.; Ogura, T.; Himeno, R.; Kume, T.; Ban, T.; Nonomura, S. Thin-Film Formation of Si Clathrates on Si Wafers. *Journal of Physics and Chemistry of Solids* **2014**, *75* (4), 518–522. https://doi.org/10.1016/j.jpcs.2013.12.009.

(108) Kume, T.; Ohashi, F.; Sakai, K.; Fukuyama, A.; Imai, M.; Udono, H.; Ban, T.; Habuchi, H.; Suzuki, H.; Ikari, T.; Sasaki, S.; Nonomura, S. Thin Film of Guest-Free Type-II Silicon Clathrate on Si (111) Wafer. *Thin Solid Films* **2016**, *609*. https://doi.org/10.1016/j.tsf.2016.03.056.

(109) Kumar, R.; Hazama, Y.; Ohashi, F.; Jha, H. S.; Kume, T. A Fabrication Method for Type-II Ge Clathrate Film by Annealing of Ge Film Covered with Na Layer. *Thin Solid Films* **2021**, *734*, 138859. https://doi.org/10.1016/j.tsf.2021.138859.

(110) Tsai, A.-P.; Cui, C. 26 - Crystal Growth of Quasicrystals. In *Handbook of Crystal Growth (Second Edition)*; Nishinaga, T., Ed.; Elsevier: Boston, 2015; pp 1113–1156. https://doi.org/10.1016/B978-0-444-56369-9.00026-5.

(111) Kanatzidis, M. G.; Pöttgen, R.; Jeitschko, W. The Metal Flux: A Preparative Tool for the Exploration of Intermetallic Compounds. *Angew Chem Int Ed Engl* **2005**, *44* (43), 6996–7023. https://doi.org/10.1002/anie.200462170.

(112) Condron, C. L.; Martin, J.; Nolas, G. S.; Piccoli, P. M. B.; Schultz, A. J.; Kauzlarich, S. M. Structure and Thermoelectric Characterization of $Ba_8 Al_{14} Si_{31}$. *Inorg. Chem.* **2006**, *45* (23), 9381–9386. https://doi.org/10.1021/ic061241w.

(113) Baran, V.; Senyshyn, A.; Karttunen, A. J.; Fischer, A.; Scherer, W.; Raudaschl-Sieber, G.; Fässler, T. F. A Combined Metal–Halide/Metal Flux Synthetic Route towards Type-I Clathrates: Crystal Structures and Thermoelectric Properties of A8Al8Si38 (A=K, Rb, and Cs). *Chemistry – A European Journal* **2014**, *20* (46), 15077–15088. https://doi.org/10.1002/chem.201403416.

(114) Urushiyama, H.; Morito, H.; Yamane, H. Single Crystal Growth and Structure Analysis of Type-I (Na/Sr)–(Ga/Si) Quaternary Clathrates. *RSC Adv.* **2019**, *9* (26), 14586–14591. https://doi.org/10.1039/C9RA01489F.

(115) Morito, H.; Yamane, H.; Umetsu, R. Y.; Fujiwara, K. Seeded Growth of Type-II Na24Si136 Clathrate Single Crystals. *Crystals* **2021**, *11* (7), 808. https://doi.org/10.3390/cryst11070808.

(116) Li, Y.; Sun, L.; Liu, H.; Wang, Y.; Liu, Z. Preparation of Single-Crystal Metal Substrates for the Growth of High-Quality Two-Dimensional Materials. *Inorganic Chemistry Frontiers* **2021**, *8* (1), 182–200. https://doi.org/10.1039/D0QI00923G.

(117) Nagatomo, Y.; Mugita, N.; Nakakohara, Y.; Saisho, M.; Tajiri, M.; Teranishi, R.; Munetoh, S. Thermoelectric Properties of Single Crystalline $Ba_8 Al_x Si_{46-x}$ Clathrate by Using Flux Czochralski Method. *J. Phys.: Conf. Ser.* **2012**, *379*, 012008. https://doi.org/10.1088/1742-6596/379/1/012008.

(118) Prokofiev, A.; Sidorenko, A.; Hradil, K.; Ikeda, M.; Svagera, R.; Waas, M.; Winkler, H.; Neumaier, K.; Paschen, S. Thermopower Enhancement by Encapsulating Cerium in Clathrate Cages. *Nature Mater* **2013**, *12* (12), 1096–1101. https://doi.org/10.1038/nmat3756.

(119) Imai, M.; Nishida, K.; Kimura, T.; Yamada, K. Synthesis of a Si-Clathrate Compound, Sr8GaxSi46−x, and Its Electrical Resistivity Measurements. *Journal of Alloys and Compounds* **2002**, *335* (1–2), 270–276. https://doi.org/10.1016/S0925-8388(01)01840-0.

(120) Liang, Y.; Böhme, B.; Reibold, M.; Schnelle, W.; Schwarz, U.; Baitinger, M.; Lichte, H.; Grin, Y. Synthesis of the Clathrate-I Phase $Ba_{8-x} Si_{46}$ via Redox Reactions. *Inorg. Chem.* **2011**, *50* (10), 4523–4528. https://doi.org/10.1021/ic2001859.

(121) Böhme, B.; Hoffmann, S.; Baitinger, M.; Grin, Y. Application of N-Dodecyltrimethylammonium Chloride for the Oxidation of Intermetallic Phases. *Zeitschrift für Naturforschung B* **2011**, *66* (3), 230–238. https://doi.org/10.1515/znb-2011-0304.

(122) Böhme, B.; Aydemir, U.; Ormeci, A.; Schnelle, W.; Baitinger, M.; Grin, Y. Synthesis of the Intermetallic Clathrate $Na_2 Ba_6 Si_{46}$ by Oxidation of $Na_2 BaSi_4$ with HCl. *Science and Technology of Advanced Materials* **2007**, *8* (5), 410–415. https://doi.org/10.1016/j.stam.2007.06.006.

(123) Böhme, B.; Guloy, A.; Tang, Z.; Schnelle, W.; Burkhardt, U.; Baitinger, M.; Grin, Y. Oxidation of $M_4 Si_4$ (M = Na, K) to Clathrates by HCl or $H_2 O$. *J. Am. Chem. Soc.* **2007**, *129* (17), 5348–5349. https://doi.org/10.1021/ja0705691.

(124) Böhme, B. An Electrochemical Approach toward the Metastable Type II Clathrate Germanium Allotrope. *Inorg. Chem.* **2020**, *59* (17), 11920–11924. https://doi.org/10.1021/acs.inorgchem.0c01796.

(125) Guloy, A. M.; Ramlau, R.; Tang, Z.; Schnelle, W.; Baitinger, M.; Grin, Y. A Guest-Free Germanium Clathrate. *Nature* **2006**, *443* (7109), 320–323. https://doi.org/10.1038/nature05145.

(126) Koga, K.; Suzuki, K.; Fukamoto, M.; Anno, H.; Tanaka, T.; Yamamoto, S. Electronic Structure and Thermoelectric Properties of Si-Based Clathrate Compounds. *J. Electron. Mater.* **2009**, *38* (7), 1427–1432. https://doi.org/10.1007/s11664-009-0730-6.

(127) Beekman, M.; Baitinger, M.; Borrmann, H.; Schnelle, W.; Meier, K.; Nolas, G. S.; Grin, Y. *Preparation and Crystal Growth of Na24Si136*. ACS Publications. https://pubs.acs.org/doi/pdf/10.1021/ja903362b (accessed 2022-08-10). https://doi.org/10.1021/ja903362b.

(128) Stefanoski, S.; Blosser, M. C.; Nolas, G. S. Pressure Effects on the Size of Type-I and Type-II Si-Clathrates Synthesized by Spark Plasma Sintering. *Crystal Growth & Design* **2013**, *13* (1), 195–197. https://doi.org/10.1021/cg3013443.

(129) Gupta, A.; Baron, G. V.; Perreault, P.; Lenaerts, S.; Ciocarlan, R.-G.; Cool, P.; Mileo, P. G. M.; Rogge, S.; Van Speybroeck, V.; Watson, G.; Van Der Voort, P.; Houlleberghs, M.; Breynaert, E.; Martens, J.; Denayer, J. F. M. Hydrogen Clathrates: Next Generation Hydrogen Storage Materials. *Energy Storage Materials* **2021**, *41*, 69–107. https://doi.org/10.1016/j.ensm.2021.05.044.

(130) Wagner, N. A.; Raghavan, R.; Zhao, R.; Wei, Q.; Peng, X.; Chan, C. K. Electrochemical Cycling of Sodium-Filled Silicon Clathrate. *ChemElectroChem* **2014**, *1* (2), 347–353. https://doi.org/10.1002/celc.201300104.

(131) Langer, T.; Dupke, S.; Trill, H.; Passerini, S.; Eckert, H.; Pöttgen, R.; Winter, M. Electrochemical Lithiation of Silicon Clathrate-II. *J. Electrochem. Soc.* **2012**, *159* (8), A1318. https://doi.org/10.1149/2.082208jes.

(132) Li, X.; Steirer, K. X.; Krishna, L.; Xiao, C.; Fink, K.; Santhanagopalan, S. Electrochemical Properties and Challenges of Type II Silicon Clathrate Anode in Sodium Ion Batteries. *J. Electrochem. Soc.* **2019**, *166* (13), A3051–A3058. https://doi.org/10.1149/2.1201913jes.

(133) Chan, K. Synthesis and Characterization of Silicon Clathrates for Anode Applications in Lithium-Ion Batteries. **2013**, 19.

(134) Ohashi, F.; Hattori, M.; Ogura, T.; Koketsu, Y.; Himeno, R.; Kume, T.; Ban, T.; Iida, T.; Habuchi, H.; Natsuhara, H.; Nonomura, S. High-Yield Synthesis of Semiconductive Type-II Si Clathrates with Low Na Content. *Journal of Non-Crystalline Solids* **2012**, *358*, 2134–2137. https://doi.org/10.1016/j.jnoncrysol.2011.12.058.

(135) Liu, Y.; Schenken, W. K.; Krishna, L.; Majid, A. A. A.; Furtak, T. E.; Walker, M.; Koh, C. A.; Taylor, P. C.; Collins, R. T. Synthesis and Characterization of Type II Silicon Clathrate Films with Low Na Concentration. *Applied Physics Reviews* **2021**, *8* (4), 041408. https://doi.org/10.1063/5.0062723.

(136) Xue, D.; Myles, C. First-Principles Study of the Electronic, Vibrational Properties and Anharmonic Effects of Some Si-Based Type-II Binary Clathrates. *Materials* **2019**, *12* (3), 536. https://doi.org/10.3390/ma12030536.

Chapter 2: Synthesis and characterization of type I and type II silicon clathrates films

2.1 Introduction

As mentioned in the prior chapter, silicon clathrates as thin films are suited for many applications. To obtain such silicon clathrate films, the preferred technique is the two-step thermal decomposition introduced by Grigorian et al.[1] and later used by the NREL[2] and the Gifu University[3]. However, such reported process often requires the use of an expensive dedicated glovebox during the loading, transfer and unloading phase of the sample. This is both to prevent reaction of the Na_4Si_4 precursor and to limit exterior contamination[4].

In this work and especially in this chapter, we will describe and investigate a two-step thermal decomposition setup free of any glovebox and its impact on the quality and properties of the silicon clathrates obtained this way.

This chapter is divided into five parts. First, we will describe the setup used for the thermal annealing required to synthesize the Na_4Si_4 precursor as a first step (called Process 1) and then the thermal annealing under dynamic vacuum as the second step of the process (called Process 2), along with explanation of both reaction mechanisms occurring during the two processes. In the second part, we will detail the effects of various experimental parameters of the two-step decomposition process in order to determine the optimal conditions toward the obtention of pure type I and type II films of most favorable quality. We will then give a thorough set of properties of the grown films. The third part concerns the thermal stability of the films using a post-growth annealing to prevent unwanted degradation upon future treatments. The fourth part is dedicated to the resulting quality of the clathrates films after annealing under mechanical pressure to reach more compact films with reduced surface roughness and low concentration of defects.

The last part concerns our experiments to fabricate thin silicon clathrate films on silicon or sapphire substrates. The first approach explores the wet and dry etching of the grown thick clathrate films. The second attempt consists in using a sodium diffusion barrier layer on the substrate silicon wafer before Process 1. The presence of the

barrier layer will change the reaction equilibrium which seems to be limited by the sodium source. Finally, we also studied the formation of thin clathrate films using silicon layers on sapphire as a substrate.

2.2 Synthesis of silicon clathrates films

A silicon substrate cleaved into 37 x 54 mm^2 rectangular piece is washed in 10% volume hydrofluoric acid to remove any native silicon oxide, rinsed in deionized water to be finally blow-dried. Silicon wafers used as substrates are p-type, n-type doped or intrinsic single crystalline silicon with (001) or (111) orientation. Unless stated otherwise the silicon clathrates are mostly obtained on a p-doped Si (100) wafer.

A sodium slice is obtained from a sodium ingot (99.8% purity, Alfa Aesar, CAS #7440-23-5) stored in paraffin oil and immediately transferred in a hermetic cyclohexane (99+% purity, Alfa Aesar, CAS #110-82-7) filled container to limit the oxidation of the exposed surface of the sodium slice. Both chemicals are managed under safety precautions by preventing any exposure of the sodium to water and using a dedicated mask to prevent any inhalation of cyclohexane vapor. The amount and shape of the sodium slice are varied to study their effect on the produced silicon clathrates.

Lastly, an Inconel boat of 54 x 18 x 13.5 mm^3 (ANALAB, ref. AR9001) washed beforehand in deionized water and dried is utilized as a container for the sodium slice closed by the silicon wafer resulting in a {Silicon + Sodium + Boat} system as schematically represented in **Figure 2.1**.
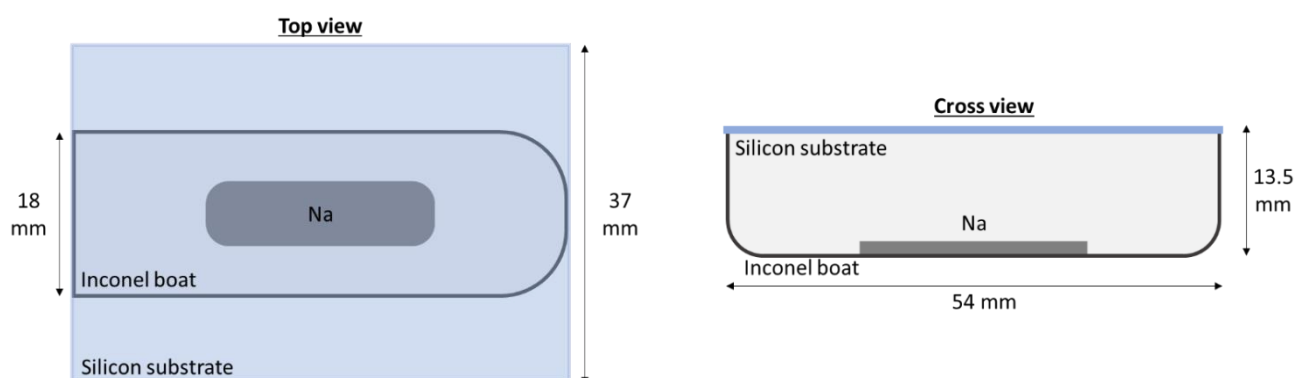
Figure 2.1. Schematic top and cross-view of the {Silicon + Sodium + Boat} system along with a photograph of the as-synthesized Silicon Clathrates sample.

2.2.1 Experimental setup

The experimental setup and its schematic representation are shown in **Figure 2.2**. Thus, the {Silicon + Sodium + Boat} system is itself assembled in a stainless-steel tube under a continuous flow of argon gas at 1.6 bar to minimize the exposure of the sodium to the ambient air. Once assembled, the system is inserted right in the middle of the tube before sealing it and heating it homogeneously using a tubular furnace. To prevent any traces of oxygen in the sealed tube, a tantalum coil has been inserted along with the Inconel boat. The tube is flushed thanks to the argon gas flow for 10 minutes, shut off by closing the valve and then heated to the required temperature between 550°C to 650°C using a heating ramp from 5°C·min^{-1} to 15°C·min^{-1}.
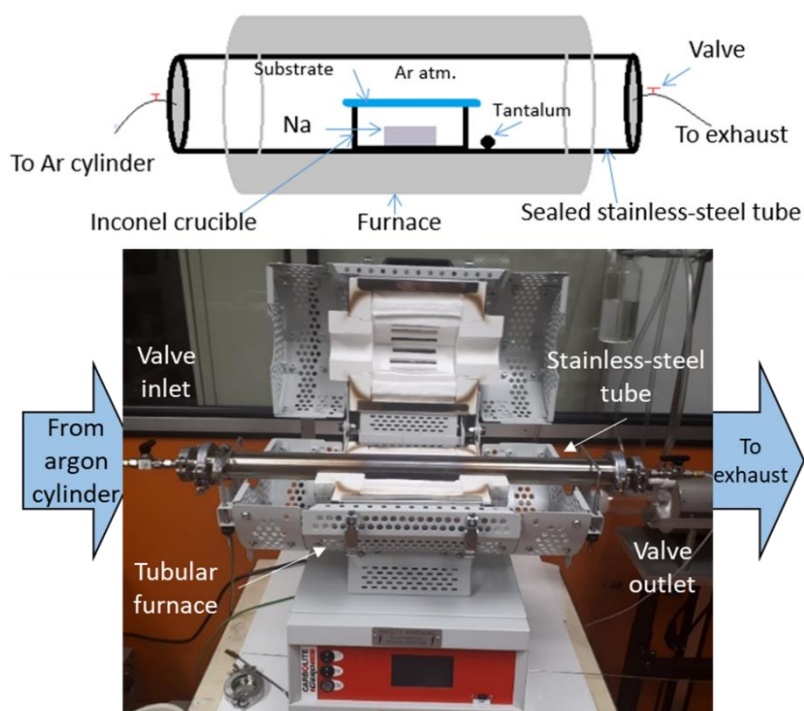
Figure 2.2. Schematic and photograph of the experimental setup used for the synthesis of the

Zintl precursor film (Process 1)

The heating is then kept at the desired temperature over a long duration. This allows the formation of the Zintl precursor Na$_4$Si$_4$. This step will be referenced in the following as Process 1.

The synthesis process can be summarized by the following mechanism, depicted in **Figure 2.3**.

- First, the temperature inside the tube is sufficient to melt the sodium but not enough to allow to reach its boiling point. Thus, only a fixed amount of sodium vapour pressure is observed until the depletion of the liquid sodium, ranging theoretically from 1.3 kPa at 550°C to 6.7 kPa at 650°C[5–7].

- One part of the sodium vapor diffuses into the silicon wafer, while another part condenses on the surface of the wafer which is then covered by a thin layer of sodium. As the sodium diffuses into the silicon versus time, it is able to react with it to form the precursor Na_4Si_4. Diffusion coefficients and solubility of sodium in the silicon wafer are increasing with temperature[8].

- As more and more sodium atoms enter the silicon wafer, the layer of Na_4Si_4 is growing more and more until either all the sodium is consumed, or the annealing is stopped.
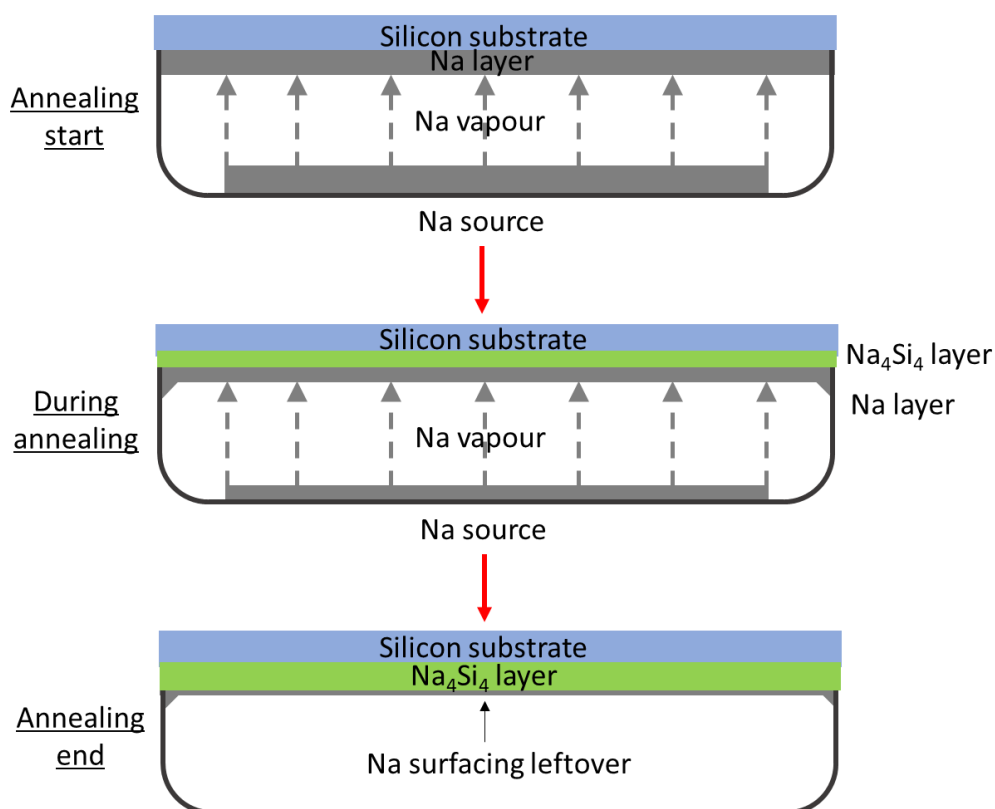
Figure 2.3. Schematically represented mechanism of the Na_4Si_4 Zintl phase formation during Process 1.

Once the annealing is finished, the tube is allowed to cool down naturally to room temperature. The tube is again flushed with argon gas for 10 minutes to make sure the atmosphere is inert when opening it. Then the system {Silicon + Sodium + Boat} is

extracted from the tube, the silicon wafer covered by the layer of Zintl precursor is quickly transferred to the quartz tube of the furnace under dynamic vacuum. The boat is washed with ethanol and deionized water to remove any trace of sodium.

As soon as the silicon wafer with Zintl precursor is installed in the quartz tube, the last is reattached to the pumping unit as the Na_4Si_4 precursor is utterly sensitive to ambient humidity. Immediately, the vacuum is initiated, and the thermal annealing is started only after the dynamic vacuum is below 1.0×10^{-6} mbar. The annealing consists in a steep heating ramp reaching the desired temperature in approximatively 40 minutes of 400°C to 420°C and will be referred to as Process 2. The whole setup used and its schematic representation are shown in **Figure 2.4**.
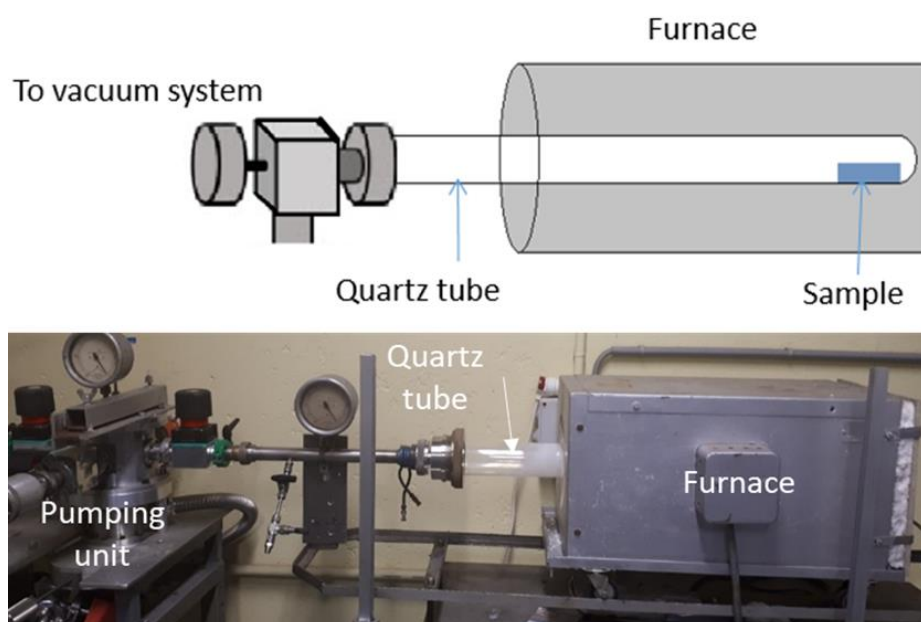

Figure 2.4. Schematic and photograph of the experimental setup used for Process 2.

During the heating step, the vacuum is slightly rising to reach a first maximum of around 1.5×10^{-5} mbar at 140°C before quickly returning to the original vacuum. Brief and intense peaks of pressure almost reaching 10^{-5} mbar pressure are observed at 310°C and 370°C simultaneously with the deposition of sodium metal on the inner wall of the quartz tube which is colder. Once again, the vacuum is then quickly restored back at 10^{-7} mbar and remains stable until the end of the annealing. At the end of the annealing, the quartz tube is left to cool down to room temperature before extracting the processed sample.

The transformation of the Na_4Si_4 precursor into the clathrate phases is a slow but severe one. The basis of the transformation is schematically represented in **Figure 2.5**. When subjected to high enough temperature while in high vacuum, the sodium cations from the Zintl phase go through sublimation out of the film. The local strains induced by the lack of the missing cations are so strong that the lattice is rearranging itself into the silicon clathrates phases.
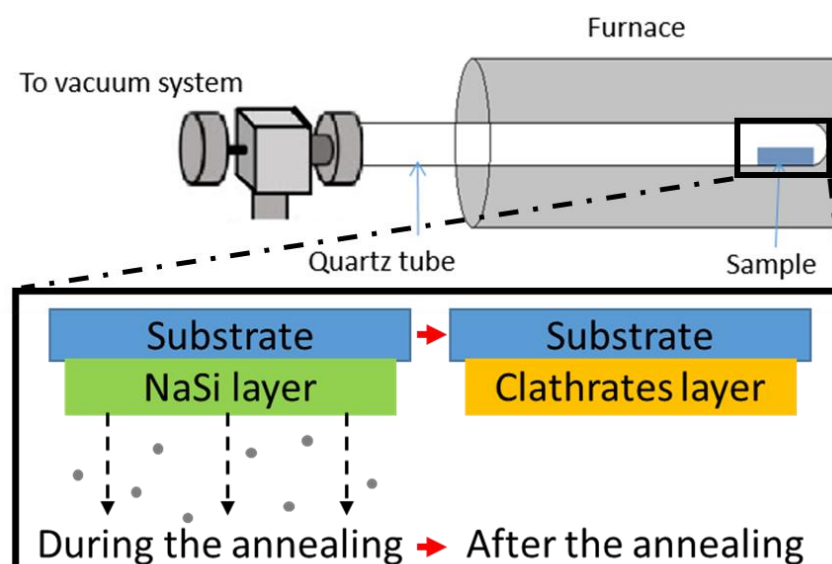
Figure 2.5. Schematically represented mechanism of the transformation of the Na_4Si_4 layer into silicon clathrates (Process 2).

The processed sample after Process 2 is finally immersed in ethanol to allow the soft removal of any possible sodium leftovers at the surface of the samples. Then the sample is put in water and bubbling is usually observed originating from the sodium leftover on the surface or in the cracks of the newly formed silicon clathrates layer. Once the bubbling vanished, the sample is left in water for five more minutes and then blow dried.

2.2.2 Optimization of the two-step thermal decomposition process

In this work, one of the goals is to synthesize homogeneous silicon clathrate films and to investigate their properties. To achieve this, formation of pure type I and type II silicon clathrate films of good structural quality must be obtained.

During this part, the two steps of the thermal decomposition process and their parameters are investigated and refined. This is in order to choose between type I and

type II silicon clathrates. A detailed discussion of the effects of the various parameters involved in the two processes of the synthesis is presented along with optimal parameters.

A. Effect of the annealing temperatures during Process 1 and 2

To better understand each of the silicon clathrate phases, there is a need to obtain selectively films with type I and type II phase and also conditions where type I and type II are competing. This study is performed through an exploration of the conditions of the reaction. It is based on previous work done on the synthesis of films within the lab team and that found in literature[9,10].

The first experimental parameter is the annealing temperatures during Process 1 and Process 2 and their effects on the films' quality. Temperatures from 550°C up to 650°C and 350°C up to 450°C for respectively Process 1 and 2 were applied and resulting surface morphology and compositions of the grown films were determined.

For the purpose of estimating the phases present in the films, the composition of the films is systematically monitored using XRD for an overall inspection. The identification of the silicon clathrates by XRD is performed thanks to the JCPDS sheet 01-089-5534 for the type I silicon clathrates while the type II relies on the sheets 01-089-5535 to 01-089-5540 for x = 1 to x = 20.5. All these files are available thanks to the work of Reny et al.[11] and whose main information are summarized in **Table 2.1**.

The XRD analysis is complemented with Raman spectroscopy measurements for a localized characterization in various spots across the surface of the grow films.

Table 2.1: Summary of the structural information from the JCPDS sheets[11] of type I and type II Silicon Clathrates.

Type I Na$_8$Si$_{46}$			Type II Na$_{0<x<24}$Si$_{136}$		
Space group	Lattice parameter (Å)	Density (g.cm^{-3})	Space Group	Lattice parameter (Å)	Density (g.cm^{-3})
$Pm\bar{3}n$	10.1983	2.311	$Fd\bar{3}m$	14.6426 to 14.7156	2.066 to 2.280
Atom site	x	y	Z	Atom site	x	y	z

Atom site	x	y	Z	Atom site	x	y	z
Si (6d)	0.25000	0.00000	0.50000	Si (8a)	0.12500	0.12500	0.12500
Si (16i)	0.18412	0.18412	0.18412	Si (32e)	0.21837	0.21837	0.21837
Si3 (24k)	0.00000	0.11719	0.30776	Si (96g)	0.06711	0.06711	0.37171
Na (2a)	0.00000	0.00000	0.00000	Na (8b)	0.37500	0.37500	0.37500
Na (6c)	0.25000	0.00000	0.50000	Na (16c)	0.00000	0.00000	0.00000

- *Films quality after Process 1*

Temperature of Process 1 is first explored from 550°C to 650°C using a mass of sodium of 0.60 g and a duration of 19h followed by Process 2 at a fixed temperature of 400°C for 4h under a chamber pressure below 1x10^{-6} mbar.

At temperatures lower than 570°C, no Na$_4$Si$_4$ precursor film is visible, and the samples show no presence of silicon clathrates under XRD or Raman spectroscopy characterizations. However, a layer of sodium droplets is observed at the end of Process 1 as shown in **Figure 2.6.**
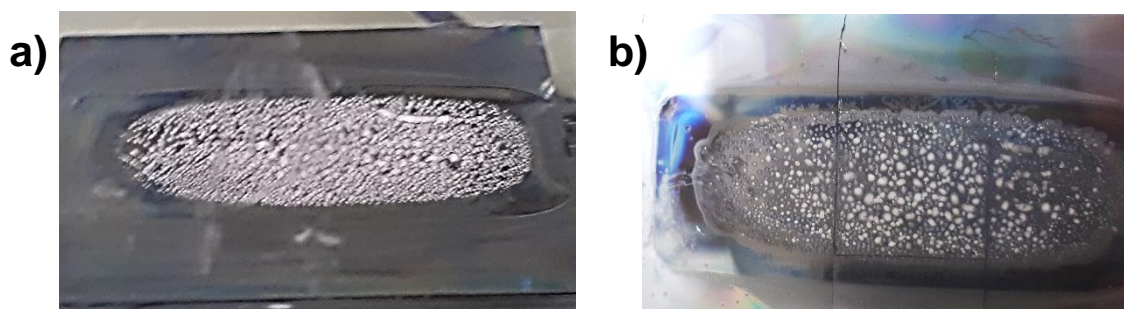
Figure 2.6. Photographs of samples submitted to Process 1 at 560°C for 19h once exited a) from the tubular furnace b) from the quartz tube

At the top of the silicon wafer serving as a substrate, traces of etching are visible due to the reaction of silicon with NaOH occurring rapidly during the transfer or pulling off of the sample.

For temperatures ranging from 570°C to less than 600°C, a layer of precursor is formed. However, it is inhomogeneous and does not cover the entire exposed silicon wafer surface at the end of Process 1. After Process 2, thick films are effectively obtained with a composition consisting of both silicon clathrate phases. Yet, these films do not cover the whole silicon substrate. Both the thickness and the composition of the layer are not uniformly distributed when investigated by Raman and XRD.

For a narrow range of temperature region centered at 600°C, films of pure type II silicon clathrates Na_xSi_{136} are systematically obtained. The XRD result of one of those films is shown in **Figure 2.7**. More discussion on the occupancy and structure of the type II films is provided later in section 2.5.
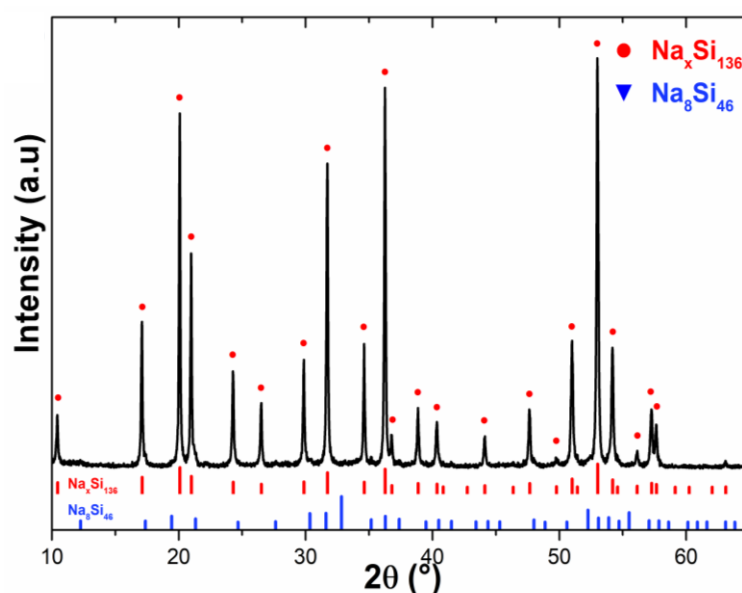
Figure 2.7. XRD patterns for a sample submitted to Process 1 at 600°C for 19h. The red circles refer to Na_1Si_{136} reflections and the blue triangles to Na_8Si_{46}.

For Process 1 carried out at temperatures in the range 600°C – 630°C, a mixture of both structures is again observed in the synthesized films. This composition is homogenous throughout the film surface when investigated by XRD and Raman. As shown in **Figure 2.8** for similar experiments both conducted at 615°C, the films have a higher fraction phase of type II than type I. These fractions are not reproducible from experiment to experiment under the same conditions. In this temperature window, as

the composition is not reproducible, there is no way to control the phase fractions with a variation of temperature in Process 1.
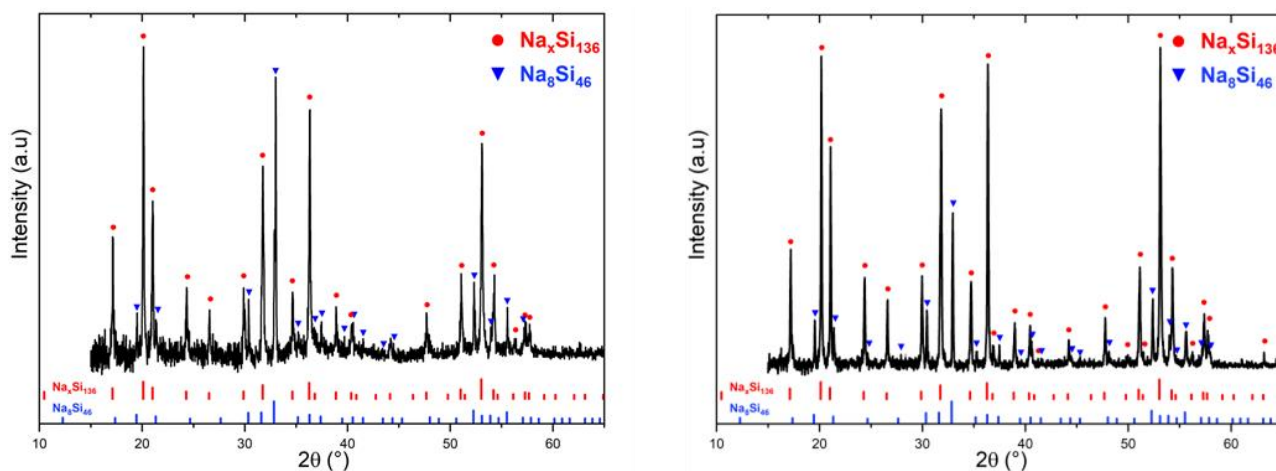
Figure 2.8. XRD patterns for two samples submitted to similar Process 1 at 615°C for 19h. The red circles refer to Na$_1$Si$_{136}$ reflections and the blue triangles to Na$_8$Si$_{46}$.

At temperatures around 630°C, almost pure type I films are generally obtained with traces of type II silicon clathrates and diamond silicon as illustrated in **Figure 2.9.** Longer and more intense bubbling is observed upon the sample washing in ethanol compared to previous samples. These almost pure type I films are less fragile than all the other films obtained before and have a distinctive blue-grey shine compared to the other darker films.
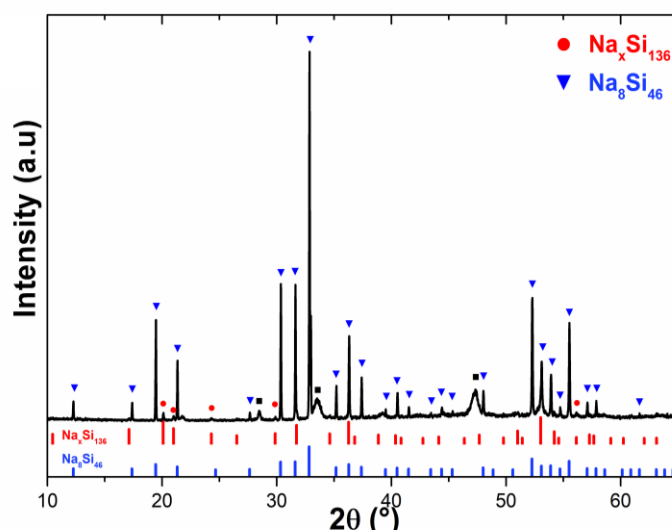
Figure 2.9. XRD patterns for a sample submitted Process 1 at 630°C for 19h. The red circles refer to Na$_1$Si$_{136}$ reflections and the blue triangles to Na$_8$Si$_{46}$.

For annealing temperatures higher than 630°C, a film is in fact synthesized at the top of the silicon substrate. However, it is not a film of silicon clathrates, but rather a

polycrystalline silicon layer as identified using XRD with some very feint peaks of type I indicating their presence in few traces.

- *Films quality after Process 2*

Process 2 was applied at different temperatures for a duration of 4h following a Process 1 performed at an annealing temperature of 600°C, 615°C or 630°C for 19h using a 0.60 g mass of sodium. For Process 2' temperatures below 370°C, the films all displayed a not complete conversion into silicon clathrates. This results in unusable samples because the leftover sodium and sodium silicide precursors generate degradation when exposed to air. For Process 2' temperatures between 370°C and 420°C, there is no impact of the temperature on films' composition and pure type I or II films are obtained as expected. For Process 2' temperatures ranging from 430°C to 450°C, type I silicon clathrates are favored, but presence of signals from polycrystalline Si (called impurities in the following) are found when analyzing by XRD. The content of these impurities rises with temperature. As expected, type I is not observed at temperatures above 450°C.

A summary of the phases obtained for the various conditions of our experiments is made in **Table 2.2**.

Table 2.2: Summary of phases observed depending on Process 1 and 2 annealing conditions

Process 1 / Process 2	600°C for 19h	615°C for 19h	630°C for 19h
350°C for 4h	No layer		
370°C for 4h	Pure Type II	Type I and Type II mixture	Type I and few traces of d-Si
390°C for 4h			
410°C for 4h			
420°C for 4h			
430°C for 4h	Type I and II mixture + d-Si	Type I and d-Si	
450°C for 4h	d-Si and traces of Type I		

- *Discussion*

In contrast to what could be expected, Process 2' temperature is not a critical parameter that impact the outcome of competing reactions between the two silicon clathrate structures. This is in fact strongly determined by the temperature of Process 1. When a given amount of sodium is inserted in Process 1, a higher temperature means a higher sodium vapour pressure in the {Silicon + Sodium + Boat} system. The sodium vapour pressure is multiplied by five, from 1.3 kPa at 550°C up to 6.67 kPa at 650°C[5], as the solubility of sodium in silicon is almost constant at 1.2×10^{-18} atoms·cm^{-3} in the same temperature range[12] meaning that a higher sodium amount is available for the reaction. This is consistent with the partial layers obtained at temperatures under 570°C indicating a lack of sodium reaching and diffusing inside the silicon wafer. This also explains the more and more intense bubbling observed during the washing step as the temperature of Process 1 is raised. Indeed, when the annealing is stopped, the silicon wafer and the precursor film are cooling slightly quicker than the Inconel boat which is in direct contact with the hot tube leading to the condensation of a sodium layer at the surface of the precursor film. As the temperature rises, the excess sodium layer on the Na_4Si_4 films becomes thicker.

When inserted in the vacuum furnace for Process 2, this excess sodium covering the precursor films results in a higher sodium vapour pressure during the transformation into silicon clathrates. The observed phases according to the temperature of Process 1 indicate that the outcome of the competing formation between types I and II is sensitive to this rising of sodium vapour pressure within the chamber. As a result of experiments, type II is favoured at low temperatures in Process 1, i.e., low sodium vapour pressure. In contrast type I is obtained for elevated temperature and thus for higher sodium vapour pressure. During Process 2, the effect of the temperature on the composition of the films is trickier and can only be used to favour type I structures with harmful diamond silicon impurities in the layer when processing at temperatures around 430°C. These observations are similar to what has been described in the literature[13]. The Type II silicon clathrate is stabilized by lowering the temperature during Process 2. In contrast, when processing at higher temperatures and even in the presence of heavy amounts of sodium vapour, type I is favoured.

For further experiments, temperature of Process 2 was fixed at 400°C in order to allow the elimination of most of sodium and preventing the formation of diamond silicon impurities. To summarize this part, an overview of the phase observed according to the temperature is shown in **Figure 2.10** for an optimal Process 2' temperature of 400°C. As visible on the several diffractograms shown before, all produced films of either type are polycrystalline with random orientation.
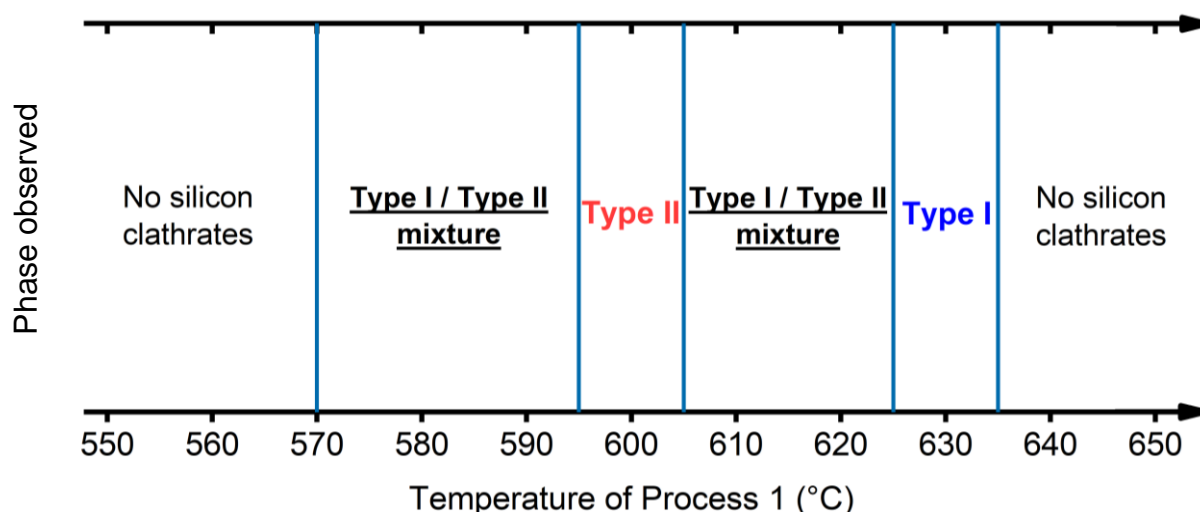
Figure 2.10 Nature of the films obtained depending on the temperature of Process 1 at a constant Process 2 temperature of 400°C

B. Effects of the sodium slice setting and mass

For the study above, temperatures of processes 1 and 2 have been varied and finally set for a fixed mass of sodium of 0.60g. These temperatures can produce selectively pure type I or type II films, and even mixed compositions if needed. Yet, these films have all in common thickness of several tens of microns, measured by profilometer and SEM, and are very brittle inducing breaking of the layer into powders at any slight shock.

Hereafter, we will investigate the effects of the sodium mass as well as that of the shape of the inserted sodium slice on the quality of the synthesized films and their types. A mass of sodium around 0.10 g up to 1.00 g was investigated for slices of various shape and placed in different settings. **Figure 2.11** depicts the surface of processed films depending on the sodium slice mass and shape after Process 1 at 600°C for 19h and Process 2 at 400°C during 4h.

Figure 2.11 Photographs of samples submitted to Process 1 at 600°C for 19h for various sodium slice mass and shape once exited from a)c)e) Process 1 b)d)f) Process 2.

<u>Single square or rectangular sodium slice of mass > 0.30 g</u>
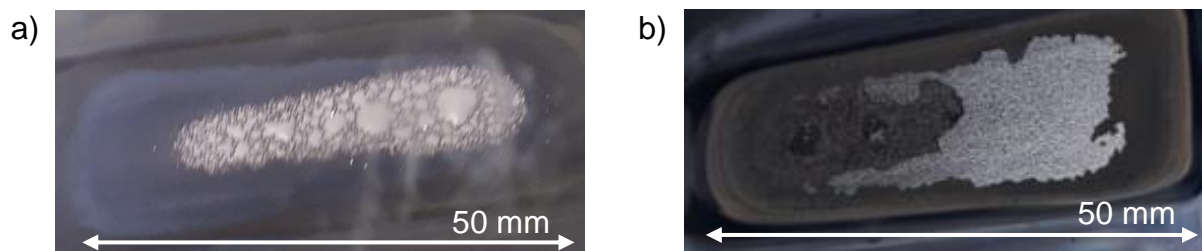
<u>Two slices of 0.15 g to 0.20 each located at both extremities of the Inconel boat</u>
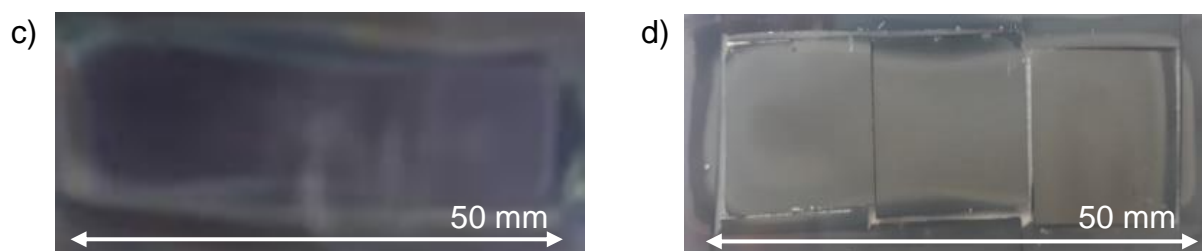
<u>Wide and thin slice of 1.0 x 4.5 cm^2 of mass from 0.10 g up to 0.30 g</u>
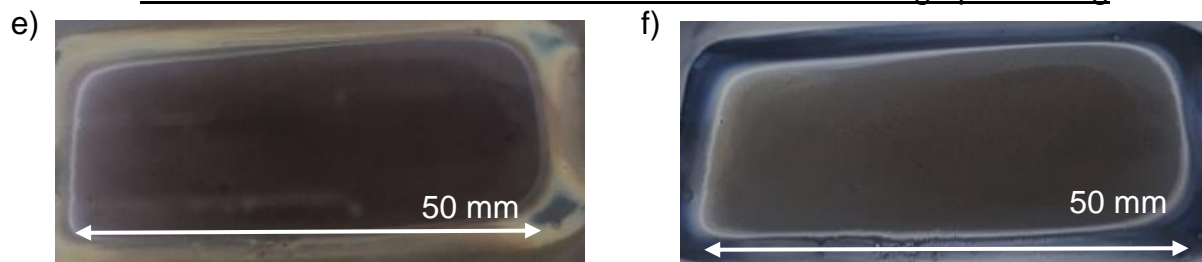
First, it rapidly appears that the effective hermetic sealing of the {boat + sodium + silicon wafer} system is a critical requirement for the reaction to be successful and reproducible. Otherwise, any small leakage disturbs the sodium vapour pressure in the system and influences the precursor formation reaction. To make sure to keep the system hermetic, the flatness of the crucible is regularly assessed and is sanded if not correct.

For process 1, we have used a 1 x 2 cm^2 rectangular slice of sodium with a mass above 0.30g. This experiment resulted in the obtention of a thick inhomogeneous layer of sodium deposited at the surface of the obtained Na_4Si_4 phase. Such layer was mostly removed after Process 2. However, this sodium excess causes the films to be so fragile and breaking into powders during the annealing or when the sample is exited from the chamber, cleaved or any manipulation which would induce strengths on the film. This is shown in **Figure 2.11.a-b**. The fragile part of the films is consistently located where the excess of sodium layer was present. Reducing the mass below 0.30 g resulted in

62

precursor Na_4Si_4 of reduced area centred right above the sodium slice, meaning that the distribution of the sodium vapour was not uniform. This is due to the small surface of the sodium slice.

Since the layer of excess sodium is centred right above the sodium slice, it appears that a single rectangular slice of 1 x 2 cm^2 is not allowing a homogeneous distribution of the sodium vapour in the Inconel boat enclosure. In order to reach a more uniform distribution of the sodium vapour, the separation of the sodium mass in two equal slices positioned at both extremities of the Inconel boat was attempted. For slices of an individual mass of 0.15 to 0.20 g each, the obtention of a smooth layer of Zintl precursor leading to a homogenous silicon clathrates layer is observed. However, the surface of the exposed silicon wafer was not fully covered, probably because the vapour diffusion cone emitted from the slices was not wide enough to cover the whole wafer surface as shown in **Figure 2.11.c-d**. Slices of heavier mass induced fragile silicon clathrate layers in a similar manner than the rectangular 1 x 2 cm^2 slice.

In another experiment, the sodium slice was cut as thin as possible to extend the rectangular shape up to 1.0 x 4.5 cm², filling as much as possible the crucible, allowing a uniform distribution of the sodium vapour in the system. The use of these several slices resulted in homogeneous films with good adhesion to the silicon wafer for mass below 0.30 g down to 0.10 g. The synthesized films are not only homogeneous, but they also cover the entire exposed silicon surface as depicted in **Figure 2.11.e-f**. Larger mass of sodium resulted in fragile layers with structural cohesion so poor that it delaminates during Process 2 or when submitted to mechanical shock.

We may conclude that the thin and wide 1.5 x 4.0 cm^2 shape of the sodium slice allowed the obtention of films of homogeneous composition and with the widest surface. This slice is placed in the Inconel boat 13.5 mm underneath the Silicon surface with an exposed area of 18 x 54 mm².The observed phases and brittleness of the films according to the temperature and sodium mass conditions using in the optimized setting are summarized in **Figure 2.12**, especially conditions to obtain the better pure type I and type II films are framed in blue and red respectively.
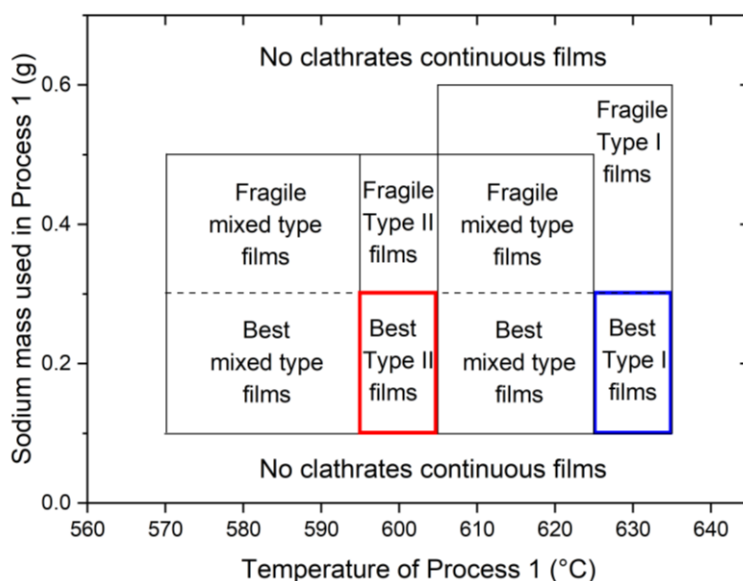
Figure 2.12 Phase in presence and quality of the films obtained depending on the temperature and the mass of the sodium slice of 1.0 x 4.5 cm^2 inserted using an hermetic {Silicon + Sodium + Boat} system.

The reduction in the amount of sodium used also helped in bringing the thickness of the silicon clathrates down to 30 μm. Yet, all the films exhibit similar surfaces with numerous cracks, defects, and a high roughness as visible in **Figure 2.13**.
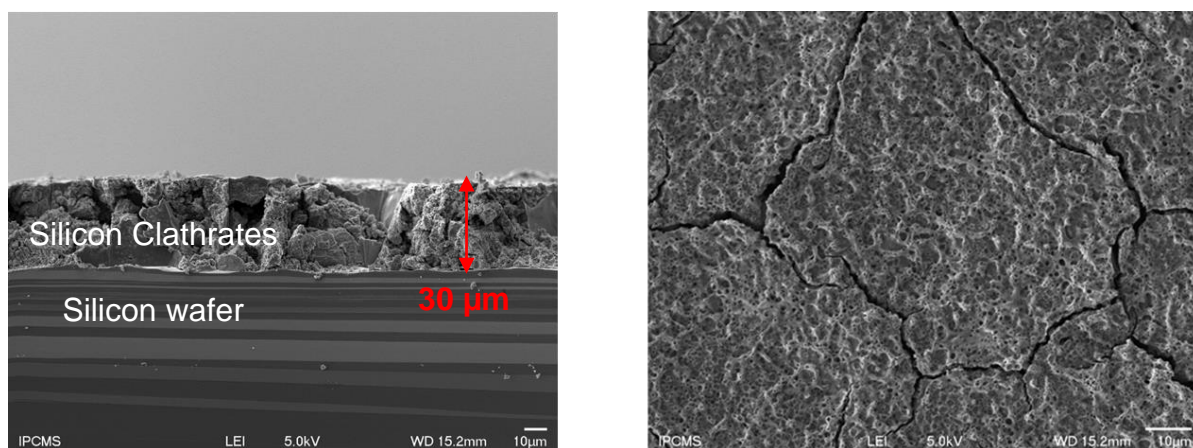
Figure 2.13 Cross-section and surface SEM observation of silicon clathrates films.

In the hope of further reducing this thickness, the annealing duration of Process 1 was tentatively reduced from the usual 19 h. Precursor films were prepared for duration of 13 h. In this case, the thicknesses are slightly reduced while the homogeneity of the film in terms of composition and roughness are greatly worsened. For duration lower than 13 h, no silicon clathrates were obtained. This is either due to too short annealing durations preventing the formation of the precursor or, when precursor films were observed, they spontaneously degrade when exposed to air. In both cases, this did not allow the decomposition into silicon clathrates and only resulted in the formation of a polycrystalline diamond silicon layer.

2.3 Characterization of the silicon clathrates films

The parameters of the two processes involved in the synthesis of the silicon clathrates films have been optimized allowing the selective synthesis of type I and type II films along with a reduced brittleness. This was performed for the first time without using a glovebox at any step of the process. In the following, we will present the properties of the films of silicon clathrates synthesized using our setup and compare them to the properties of previously silicon clathrates films[14], single crystals[15,16] and powders[11,17].

2.3.1 Properties of the Type I, Na_8Si_{46}, films

Type I silicon clathrates are synthesized with a total occupation of the polyhedral cages leading to a Na_8Si_{46} formula using the required thermal decomposition conditions determined above.

In this first part, the properties of the type I silicon clathrates films will be given and discussed at the light of previous work starting from the crystallographic structure of these films before providing their opto-electronics properties.

<u>A. Structural properties of type I silicon clathrate films</u>

The type I films were prepared using Process 1 at 630°C for 19h with a 0.30 g sodium mass, and a Process 2 at 400°C for 4h.

The crystallographic structure of the type I films was assessed thanks to XRD analysis using the reference[11] cited in the previous section with additional refinement of the structural parameters using LeBail and Rietveld refinements. Complementary analysis of the structure is also performed by Raman spectroscopy and electronic microscopy observations.

From the diffractograms measurements on the polycrystalline type I films synthesized, the average crystallites size is of 64 ± 3 nm. To precisely define the structural parameters of the type I phase synthesized here, Le Bail followed by Rietveld refinements of the Na$_8$Si$_{46}$ films are performed using the Jana2006 software[18] using the data reported by Yamanaka et al.[19] for type I single crystals. The result of this refinement and its fitting with the original diffractogram is shown in **Figure 2.14**.
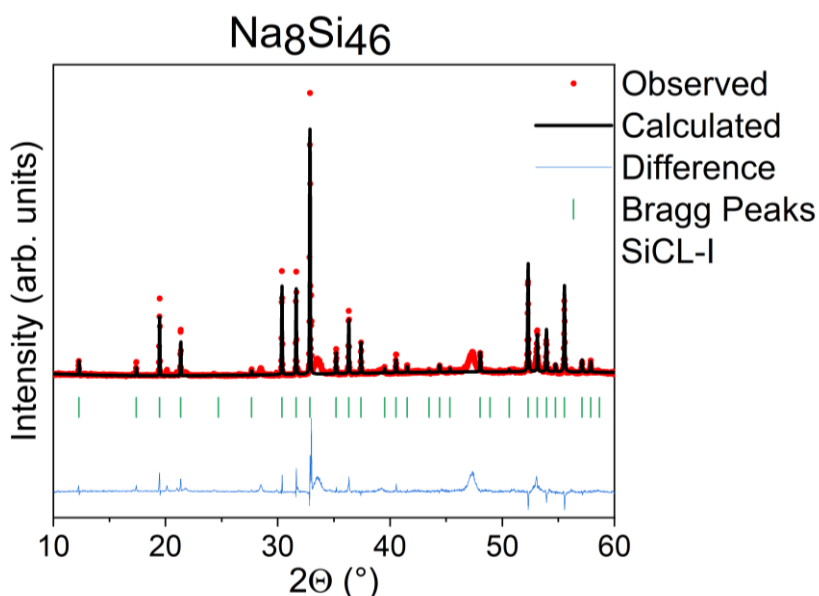
Figure 2.14 XRD diffractogram fitted using Rietveld Refinement for a Na$_8$Si$_{46}$ composition.

The structural parameters and fitting constants are reported in **Table 2.3**. Additional information on the silicon and sodium atoms positions are available in the annex A.2.1 section.

Table 2.3 Structural parameters of the refined Na$_8$Si$_{46}$ film

Refined formula	Na$_8$Si$_{46}$
Lattice parameters a = b = c (Å)	10.1979(3)
Cell volume V (Å^3)	1061.3(5)
Calculated density Dcal (g/cm3)	2.31
Weighted profile residual wRp	0.074
Reliability factor Rp	0.068
Goodness of fit	1.87

Using Rietveld refinement, the lattice parameter of the type I phase is of 10.1979 ± 0.0003 Å which is in complete agreement with the 10.1983 reported on the 01-089-

5534 JCPDS mentioned as a reference in the 2.3 section. The similarity between both values of lattice parameters between the reference powder and the film of this work indicate that the films here is not under internal strain. All cages of the type I structure synthesized are each filled with a sodium guest atom as expected from this clathrate structure. This complete occupation is systematic with the type I structure of the clathrates in the binary Na-Si system.

Raman investigation of the Na_8Si_{46} films, shown in **Figure 2.15**, led to the measurements of peaks whose signatures are in agreements both with theoretical[20–22] and experimental[23] studies with only a slight shift of the vibration for the $3E_g$ and $1A_{1g}$ modes. The identified peaks are highlighted in **Figure 2.15** and are compared to previous experimental results in **Table 2.4**[23]. As it can be seen from the spectrum, the peaks are not all well-defined, even though the spectrum was the best one obtained for type I clathrates. The low resolution of the observed vibrations is likely due to the expected metallic character of the phase, lowering the efficiency of the polarization change of the molecular vibration on which the Raman spectroscopy relies.
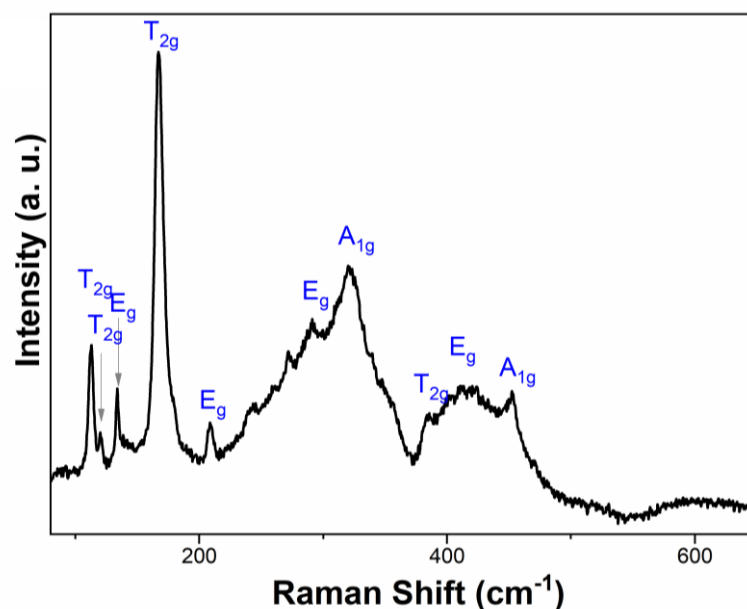
Figure 2.15 Raman spectrum of the Na_8Si_{46} film.

Table 2.4 Energies of the various Raman vibrations for the Na$_8$Si$_{46}$ film compared to tabulated values.

Vibration mode	Na$_8$Si$_{46}$ by Fang et al.[23] (cm^{-1})[23]	Na$_8$Si$_{46}$ (cm^{-1})
1T$_{2g}$	106.2	112.9
2T$_{2g}$	123.1	120.0
1E$_g$	129.8	133.8
3T$_{2g}$	175.2	170.0
2E$_g$	-	208.6
3E$_g$	283.1	291.2
1A$_{1g}$	313.1	320.2
4T$_{2g}$	382.9	389.6
4E$_g$	405.3	410.6
2A$_{1g}$	453.8	452.2

All the synthesized type I silicon clathrate films demonstrated good adhesion to the silicon wafer substrates and reduced fragility compared to other films. This could be due to their epitaxial growth from the zintl phase as previously observed[24]. SEM observations of the type I films cross-section and surface reveal a well crystallized polycrystalline material as shown on **Figure 2.16.** The film is about 40 micrometers thick.

Some type I silicon clathrates films were grinded down to powder to investigate their crystallinity thanks to TEM analysis. **Figure 2.16b** confirms the good crystallinity of the powder and crystallite of 58 ± 1 nm, which is consistent with the data determined by XRD. EDX measurements confirm the chemical composition of the type I Na$_8$Si$_{46}$ with a detected 13.9 %at of sodium to be compared to the expected one namely 14.8 %at.
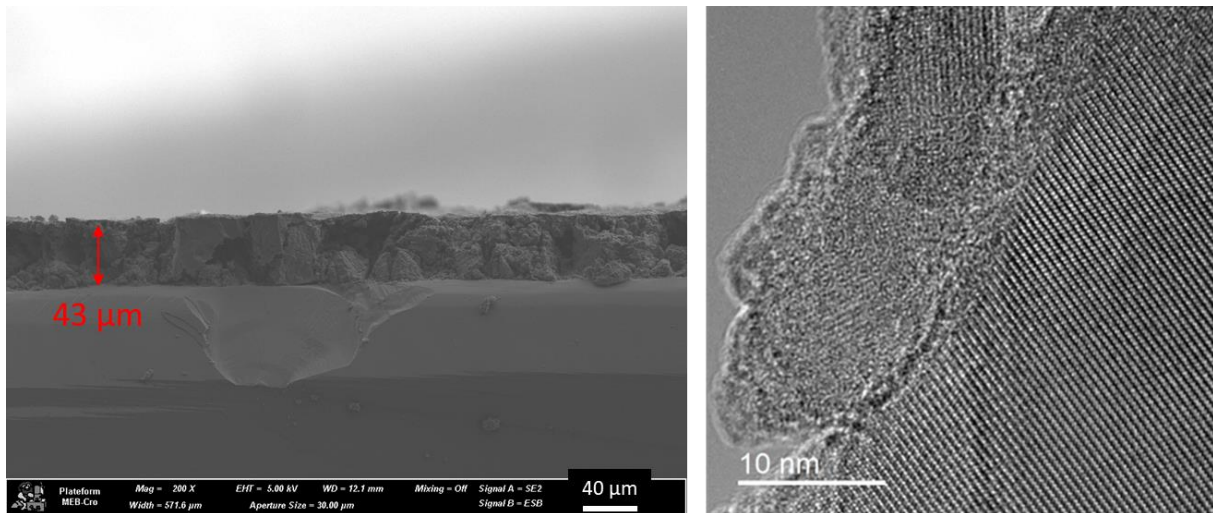
Figure 2.16 SEM and TEM (grinded into powders) observations of Na_8Si_{46}.

B. Optoelectronic properties of type I silicon clathrates films

The optical properties of the type I were investigated thanks to spectroscopic ellipsometry measurements at wavelength from 210 nm up to 885 nm. The absorption coefficients were extracted from the ellipsometry data without modelling under the semi-infinite medium assumption that the measurement is carried out on a silicon clathrate layer thick enough (40 µm) to absorb and reflect UV to near infrared wavelengths, and none is reaching the underlying silicon substrate.

The absorption coefficients of the type I silicon clathrate versus the photon energy is plotted in **Figure 2.17**, and compared those of an intrinsic silicon. It is clear that the type I films absorb much better in the near infrared and the visible range as compared to a single crystalline silicon. Its absorption coefficient is consistently above 10^5 cm^{-1} in this range. With such absorption coefficient, close to the ones reported for hydrogenated amorphous silicon, layer of less than a tenth of a micron thick of type I silicon clathrates would be enough to absorb more than 95% of light according to Beer Lambert law. No light absorption data are available for type I silicon clathrates in any form. Due to its metallic behavior, no Tauc plot were correctly fitted using the absorption coefficients and logically no PL peak were observed for the type I film.
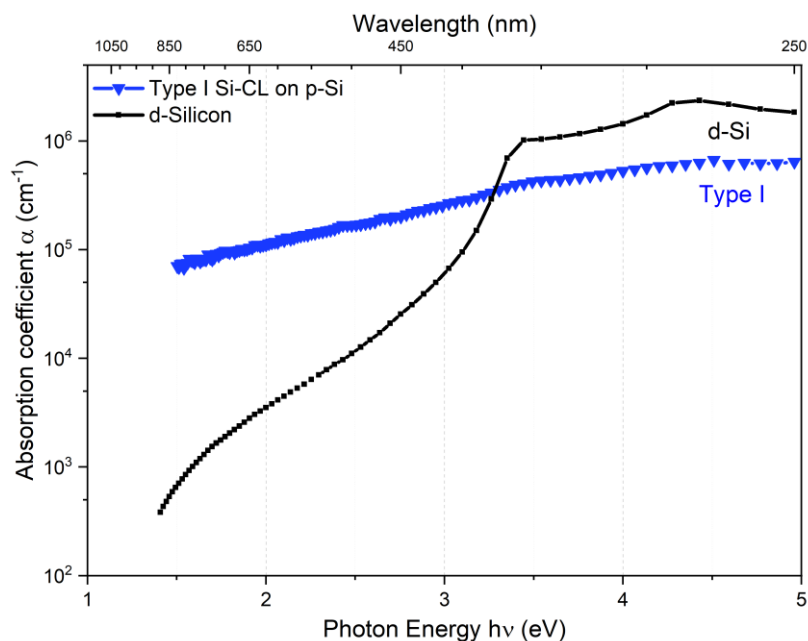
Figure 2.17 Absorption coefficient estimated by ellipsometry of Na_8Si_{46} and compared to the diamond silicon.

The electrical properties of type I film were studied on a sample purposely grown on intrinsic diamond silicon (100) wafer. Firstly, the Hall measurements of Na_8Si_{46} film confirmed the expected metallic behaviour with a resistivity of 4×10^{-2} $\Omega \cdot cm$, a mobility of 40 $cm^2/(V \cdot s)$ for a charge carrier density of -1.5×10^{19} cm^{-3}. This resistivity is two order of magnitude higher than one reported for type I single crystals grown either by thermal decomposition[16] or Na-Sn flux[27] both of around 2×10^{-4} $\Omega \cdot cm$. The more resistive type I films can be explained by the hindrance of the electrical conduction by the numerous defect and cracks shown by the layer. The Na_8Si_{46} is a pseudo metal material in which the conduction in done by the excess electrons given by the sodium guest atoms to the silicon framework.

Type I film appears a little more resistive than the polycrystalline material[28] with less than an order of magnitude difference. It can be explained by the smaller grains of the films compared to the reported one, limiting the efficiency of the electron transport across the layer.

2.3.2 Properties of the Type II, Na$_x$Si$_{136}$, films

In contrast to the type I silicon clathrates, type II films are synthesized with a varying and incomplete sodium occupation of the polyhedral cages. In this first part, the properties of the type II silicon clathrates films with composition Na$_x$Si$_{136}$ with x ranging from 2 to 10, are presented and compared to data reported in literature.

The type II films were prepared using Process 1 at 600°C for 19h with a 0.15 g sodium mass, and a Process 2 at 400°C for various duration, which will affect the sodium content of the layer.

A. Structural properties of type II silicon clathrates films

The crystallographic structure of the type II films was explored thanks to XRD analysis using the references cited in the previous section with additional refinement of the structural parameters. Complementary studies of the structure and the sodium occupation are performed by Raman spectroscopy and electronic microscopy observations. We will focus on the obtention of various sodium occupation in the cages and the consequence on the properties.

Figure 2.18a shows the expected diffractograms and **Figure 2.18b** one experimentally obtained for x = 4.2. XRD analysis of synthesized type II silicon clathrate films for various occupation show consistent crystallites size of around 49 ± 7 nm. Similarly, to the previously discussed type I, type II silicon clathrates were refined by the Rietveld method using this time structures reported by Stefanoski et al. for various sodium content[15].

Indeed, this time the number of guest atoms hosted by the structure will vary depending on the synthesis conditions. Various amounts and positions of sodium atoms in the structure are inducing different structural parameters and thus impacting the intensity of the reflections observed by XRD. For a better observation' of the sodium effect on the diffractogram profile, the VESTA software[29] was used for the calculations of

theoretical diffractogram as the cages are filled in **Figure 2.18a** where peaks subject to most change are highlighted in red.
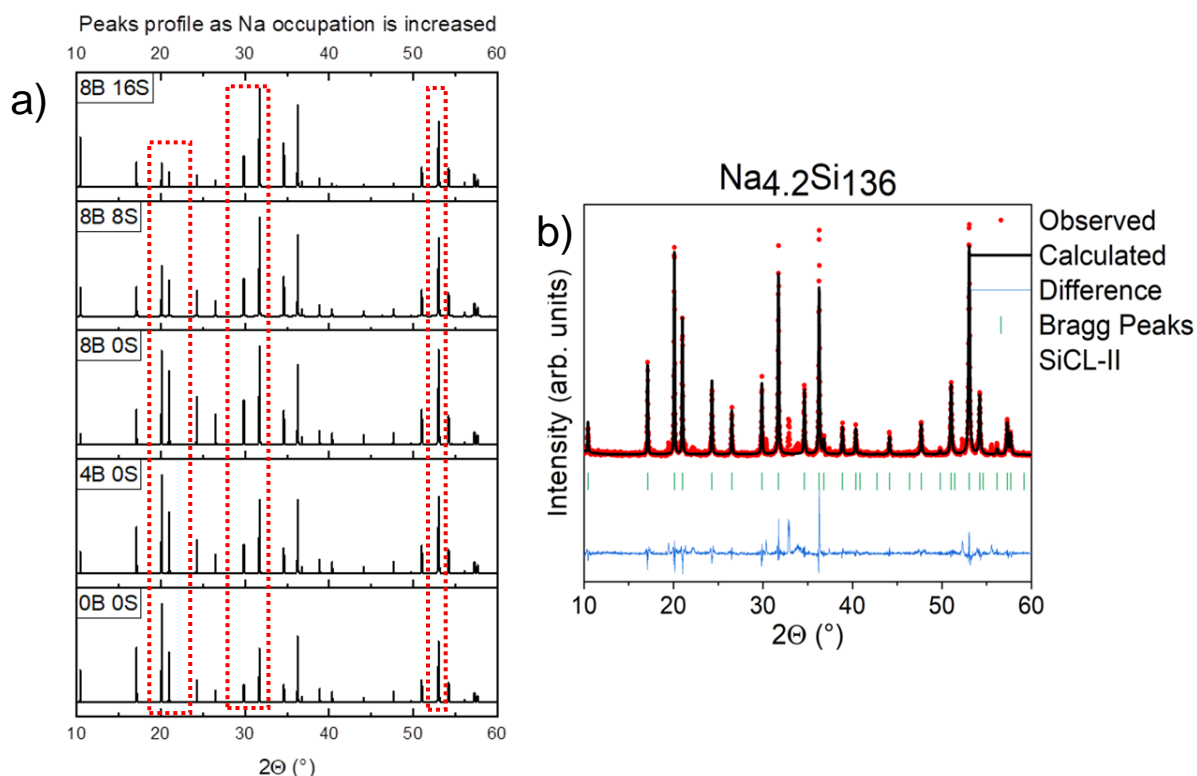
Figure 2.18 On the left, diffraction patterns variation expected as the cages of the type II silicon clathrates are being filled calculated using VESTA. The numbers before the letter B and the letter S refer to the number of Si$_{28}$ or Si$_{20}$ cages, respectively, currently filled. Nature of the films obtained depending on the temperature Process 1. On the right, XRD diffractogram fitted using Rietveld Refinement for a Na$_{4.2}$Si$_{136}$ composition.

As an example, the diffractogram of type II silicon clathrates films routinely obtained for a Process 1 at 600°C followed by Process 2 at 400°C for 4h is also shown in **Figure 2.18b**. Rietveld refinement on this film indicates a composition of Na$_{4.2}$Si$_{136}$ in which only the large Si$_{28}$ cages are filled.

Type II films were synthesized under the above conditions except for the duration of Process 2 which was changed. The variation of the duration of the annealing time resulted in different peak profiles of the XRD spectra, indicating a change in the occupation of the silicon clathrate polyhedral cages. Rietveld refinements were performed for films obtained for various duration of Process 2 and the results are given in **Table 2.5**.

Table 2.5 Structural parameters of the various refined type II film for Process 2 duration

Refined formula	Na2.28 Si136	Na3.47 Si136	Na2.98 Si136	Na4.35 Si136	Na5.67 Si136	Na9.96 Si136
Process 2 duration(h)	24	16	10	4	3	2
Lattice parameters a = b = c (Å)	14.6345(4)	14.6347(8)	14.6363(3)	14.6371(5)	14.6373(5)	14.6388(7)
Cell volume V ($Å^3$)	3134.25(15)	3134.1(3)	3135.18(11)	3136.52(18)	3136.4(2)	3137.3(3)
Calculated density Dcal (g/cm^3)	2.051	2.066	2.059	2.076	2.092	2.143
Weighted profile residual wRp	0.022	0.036	0.025	0.053	0.027	0.326
Reliability factor Rp	0.032	0.038	0.032	0.069	0.032	0.477
Goodness of fit	1.41	1.65	1.26	1.81	1.65	1.73

Refined lattice parameters of the type II films exhibit a very slight contraction of the lattice from 14.6388 ± 0.0007 Å to 14.6345 ± 0.0004 Å as the duration is increasing from 2h to 24h. The most impacted parameter is the sodium occupation x of the type II Na_xSi_{136} which is found to be reduced from x = 10 for a 2h duration down to x = 2.3 for a 24h long Process 2. Refinements of the atoms' positions and their occupations, summarized in the annex A.2.1 section, also indicate the systematic filling of the large Si_{28} cages with the available sodium atoms. In contrast, the small Si_{20} cages are filled only when the Si_{28} ones are filled. This means that Si_{20} cages are always empty for occupation x lower than 8. The gradual extraction of the sodium atoms from the cages of the type II silicon clathrates versus the duration of Process 2 is reported in **Figure 2.19**.
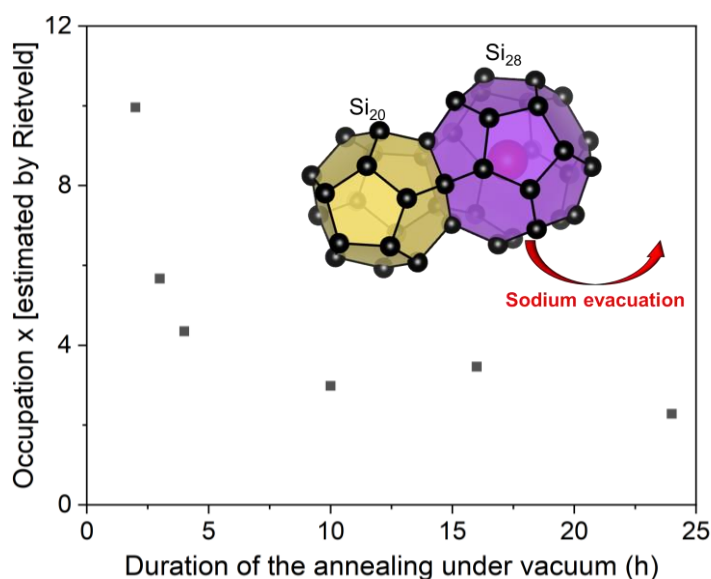
Figure 2.19 Sodium occupation of the type II structure depending on the duration of the duration of the thermal decomposition of the Zintl phase

Figure 2.20 shows the Raman spectrum of a $Na_{4.35}Si_{136}$ film. The spectra of type II films for x up to 5.7 are very similar to the one obtained for x = 4.4. The identified features are listed in **Table 2.6**.
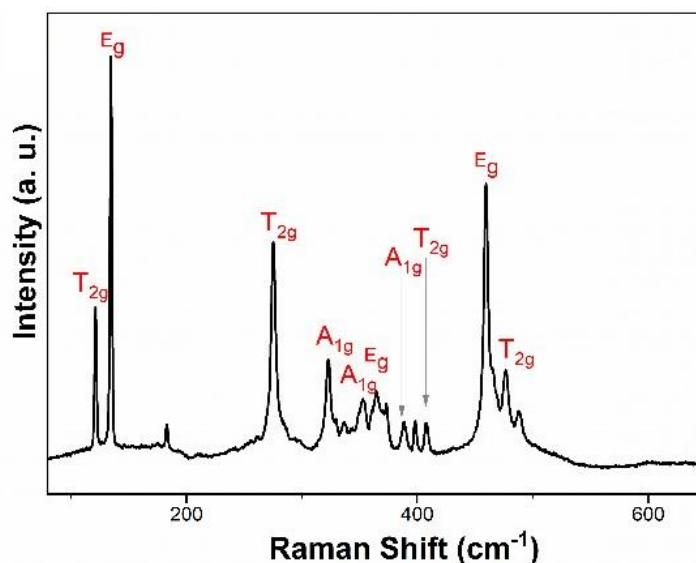
Figure 2.20 Raman spectrum of the $Na_{4.35}Si_{136}$ film.

Table 2.6 Energies of the various Raman vibrations for the $Na_{4.35}Si_{136}$ film compared to tabulated values.

Vibration mode	Si_{136} theory by Nolas et al. (cm^{-1})[30]	$Na_{4.35}Si_{136}$ (cm^{-1})
$1T_{2g}$	121	121.6
$1E_g$	130	134.9
$2T_{2g}$	176	183.5
$3T_{2g}$	267	275.7
$1A_{1g}$	316	323.8
$4T_{2g}$	325	330.2
$2E_g$	360	365.4
$2A_{1g}$	397	398.4
$5T_{2g}$	406	407.8
$3A_{1g}$	458	460.6
$3E_g$	463	Not resolved from $3A_{1g}$
$6T_{2g}$	466	
$7T_{2g}$	473	477.1
$8T_{2g}$	487	488.4

All peaks observed can be related to their vibration modes thanks to tabulated values obtained by theoretical studies. The only different spectrum was obtained for x = 10 for which the peaks were strikingly less defined than the ones for which only the large cages were filled.

The observed preferential filling of the large Si_{28} cages over their smaller Si_{20} counterparts is counterintuitive. This preferential filling is specific to the type II silicon clathrates and is explained thanks to reported studies done on type II silicon clathrates powders[31]. This is explained as due to a better stabilization in the Si_{28} cages due to sodium-sodium interaction between neighbouring similar cages. This preferential occupation of the large cages also explains the observed stability of the structure lattice parameter. This parameter only rises from 14.6345 ± 0.0004 Å to 14.6373 ± 0.0005 Å for structures of occupation up to x = 8 for which only the large cages are filled. The large cages being wide enough to afford hosting two sodium atoms simultaneously, they are not expanding by the presence of a lone one. However, a similar increase from 14.6373 ± 0.0005 Å up to 14.6388 ± 0.0007 Å is observed as soon as the small cages start to be filled for occupation x = 10 due to the tightest fit of the sodium atoms in their core. Similarly to the observation done on the type I film, the spectrum obtained for occupations above 8 could mean that those films are becoming closer to a metallic behaviour which would agree with the expected semiconductor to metal transition reported for x around 8 to 10[32].

Compared to type I films, the type II films exhibit weaker adhesion to the silicon substrate and their surface are almost more fractured and rougher than their counterpart. This additional damage to the films should be linked to the higher amount of sodium which has to be extracted during Process 2. SEM Cross-sectional study of the type II films highlighted the possible presence of a more porous and disordered sodium silicide material at the surface of the films as it can be seen in **Figure 2.21**. This component has been detected likewise on silicon clathrates films using glovebox and is suspected to be some kind of silicon sodium oxide[9]. Type II films remain thick with usual thickness around 30 up to 50 µm. TEM observations confirm the polycrystalline nature of the materials with crystallites sizes of 53 ± 1 nm with good crystallinity. EDS measurements systematically confirm the value of sodium occupation determined using the Rietveld refinements method.
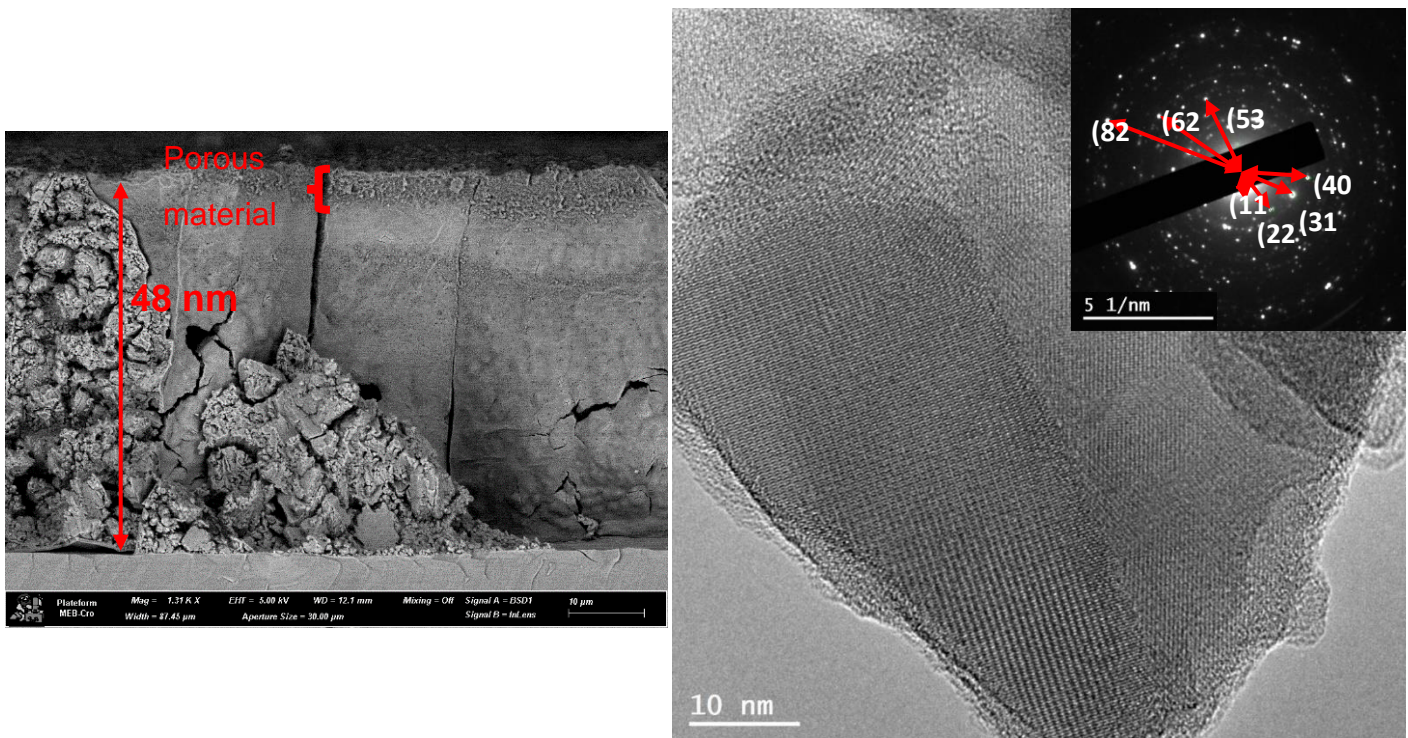
Figure 2.21 SEM and TEM observations of type II material.

B. Optoelectronic properties of type II silicon clathrates films

The absorption coefficients of type II films were investigated using spectroscopic ellipsometry under the same assumption than type I that the silicon clathrates films were thick enough to not let any light reaching the underlying silicon substrate (semi-infinite medium). **Figure 2.22** plots the absorption coefficient of the Na$_{4.35}$Si$_{136}$ which is found to be one order of magnitude lower than the ones observed for the type I films. The type II absorption coefficients reported here are slightly higher than the one obtained using transmission measurements or diffuse reflection spectroscopy but remain of the same order of magnitude.
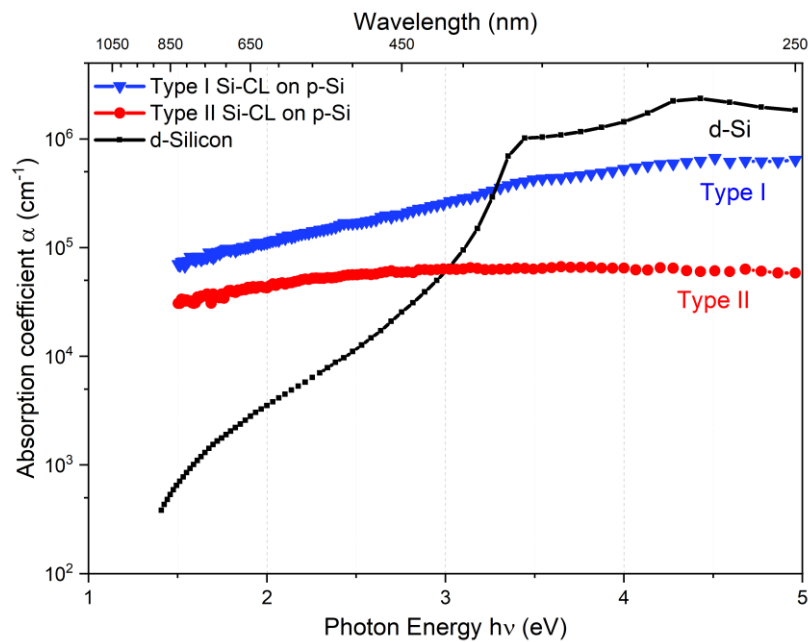
Figure 2.22 Absorption coefficient estimated by ellipsometry of Na$_8$Si$_{46}$ and compared to the Na$_8$Si$_{46}$, diamond silicon.

As the type I films, the type II films are better light absorbers than a single crystalline silicon in the near infrared and visible range by up to two orders of magnitude. From the values of the absorption coefficients and the Beer Lambert law, it can be determined than a type II layer of thickness around a micrometer would be enough to absorb at least 95% of the light.

Figure 2.23 gives the Tauc plots drawn for the type II film for both direct, $(\alpha.E_{Ph})^2 \; vs \; E_{Ph}$, and indirect, $(\alpha.E_{Ph})^{\frac{1}{2}} \; vs \; E_{Ph}$, bandgap assumption. Under the assumption of a direct bandgap of Na$_{4.35}$Si$_{136}$, a value around 1.9 eV is obtained while the indirect plot shows no fit. The value determined by Tauc plot has to be considered with care as no absorption band is visible in the absorption spectra.

Similar values of direct bandgap have been determined by Tauc plot from type II films[9] and powders[33] with values ranging from 1.7 to 2.0 eV even though no absorption band is clearly evidenced from the respective spectra. Alternative methods to determine the bandgap nature and value have to be explored before concluding on the material bandgap nature and value.
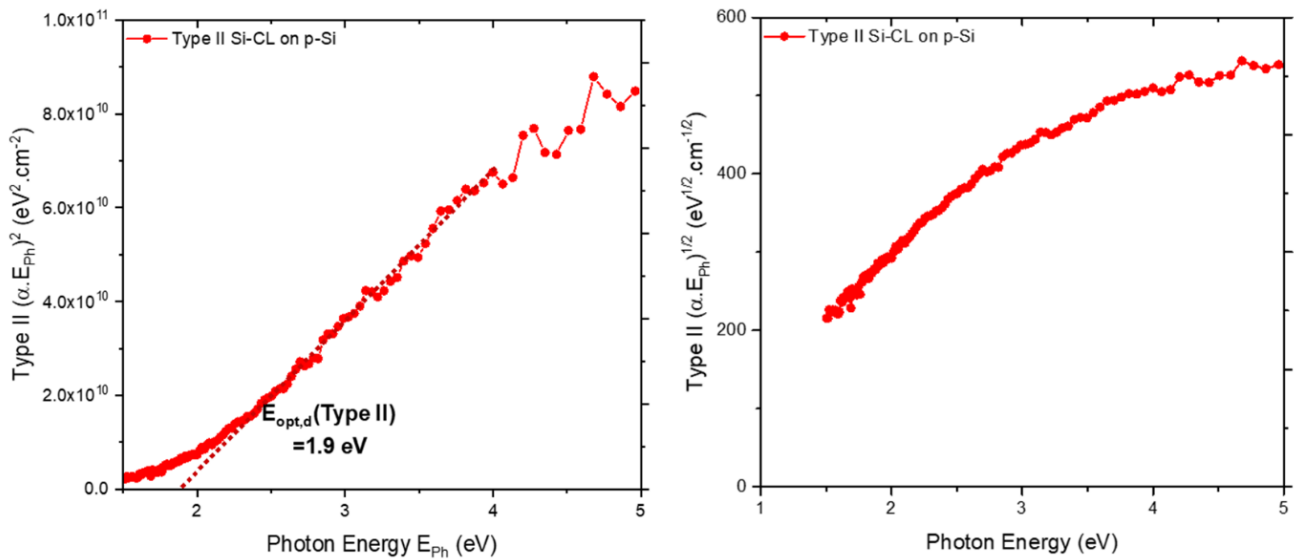
Figure 2.23 Tauc plot for the Na$_{4.35}$Si$_{136}$ film under the assumption of a) direct bandgap b) indirect bandgap.

Figure 2.24 plots the photoluminescence spectrum of the type II silicon clathrate. The PL measurements shows a broad peak centre in the 1.7 to 2.0 eV region. The broadness of the peak is commonly witnessed for type II silicon clathrates films[4,9] and is an effect of extensive amounts of defects within the films.
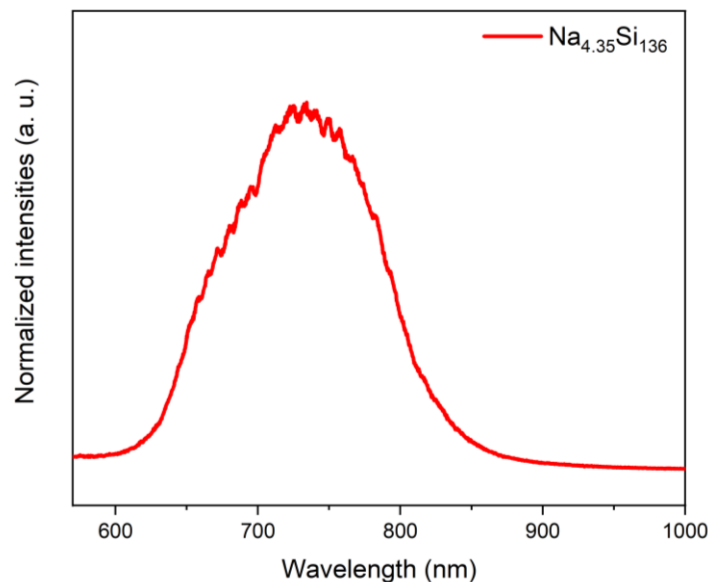
Figure 2.24 PL spectrum of the type II Na$_{4.35}$Si$_{136}$ films performed using a 532 nm laser

Additional type II films were synthesized on intrinsic silicon wafer to allow the measurements of their electrical properties. Films of occupation x = 2.1, 4.2, 4.35 and 7.3 were synthesized and then their carrier transport properties were measured using

Hall Effect setup. The data are reported in **Table 2.7**. All measured samples have sodium guest atoms located in the large Si_{28} cages. On this range of occupation which remains below 8, the overall trend seems to tend toward a reduction of the resistivity as the sodium content is increased and thus as the electron concentration raised.

Table 2.7 Electrical properties of the type II silicon clathrates for various composition.

Formula	Carrier concentration (cm^{-3})	Resistivity ($\Omega.cm$)	Mobility ($cm^2/(V.s)$)
$Na_{2.1}Si_{136}$	-9.5×10^{16}	24.7	18
$Na_{4.2}Si_{136}$	-2.1×10^{17}	4.2	7.1
$Na_{4.35}Si_{136}$	-3.0×10^{17}	2.2	8.0
$Na_{7.3}Si_{136}$	-1.03×10^{18}	6.8×10^{-1}	9.3

Our measured resistivity values are comparable to those reported elsewhere on silicon clathrates films of similar occupation[10]. However, they remain lower than the one reported for powders samples hot-pressed into pellet[17] with close to two order of magnitude factor and are higher than the value reported for single crystals by a three order of magnitude factor[15]. The more the silicon clathrate material is subject to a high concentration of defects, the more its resistivity drastically raises. These observations highlight the importance to take into account of the large concentration of defects and cracks caused by the thermal decomposition process in the electrical properties of the silicon clathrate material. This also hint toward the formation of a disordered and resistive material at the junction of the silicon clathrates grains.

However, the evolution of the resistivity with the sodium occupation is a trend observed in the synthesized films and in other reported forms of type II silicon clathrates. This trend is likely due to the higher contribution of donated electrons to the framework as the number of the sodium guest atoms increases[34,35]. This is also coherent with n-type charge carriers identified both by Hall effect and the hot probe method as these carriers would be the electrons donated by the sodium atoms.

Figure 2.25 draws the resistance versus temperature of the type II film with a $Na_{4.2}Si_{136}$ composition. The resulting behaviour of the type II film hints toward a semiconducting character of the layer. This can be explained by the presence of sodium cations inside the cages since they give their electrons to the silicon framework. The resistivity of the
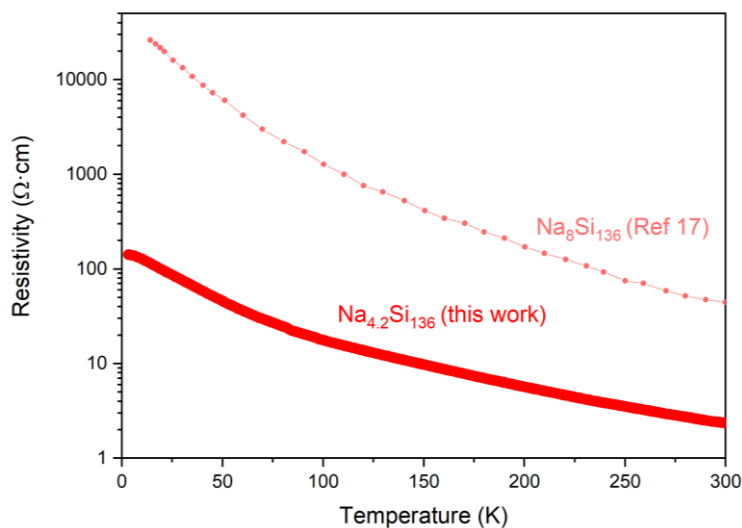
Figure 2.25 Resistance versus temperature behavior of the $Na_{4.2}Si_{136}$ film compared to literature hot-pressed pellets of Na_8Si_{136}[17].

synthesized film is also compared to that of a hot-pressed pellets[17] of Na_8Si_{136} which shows a higher resistance despite a higher occupation. As explained before, this is attributed to the higher quantities of defect in the pressed pellets further limiting the electron conduction.

2.4 Post-synthesis annealing of the silicon clathrate films

The properties of both type of the silicon clathrates films have been investigated and the type II structure shows alluring high light absorption suitable for photovoltaic applications. Yet, the thermal stability of the grow Si clathrate films is also of interest. For instance, reduction of the previously mentioned high concentration of defect is strongly suited.

The as-grown silicon clathrates films were thermally annealed either under atmospheric pressure or under mechanical pressure and the properties of the resulting

films are investigated. The annealing under mechanical pressure aims at reaching a more compact layer and a smoother surface.

2.4.1 Thermal stability of the silicon clathrates

The silicon clathrates are materials known to decompose into diamond like silicon when submitted to high temperatures. For type I, this decomposition temperature, thanks to thermogravimetric measurements on powders, were found in literature to be at 606°C and while it is of 624°C for the type II structure[17].

Our grown films were thermally annealed at various temperature for a minute under argon atmosphere using halogen lamps (RTA), and then characterized by XRD.

The type II films were annealed at 450°C, leading to the formation of a minor polycrystalline diamond silicon phase as visible by XRD in **Figure 2.26**. Increasing the temperature up to 550°C resulted in a complete conversion of the type II silicon clathrates into a mixture of polycrystalline diamond silicon and $NaSi_6$ materials. Annealing at temperatures equal or higher than 650°C led to the total decomposition of the silicon clathrates into the elementary diamond silicon in a polycrystalline material. Experiments on type I films revealed similar degradation patterns as the temperature is above 450°C.

It should also be noted that annealing in air was also investigated and led to even more easily degraded silicon clathrate films with conversion to diamond silicon already observed at temperatures as low as 450°C.

In order to limit the damages sustained by the type II silicon clathrates, the adequate temperature of the RTA step is set thus at 450°C. This temperature may seems low compared to usual activation temperature of 850°C used for single crystalline silicon[38] but the materials have totally different thermal stability and behaviour.
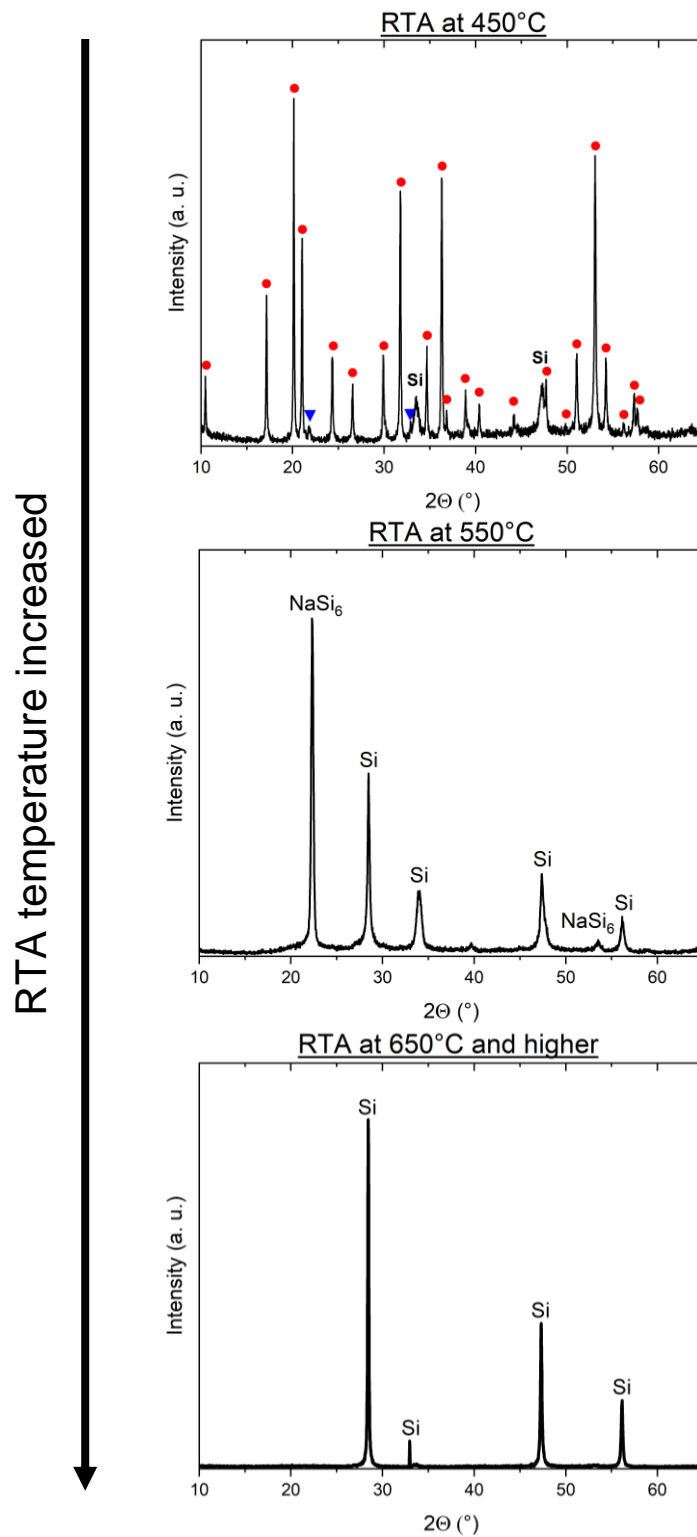
Figure 2.26. XRD patterns of a type II films after being submitted to RTA under Argon atmosphere at various temperature for a minute.

2.4.2 Annealing of the silicon clathrates under mechanical pressure

As mentioned earlier, one of the limitations of the silicon clathrates films is not only their thicknesses, but also their damaged structure due to the violent thermal decomposition step.

To improve the overall quality of the type I and type II silicon clathrate films, they were thermally heated under low compression thanks to a heating press system (**Figure 2.27**). The system to perform this treatment is a hydraulic system (Rondol) and two heating elements consisting of steel plates equipped with integrated and regulated heating. This treatment was operated by Céline Chevalier at the INL laboratory, Lyon.
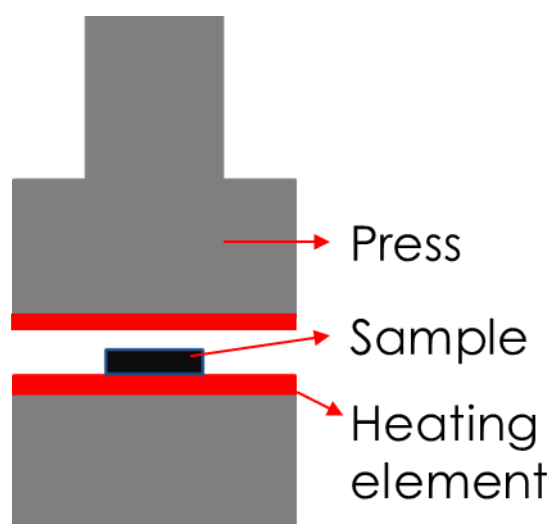
Figure 2.27. Schematic of the heating press setup

Using this system, both type I and type II films were annealed at temperatures of 200°C or 250°C and pressures of 2 kN or 4 kN.

Initially, predominantly type I films were submitted to annealing under pressure at 2 kN at both 200°C and 250°C. The aim was to densify the damaged and porous casually observed for the silicon clathrates films and to obtain a less rough surface. Once submitted to the treatment, the samples were investigated by SEM and compared to the previous observations as compared in **Figure 2.28**.
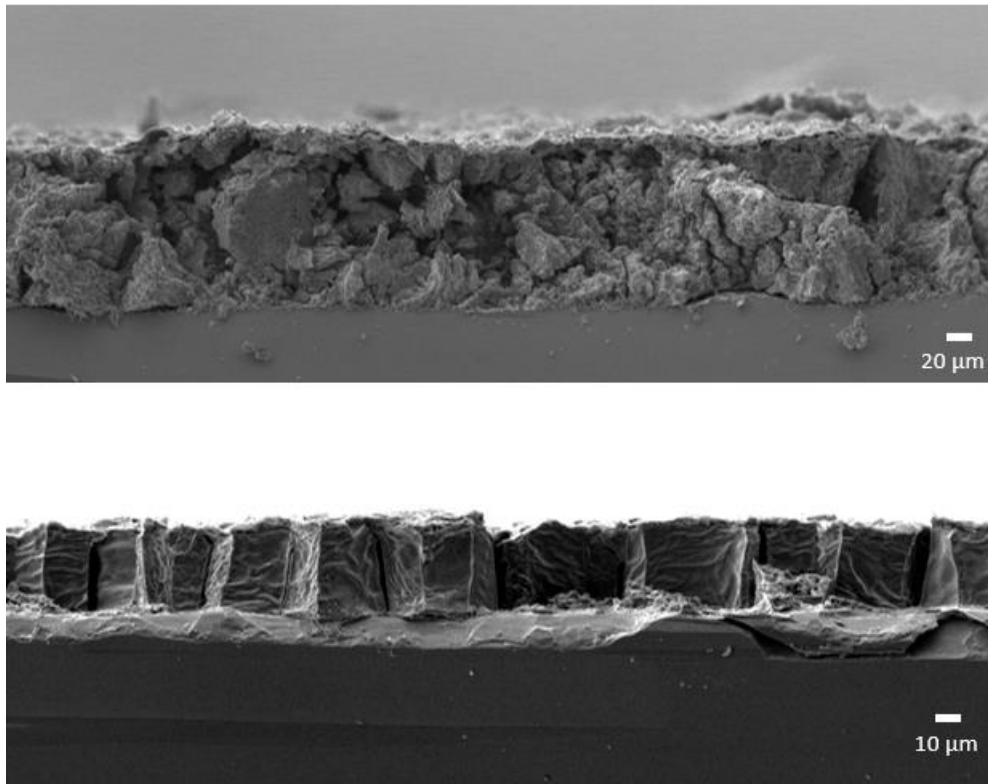
Figure 2.28. SEM Cross-section of the type I films before (top) and after press annealing at 250°C and 2kN

As it is clearly visible, the press annealing of the predominantly type I film allowed the reduction of the thickness of the film, but more importantly, a much denser film is achieved. The porous structure visible in the cross-section has almost disappeared giving rise to a layer with an apparent higher crystallinity. The surface of the pressed film is also much smoother than the pristine film which motivated the investigation of the sample by AFM as shown on **Figure 2.29**.
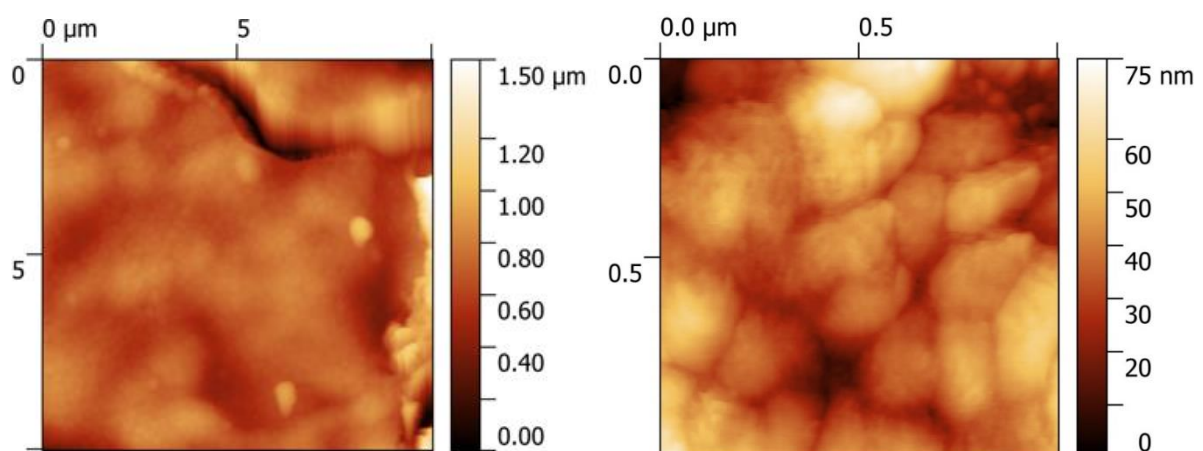
Figure 2.29 Topographic AFM measurements at the surface of a type I silicon clathrates films after press annealing at 250°C and 2 kN.

For the first time, it was possible to successfully measure the roughness of a silicon clathrate film by AFM which was previously impossible due to the consequent roughness of the untreated films. Based on the measurements, the grain size of the pressed material is close to 200 nm, which is four time higher than that of the as synthesized one. Depending on the size of the investigated area, the RMS roughness is about 100 nm and down to 10 nm for the 5 x 5 µm^2 and 1 x 1 µm^2 ones. Taking into account the large thickness of the film of around 20 to 30 µm, the state of the starting material and the synthesis method, these roughness values were unexpected.

When investigated by XRD, it became obvious that the annealing under pressure of the predominantly type I film not only changed the morphology of the film but also induced its reorientation along two main planes, the (320) and (321) ones as shown in **Figure 2.30**.
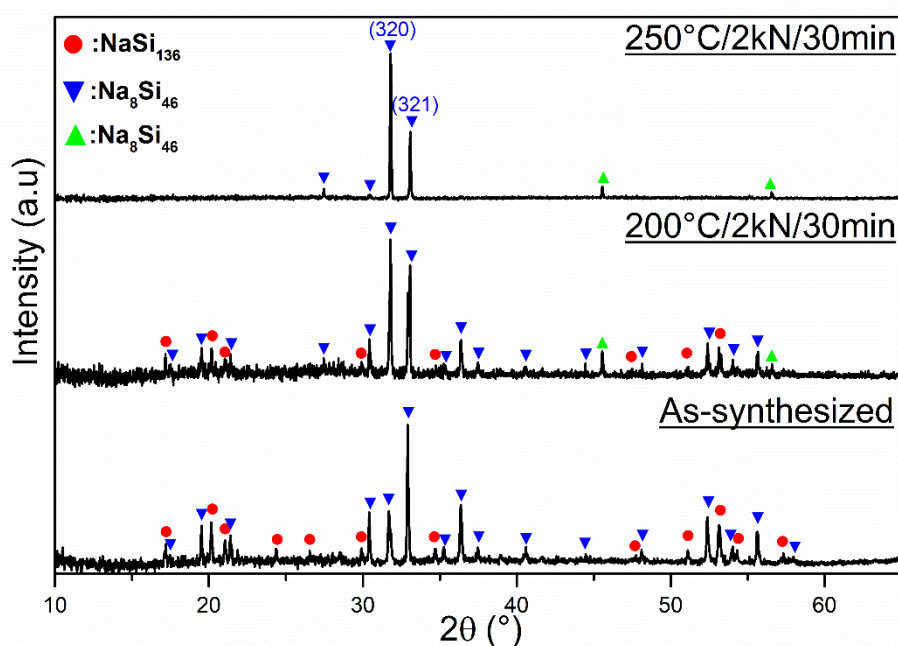
Figure 2.30. XRD pattern for the mainly type I film submitted to press annealing at 200°C and 250°C with a force of 2kN for 30 minutes.

At 200°C, both the conversion of the type II phase into the predominant type I and the preferred orientation of the type I structure along two main planes are becoming obvious. No shift in the position of the peaks is observed. When the temperature is increased to 250°C, the two main peaks of the oriented type II are again present and have seen their intensity greatly increased. Moreover, no type II phase is identified on the diffractogram, hinting that it was fully converted into type I Na_8Si_{46}. This surprising

reorientation of the silicon clathrate material could be related to the proximity between the (320) and (321) planes of Na_8Si_{46} with the (100) plane of the single crystalline diamond silicon substrate used.

Motivated by these promising results, type II silicon clathrates films were also annealed under pressure at both 2kN and 4kN at temperatures of 200°C and 250°C. Similarly, to the type I film, visible improvement of the film morphology is witnessed when the samples were investigated by SEM as reported in **Figure 2.31**. The surface of the films is effectively smoothed.
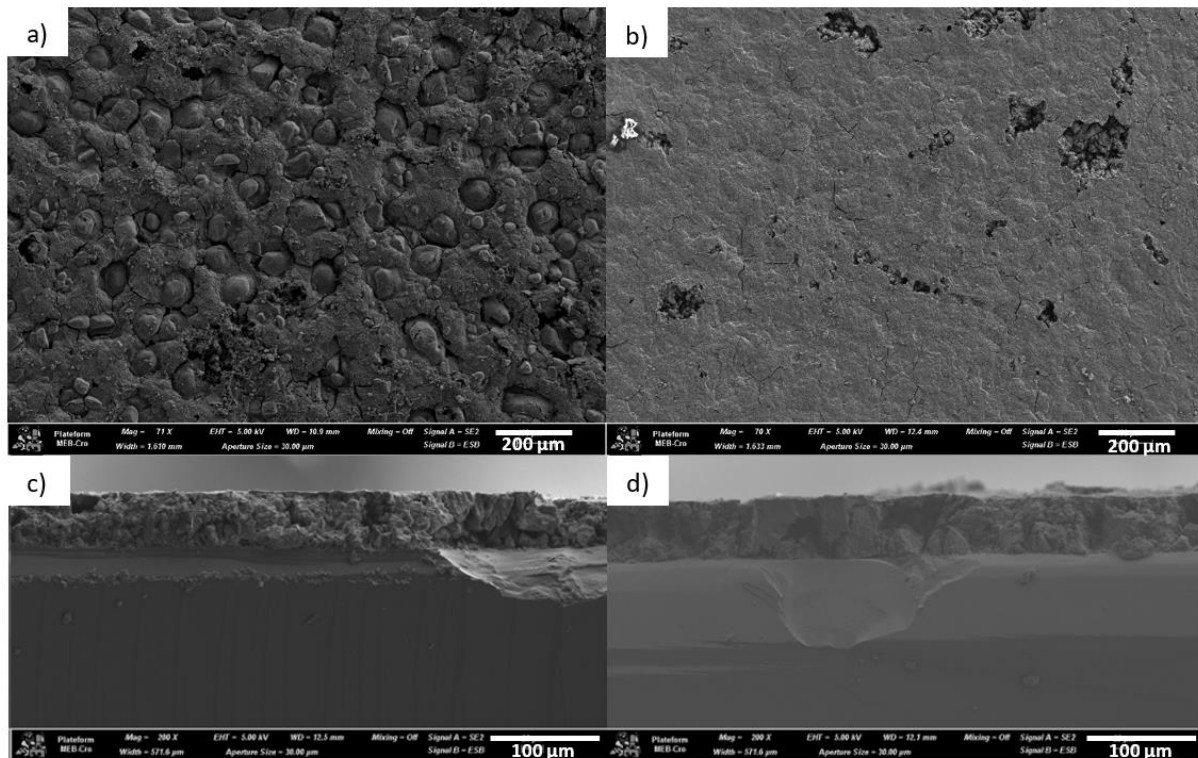
Figure 2.31. Surface observed by SEM of type II films a) before and b) after press annealing at 250°C/4kN/30min and cross-section c) before and d) after press annealing at 250°C/4kN/30min.

However, in this case no change in the type II film thickness was observed before and after press annealing even if the layer appears denser. The crystallinity of the resulting films also seems to have been improved after the treatment, even though more defects are visible than for the pressed type I film.

The type II pressed films were also investigated by XRD to identify any possible changes in the crystallographic orientation of the phase as observed for type I sample. However, based on XRD data of **Figure 2.32**, no modification of the orientations was detected.
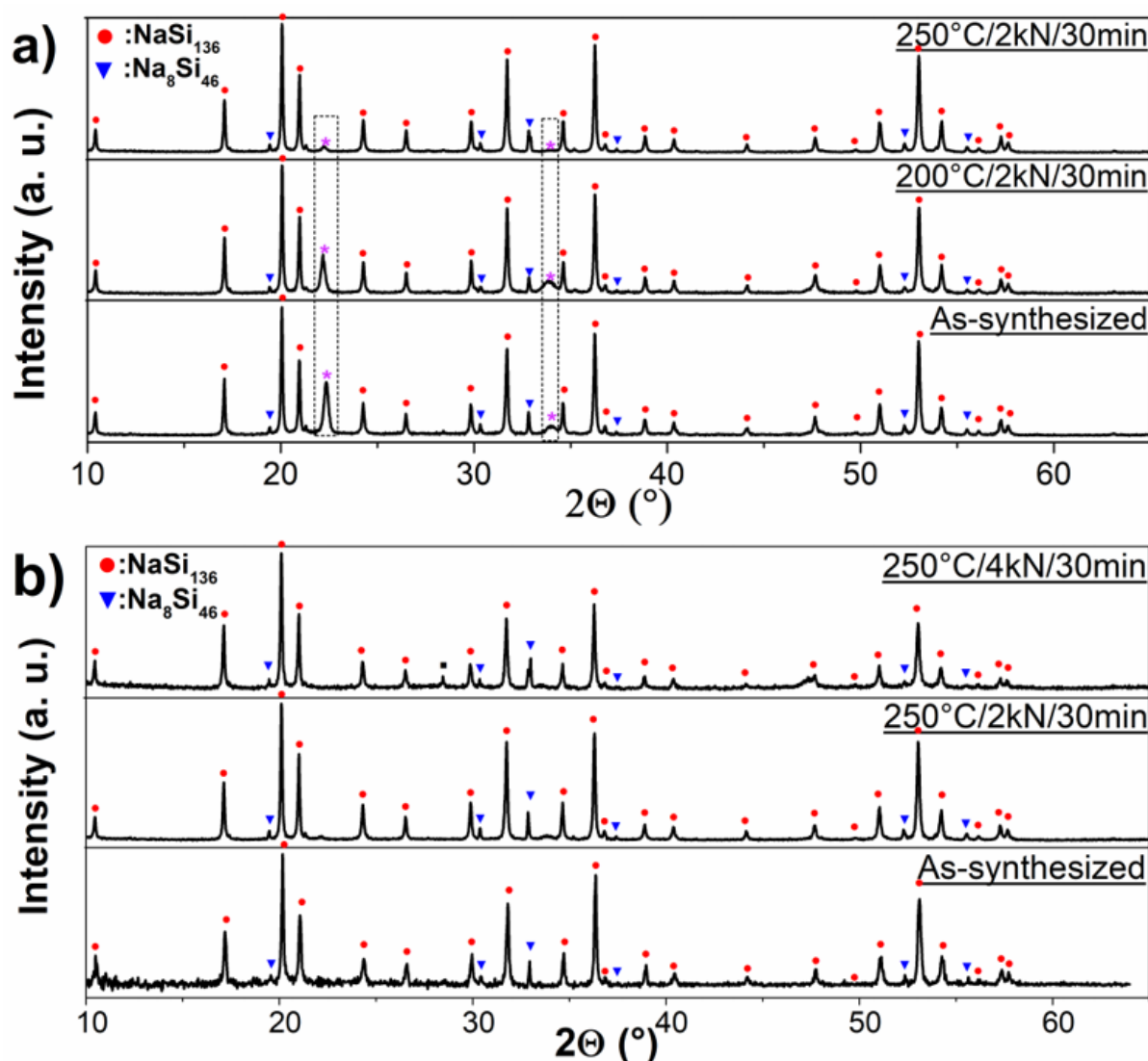
Figure 2.32. XRD pattern for type II films submitted to press annealing a) at 200°C and 250°C with a force of 2kN b) under 2kN and 4kN at 250°C for 30 minutes. Purple asterisks are imparted to the surfacing impurities.

When comparing the XRD spectrum of the pressed samples to the as-synthesized one, the type II phases show similar peaks profile. There is only a slight change in some peaks' intensities due to the small reduction of the sodium content during the annealing under mechanical pressure. It also appears that the minor phases such as type I, indicated in blue in **Figure 2.32**, is gradually reduced both as the pressure and the temperature is increased, which is similar to the type I observation. One of the type II film was also covered by a consequent amount of the disordered sodium rich layer at the surface[9], as visible on **Figure 2.32-a** in purple. This impurity is also gradually converted to the predominant type II as the temperature is increased. Presence and removal of this surfacing impurity phase is also witnessed by Raman spectroscopy as shown in **Figure 2.33** by the envelope located in the red frame.
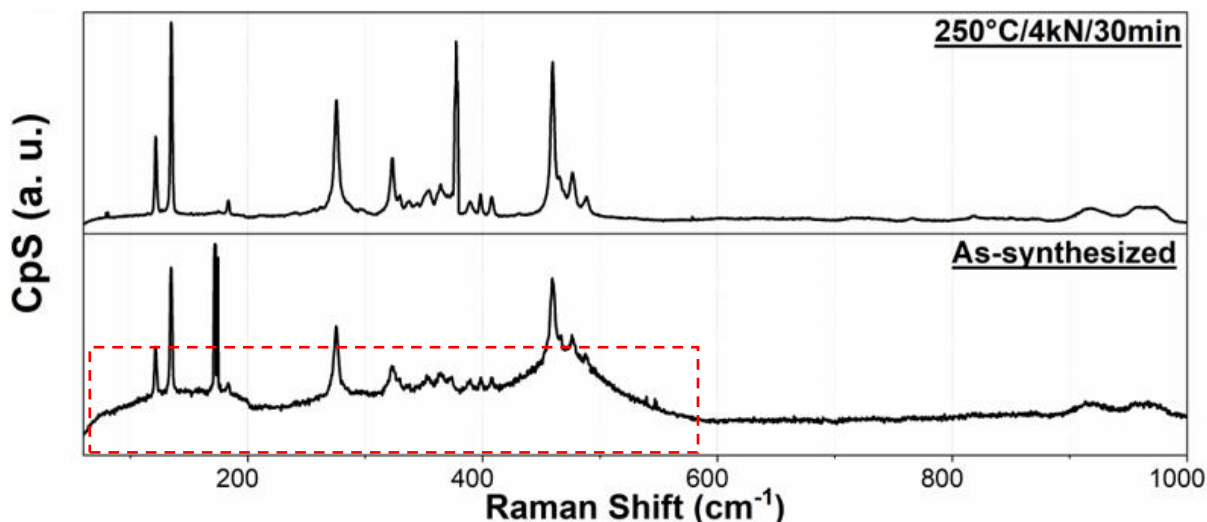
Figure 2.33. Raman spectra for a type II film before and after press annealing at 250°C under a force of 4kN for 30 minutes.

The as-synthesized type II material show the expected peaks which are drowned in a broad envelope for wavenumbers from 75 to 480 cm^{-1}, as visible framed in red in **Figure 2.33b**, along with a type I impurities peak around 170 cm^{-1}. After annealing under pressure, the wide envelope disappeared giving rise to nicely defined type II peaks and the contribution of type I impurities is gone. Further observations by SEM shows a kind of porous crust formed at the surface (**Figure 2.34**) of the layer while EDS measurements reveal that this top layer is richer in sodium than the bulk silicon clathrates. The thickness of this crust is also greatly reduced by the annealing under pressure step as measured in **Figure 2.34b** which is in agreement with the XRD and Raman observations.

As a summary of this part, annealing of the silicon clathrates films under mechanical pressure is an efficient method to obtain the smoothest surface of silicon clathrates films and a more compact layer. It seems also to be a way to reduce the thickness of the disordered sodium rich and porous crust observed at the surface of the silicon clathrates films.
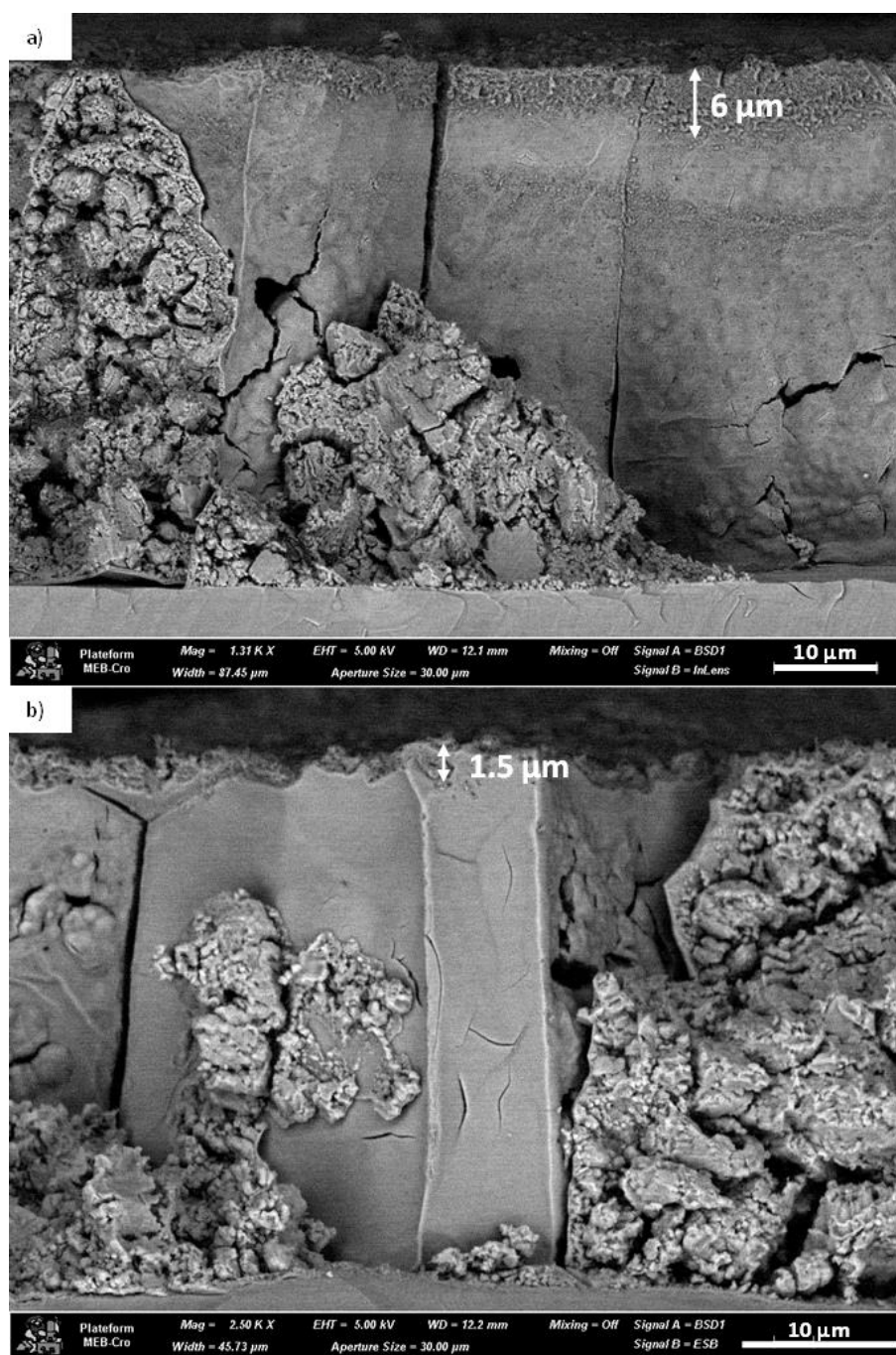
Figure 2.34. Zoomed in cross-sectional view of the Type II Silicon Clathrates films a) As-synthesized b) After Press under annealing at 250°C/4kN/30min.

2.5 Toward thin films

The surface of the silicon clathrates films has been demonstrated to be efficiently smoothed using annealing under mechanical pressure. This a one step toward making the alluring type II usable for photovoltaic application. However, so far the thickness of the films is ranging from 25 μm up to 60 μm using the previously optimized parameters of Process 1 and 2.

To reach thinner films, two main approaches were considered: the first and obvious one is the etching of as grown (or pressured) thick silicon clathrates layers. The second approach consists in limiting the reaction of sodium with the silicon substrate, either by using a barrier layer or by reducing the reaction duration. The later was already mentioned in the previous section and did not bring positive results. Another different approach to obtain a thin silicon clathrate film is to use a thin crystalline silicon layer as a substrate for process 1 and then process 2. These various strategies are schematically depicted in **Figure 2.35**.
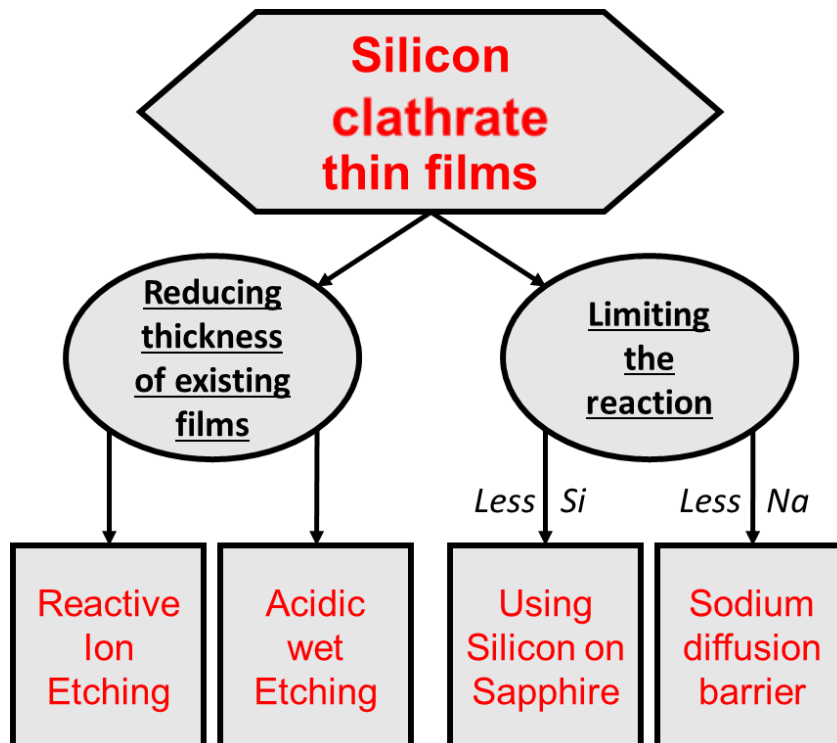
Figure 2.35 Strategies used toward the obtention of silicon thin films

2.5.1 Etching of the silicon clathrates

In this section, we will use wet and dry etching in an attempt to reduce the thickness of our films down to dimensions lower than the micrometer. Etching the silicon clathrate films also provides access to the bulk of the layer and provides the opportunity to remove detrimental material that forms at the layer surface[9].

A. Wet etching

The wet etching was firstly performed using a mixture of aqueous HNO_3/HF with the HF concentration fixed at 0.4 mol.l^{-1} at room temperature. The etching rate for the type II silicon clathrates was observed to be increased by adding more HNO_3 in the mixture. The etching rates were estimated by profilometer measurements after the immersion of the sample for a given time to be around 1 µm.min^{-1} for $c(HNO_3)$ = 1.5 mol.L^{-1} up to 3.5 µm.min^{-1} for $c(HNO_3)$ = 4 mol.l^{-1}. The addition of nitric acid up to 8 mol.l^{-1} induced the removal of the whole film in less than 4 minutes.

For the type I silicon clathrates, using HF acid induced the fast removal of the whole layer and no mix where yet found to reach controllable rates. The drawback of the wet etching method is its unreliability due to the fractured surface and porous nature of the silicon clathrates films, allowing the acidic mixture to sometimes reach the silicon clathrate / silicon wafer interface faster than expected. This results in the delamination of the clathrate layer from the silicon substrate.

B. Dry Etching

Reactive Ion Etching was also investigated using SF_6 as the etching gas as suggested in the literature[9]. For thickness measurements and characterization purposes, the Si clathrate films on substrate submitted to RIE were partially covered using thick pieces of silicon wafer. Thanks to measurements using profilometer and SEM measurements, the etching rate was estimated to be of about 4 µm.min^{-1} for a RF power of 400 W in

50 sccm of SF_6 and 20 sccm of He. From XRD measurements performed before and after the dry etching, the etched type II silicon clathrates films show no conversion into diamond silicon or any other phases. Moreover, it is also a convenient way to remove the surface' contaminant from the type II silicon clathrates. This is witnessed by the PL measurements shown in **Figure 2.36** where the PL plot of the darker etched part exhibits only the contribution of the type II structure located around 1.7 eV in contrast to the broad PL peak obtained from the non-etched part.
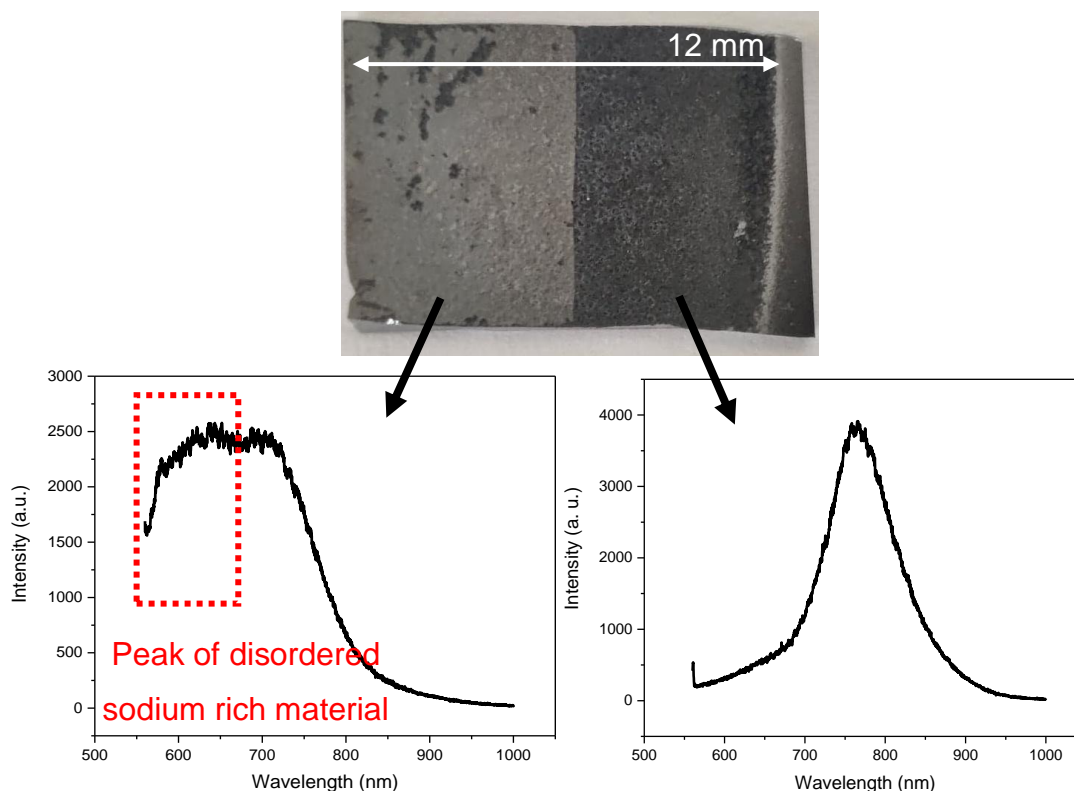
Figure 2.36 Photograph of non-etched (light gray) and etched (dark grey) area of a sample under RIE and the corresponding PL measurements using a 532 nm laser.

2.5.2 Sodium Diffusion Barrier

Let's remind that a strong reduction of the mass of the sodium slice did not allow to synthesize silicon clathrate because there was not enough sodium vapour pressure needed to allow the diffusion and the reaction to happen. Thus, a diffusion barrier was thought as an alternative to limit the amount of sodium reaching the silicon wafer while using a sufficient mass of the slice to sustain a high enough sodium vapour pressure.

To reach this, the candidate layer should present lower diffusion coefficient and solubility of sodium than silicon at the temperature of the reaction. Silicon nitride[39] was thus identified as a promising material as it fulfilled those conditions with a diffusion coefficient for sodium around 10^{-14} cm$^2 \cdot$s^{-1} in the temperature range[40] compared to the 5×10^{-11} cm$^2 \cdot$s^{-1} of the single crystalline silicon[41] and a lowered sodium solubility. Three different thicknesses of silicon nitride were then deposited on top of p-doped silicon wafer using a PECVD setup: 40, 80 and 120 nm. The silicon nitride coated silicon wafers were then submitted to a Process 1 at 600°C for 13 h using a 0.20 g sodium slice. Process 1 was followed by Process 2 at 400°C for 4h. Type II silicon clathrate is expected as the major product.

For the 40 nm thick silicon nitride layer coated silicon clathrate film, the resulting surface image and the XRD spectrum are shown in **Figure 2.37**. At the end of the thermal decomposition process, the sample results in a broken silicon nitride layer revealing an inhomogeneous type II silicon clathrates film with an overall thickness of 20 μm. The silicon nitride breakage may be due to the expansion of the silicon clathrates layer growing underneath it, meaning that the diffusion barrier was too thin to sufficiently limit the reaction. Yet, it also means that the silicon nitride is not preventing the sodium to access the silicon wafer surface.
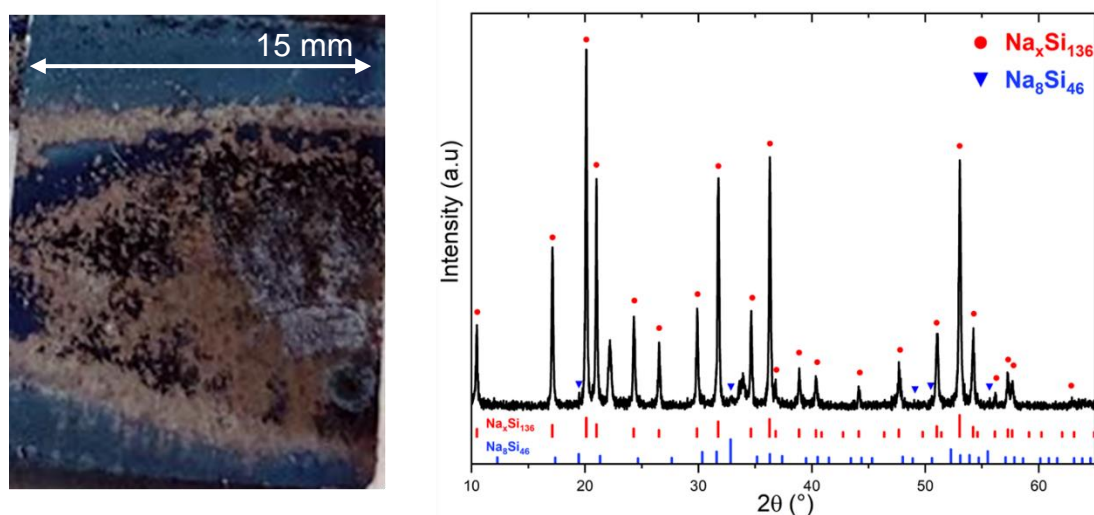
Figure 2.37 Photograph and XRD patterns for a sample covered by a 40 nm thick silicon nitride layer submitted to Process 1 at 600°C for 13h. The red circles refer to Na₁Si₁₃₆ reflections and the blue triangles to Na₈Si₄₆.

Performing the same process with the 80 nm thick silicon nitride layer, the resulting sample exhibited an almost undamaged silicon nitride layer with darker area underneath it across the silicon wafer surface as visible in **Figure 2.38**. Using XRD, type II silicon clathrates are identified as the darker spots visible on the silicon wafer surface. As confirmed by local inspection using Raman spectroscopy, no continuous film of silicon clathrate is obtained using this thickness of the diffusion barrier. On the other hand, when the diffusion barrier thickness is increased to 120 nm, no clathrates formation is observed.
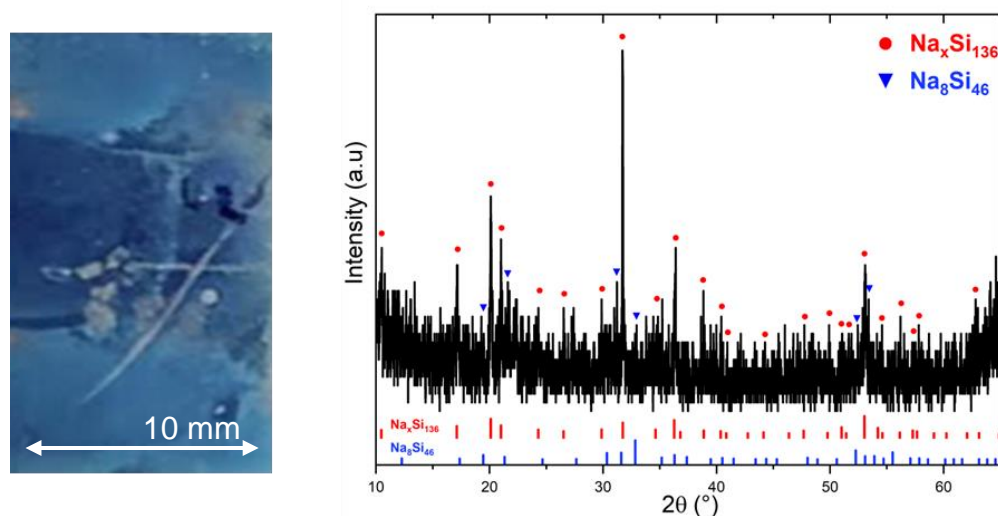
Figure 2.38 Photograph and XRD patterns for a sample covered by an 80 nm thick silicon nitride layer submitted to Process 1 at 600°C for 13h. The red circles refer to Na_1Si_{136} reflections and the blue triangles to Na_8Si_{46}.

Silicon nitride as a diffusion barrier is an effective way to reduce the amount of sodium reacting with the silicon wafer which can be tuned according by the thickness of the PECVD deposited silicon nitride layer. However, throughout these experiments a common point was found for both 40 and 80 nm thick silicon nitride layer: the obtained silicon clathrates layer is not uniform across the surface supposedly due to inhomogeneities in the diffusion barrier resulting in various diffusion coefficients in some areas of the films.

2.5.3 Use of a Silicon on Sapphire substrate.

Another way of restricting the reaction is to limit the quantity of available initial silicon to be transformed into clathrate. The use of thin single crystalline silicon on sapphire[2,42]

(SOS) as a substrate for the two-step process is proposed as an alternative to obtain thin clathrate silicon layers.

In this work, SOS structures with a 400 nm thick silicon (100) layer cut into of 1 x 1 cm² pieces were used. To expose those pieces to the sodium vapour, they were glued using silver paste to a sapphire substrate slightly larger than the Inconel boat as depicted on **Figure 2.39**. To keep track of the reaction and compare it with the one using silicon wafer, silicon pieces were also cut from a single crystalline silicon substrate into 1 x 1 cm² pieces and stick on the sapphire substrate close to the SOS ones. The samples were introduced into the furnace to start the process.
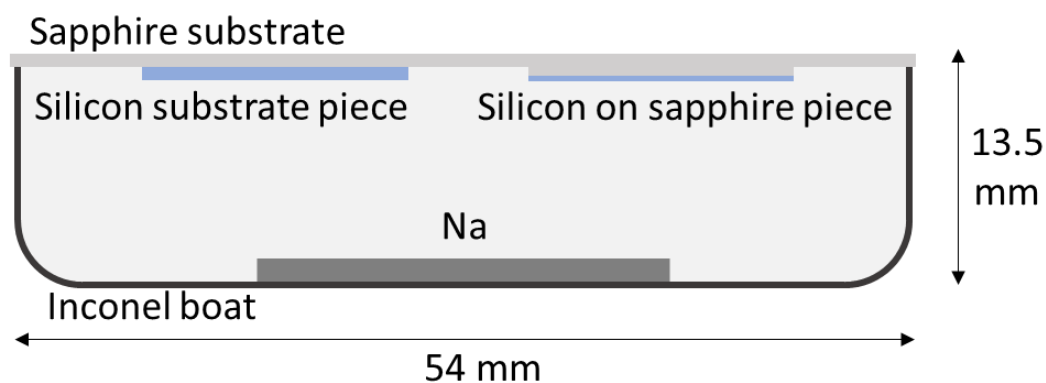
Figure 2.39 Cross-sectional schematic representation of the system used for the synthesis of silicon clathrates thin films.

Process 1 was performed at 600°C using 0.1 g of sodium for various duration, which was then followed by Process 2 at 400°C for 4 h. For duration between 13h to 19h, routinely used for the synthesis using silicon wafer, type II silicon clathrates films were effectively obtained on the piece of silicon substrate. However, Process 1 induces a complete etching of the thin silicon film on sapphire. By gradually reducing the duration of Process 1 below 45min, a more and more wide layer of type II silicon clathrates was observed on the SOS samples. The possible mechanism is the formation of the zintl precursor using the whole 400 nm silicon layer early in the reaction which is then still submitted to hot sodium vapor inducing its degradation.

Finally, the best thin films were obtained for Process 1 for a duration of 45 min at the end of which the tubular furnace is open to let the steel tube cool faster to allow an earlier removal of the precursor film and to limit as much as possible its reaction with

the sodium leftover. The duration of Process 2 was also extended up to 24 h to evaporate most of the sodium left at the surface. An image of such thin films is shown in **Figure 2.40** along with its XRD spectrum.
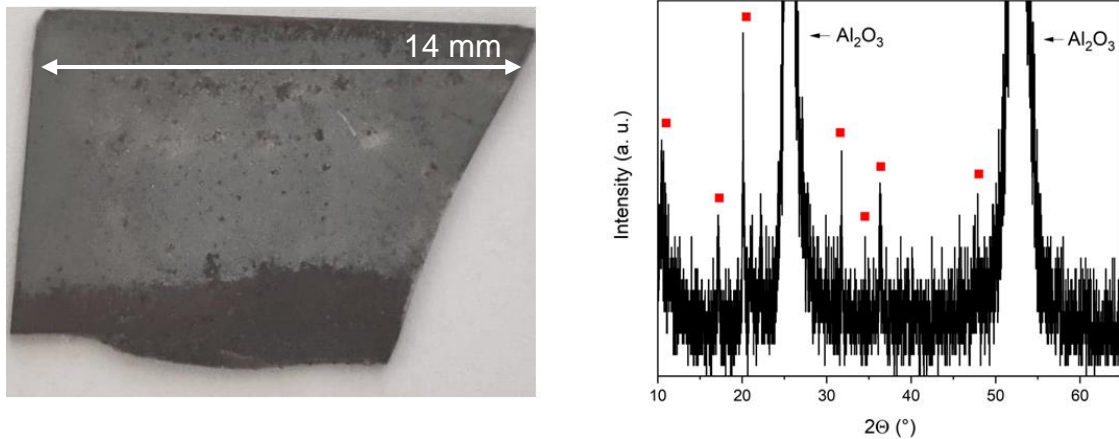
Figure 2.40 Photograph and XRD patterns for a SOS sample submitted to Process 1 at 600°C for 45min. The red circles refer to Na_1Si_{136} reflections and the blue triangles to Na_8Si_{46}.

As it can be seen from the photograph of the sample, the thin films are not yet optimal, with the light grey area being an inhomogeneous layer of type II silicon clathrates in a matrix of disordered sodium silicide materials[43] as inspected by SEM and shown in **Figure 2.41.a.** The darker part is where the silicon clathrate layer is the more continuous as reported in **Figure 2.41.b**
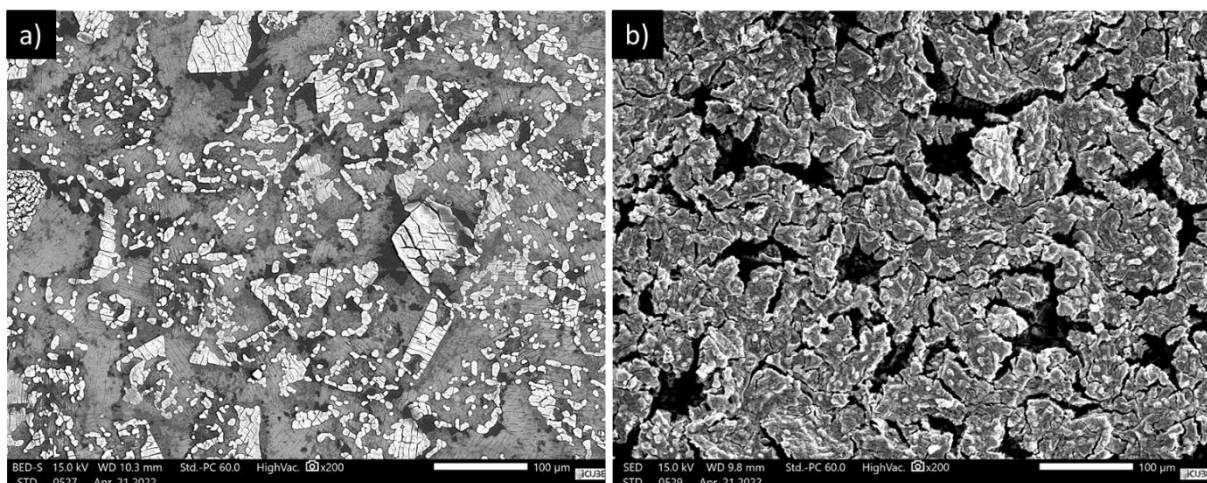
Figure 2.41 SEM observations of the a) light grey area b) dark grey area of the silicon thin film obtained on SOS sample.

Thus, using pieces of SOS wafer to grow silicon clathrates allowed great progress toward the formation of thin silicon clathrate films. **Figure 2.42** plots the photoluminescence spectrum of the thin silicon clathrate film. In this case, a well-defined PL peak is measured as compared to the broad peak obtained for thicker films due to the presence of defects. Better defined PL spectrum also help identifying the PL peak related to the disordered layer at the surface which covers some type II films[9]. However, as the thickness of the precursor and silicon clathrates is greatly reduced, its degradation when exposed to sodium and/or the ambient humidity is more visible on the resulting thin film quality. Pathways to protect the films from air exposition may be the missing point toward the obtention of continuous thin films
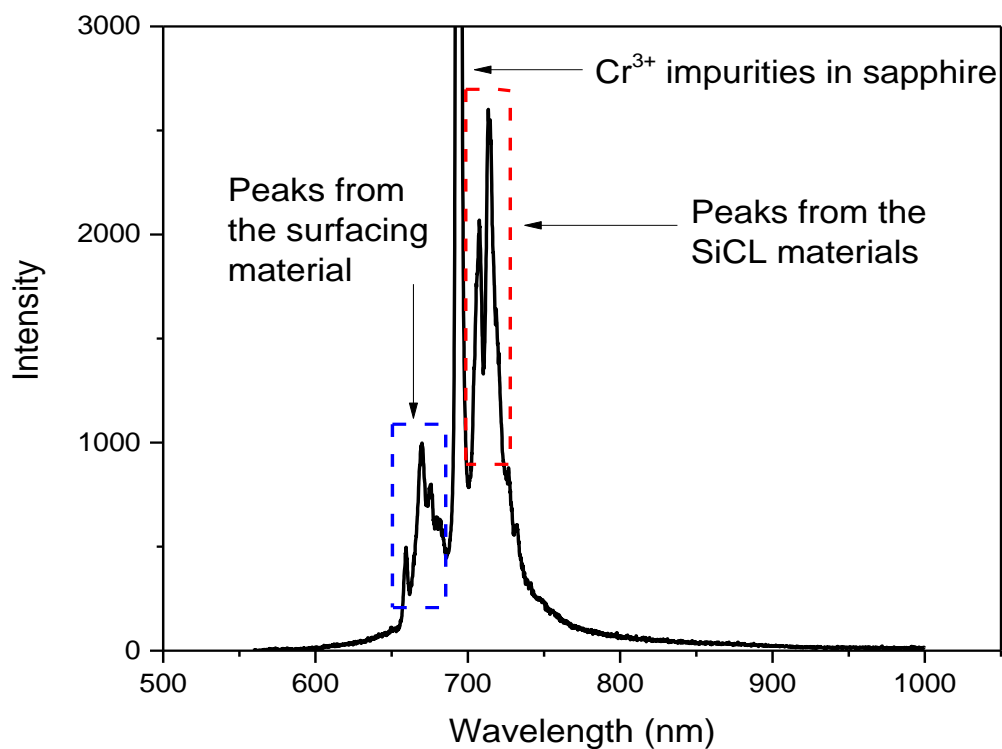
Figure 2.42 PL peaks measured on the type II thin film obtained using a SOS slice

2.6 Summary of Chapter 2

In this chapter, we have investigated the experimental parameters of the two-step thermal decomposition process and their refinement in order to achieve the selective formation of both silicon clathrates phase under the form of homogeneous films. For each structure, only a narrow window of temperature allows the formation of pure films. At 600°C, pure type II Na_xSi_{136} films are obtained, thanks to a lower sodium vapour pressure. At 630°C, pure type I Na_8Si_{46} is reached due to the high vapour pressure induced during Process 1. The mass of sodium introduced during process 1 has to be high enough to sustain the vapour pressure of sodium during the whole annealing step. However, it must not be too high otherwise macroscopic condensation of sodium on the silicon substrate will instantly damage it when exposed to air.

Both silicon clathrate types were thoroughly characterized. The metallic behaviour and efficient near infrared and visible light absorber of the obtained Na_8Si_{46} film (type I) was evidenced. The way to reach Na_xSi_{136} (type II) from x = 2.28 to 9.96 by tuning the thermal decomposition duration was discussed, and the semiconducting behaviour of the material for x < 8 /10 was demonstrated.

We have shown that the silicon clathrates films are stable only up to 450°C limiting the possible treatment they can undergo. Submitting the films to simultaneous heating and mechanical compression resulted in a much smoother surface and better crystallinity. Type I films are even subject to the crystallographic reorientation of the phases along two main planes due to their proximity to the plane of the silicon substrate. This annealing under pressure treatment also helped reaching purer silicon clathrates phases as conversion into predominant phase appears systematically favoured by the process.

Finally, various methods were studied to reach thin silicon clathrates films, revealing the two promising one: (i) using Reactive Ion Etching to etch the pre-existing micron-thick films down to the wished thickness and exposing a purer buried material, or (ii) using SOS wafer to limit the amount of silicon available for the reaction.

References of Chapter 2

(1)   Grigorian, L.; Eklund, P.; Fang, S. Clathrate Structure for Electronic and Electro-Optic Applications. US6103403A, August 15, 2000.

(2)   Martinez, A.; Krishna, L.; Baranowski, L.; Lusk, M.; Toberer, E.; Tamboli, A. Synthesis of Group IV Clathrates for Photovoltaics. *Photovoltaics, IEEE Journal of* **2013**, *3*, 1305–1310. https://doi.org/10.1109/JPHOTOV.2013.2276478.

(3)   Ohashi, F.; Iwai, Y.; Noguchi, A.; Sugiyama, T.; Hattori, M.; Ogura, T.; Himeno, R.; Kume, T.; Ban, T.; Nonomura, S. Thin-Film Formation of Si Clathrates on Si Wafers. *Journal of Physics and Chemistry of Solids* **2014**, *75* (4), 518–522. https://doi.org/10.1016/j.jpcs.2013.12.009.

(4)   Kume, T.; Iwai, Y.; Sugiyama, T.; Ohashi, F.; Ban, T.; Sasaki, S.; Nonomura, S. NaSi and Si Clathrate Prepared on Si Substrate. *physica status solidi (c)* **2013**, *10*. https://doi.org/10.1002/pssc.201300397.

(5)   Fink, J. K. *Tables of Thermodynamic Properties of Sodium*; ANL-CEN-RSD-82-4, 6856038; 1982; p ANL-CEN-RSD-82-4, 6856038. https://doi.org/10.2172/6856038.

(6)   Makansi, M. M.; Muendel, C. H.; Selke, W. A. Determination of the Vapor Pressure of Sodium. *J. Phys. Chem.* **1955**, *59* (1), 40–42. https://doi.org/10.1021/j150523a012.

(7)   Makansi, M.; Selke, W. A.; Bonilla, C. F. Thermodynamic Properties of Sodium. *J. Chem. Eng. Data* **1960**, *5* (4), 441–452. https://doi.org/10.1021/je60008a011.

(8)   Švob, L. Solubility and Diffusion Coefficient of Sodium and Potassium in Silicon. *Solid-State Electronics* **1967**, *10* (10), 991–996. https://doi.org/10.1016/0038-1101(67)90148-7.

(9)   Liu, Y.; Schenken, W. K.; Krishna, L.; Majid, A. A. A.; Furtak, T. E.; Walker, M.; Koh, C. A.; Taylor, P. C.; Collins, R. T. Synthesis and Characterization of Type II Silicon Clathrate Films with Low Na Concentration. *Applied Physics Reviews* **2021**, *8* (4), 041408. https://doi.org/10.1063/5.0062723.

(10)   Kume, T.; Ohashi, F.; Nonomura, S. Group IV Clathrates for Photovoltaic Applications. *Jpn. J. Appl. Phys.* **2017**, *56* (5S1), 05DA05. https://doi.org/10.7567/JJAP.56.05DA05.

(11)   Reny, E.; Gravereau, P.; Cros, C.; Pouchard, M. Structural Characterisations of the NaxSi136 and Na8Si46 Silicon Clathrates Using the Rietveld Method. *J. Mater. Chem.* **1998**, *8* (12), 2839–2844. https://doi.org/10.1039/A804565H.

(12)   Songster, J.; Pelton, A. D. The Na-Si (Sodium-Silicon) System. *JPE* **1992**, *13* (1), 67–69. https://doi.org/10.1007/BF02645381.

(13)   Krishna, L.; Baranowski, L. L.; Martinez, A. D.; Koh, C. A.; Taylor, P. C.; Tamboli, A. C.; Toberer, E. S. Efficient Route to Phase Selective Synthesis of Type II Silicon Clathrates with Low Sodium Occupancy. *CrystEngComm* **2014**, *16* (19), 3940–3949. https://doi.org/10.1039/C3CE42626B.

(14)   Kume, T.; Ohashi, F.; Sakai, K.; Fukuyama, A.; Imai, M.; Udono, H.; Ban, T.; Habuchi, H.; Suzuki, H.; Ikari, T.; Sasaki, S.; Nonomura, S. Thin Film of Guest-Free Type-II Silicon Clathrate on Si (111) Wafer. *Thin Solid Films* **2016**, *609*. https://doi.org/10.1016/j.tsf.2016.03.056.

(15)   Stefanoski, S.; Malliakas, C. D.; Kanatzidis, M. G.; Nolas, G. S. Synthesis and Structural Characterization of Na$_x$Si$_{136}$ ($0 < x \leq 24$) Single Crystals and Low-Temperature Transport of Polycrystalline Specimens. *Inorg. Chem.* **2012**, *51* (16), 8686–8692. https://doi.org/10.1021/ic202199t.

(16)   Stefanoski, S.; Martin, J.; Nolas, G. S. Low Temperature Transport Properties and Heat Capacity of Single-Crystal Na8Si46. *J Phys Condens Matter* **2010**, *22* (48), 485404. https://doi.org/10.1088/0953-8984/22/48/485404.

(17)   Beekman, M.; Nolas, G. S. Synthesis and Thermal Conductivity of Type II Silicon Clathrates. *Physica B: Condensed Matter* **2006**, *383* (1), 111–114. https://doi.org/10.1016/j.physb.2006.03.070.

(18)   Petříček, V.; Dušek, M.; Palatinus, L. Crystallographic Computing System JANA2006: General Features. *Zeitschrift für Kristallographie - Crystalline Materials* **2014**, *229* (5), 345–352. https://doi.org/10.1515/zkri-2014-1737.

(19)   Yamanaka, S.; Komatsu, M.; Tanaka, M.; Sawa, H.; Inumaru, K. High-Pressure Synthesis and Structural Characterization of the Type II Clathrate Compound Na$_{30.5}$Si$_{136}$ Encapsulating Two Sodium Atoms in the Same Silicon Polyhedral Cages. *J. Am. Chem. Soc.* **2014**, *136* (21), 7717–7725. https://doi.org/10.1021/ja502733e.

(20)   Kahn, D.; Ping Lu, J. Structural Properties and Vibrational Modes of Si 34 and Si 46 Clathrates. *Phys. Rev. B* **1997**, *56* (21), 13898–13901. https://doi.org/10.1103/PhysRevB.56.13898.

(21) Alben, R.; Weaire, D.; Smith, J. E.; Brodsky, M. H. Vibrational Properties of Amorphous Si and Ge. *Phys. Rev. B* **1975**, *11* (6), 2271–2296. https://doi.org/10.1103/PhysRevB.11.2271.

(22) Menon, M.; Richter, E.; Subbaswamy, K. R. Structural and Vibrational Properties of Si Clathrates in a Generalized Tight-Binding Molecular-Dynamics Scheme. *Phys. Rev. B* **1997**, *56* (19), 12290–12295. https://doi.org/10.1103/PhysRevB.56.12290.

(23) Fang, S. L.; Grigorian, L.; Eklund, P. C.; Dresselhaus, G.; Dresselhaus, M. S.; Kawaji, H.; Yamanaka, S. Raman Scattering from Vibrational Modes in Si46 Clathrates. *Phys. Rev. B* **1998**, *57* (13), 7686–7693. https://doi.org/10.1103/PhysRevB.57.7686.

(24) Hutchins, P. T.; Leynaud, O.; O'Dell, L. A.; Smith, M. E.; Barnes, P.; McMillan, P. F. Time-Resolved in Situ Synchrotron X-Ray Diffraction Studies of Type 1 Silicon Clathrate Formation. *Chem. Mater.* **2011**, *23* (23), 5160–5167. https://doi.org/10.1021/cm2018136.

(25) Ge, J.; Tang, M.; Wong, J.; Zhang, Z.; Dippell, T.; Doerr, M.; Hohn, O.; Huber, M.; Wohlfart, P.; Aberle, A. G.; Mueller, T. Excellent Silicon Surface Passivation Achieved by Industrial Inductively Coupled Plasma Deposited Hydrogenated Intrinsic Amorphous Silicon Suboxide. *International Journal of Photoenergy* **2014**, *2014*, e752967. https://doi.org/10.1155/2014/752967.

(26) Yan, B.; Yue, G.; Sivec, L.; Jiang, C.-S.; Yan, Y.; Alberi, K.; Yang, J.; Guha, S. On the Bandgap of Hydrogenated Nanocrystalline Silicon Thin Films. In *2010 35th IEEE Photovoltaic Specialists Conference*; 2010; pp 003755–003760. https://doi.org/10.1109/PVSC.2010.5616075.

(27) Morito, H.; Shimoda, M.; Yamane, H. Single Crystal Growth of Type I Na–Si Clathrate by Using Na–Sn Flux. *Journal of Crystal Growth* **2016**, *450*, 164–167. https://doi.org/10.1016/j.jcrysgro.2016.06.031.

(28) Kurakevych, O. O.; Strobel, T. A.; Kim, D. Y.; Muramatsu, T.; Struzhkin, V. V. Na-Si Clathrates Are High-Pressure Phases: A Melt-Based Route to Control Stoichiometry and Properties. *Crystal Growth & Design* **2013**, *13* (1), 303–307. https://doi.org/10.1021/cg3017084.

(29) Momma, K.; Izumi, F. *VESTA 3* for Three-Dimensional Visualization of Crystal, Volumetric and Morphology Data. *J Appl Crystallogr* **2011**, *44* (6), 1272–1276. https://doi.org/10.1107/S0021889811038970.

(30) Nolas, G. S.; Kendziora, C. A.; Gryko, J.; Dong, J.; Myles, C. W.; Poddar, A.; Sankey, O. F. Raman Scattering Study of Stoichiometric Si and Ge Type II Clathrates. *Journal of Applied Physics* **2002**, *92* (12), 7225–7230. https://doi.org/10.1063/1.1523146.

(31) Beekman, M.; Nenghabi, E. N.; Biswas, K.; Myles, C. W.; Baitinger, M.; Grin, Y.; Nolas, G. S. Framework Contraction in Na-Stuffed Si(*CF* 136). *Inorg. Chem.* **2010**, *49* (12), 5338–5340. https://doi.org/10.1021/ic1005049.

(32) Connétable, D. Structural and Electronic Properties of p-Doped Silicon Clathrates. *Phys. Rev. B* **2007**, *75* (12), 125202. https://doi.org/10.1103/PhysRevB.75.125202.

(33) Himeno, R.; Ohashi, F.; Kume, T.; Asai, E.; Ban, T.; Suzuki, T.; Iida, T.; Habuchi, H.; Tsutsumi, Y.; Natsuhara, H.; Nonomura, S. Optical Band Gap of Semiconductive Type II Si Clathrate Purified by Centrifugation. *Journal of Non-Crystalline Solids* **2012**, *358*, 2138–2140. https://doi.org/10.1016/j.jnoncrysol.2011.12.064.

(34) Yamaga, M.; Kishita, T.; Kume, T.; Uehara, K.; Nomura, M.; Ohashi, F.; Ban, T.; Nonomura, S. Electron-Spin Resonance of Type II Si-Clathrate Thin Film for New Solar Cell Material. **2016**, 213–219. https://doi.org/10.1007/978-3-319-45677-5_26.

(35) Yamaga, M.; Kishita, T.; Goto, K.; Sunaba, S.; Kume, T.; Ban, T.; Himeno, R.; Ohashi, F.; Nonomura, S. Electron Spin Resonance, Dynamic Jahn-Teller Effect, and Electric Transport Mechanism in Na-Doped Type II Silicon Clathrates. *Journal of Physics and Chemistry of Solids* **2020**, *140*, 109358. https://doi.org/10.1016/j.jpcs.2020.109358.

(36) Yildiz, A.; Serin, N.; Serin, T.; Kasap, M. Crossover from Nearest-Neighbor Hopping Conduction to Efros–Shklovskii Variable-Range Hopping Conduction in Hydrogenated Amorphous Silicon Films. *Jpn. J. Appl. Phys.* **2009**, *48* (11R), 111203. https://doi.org/10.1143/JJAP.48.111203.

(37) Moen, K. A. Modeling of Minority Carrier Recombination and Resistivity in SiGe BICMOS Technology for Extreme Environment Applications, Georgia Institute of Technology, 2008.

(38) Kinoshita, H.; Huang, T. H.; Kwong, D. L. Modeling of Suppressed Dopant Activation in Boron- and BF2-implanted Silicon. *Journal of Applied Physics* **1994**, *75* (12), 8213–8215. https://doi.org/10.1063/1.356525.

(39) Burgess, T. E.; Baum, J. C.; Fowkes, F. M.; Holmstrom, R.; Shirn, G. A. Thermal Diffusion of Sodium in Silicon Nitride Shielded Silicon Oxide Films. *J. Electrochem. Soc.* **1969**, *116* (7), 1005. https://doi.org/10.1149/1.2412126.

(40) von Gastrow, G.; Martinez-Loran, E.; Scharf, J.; Clenney, J.; Meier, R.; Bandaru, P.; Bertoni, M. I.; Fenning, D. P. Quantification of Sodium-Ion Migration in Silicon Nitride by Flatband-Potential

Monitoring at Device-Operating Temperatures. *physica status solidi (a)* **2020**, *217* (16), 2000212. https://doi.org/10.1002/pssa.202000212.

(41) McCaldin, J. O.; Little, M. J.; Widmer, A. E. The Solubility of Sodium in Silicon. *Journal of Physics and Chemistry of Solids* **1965**, *26* (7), 1119–1123. https://doi.org/10.1016/0022-3697(65)90007-7.

(42) Kumar, R.; Maeda, T.; Hazama, Y.; Ohashi, F.; Jha, H. S.; Kume, T. Growth of Ge Clathrate on Sapphire and Optical Properties. *Jpn. J. Appl. Phys.* **2020**, *59* (SF), SFFC05. https://doi.org/10.35848/1347-4065/ab6e0a.

(43) Schenken, W. K.; Liu, Y.; Krishna, L.; Majid, A. A. A.; Koh, C. A.; Taylor, P. C.; Collins, R. T. Electron Paramagnetic Resonance Study of Type-II Silicon Clathrate with Low Sodium Guest Concentration. *Phys. Rev. B* **2020**, *101* (24), 245204. https://doi.org/10.1103/PhysRevB.101.245204.

Chapter 3: Modification of the properties of the silicon clathrates films

3.1 Introduction

In the previous chapter, the synthesis of the silicon clathrate films has been optimized and the properties of the obtained materials have been investigated. Based solely on thermal decomposition, the fabricated type II silicon clathrate films show compositions Na_xSi_{136} only comprised in the range $2 < x < 9$. To demonstrate the potential of silicon clathrate films, various approaches are explored in this chapter, which is divided into two sections as shown in **Figure 3.1**.
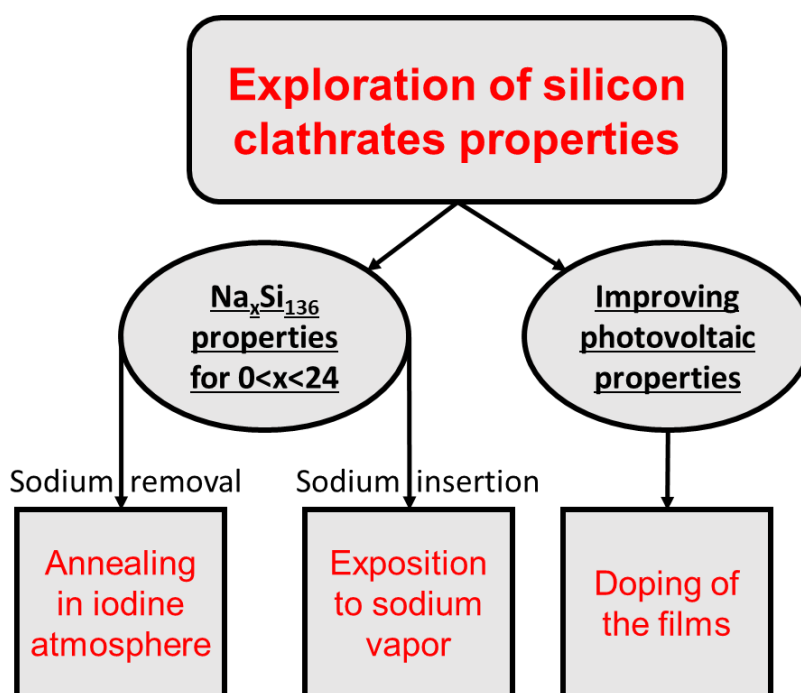
Figure 3.1. Pathways used toward the silicon clathrates properties exploration.

In the first part, we discuss the evolution of the properties of the type II silicon clathrate films according to their occupation by the guest sodium atoms. We will show that mainly the electrical properties of these films are governed by the sodium content. We performed DFT calculations of the silicon clathrates electronic structures according to their sodium occupations to confirm the experimental observations. Then, we present preliminary studies of implantation in silicon clathrates using arsenic ionic implantation and thermal annealing. We demonstrate that the implantation and activation of dopants

by rapid thermal annealing is possible while preserving the clathrate structure. We also show that the implanted arsenic dose has an impact on the photovoltaic properties of the type II silicon clathrates films.

3.2 Effects of sodium content on the properties of the type II silicon clathrates films

In contrast to most of the other clathrate structures, the type II clathrate features the ability to let guest atoms move in and out of their cages. Obviously, depending on the nature and number of guest atoms, clathrates have varying properties. This assessment is crucial for type II silicon clathrates, which can thus exhibit different features as its guest atoms are removed, inserted or substituted.

Here, the experiment addresses the insertion and removal of sodium as guest atoms, in contrast to other studies which use other alkali metals[1,2]. The main aim is understanding the conditions needed to reach a given Na_xSi_{136} composition using routinely synthesized films. It will be followed by the investigation of the impact of the effects occupations on the properties of the obtained films.

3.2.1 Insertion and removal of sodium atoms in the polyhedral cages

It was reported in the previous chapter that relying only on two-step thermal decomposition could only produce compositions with a sodium occupation as low as Na_2Si_{136} or as high as $Na_{10}Si_{136}$. In order to get closer to both the guest-free Si_{136} or fully occupied $Na_{24}Si_{136}$ structures, methods previously used on powder clathrate samples are adapted here to be applied to silicon clathrates films.

Figure 3.2 shows the diffractograms of type II silicon clathrates films for sodium occupations x close to x = 0, x = 4 and x = 23 as calculated using Rietveld refinements.
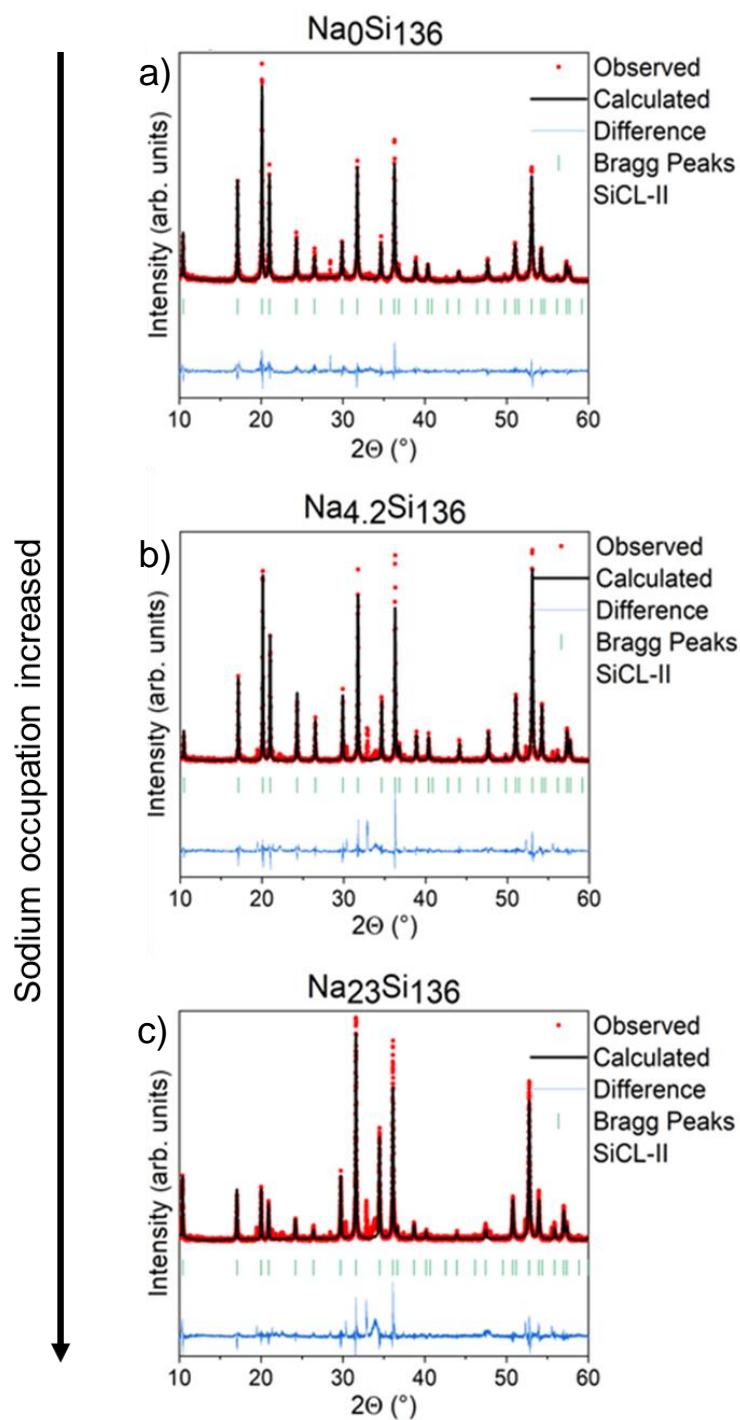
Figure 3.2 XRD diffractograms fitted by LeBail and Rietveld refinement for type II silicon clathrates with various sodium contents: a) low occupation b) classic occupation and c) high occupation. Observed curves are here the measured intensities of the reflections from XRD.

<u>A. Insertion of sodium atoms by exposure to hot sodium vapor</u>

- *Experiment*

To reach high concentrations of sodium up to the fully occupied structure, sodium insertion is needed. An insertion of this type has been previously demonstrated by exposing silicon clathrate powders to sodium vapour at moderate temperature and for a long period of time[3]. This insertion of sodium or other species such as lithium has also been reported during cycling experiments using silicon clathrates as anode materials for batteries applications[4,5].

Here, type II silicon clathrate films have been exposed to sodium vapour in a similar way that the method used for the synthesis of thin silicon clathrate films with SOS substrates. A cleaved silicon clathrate on p-doped single crystalline silicon substrate film of 1 x 1 or 1.5 x 1.5 cm^2 is glued to a sapphire wafer with silver paste. The crucible is filled with an increased mass of sodium of around 0.4g to ensure sufficient vapour pressure to fill all the empty cages. Once done, the clathrate film is inserted in the same furnace used for Process 1. This last step was carried out at temperatures from 320°C up to 380°C and durations from 50h up to 100h.The temperature is held at the desired temperature long enough that the sodium vapor enters the cages of the clathrate structure.

Atomic positions and occupations of sodium and silicon atoms determined by Rietveld refinement can be found in annex A.3.1 section.

- *Results*

The lowest temperature tested was 320°C during 50h or 100h. Slight bubbling was observed during the washing of the samples. This temperature did not give any hint of sodium addition in the cages when analysed by XRD and EDS.

When heated up to 350°C, effective filling of the cages was observed even though the only cages filled were the largest Si_{28} cages left vacant as evidenced by Rietveld

refinement. Upon an annealing at 350°C for 50h, the Rietveld refinement of the film shows an occupation of x = 6.8. This means that three more cages were filled as compared to the starting material, while one cage remains empty. When the annealing was performed for 100h at the same temperature, all the Si_{28} cages were successfully filled with very few amounts of sodium starting to take place in the small Si_{20} cages resulting in a $Na_{8.3}Si_{136}$. The structures $Na_{6.8}Si_{136}$ and $Na_{8.3}Si_{136}$ obtained by this method exhibit similar lattice parameters of 14.6387 ± 0.0006 Å and 14.6385 ± 0.0006 Å, as shown in **Table 3.1**, slightly expanded from the 14.6371 ± 0.0005 Å of the starting material.

Table 3.1 Structural parameters of the various refined type II film for different sodium vapour annealing conditions

Refined formula	Na6.834Si136	Na8.294Si136	Na23.087 Si136
Treatment	*Sodium vapor 350°C for 50h*	*Sodium vapor 350°C for 100h*	*Sodium vapor 380°C for 50h*
a = b = c (Å)	14.6387(6)	14.6385(6)	14.7094(4)
V (Å^3)	3137.0(2)	3136.8(2)	3182.7(2)
Dcal (g/cm^3)	2.11	2.12	2.27
wRp	0.034	0.051	0.038
Rp	0.046	0.063	0.053
Goodness of fit	1.69	1.71	1.57

New samples were prepared at an annealing temperature of 380°C for a duration of 50h. This was done in order to overcome the energy needed to fill in the Si_{20} cages starting from a Na_4Si_{136} film. These conditions resulted in a successful filling of nearly all the cages leading to a $Na_{23.1}Si_{136}$ structure with a slight blueish hue whose diffractogram is compared to routinely obtained occupation in **Figure 3.3b-c**. This almost fully filled type II silicon clathrate shows a consequent increase of its lattice parameter to 14.7094 ± 0.0004 Å, reported in **Table 3.1**, from the starting 14. 6373 ± 0.0005 Å. The reduction of the sodium vapour exposure time to 10h at 380°C resulted again in almost a full occupation, namely a $Na_{23}Si_{136}$ structure

The difficulty in filling the small cages at temperatures below 380°C can be attributed to either the kinetic of the sodium insertion reaction in the small cages is indefinitely slow at this temperature or that the temperature of the annealing is too low to overcome the energy barrier needed to fill in the smaller cages. The second suggestion is the

most likely explanation as exposing the $Na_{8.3}Si_{136}$ sample to an additional 50h of annealing at 350°C did not improve the sodium content within the sample. The obtained structures $Na_{6.8}Si_{136}$ and $Na_{8.3}Si_{136}$ exhibit similar lattice parameters of 14.6387 ± 0.0006 Å and 14.6385 ± 0.0006 Å which is closely related to the 14. 6371 ± 0.0005 Å of the starting material for x = 4 meaning that close to no expansion of the lattice is occurring upon filling of the Si_{28} cages. The S_{28} cages being too large to be stretched by the sodium guest atoms they host.

The drastic increase in sodium content when raising the temperature up to 380°C reveals that the energy needed to fill in the Si_{28} or the Si_{20} cages are different. This energy is lower for the widest Si_{28} cages. This is consistent with previous theoretical studies on the energy needed for the sodium to cross the various faces of the cages[6]. The wide hexagonal faces of the Si_{28} allow better diffusion than the pentagonal faces forming the Si_{20} cages. A complementary explanation is that the rise in temperature is increasing the presence of point defects[7] in the silicon framework. This results in an easiest migration of the sodium atoms across the hexagonal and pentagonal faces of the polyhedral cages.

The $Na_{23}Si_{136}$ structure shows an increase of the lattice parameter on a scale never observed during our previous refinement, from 14.6371 ± 0.0005 Å to 14.7094 ± 0.0004 Å. This expansion is observed in similar studies on type II silicon clathrates powders as soon as the smaller Si_{20} cages are being filled[8]. This sudden increase is explained by two factors: the first one being that the Si_{20} cages are expanding slightly due to the presence of sodium atoms thanks to steric hindrance[9]. Another smallest contribution is the repulsion of neighbouring sodium atoms, which increases as more and more cages are filled. The structural parameters of the forementioned structures are summarized in **Table 3.1** and in the annex A.3.1 section.

B. Removal of sodium atoms by iodine treatment

- *Experiment*

Several techniques have been developed in order to obtain the desired guest-free silicon clathrates. Concerning powders, for a long time the lowest sodium concentrations were obtained by extending the duration of the annealing under vacuum up to several days[3]. The suggestion by Ammar et al.[10] to use iodine has led to a subsequent breakthrough. The reaction between iodine and sodium at elevated temperature forming sodium iodide is exploited to extract the sodium atoms located in the silicon clathrate cages. An even more efficient process has been reported for single crystals by Iwasaki et al.[7], which uses a layer to capture sodium cations as they migrate when an electric field is applied. This allows homogeneous removal of sodium from the cages on a macroscopic scale.

In this study, we used the annealing under iodine atmosphere method. In literature, the process involves inserting both iodine and powdery silicon clathrates in an ampoule, generating a vacuum in it, and then sealing it.

In our case, we adapted the last setup by using a glass test tube as the recipient for both iodine (99+%, AnalaR NORMAPUR, CAS #7553-56-2) and the silicon clathrate films on p-doped silicon samples. The latest were cut into 1 x 1 cm^2 pieces. This test tube is then put under fine vacuum below 10^{-2} mbar and closed. The test tube is then heated, and the formation of purple iodine vapour was visible. The experimental setup, adapted from the heating and pumping units of a BET apparatus is pictured in **Figure 3.3**.


Figure 3.3 Adapted BET heating and pumping unit used for the iodine annealing of the silicon clathrates films.

The heating is stopped after 10h. The formation of iodine crystals on the test tube inner surface was visible. The sample is extracted from the tube and cleaned with acetonitrile followed by deionized water and blow-dried with nitrogen. Some samples are left in the tube to be subjected to additional cycle. The iodine treated silicon clathrates films are then characterized by XRD and SEM to estimate their sodium concentration. Samples obtained using intrinsic silicon were also submitted to this step to investigate the effect of reduced sodium occupations on the electrical properties of the type II silicon clathrate films.

- *Results*

The starting material for these experiments is Na_4Si_{136}. Some pieces were submitted to a single annealing cycle while others received two additional cycles. No traces of iodine were detected by EDS analysis after the samples were washed.

Whatever is the number of cycles under iodine vapour, the resulting XRD patterns are typical of low sodium occupations with x ≤ 1 as visible on **Figure 3.2a**. However, when trying to fit these patterns by Rietveld, the sodium occupations systematically converged toward zero. This would mean that the suited Si_{136} structure is reached, which is unlikely since even similar studies carried out on powders did not yield such low occupations[10]. In the calculated patterns using VESTA[11] in **Figure 3.4**, the peaks with the most intense variations upon change in sodium content are highlighted in red. The convergence toward null occupation is likely due to the striking similarities of the XRD patterns for x = 0 and x = 1. The peak intensities only begin to change for x = 2 and above. As x is increased from 0 to 4, the reflections at 20.1°, 21° and 31.7° are the peaks with the most marked increase in intensity. On the same range, the (111) reflection peak at 10.45° sees its relative intensity reduced by half.
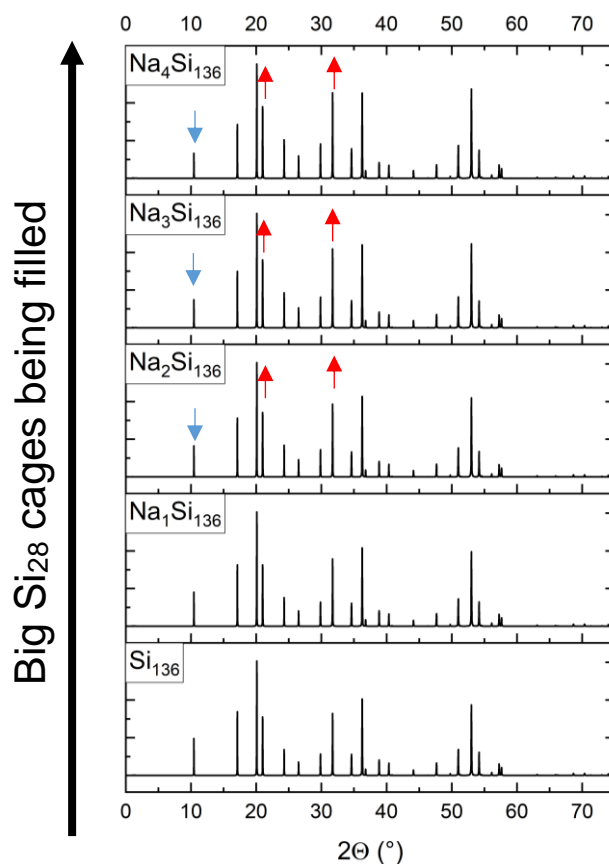
Figure 3.4. XRD diffractograms expected as the big cages of the type II silicon clathrates are being filled, calculated using VESTA.

As Rietveld refinements are unreliable as the occupation is reduced below $x \leq 1$, EDS analysis was performed on the samples to estimate the sodium occupation. The trust on the EDS measurements was assessed by measuring the content of the previously mentioned $Na_{8.3}Si_{136}$ and $Na_{23.1}Si_{136}$. This led to EDS measured occupations of $x = 7.8$ and $x = 24.1$ respectively as shown in **Table 3.2**.

Table 3.2 Compositions of the various type II films estimated by EDS according to the treatment they have been subjected to.

Treatment	Elements	Mass ratio (%)	Atomic ratio (%)	Resulting formula
1 cycle of iodine atmosphere annealing	Na	0.66 ± 0.18	0.82 ± 0.21	$Na_{1.1}Si_{136}$
	Si	99.33 ± 2.23	99.18 ± 2.37	
3 cycles of iodine atmosphere annealing	Na	0.05 ± 0.08	0.07 ± 0.11	$Na_{\sim0.1}Si_{136}$
	Si	99.95 ± 2.25	9.93 ± 2.25	
Sodium vapor at 350°C for 100h	Na	4.50 ± 0.94	5.44 ± 1.14	$Na_{7.8}Si_{136}$
	Si	95.50 ± 4.43	94.56 ± 4.38	
	Na	12.66 ± 0.51	15.05 ± 0.60	$Na_{24.1}Si_{136}$

Sodium vapor at 380°C for 50h	Si	87.34 ± 1.42	84.95 ± 1.38

The iodine treated samples analysed by EDS exhibit a reduced occupation of x = 1.1 for a single cycle, down to x = 0.1 - close to the EDS detection limit - for three consecutive cycles. According to the EDS data reported in **Table 3.2**, the removal rate of sodium atoms in this work seems slower than in similar studies on powders[12]. This is partially because of the lower temperature used here due to the custom setup limitations. Another explanation of this slower sodium removal is the dimensionality of the films compared to powders. In case of films, the sodium has diffused out of the cages along the channels they form up to several tens of micrometers. This is much more than for powders, whose diffusion lengths are easily under the micrometer. In spite of this, reduced sodium occupations are achieved by annealing under an iodine atmosphere in a reproducible manner. It thus enables low occupations, previously non reachable with only Process 2.

C. Summary

Thanks to the two different methods described above, both almost guest-free structure and highly occupied structures of type II silicon clathrate films have been achieved. Their XRD patterns fitted by Rietveld using JANA2006[13] are reported in **Figure 3.2** along with the one of the starting material $Na_{4.2}Si_{136}$ film for comparison purpose.

Taking advantage of both methods, compositions of type II silicon clathrates from x = 0.1 to 23.1 are reachable, as summed-up in **Figure 3.5**, from the same starting material and, even more important, in a reproducible and reversible manner. This allows to easily control the sodium content x of the Na_xSi_{136} structure depending on the suited properties as described later.

Type I films were also submitted to these methods, but no modification of the sodium occupation was attained. So far, guest-free type I clathrates were only obtained via Hoffman redox reaction[14].
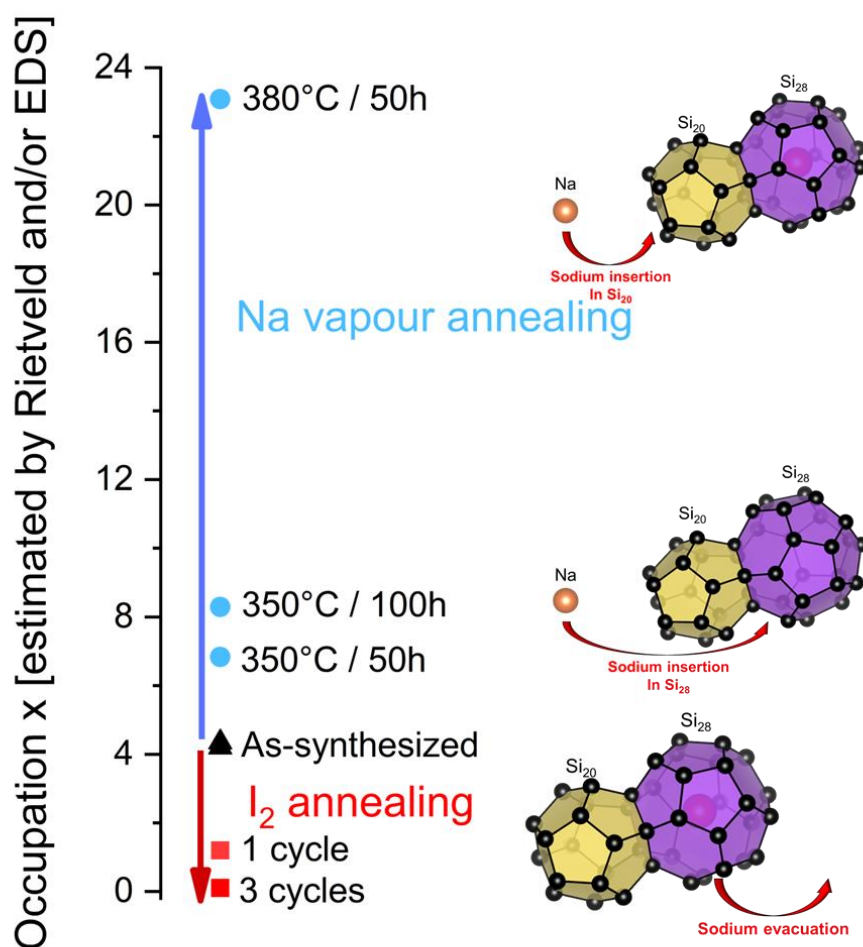
Figure 3.5. Type II silicon clathrates compositions obtained for annealing under iodine atmosphere for the red squares and sodium vapour annealing for the blue circles.

3.2.2 Properties of the films versus the sodium content

- *Raman Spectroscopy*

The properties of the type II silicon clathrates from the nearly guest-free structure up to the almost fully occupied one will be detailed in this section.

Figure 3.6 shows the Raman spectra of silicon clathrate films with various sodium contents. A clear difference is visible for cases with occupation below $x = 6.9$ and higher occupation above $x = 8$. For low occupation, all the peaks are nicely defined and distinguishable, with a high signal to noise ratio. On the other hand, samples with

occupations above x = 6.9 have a poor signal to noise ratio and only few peaks can be indexed. As discussed in Chapter 2 when comparing type I and type II silicon clathrates, such feature might indicate that the fabricated structure is semiconductive for low occupation cases and shifts to more metallic behaviour for those with
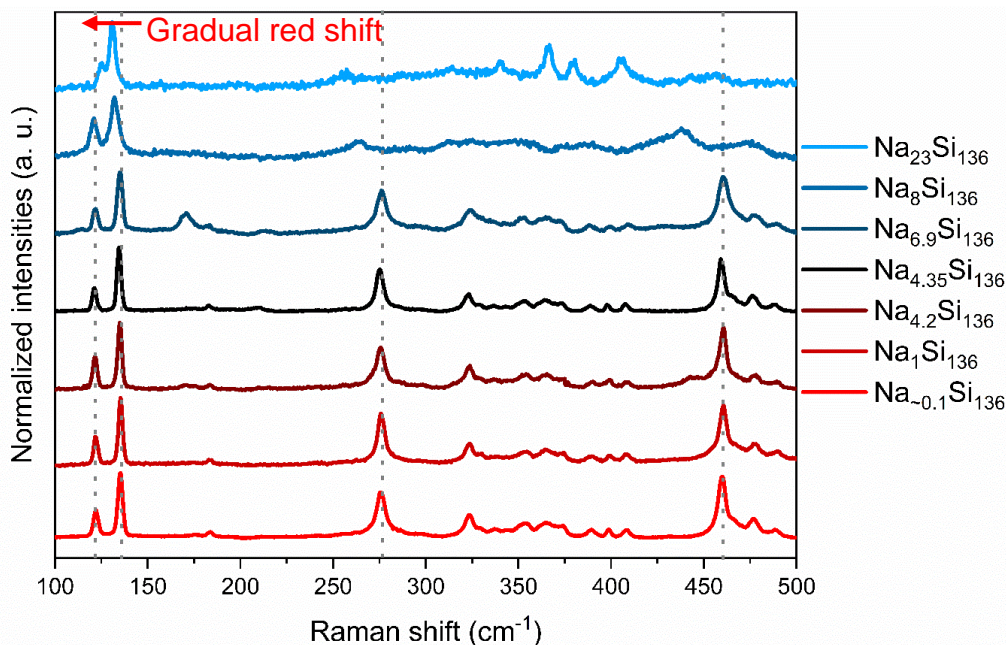
Figure 3.6 Raman spectra of the type II silicon clathrate films for various sodium occupations.

occupations above 8.

Looking now more closely at all the spectra and the energies of the vibrational modes, a steady shift of all the vibrations toward lower frequencies is visible as the sodium content is increasing. The peaks for which this shift is the most visible are the ones related to the $1T_{2g}$, $1E_g$, $3T_{2g}$ and $3A_{1g}$ modes. Grey spotted lines were plotted to help visualising the peak shifts.

This order of magnitude of the shift is not proportional to the content of sodium. Low sodium occupation, i.e., when only large Si_{28} cages are being filled, shows only a slight shift. In contrast, the shift is much more significant when comparing the $Na_{6.9}Si_{136}$, Na_8Si_{136} and $Na_{23}Si_{136}$ spectra. The energies of the vibrational modes for the two extreme cases and the routinely synthesized Na_4Si_{136} are reported in **Table 3.3**.

Table 3.3 Wavenumber of the various Raman vibrations for various occupations of sodium compared to tabulated theoretical values.

Vibration mode	Si_{136} theory by Nolas et al.[15] (cm^{-1})	$Na_{0.1}Si_{136}$ (cm^{-1})	$Na_{4.35}Si_{136}$ (cm^{-1})	$Na_{23}Si_{136}$ (cm^{-1})
$1T_{2g}$	121	122.7	121.6	-
$1E_g$	130	135.9	134.9	131.6
$2T_{2g}$	176	184.3	183.5	-
$3T_{2g}$	267	276.7	275.7	257.0
$1A_{1g}$	316	323.9	323.8	314.5
$4T_{2g}$	325	330.7	330.2	-
$2E_g$	360	365.8	365.4	367.2
$2A_{1g}$	397	398.2	398.4	-
$5T_{2g}$	406	408.4	407.8	406.7
$3A_{1g}$	458	461.1	460.6	442.5
$3E_g$	463	Not resolved from $3A_{1g}$		456.0
$6T_{2g}$	466			-
$7T_{2g}$	473	477.2	477.1	-
$8T_{2g}$	487	489.4	488.4	-

In general, red shifts are often associated with either the increase in crystallinity of the phase or with materials being subjected to tensile stress meaning that the chemical bonds are elongated. In the present case, it is surely due to the expansion of the lattice as the sodium atoms being inserted in the matrix. This is consistent with the observed very small shift for the filled large cages case whose lattice parameter is around 14.64 Å while it quickly rises up to 14.71 Å when the small cages are fully occupied.

- *Hall effect measurements*

The electrical properties of type II films have been investigated using samples synthesized starting from intrinsic silicon wafers and subjected to both methods mentioned earlier. The results are shown in **Table 3.4**.

Table 3.4 Electrical properties of the silicon clathrates films as synthesized and submitted to various post-synthesis annealing.

Silicon Clathrates	Treatment	Formula	Carrier concentration (cm^{-3})	Resistivity ($\Omega \cdot cm$)	Mobility ($cm^2/(V \cdot s)$)
Type I	*As synthesized*	Na_8Si_{46}	-1.5×10^{19}	4.3×10^{-2}	43
Type II	*3 Cycles of I2 annealing*	$Na_{\sim0.1}Si_{136}$	-3.6×10^{16}	110	15
	1 Cycle of I2 annealing	Na_1Si_{136}	-9.2×10^{16}	40.7	21
	As synthesized	$Na_{2.1}Si_{136}$	-9.5×10^{16}	24.7	18
		$Na_{4.2}Si_{136}$	-2.1×10^{17}	4.2	7.1
		$Na_{4.35}Si_{136}$	-3.0×10^{17}	2.2	8.0
		$Na_{7.3}Si_{136}$	-1.03×10^{18}	6.8×10^{-1}	9.3
	Na vapor 350°C for 50h	$Na_{6.9}Si_{136}$	-9.2×10^{17}	6.3×10^{-1}	13.3
	Na vapor 350°C for 100h	Na_8Si_{136}	-6.5×10^{18}	3.3×10^{-1}	6.1
	Na vapor 380 for 50H	$Na_{23}Si_{136}$	-5.4×10^{20}	1.1×10^{-2}	4.1

As expected from the literature[16] and hinted by the Raman spectra, the resistivity of the type II silicon clathrate is increasing as the sodium atoms are diffused out from the polyhedral cages. From x = 1 to x = 6, the evolution is quite slow and becomes more pronounced as the composition approaches either the guest free Si_{136} structure or the completely filled $Na_{24}Si_{136}$ structure. The films are n-type semiconductors up to x = 6.9, and then show a much more conductive behaviour as the occupation is increased. No
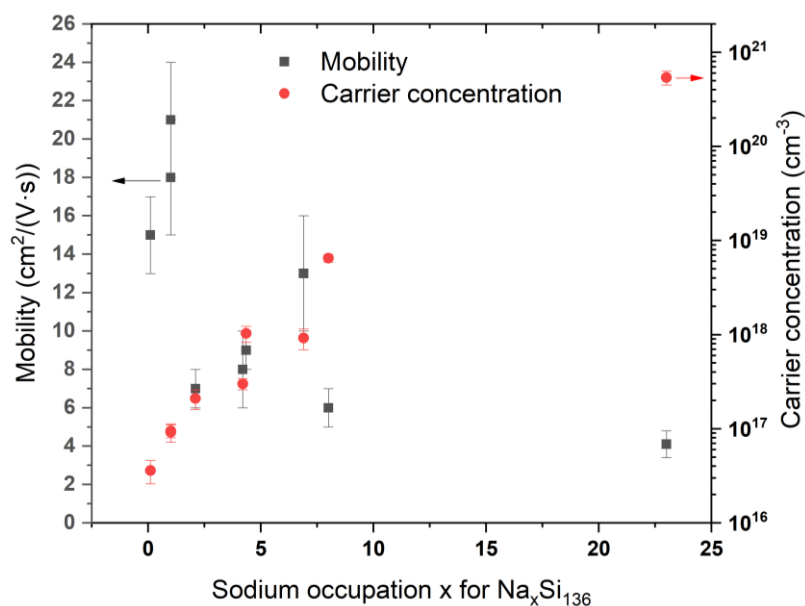
Figure 3.7 Evolution of the charge carrier mobility and concentration of the type II films according to the sodium content.

major variation in terms of electron mobility is observed as the sodium content is tuned. There is a slight decreasing for samples with high occupancy as shown in **Figure 3.7**. The mobility seems to be reduced when the small cages are starting to be filled and that the phase is becoming more and more metallic. The carrier concentration increases with the sodium content as they donate more and more electrons to the framework. The amplitude of the variation of the resistivity is similar to previous studies on agglomerated crystals[16].

The Hall effect measurements were completed by Resistance versus Temperature measurements carried out on the two extreme situations - almost guest-free and highly
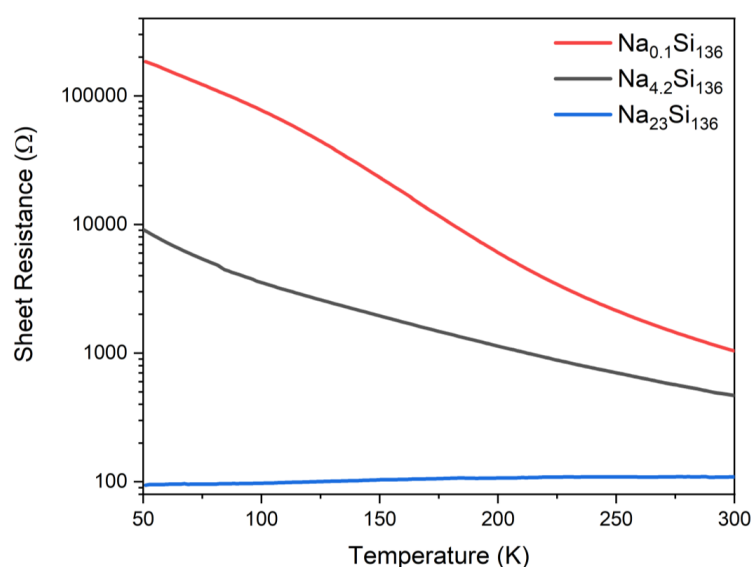

Figure 3.8 Resistance versus temperature measurements for type II films with different sodium concentration.

occupied - in addition to the starting material $Na_{4.2}Si_{136}$ film. These measurements are plotted in **Figure 3.8**.

These measurements confirm the gradual transition from a semiconducting$Na_{0.1}Si_{136}$ material to a clearly much more electrically conductive $Na_{23}Si_{136}$ as suggested by both the Hall measurements and the Raman spectroscopy analysis. This behaviour is similar to those previously reported for powders[17] and single-crystals[7] of type II silicon clathrates. As the sodium content x of Na_xSi_{136} is increased, more and more excess electrons are given by the sodium guest atoms. In the high occupancy case, the number of electrons which become delocalized[3] in addition to the presence of sodium cations in most of the cages, results in an efficient charge conduction through the structure. In contrast, as the occupation is reduced, the increasing isolation and localization of sodium atoms and clusters within the structure is reducing the electron conduction. This is confirmed by an Electron Spin Resonance study performed at low temperatures[18].

A summary of the evolution of both the resistivity of the films and their lattice parameters refined by Rietveld as the sodium occupation is changing is available in **Figure 3.9**.
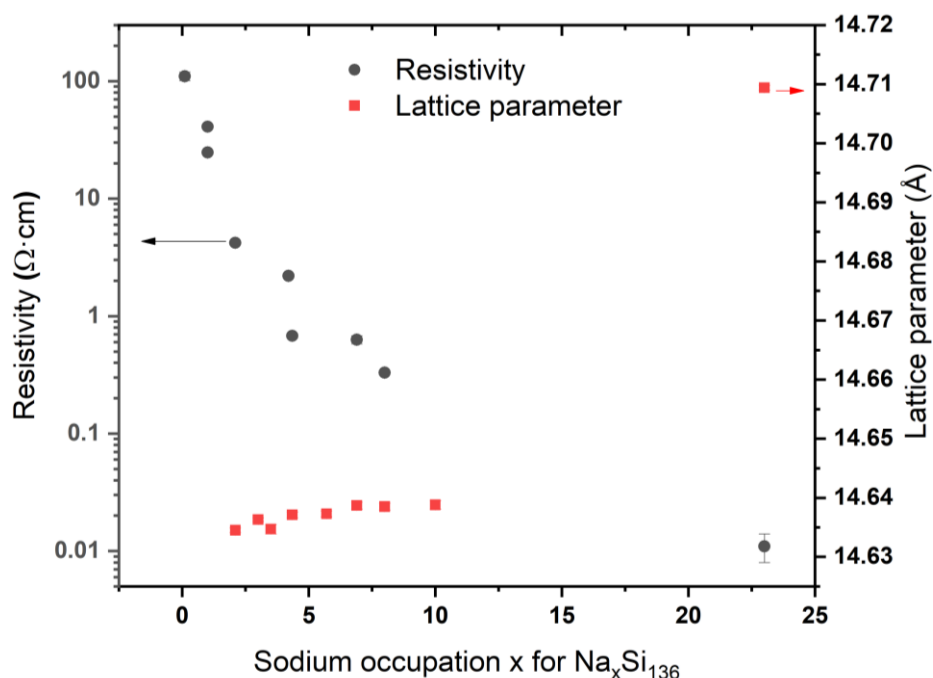
Figure 3.9 Evolution of the resistivity and of the lattice parameters of the type II films according to the sodium content.

- *Photoluminescence*

Figure 3.10 plots the photoluminescence measurements for x = 0 and x = 4.35. The PL peaks are similar to previous measurements[19–21] and indicate a slight shift toward lower energy as x is reduced.
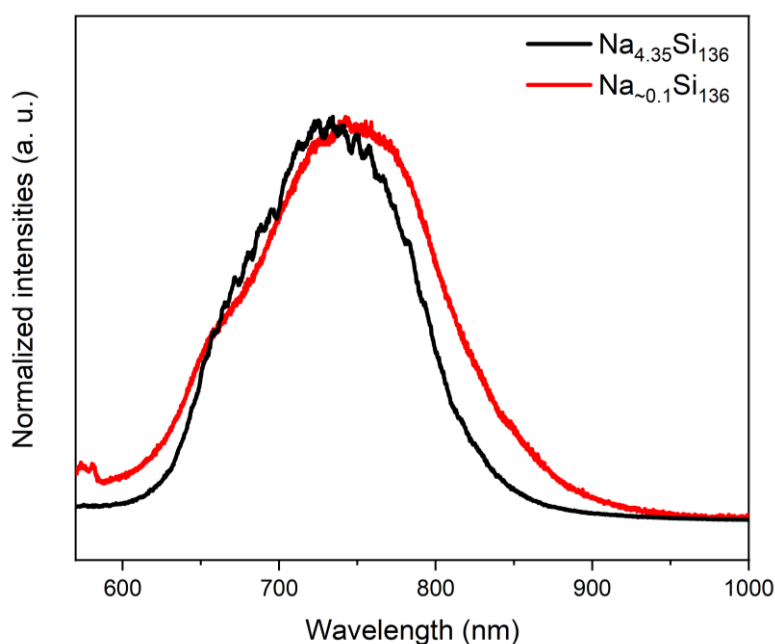
Figure 3.10 Photoluminescence measurements on the type II films for various sodium occupations.

A slight shift of the PL peak toward higher wavelength as the occupation is reduced could indicate a small reduction in the energy bandgap. A possible reduction of the bandgap was observed in a previous study on powders[22].

A slight shift of the PL peak toward higher wavelength could indicate a small reduction of the bandgap as the occupation is reduced. Investigation under spectroscopic ellipsometry was not precise enough to pinpoint this shift as the sodium occupation is changing.

Figure 3.11 compares the PL spectra obtained from the films before (Na_4Si_{136}) and after ($Na_{23}Si_{136}$) being exposed to hot sodium vapor at 380°C for 50h. The PL spectrum of the starting type II silicon clathrate film exhibit a peak centred at around 750 nm in

addition to a shoulder band around 660 nm attributed to the disordered material impurities at the surface of the layer[19].

After sodium insertion up to x = 23, the intense peak of type II silicon clathrates is no longer visible and all that remains is the impurities' band. This disappearance of the PL peak of the type II silicon clathrates, while the phase is effectively detected by XRD and Raman spectroscopy, confirms the transition from a semiconductive starting material with a direct energy bandgap to a pseudo metallic one.
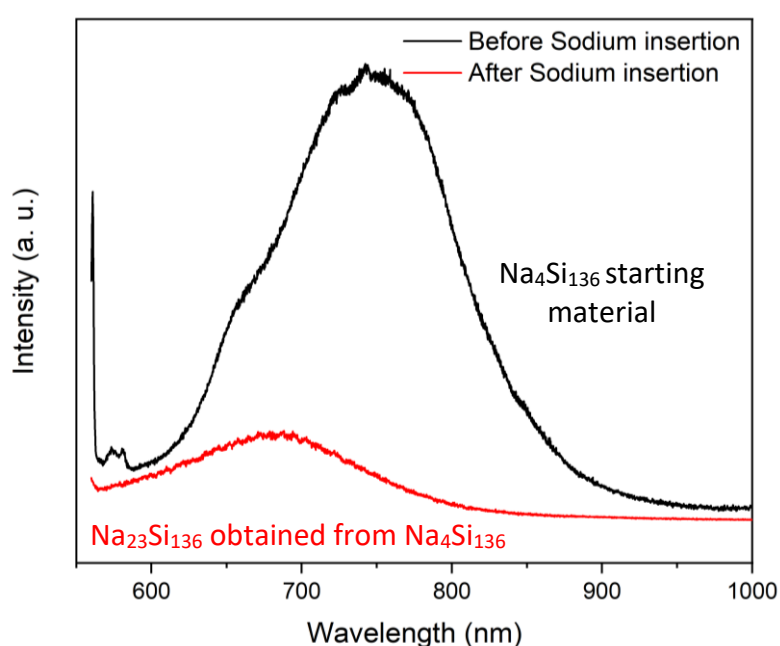
Figure 3.11 Photoluminescence measurements on a type II film before and after sodium was inserted into the structure by sodium vapor annealing at 380°C for 50h.

Thanks to the two post-synthesis methods of removing or inserting sodium in the type II cages, the chemical composition of the phase can be changed reversibly, resulting in valuable films covering a four-order-of-magnitude resistivity range, from semiconductor to metallic. This reversibility is, because to the unique cage structure of the type II silicon clathrates, allowing insertion with a minimal lattice expansion, from 14.64 Å to 14.71 Å when fully occupied.

3.2.3 DFT calculations of silicon clathrates

Since a variety of sodium occupation of the type II cages has been achieved thanks to the tuning of the synthesis conditions and post- treatment, it appears that the lower the sodium content, the higher the resistivity of the material is. This naturally stimulates interest in exploring the possible properties of both types of silicon clathrate. Additionally, even though the type I silicon clathrate material is synthesized with a constant amount of sodium, it is of interest to explore its properties for various occupations to better comprehend how sodium guest atoms interact with the silicon clathrate framework in general. Hence, DFT calculations of the density of states and band structures for various occupations of sodium within the clathrates were also conducted.

A. Calculations methods

Band structure calculations were performed by Daniel Stoeffler at IPCMS laboratory of Strasbourg using the Vienna Ab initio Simulation Package (VASP5.4)[23,24] in order to determine accurately the electronic structure of the considered system. It uses so-called Augmented Plane Waves and is based on the Projector Augmented Wave (PAW)[25] method using pseudopotentials to determine the wave function outside the augmentation region. For large cells such as the silicon clathrate ones, all calculations are performed with the GGA functional[26], a cut-off energy of 600 eV and a k-points sampling of 8x8x8 or 6x6x6 depending on the symmetry of the Brillouin Zone. After full relaxation of the lattice parameters and the internal structural position for all atoms, the total density of states (TDOS) and the band structure (BS) were obtained. Taking as example a given Na_xSi_{136} system, a symmetry analysis allowed to identify the equivalent cells and to investigate only one cell per group. For example, for x = 4 the 70 possible cells reduce to 4 groups having 2, 12, 24 and 32 equivalent elements. The TDOS is obtained by a weighted average over individual TDOS with a unique Fermi level set as the energy origin.

B. Results and discussion

As it can be seen from **Figure 3.12**, the TDOS of both guest-free structures are quite similar as a result of their quite similar structure and composition. The top-valence band originating from the p states of the silicon framework while the bottom is due almost exclusively to the s states and the conduction band is originating both from p states and a non-negligible s states contribution.
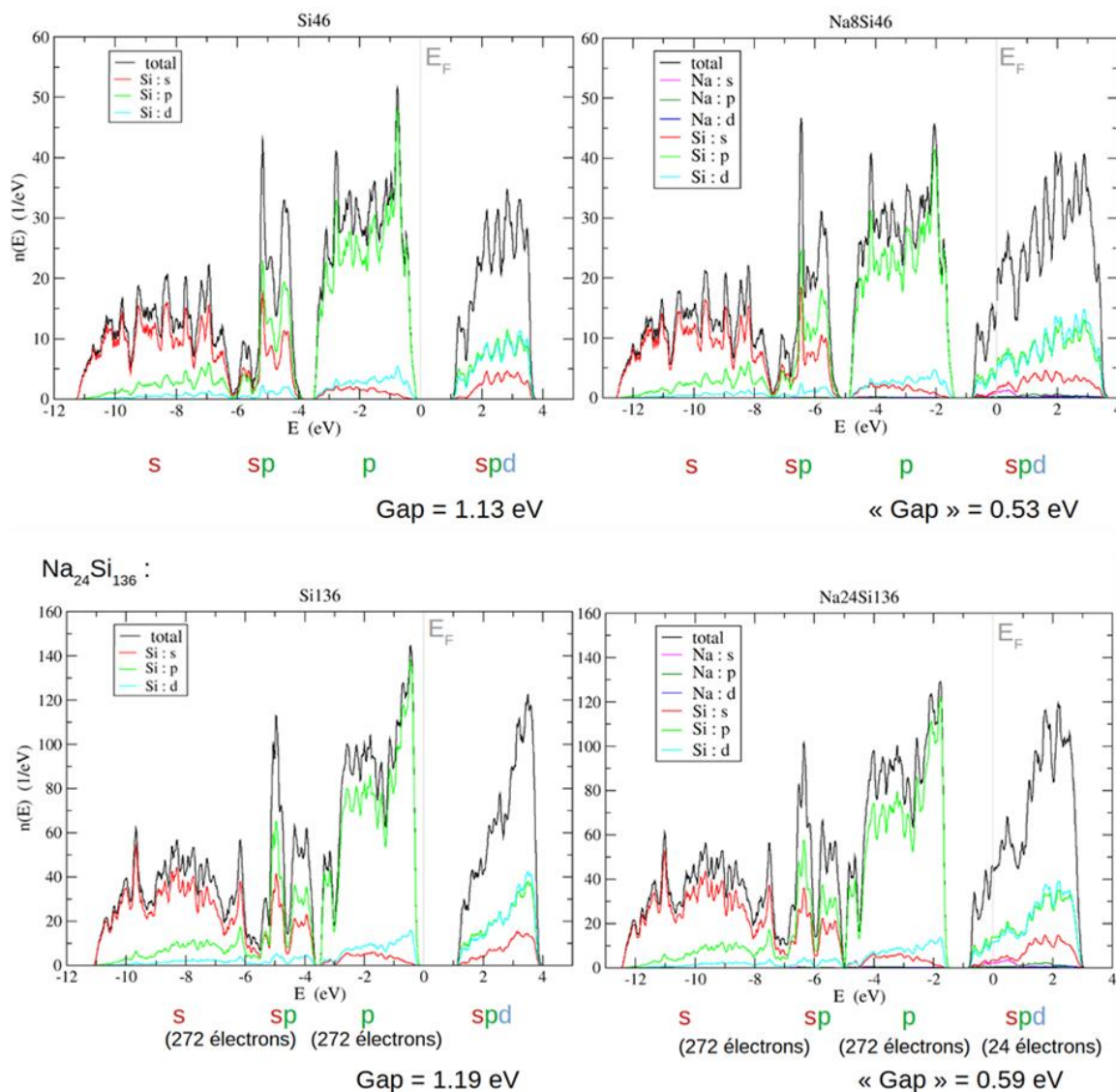
Figure 3.12 TDOS of type I and type II guest-free and fully occupied structures.

Then, the cages of both structures are theoretically fully filled with sodium guest atoms. Barely no changes are visible in the valence band of the structure when compared to the guest-free situation. However, the addition of sodium atoms results in the addition of electrons given to the framework. This contribution from sodium electrons s states

is therefore causing an extension of the conduction band due to their hybridization with silicon framework states[27]. Thus, the Fermi level is now located in the conduction band, indicating a metallic behaviour while the energy gaps between the two bands is reduced to 0.53 eV for Na_8Si_{46} and 0.59 eV for $Na_{24}Si_{136}$.

Si_{46} and Si_{136} also have similar estimated gaps between the valence and conduction bands that are compared to other values in **Table 3.5**. These values are of 1.13 eV for the type I and 1.19 eV for the type II even though these values are unreliable they remain in close agreement with DFT calculation reported by Connétable[28]. They do differ, however, from calculations using the Hyed-Scuseria-Ernzerhof hybrid functional method (HSE)[29] that gave a 1.95 eV direct bandgap for Si_{46} and local density approximation (LDA)[30] that gave a 1.92 eV bandgap for Si_{136}. No experimental value of Si_{46} bandgap has been reported yet, and guest-free Si_{136} silicon clathrates demonstrate a 1.9 eV bandgap[10]. Therefore, both guest free structures indicate a specific opening of the gap in comparison with the fully occupied structures. Nevertheless, the exact values obtained from the DFT calculations have to be considered with care as they seem quite astray from the experimental value in the type II situation.

Table 3.5 Values of the band determined for Si_{46} and Si_{136} determined by DFT and compared to reported values[22].

Calculation method	Si_{46}	Calculation method	Si_{136}
DFT (this work)	1.13 eV	DFT (this work)	1.19 eV
DFT[28]	1.2 eV	DFT[28]	1.3 eV
HSE[29]	1.95 eV	LDA[30]	1.92 eV
Experimental value	N.A.	Experimental value[22]	1.9 eV

Figure 3.13 shows the TDOS evolution for both structures upon gradual filling of the cages with sodium atoms. For the type II structure, TDOS has been calculated following a gradual filling of the structure, in a similar manner to Xue et al. study[31]. In type II, the 8 Si_{28} cages were filled first, then the 16 Si_{20} cages. No definite filling order was defined for the type I structure. When a sodium atom is inserted into the structure, the hybridization causes the Fermi level to be located at the edge of the conduction

band. This decreases the gap between the bands. The gap is "closing" gradually as the occupation increases, reaching a minimum at the fully occupied structure where the gap is only 0.53 eV or 0.59 eV with the Fermi level occurring inside the conduction band.
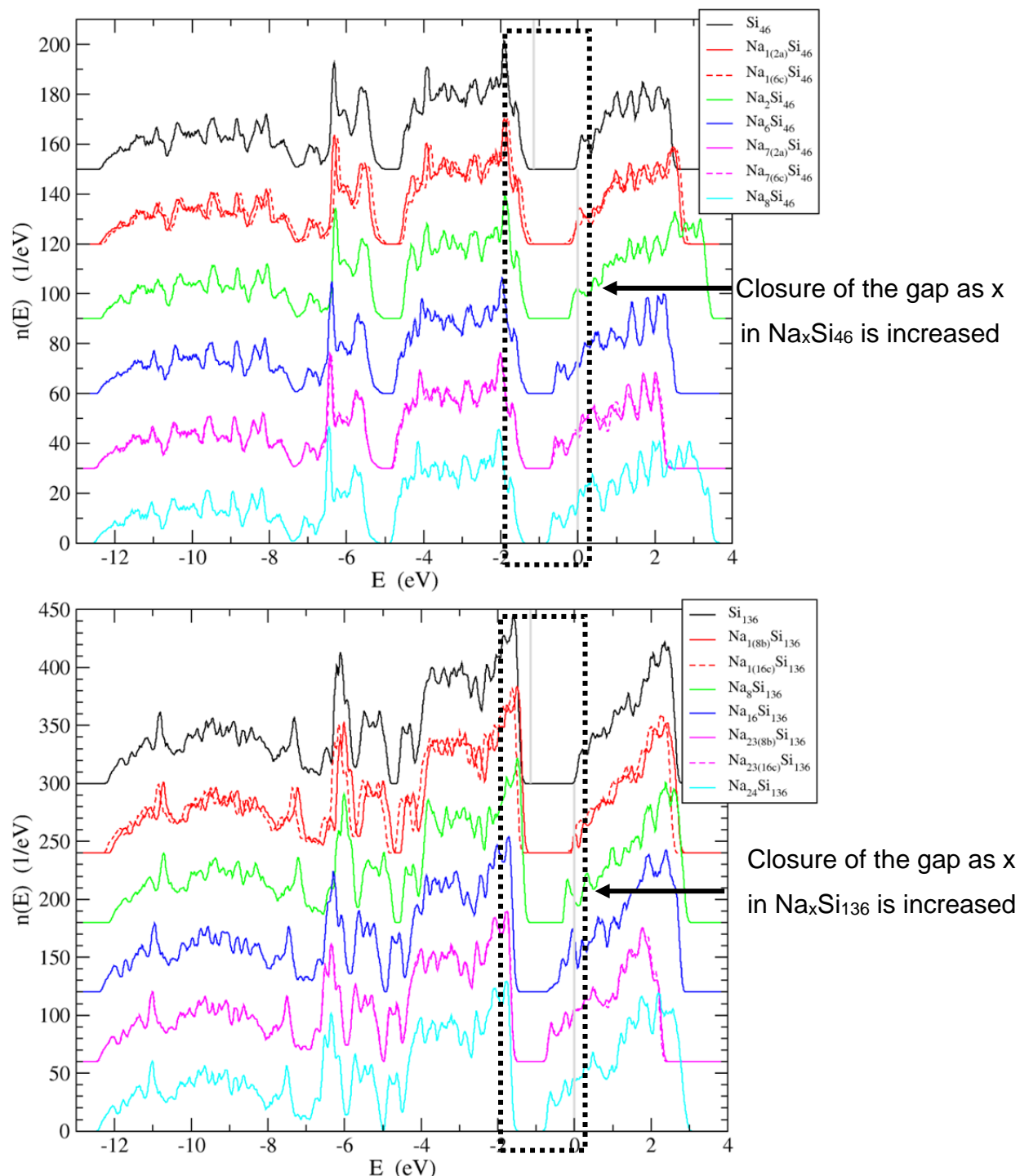
Figure 3.13 TDOS of type I and type II for various occupations values.

The closing of the gap with increasing sodium content x is to compare with the measured increase in resistivity as sodium is inserted in the structure (**Figure 3.9**).

This is also consistent with the slight shift of the bandgap toward lower value as x is reduced shown in **Figure 3.10** also reported by Kume et al[22].

In summary, DFT calculations show that increasing the sodium content of the two structures yields a transition from semiconducting guest-free materials to metallic fully occupied materials. Calculated band structures for starting from x = 0 up to x = 8, available in the annex A.3.2 section, highlight this gradual closure of the gap between the bands while indicating a change of its nature from direct to slightly indirect. These results are in agreement with the increase in resistivity as the sodium amount is

reduced as observed in the prior section for the type II structure and the underlying mechanism due to the transition from a semiconductive to a pseudo metallic material.

3.3 Photovoltaic properties of the silicon clathrates films

In this part the response to light of the as-grown silicon clathrate films are investigated. Then, the effects of implanted arsenic dose on these properties are explored and discussed.

3.3.1. Optoelectronic properties of as-grown silicon clathrate films

The test cell structure consists in a mixed type I/type II clathrate film grown on lightly doped p-type silicon wafers for a Process 1 temperature of 615°C and a Process 2 temperature of 400°C. It is considered as a np junction as the silicon clathrate film is n-type[19,30] due to excess of electrons donated by the sodium guest atoms. The front and back contacts are silver, fingers at the front and plane at the back. The resulting IV characteristics, from Fix et al.[32] , are reported in **Figure 3.14** and are similar to the previous reported ones on silicon clathrate cell[12].
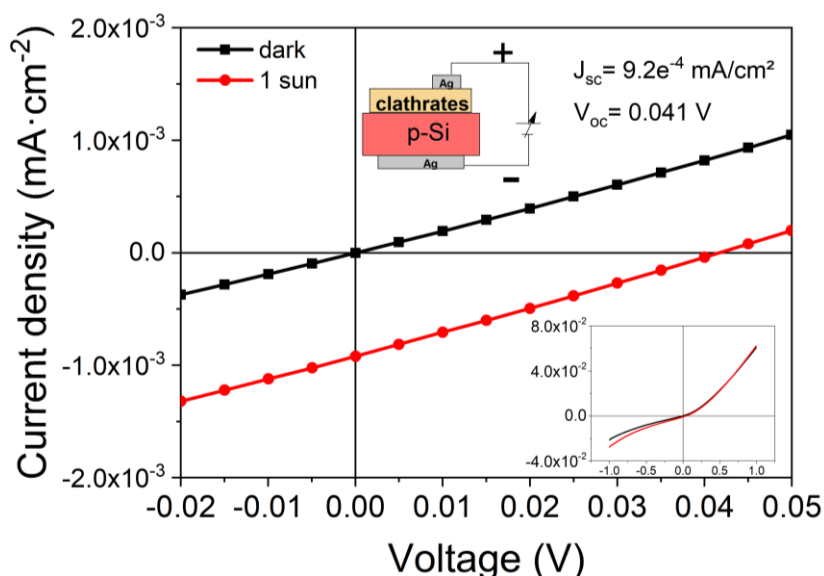
Figure 3.14 Current density vs. voltage characteristics in the dark and under 1 sun (AM1.5G) for a mixed type of silicon clathrates unpressued film

The resulting photovoltaic properties are quite poor: a very limited short circuit current density of 9.2×10^{-4} mA/cm^2 for an open circuit voltage of 41 mV are measured. The low short circuit current does not allow for external quantum efficiency measurements, and it was not yet clear if the carriers were effectively generated in the silicon clathrates.

To comprehend further, the optoelectronic properties of 30 µm type II silicon clathrate films $Na_{4.2}Si_{136}$ (Process 1 at 600°C, Process 2 at 400°C during 4h) were investigated by using Surface Photovoltage (SPV) using a Kelvin Probe system equipped with a tunable white light allowing transient SPV and SPV vs. illumination measurements. The results are shown in **Figure 3.15** for silicon clathrate types grown on a p-doped silicon wafer.

These silicon clathrates are subject to a change of contact potential difference under dark / light cycles, meaning they both have a photovoltaic response. As type I films were confirmed as a metallic material in Chapter 2 with slight presence of diamond silicon traces, the observed response is most probably due to these traces along to the light reaching the underlying p-doped substrate through the cracks. The p-type of the silicon wafer carriers is coherent with a CPD value higher during illumination than in the dark, as indicated in annex A.3.3 section. For the type II material however, the CPD value is higher in the dark than during light exposition, which is in accordance with its expected n-type behaviour[33] previously determined by the Hall effect and the hot probe method.
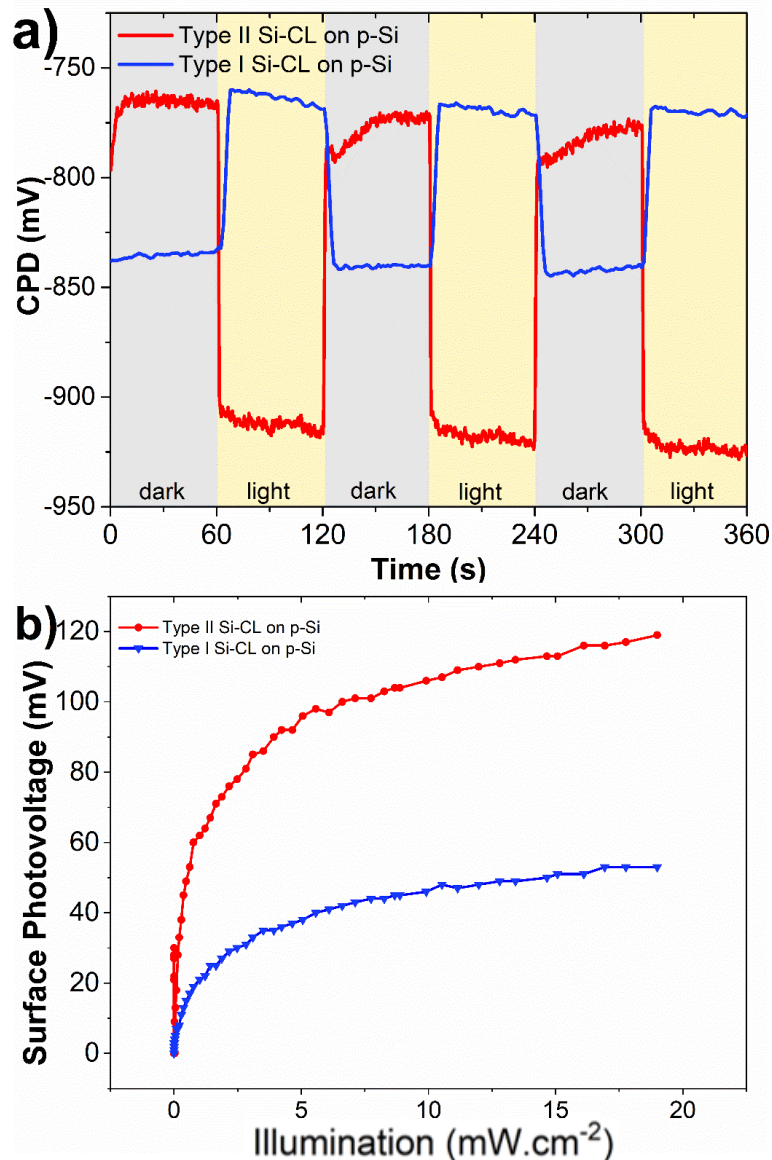
Figure 3.15 a) Variation of the Contact Potential Difference (CPD) measured on the silicon clathrates films during cycle between illumination by halogen visible light and dark. b) Surface Photovoltage (SPV) of the silicon clathrates samples according to the illumination delivered by the halogen visible light.

The second measurement consists in measuring $SPV(Illumination) = |CPD(Illumination) - CPD_{dark}|$ as the illumination is increased. For type I and type II, the SPV value increases logarithmically with illumination, as expected for semiconductors, toward a maximum non-saturated value of 50 mV and 120 mV respectively for a maximum illumination of 19 mW/cm2. Similar measurement was done on p-doped single crystalline silicon and is presented in annex A.3.2 section.

To confirm that the measured data are those of the investigated silicon clathrates, complementary Spectroscopic Surface Photovoltage was carried out on both types I and II. This allows to plot the SPV normalized by the photon flux at various wavelengths delivered by the monochromator, as shown in **Figure 3.16**. This method is quite similar to EQE measurements while allowing the detection of a low short circuit current density. The measurement was also performed on a p-doped single crystal silicon of 1-5 Ω·cm resistivity used as a reference.
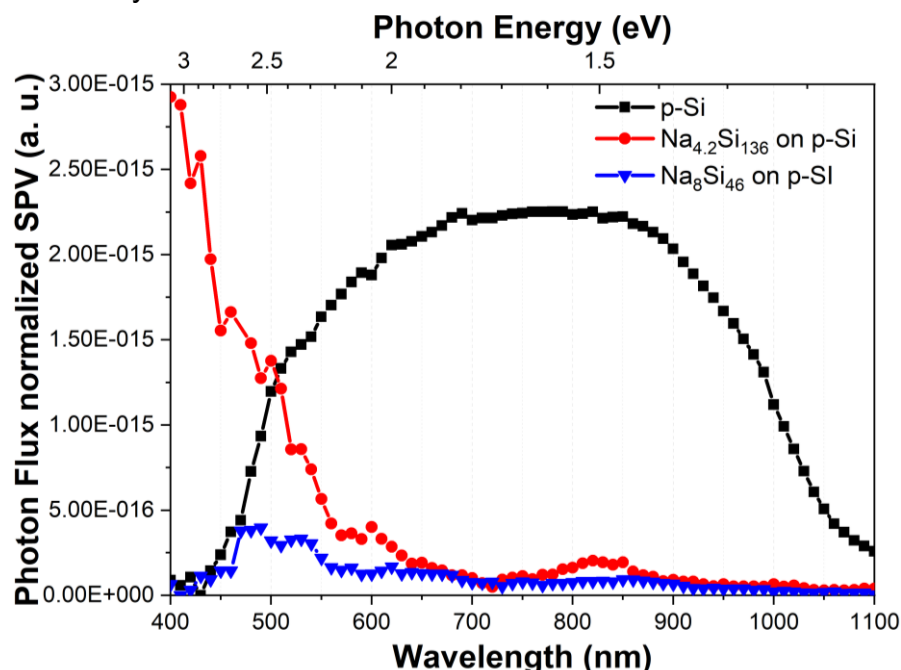
Figure 3.16 Surface Photovoltage Spectroscopy of the Silicon Clathrates samples and p-doped silicon of 1-5 Ω·cm resistivity by normalizing the SPV by the photon flux versus the wavelength of the light.

For the type I silicon clathrate film, almost no signal can be differentiated from the noise. In contrast, the type II signal is high at a wavelength of 400 nm and steadily goes down to reach almost no signal at 650 nm. This clearly demonstrates that the SPS signal does not originate from the silicon substrate and is rather a response of the type II silicon clathrates. Moreover, the zero-signal at wavelengths above 650 nm is in agreement with the bandgap of 1.9 eV.

Based on these studies, it has now been demonstrated that type II silicon clathrates are photoactive and this prompted the enhancement of their photovoltaic properties by implanting the film using arsenic ion , based on work previously done on single crystalline silicon[34].

3.3.2 Ionic implantation of the silicon clathrates

With the aim to improve the photovoltaic response of the type II silicon clathrates grown on p-doped silicon wafers, implanting arsenic ions and subsequent thermal annealing was performed in order to obtain a heavily n-doped zone in the silicon clathrate film.

This study was conducted in an exploratory manner because ion implantation of silicon clathrates is novel. Arsenic ions were implanted at various energy from 30 keV to 160 keV and at different doses from 5×10^{15} at.cm^{-2} to 10^{17} at.cm^{-2}. The As implanted silicon clathrate films were then thermally annealed using halogen lamps (RTA) at a temperature of 450°C and a duration of 30 s. The arsenic distribution profile within the silicon clathrate was determined by Rutherford Backscattering Spectroscopy (RBS) technique using a 1.5 MeV He beam The RBS spectra are plotted in **Figure 3.17.** More details are available in annex A.3.4.
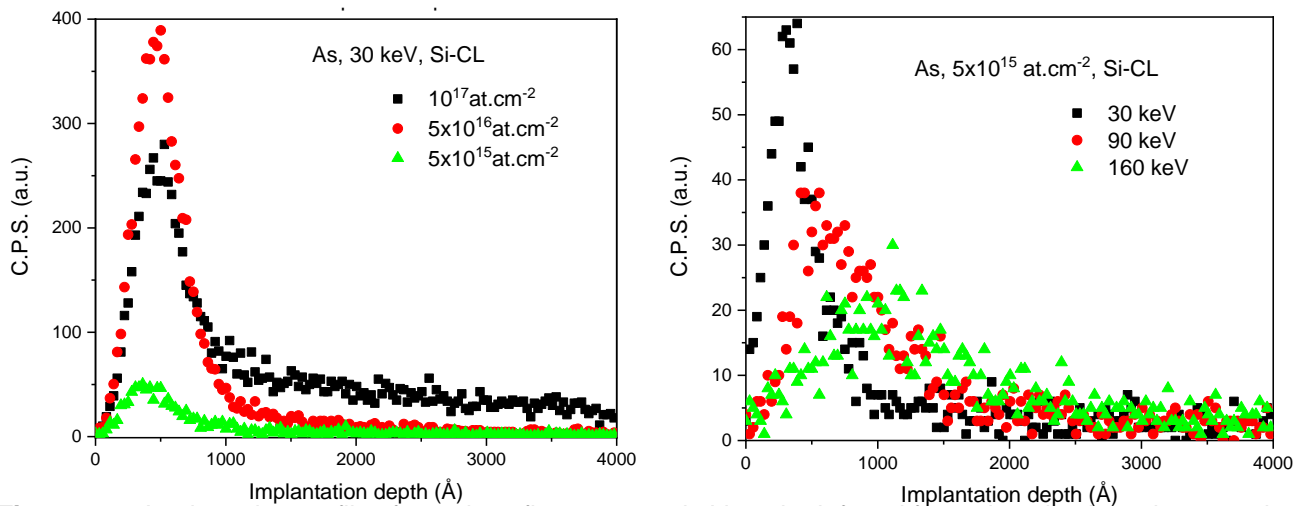
Figure 3.17 Implantation profiles for various fluence at 30 keV on the left and for various implantation energies at a 5×10^{15} at.cm^{-2} of Arsenic after RTA at 450°C, obtained from RBS measurements done at 1.5 MeV.

Figure 3.17a shows that changing the arsenic implanted dose increases the amount of arsenic inserted in the silicon clathrate film, with a maximum depth range of about 100nm for an implantation energy of 30KeV, to be compared to the thickness of the silicon clathrate of about 30 μm.

On the other hand, increasing the energy of the ions from 30 to 160 KeV led to a much deeper penetration of the arsenic ions, a little above 200nm. The implanted and annealed films were also investigated by XRD to make sure no amorphization or degradation of the films happened during implantation. For all implantation energies and doses lower than 10^{17} at.cm^{-2}, no degradation is observed as witnessed in **Figure 3.18**. However, for an implantation dose of 10^{17} at.cm^{-2}, the amorphization of the silicon clathrates film was observed.
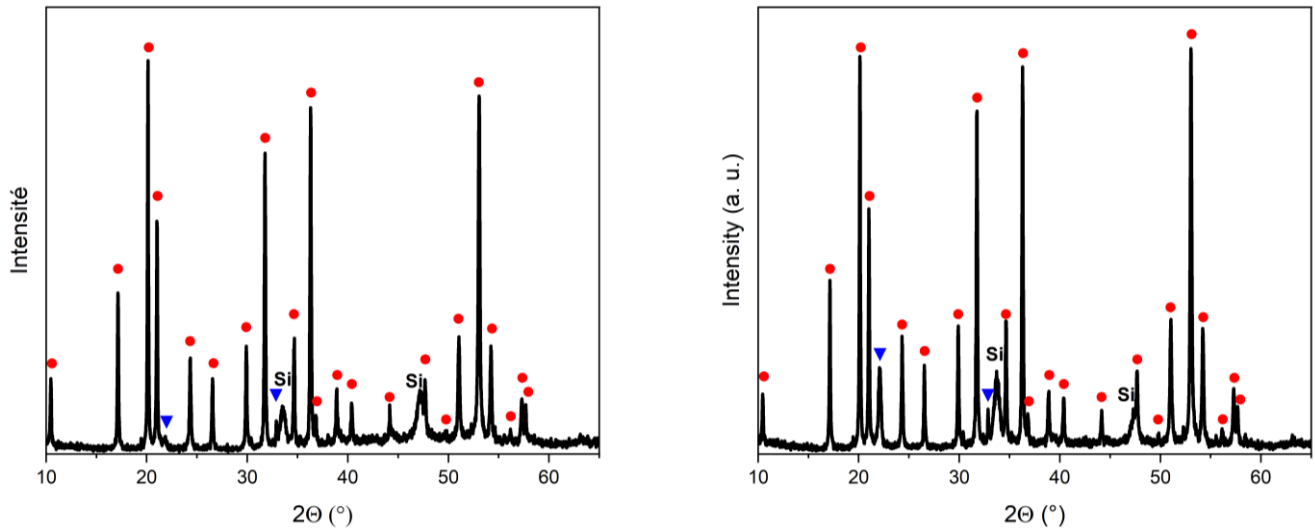
Figure 3.18. XRD patterns of type II films submitted to RTA at 450°C after being implanted with arsenic at a) 30 keV and a fluence of 5x10^{16} at.cm^{-2} b) 90 keV and a fluence of 5x10^{15} at.cm^{-2}.

Under similar implantation parameters, the sodium occupation of the implanted type II films has no effect on the depth of implantation arsenic. This range has been plotted in **Figure 3.19** according to the implantation energy and is compared to the same ranges obtained for implantation in single crystalline silicon[35].
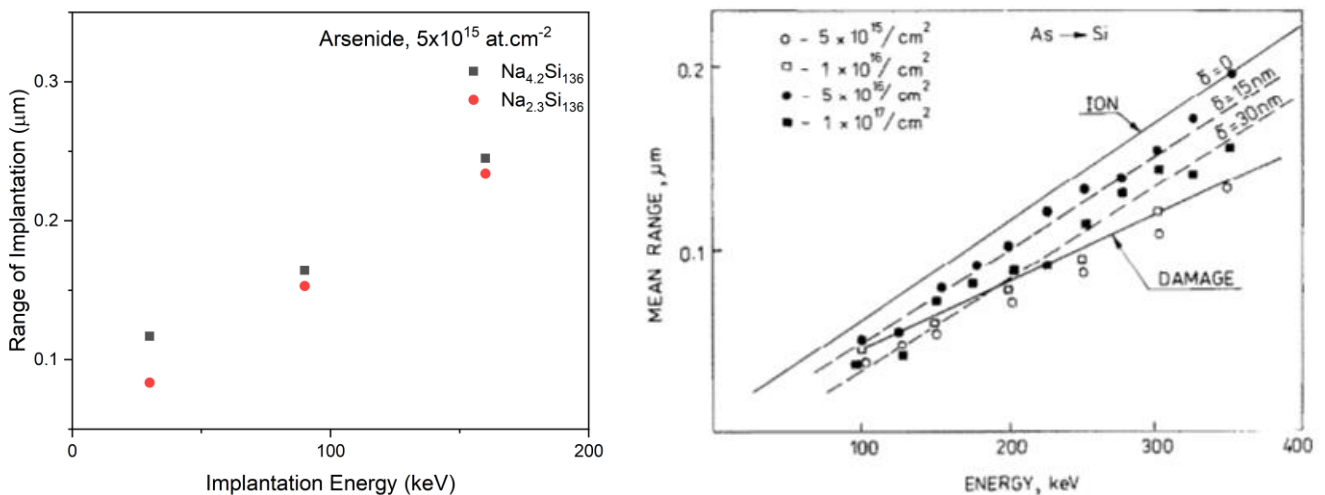

Figure 3.19 Range of implantation experimentally obtained for arsenic in type II silicon clathrates compared to the diamond silicon situation[35].

For a similar implantation energy, it seems that the penetration depth of arsenic ions is slightly larger in silicon clathrate than in single crystalline silicon. This is due to the slightly less dense material and the channels formed by the intertwined polyhedral cages. This allows the incoming dopants to have higher mean free paths through the structure than in diamond silicon.

3.3.3 Photovoltaics properties of the doped silicon clathrate films

Now that the type II films are successfully doped without damaging the clathrate structure, the effect of this implantation process on the photovoltaic response of the simple arsenic doped silicon clathrates/silicon clathrates/p-doped single crystalline silicon cells can be investigated.

The As implantation energy was fixed at 30 keV while the dose was modified to test how it impacts the properties. Conservation of the silicon clathrates films quality is proved by XRD patterns in **Figure 3.20**.
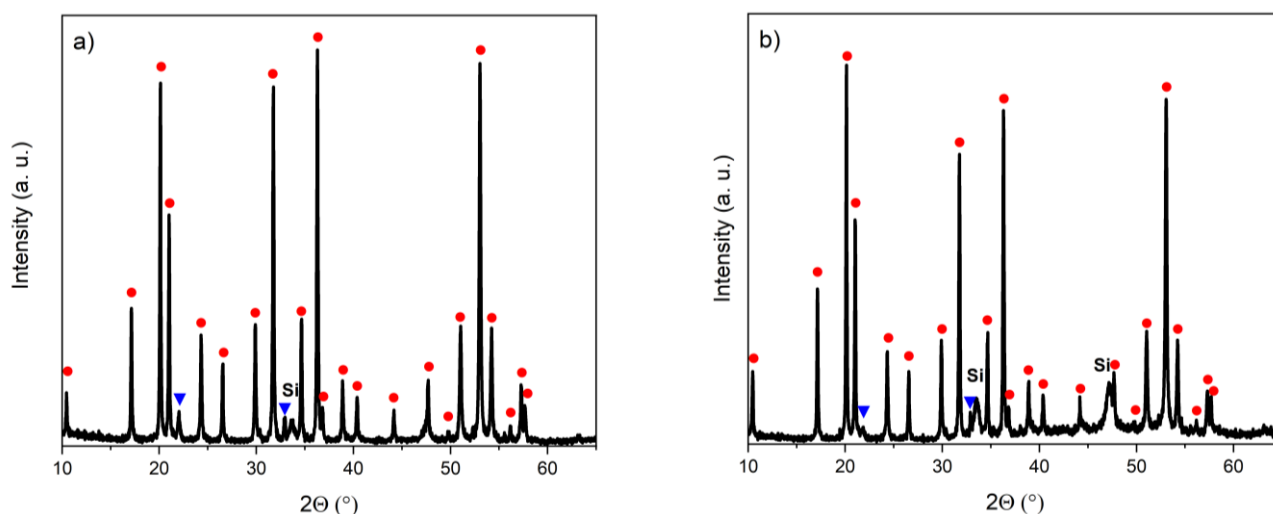
Figure 3.20 XRD patterns of type II films a) before and b) after being implanted at 30 keV and an arsenic fluence of 5×10^{15} at.cm^{-2} and submitted to RTA in argon gas at 450°C during 30 seconds.

Both undoped and doped type II films were investigated under Solar Simulator for 1 sun irradiation. The undoped type II cell shows (**Figure 3.21**) an open circuit voltage of 39 mV, comparable to the value obtained for the mixed type described earlier, while exhibiting a lower short circuit current density of 2.8×10^{-6} mA/cm^{-2}.
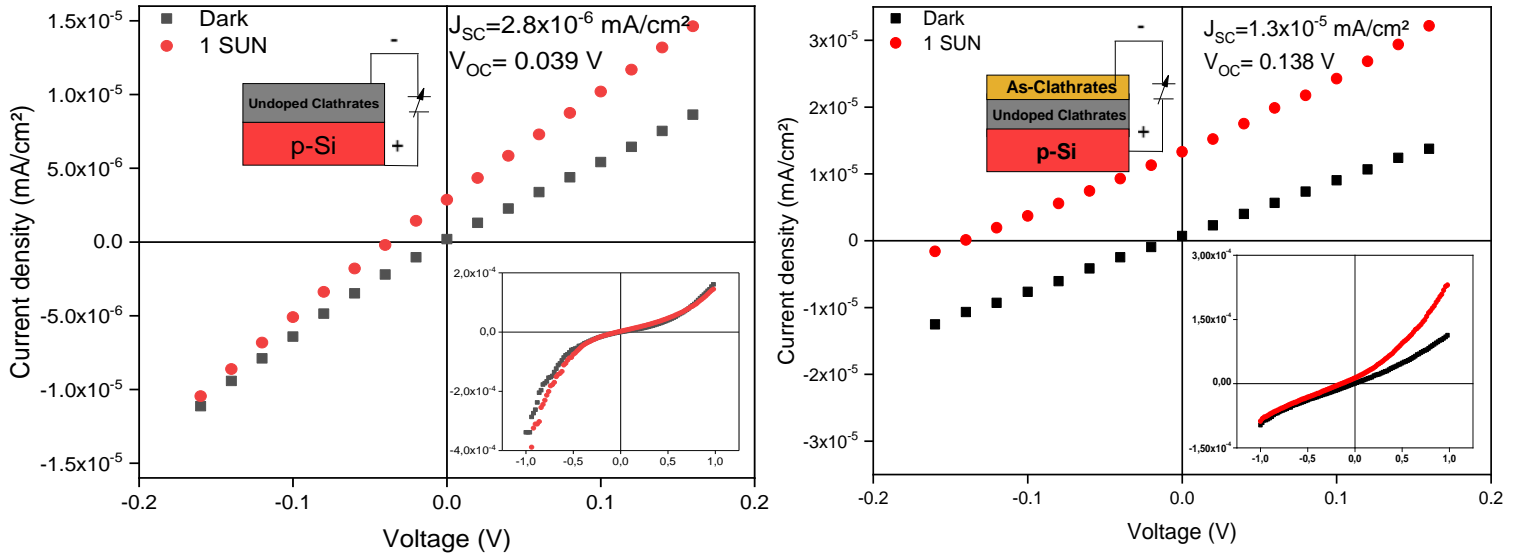
Figure 3.21 Current density vs. voltage characteristics in the dark and under 1 sun (AM1.5G) for a type II film as-synthesized on the left, and after being implanted at 30 keV and a fluence of 5×10^{15} at.cm^{-2} and submitted to RTA.

The doped silicon clathrate cell obtained by implanting arsenide at 30 keV and at a 5×10^{15} at/cm^{-2} dose shows better V_{OC}. The resulting short circuit current density has been improved by almost one order of magnitude, up to 1.3×10^{-5} mA/cm^{-2}, while the open circuit voltage has almost tripled to reach a value of 138 mV. This measurement shows the modification of the photovoltaic response of the material due to the implantation process of the top surface of the silicon clathrate. The doped films were also investigated by SPV and compared to the value obtained for the starting material as shown in **Figure 3.22.**
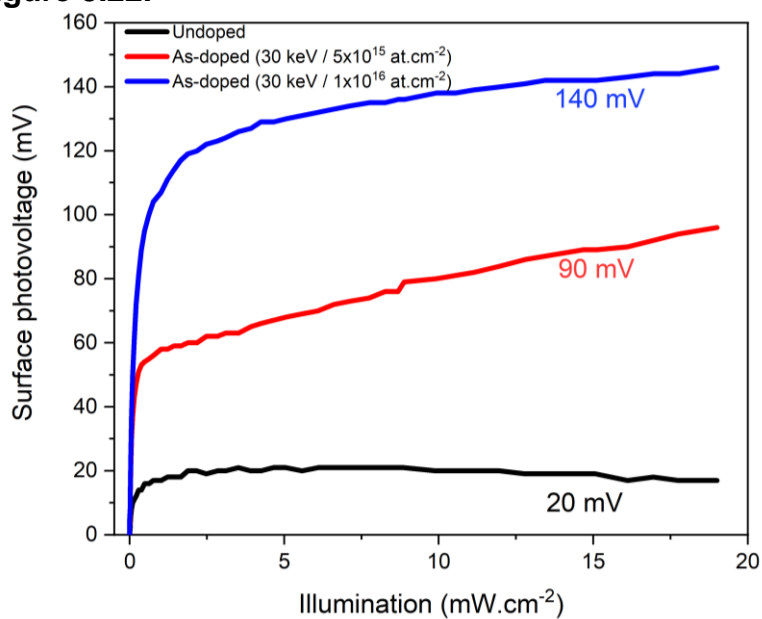
Figure 3.22 Surface Photovoltage of the Silicon Clathrates samples according to the illumination delivered by the halogen visible light for undoped and doped type II silicon clathrates films.

As reported in **Table 3.6**, the SPV value for the maximum illumination is higher when the amount of arsenic dopants is high, even though only the very surface of the silicon clathrate film has been doped. This implies that more photocarriers are generated under the same illumination level when the content of arsenic is high. Complementary measurements using both Solar Simulator and SPV show similar trends. Increased dose increases both the SPV and the V_{OC} of the cell, emphasizing its importance in producing a more efficient photovoltaic response in the type II silicon clathrate.

Table 3.6 Impact of the arsenic implantation on the SPV value at saturation and V_{OC} of the type II Silicon clathrates films.

Type II Silicon Clathrate implanted with Arsenic ions at 30 keV	Arsenic dose (at/cm²)			
	Not doped	$1,00 \cdot 10^{15}$	$5,00 \cdot 10^{15}$	$1,00 \cdot 10^{16}$
SPV$_{sat}$ [mV]	19±4	40±3	98±7	142±8
V$_{OC}$ (Solar simulator) [mV]	39±6	59±5	143±10	203±10

Yet, both the undoped and doped type II films exhibit very low J_{SC} values, even lower than that measured for the first cell obtained using a mix of clathrates. This could be due to the better adhesion of the type I structure to the silicon substrate resulting in a more efficient response. On the other hand, the improvement of the photovoltaic response as the arsenic dose increases can be due to a better collection of the minority carriers thanks to a more efficient contact between the semiconducting silicon clathrate and the front metallic contact. One purpose of this experiment is to assess the feasibility and effectiveness of the ion implantation for improving the photovoltaic properties of silicon clathrate. This paves the way toward implantation of silicon clathrate thin films. Having the opportunity to dope the complete layer will allow the improvement of the photovoltaic response to be studied again in accordance with Hall effect, SPV, and SPS measurements of such n/p junctions.

3.4 Summary of Chapter 3

In this chapter, various pathways have been used for tuning the properties of the silicon clathrate films toward a better understanding of the silicon clathrate films and their optimization for photovoltaic applications.

Post-synthesis treatment to control the sodium content, has been adapted from silicon clathrate powder studies to our grown silicon clathrate films. For the type II silicon clathrates, almost guest-free semiconductive structure can be obtained by exposing the as-grown films to hot iodine vapor in low vacuum. On the other hand, fully occupied structures are reached thanks to extended exposition to sodium vapour at moderate temperature. As a result, by using these methods of filling or emptying by sodium atoms, silicon clathrate films with resistivities ranging from 10^{-2} to 10^{2} $\Omega \cdot cm$ can be obtained in a reversible manner. Indeed, due to the almost negligible lattice expansion as the sodium cages are being either filled or emptied, virtually no damage is caused to the silicon clathrate structures even on successive treatments. The suspected role of the sodium states on the optoelectronic properties of the silicon clathrates was confirmed by DFT calculations.

Finally, the generation of photocarriers upon illumination of the type II silicon clathrates has been confirmed by complementary investigation using Solar Simulator and Surface Photovoltage techniques. Yet, the measured photovoltaic response is very low, mainly due to the very weak short circuit current density. Implantation using Arsenic ion and post-synthesis annealing into the type II structure enhanced the photovoltaic response but with only minor changes to the short circuit current density. This low value of J_{SC} could be attributed to the weak adhesion of the type II films to the silicon substrate as a higher J_{SC} value was obtained for a basic cell using a film containing both types of clathrates. This result is a first step toward better photovoltaic response of silicon clathrate films, which will be further explored on ultra-thin silicon clathrate films.

References of Chapter 3

(1) Gunatilleke, W. D. C. B.; Ojo, O. P.; Poddig, H.; Nolas, G. S. Synthesis and Characterization of Phase-Pure Clathrate-II Rb12.9Si136. *Journal of Solid State Chemistry* **2022**, *311*, 123152. https://doi.org/10.1016/j.jssc.2022.123152.

(2) Dopilka, A.; Weller, J. M.; Ovchinnikov, A.; Childs, A.; Bobev, S.; Peng, X.; Chan, C. K. Structural Origin of Reversible Li Insertion in Guest-Free, Type-II Silicon Clathrates. *Adv Energy Sustain Res* **2021**, *2* (5), 2000114. https://doi.org/10.1002/aesr.202000114.

(3) Reny, E.; Ménétrier, M.; Cros, C.; Pouchard, M.; Sénégas, J. A 23Na NMR study of NaxSi136 and Na8SI46 silicon clathrates. *Comptes Rendus de l'Académie des Sciences - Series IIC - Chemistry* **1998**, *1* (2), 129–136. https://doi.org/10.1016/S1251-8069(97)86272-0.

(4) Chan, K. S.; Miller, M. A.; Liang, W.; Ellis-Terrell, C.; Chan, C. K. First Principles and Experimental Studies of Empty Si46 as Anode Materials for Li-Ion Batteries – CORRIGENDUM. *J. Mater. Res.* **2017**, *32* (13), 2628. https://doi.org/10.1557/jmr.2017.160.

(5) Warrier, P.; Koh, C. A. Silicon Clathrates for Lithium Ion Batteries: A Perspective. *Applied Physics Reviews* **2016**, *3* (4), 040805. https://doi.org/10.1063/1.4958711.

(6) Li, X.; Steirer, K. X.; Krishna, L.; Xiao, C.; Fink, K.; Santhanagopalan, S. Electrochemical Properties and Challenges of Type II Silicon Clathrate Anode in Sodium Ion Batteries. *J. Electrochem. Soc.* **2019**, *166* (13), A3051–A3058. https://doi.org/10.1149/2.1201913jes.

(7) Iwasaki, S.; Morito, H.; Komine, T.; Morita, K.; Shibuya, T.; Nishii, J.; Fujioka, M. A Novel Technique for Controlling Anisotropic Ion Diffusion: Bulk Single-Crystalline Metallic Silicon Clathrate. *Advanced Materials* **2022**, *34* (9), 2106754. https://doi.org/10.1002/adma.202106754.

(8) Beekman, M.; Nenghabi, E. N.; Biswas, K.; Myles, C. W.; Baitinger, M.; Grin, Y.; Nolas, G. S. Framework Contraction in Na-Stuffed Si(*CF* 136). *Inorg. Chem.* **2010**, *49* (12), 5338–5340. https://doi.org/10.1021/ic1005049.

(9) Reny, E.; Gravereau, P.; Cros, C.; Pouchard, M. Structural Characterisations of the NaxSi136 and Na8Si46 Silicon Clathrates Using the Rietveld Method. *J. Mater. Chem.* **1998**, *8* (12), 2839–2844. https://doi.org/10.1039/A804565H.

(10) Ammar, A.; Cros, C.; Pouchard, M.; Jaussaud, N.; Bassat, J.-M.; Villeneuve, G.; Duttine, M.; Ménétrier, M.; Reny, E. On the Clathrate Form of Elemental Silicon, Si136: Preparation and Characterisation of NaxSi136 (X→0). *Solid State Sciences* **2004**, *6* (5), 393–400. https://doi.org/10.1016/j.solidstatesciences.2004.02.006.

(11) Momma, K.; Izumi, F. *VESTA 3* for Three-Dimensional Visualization of Crystal, Volumetric and Morphology Data. *J Appl Crystallogr* **2011**, *44* (6), 1272–1276. https://doi.org/10.1107/S0021889811038970.

(12) Kume, T.; Ohashi, F.; Sakai, K.; Fukuyama, A.; Imai, M.; Udono, H.; Ban, T.; Habuchi, H.; Suzuki, H.; Ikari, T.; Sasaki, S.; Nonomura, S. Thin Film of Guest-Free Type-II Silicon Clathrate on Si (111) Wafer. *Thin Solid Films* **2016**, *609*. https://doi.org/10.1016/j.tsf.2016.03.056.

(13) Petříček, V.; Dušek, M.; Palatinus, L. Crystallographic Computing System JANA2006: General Features. *Zeitschrift für Kristallographie - Crystalline Materials* **2014**, *229* (5), 345–352. https://doi.org/10.1515/zkri-2014-1737.

(14) Chan, K. S.; Miller, M. A.; Ellis-Terrell, C.; Chan, C. K. Synthesis and Characterization of Empty Silicon Clathrates for Anode Applications in Li-Ion Batteries. *MRS Advances* **2016**, *1* (45), 3043–3048. https://doi.org/10.1557/adv.2016.434.

(15) Nolas, G. S.; Kendziora, C. A.; Gryko, J.; Dong, J.; Myles, C. W.; Poddar, A.; Sankey, O. F. Raman Scattering Study of Stoichiometric Si and Ge Type II Clathrates. *Journal of Applied Physics* **2002**, *92* (12), 7225–7230. https://doi.org/10.1063/1.1523146.

(16) Stefanoski, S.; Malliakas, C. D.; Kanatzidis, M. G.; Nolas, G. S. Synthesis and Structural Characterization of Na $_x$ Si $_{136}$ (0 < *x* ≤ 24) Single Crystals and Low-Temperature Transport of Polycrystalline Specimens. *Inorg. Chem.* **2012**, *51* (16), 8686–8692. https://doi.org/10.1021/ic202199t.

(17) Cros, C.; Pouchard, M.; Hagenmuller, P. Sur une nouvelle famille de clathrates minéraux isotypes des hydrates de gaz et de liquides. Interprétation des résultats obtenus. *Journal of Solid State Chemistry* **1970**, *2* (4), 570–581. https://doi.org/10.1016/0022-4596(70)90053-8.

(18) Yamaga, M.; Kishita, T.; Goto, K.; Sunaba, S.; Kume, T.; Ban, T.; Himeno, R.; Ohashi, F.; Nonomura, S. Electron Spin Resonance, Dynamic Jahn-Teller Effect, and Electric Transport Mechanism in Na-Doped Type II Silicon Clathrates. *Journal of Physics and Chemistry of Solids* **2020**, *140*, 109358. https://doi.org/10.1016/j.jpcs.2020.109358.

(19) Liu, Y.; Schenken, W. K.; Krishna, L.; Majid, A. A. A.; Furtak, T. E.; Walker, M.; Koh, C. A.; Taylor, P. C.; Collins, R. T. Synthesis and Characterization of Type II Silicon Clathrate Films with Low Na Concentration. *Applied Physics Reviews* **2021**, *8* (4), 041408. https://doi.org/10.1063/5.0062723.

(20) Vollondat, R.; Roques, S.; Chevalier, C.; Bartringer, J.; Rehspringer, J.-L.; Slaoui, A.; Fix, T. Synthesis and Characterization of Silicon Clathrates of Type I Na8Si46 and Type II NaxSi136 by Thermal Decomposition. *Journal of Alloys and Compounds* **2022**, *903*, 163967. https://doi.org/10.1016/j.jallcom.2022.163967.

(21) Krishna, L.; Martinez, A. D.; Baranowski, L. L.; Brawand, N. P.; Koh, C. A.; Stevanović, V.; Lusk, M. T.; Toberer, E. S.; Tamboli, A. C. Group IV Clathrates: Synthesis, Optoelectonic Properties, and Photovoltaic Applications. In *Physics, Simulation, and Photonic Engineering of Photovoltaic Devices III*; SPIE, 2014; Vol. 8981, pp 29–39. https://doi.org/10.1117/12.2040056.

(22) Kume, T.; Ohashi, F.; Nonomura, S. Group IV Clathrates for Photovoltaic Applications. *Jpn. J. Appl. Phys.* **2017**, *56* (5S1), 05DA05. https://doi.org/10.7567/JJAP.56.05DA05.

(23) Kresse, G.; Furthmüller, J. Efficient Iterative Schemes for *Ab Initio* Total-Energy Calculations Using a Plane-Wave Basis Set. *Phys. Rev. B* **1996**, *54* (16), 11169–11186. https://doi.org/10.1103/PhysRevB.54.11169.

(24) Kresse, G.; Joubert, D. From Ultrasoft Pseudopotentials to the Projector Augmented-Wave Method. *Phys. Rev. B* **1999**, *59* (3), 1758–1775. https://doi.org/10.1103/PhysRevB.59.1758.

(25) Blöchl, P. E. Projector Augmented-Wave Method. *Phys. Rev. B* **1994**, *50* (24), 17953–17979. https://doi.org/10.1103/PhysRevB.50.17953.

(26) Perdew, J. P.; Burke, K.; Ernzerhof, M. Generalized Gradient Approximation Made Simple. *Phys. Rev. Lett.* **1996**, *77* (18), 3865–3868. https://doi.org/10.1103/PhysRevLett.77.3865.

(27) Zhang, W.; Chen, Q.-Y.; Zeng, Z.-Y.; Cai, L.-C. Structural, Elastic, and Electronic Properties of Sodium Atoms Encapsulated Type-I Silicon–Clathrate Compound under High Pressure. *Chinese Phys. B* **2015**, *24* (10), 107101. https://doi.org/10.1088/1674-1056/24/10/107101.

(28) Connétable, D. Structural and Electronic Properties of p-Doped Silicon Clathrates. *Phys. Rev. B* **2007**, *75* (12), 125202. https://doi.org/10.1103/PhysRevB.75.125202.

(29) Chan, K. Hybrid Carbon-Based Clathrates for Energy Storage. *C* **2018**, *4* (1), 7. https://doi.org/10.3390/c4010007.

(30) Dong, J.; Sankey, O. F.; Kern, G. Theoretical Study of the Vibrational Modes and Their Pressure Dependence in the Pure Clathrate-II Silicon Framework. *Phys. Rev. B* **1999**, *60* (2), 950–958. https://doi.org/10.1103/PhysRevB.60.950.

(31) Xue, D.; Myles, C. First-Principles Study of the Electronic, Vibrational Properties and Anharmonic Effects of Some Si-Based Type-II Binary Clathrates. *Materials* **2019**, *12* (3), 536. https://doi.org/10.3390/ma12030536.

(32) Fix, T.; Vollondat, R.; Ameur, A.; Roques, S.; Rehspringer, J.-L.; Chevalier, C.; Muller, D.; Slaoui, A. Silicon Clathrate Films for Photovoltaic Applications. *J. Phys. Chem. C* **2020**, *124* (28), 14972–14977. https://doi.org/10.1021/acs.jpcc.0c02712.

(33) Jaramillo-Quintero, O. A.; Rincón, M. E.; Vásquez-García, G.; Nair, P. K. Influence of the Electron Buffer Layer on the Photovoltaic Performance of Planar $Sb_2(S_x Se_{1-x})_3$ Solar Cells. *Prog Photovolt Res Appl* **2018**, *26* (9), 709–717. https://doi.org/10.1002/pip.3007.

(34) Chisholm, J.; Stephen, J.; Turner, J.; Dobson, P.; Francis, R.; Williams, E. An Analysis of Arsenic Ion Implantation for Use in Silicon Bipolar Devices. In *Ion Implantation in Semiconductors: Science and Technology*; Namba, S., Ed.; Springer US: Boston, MA, 1975; pp 641–646. https://doi.org/10.1007/978-1-4684-2151-4_81.

(35) Kisielewicz, M. Measurements and Calculation of Low-Energy Heavy Ion Profiles in Silicon. *Nuclear Instruments and Methods in Physics Research* **1983**, *216* (3), 511–516. https://doi.org/10.1016/0167-5087(83)90521-5.

Conclusion and perspectives

The main aim of this thesis work was to investigate the structural, optical, electrical and photovoltaic properties of silicon clathrate films. The investigated films, of type I (Na_8Si_{46}) and type II (Na_xSi_{136}) were synthesized through the thermal decomposition using a two-step process. As low-density silicon allotropes exhibit direct band gaps, these guest-free specific structures are examined as an alternative to conventional single crystal silicon as absorbers to achieve higher PV efficiencies. Before being stripped from their atoms, silicon clathrates are guest-host compounds made of a framework of silicon cages containing sodium atoms.

In the first part, we have shown that silicon clathrate films can be produced by the so-called two-step thermal decomposition pathway which relies on the formation of a Na_4Si_4 and its subsequent transformation into the desired silicon clathrates. As a difference to other laboratories, the setup used in this work does not require the use of any glovebox allowing less costly synthesis. The conditions of the synthesis were successfully optimized to produce films with the highest structural quality. In addition, the films were optimized to selectively obtain each of the two phases by taking advantage of the sodium vapour pressure to influence their competing formation.

We have demonstrated that the synthesized type I silicon clathrate films are uniformly Na_8Si_{136} in composition and of metallic character. On the other hand, the type II silicon clathrate are found to have various compositions as refined by Rietveld and confirmed by EDS, in addition to exhibit semiconductive properties. Thus, the sodium concentration can be tuned using longer annealing duration under vacuum leading to structures with compositions from Na_9Si_{136} to Na_2Si_{136}. Furthermore, the electrical properties of the films are also affected by the reduction in sodium concentration within the films.

Thermal stability of the silicon clathrate was also studied. We have shown that the severe thermal decomposition process causes high defects concentrations and rough surfaces. As an alternative, we have shown that annealing under mechanical pressure has resulted in the effective compacting of the silicon clathrate layer allowing to get the first ever AFM picture of silicon clathrates. The crystallographic structural

rearrangement of the type I films was also observed after this treatment, which did not occur for the type II.

The required quantity of sodium to sustain the reaction during the synthesis process resulted in fabricating thick films of several tens of microns. Various pathways were presented to reduce this thickness such as wet and dry etching as well as using thin silicon on sapphire substrates as a substrate to initiate the reaction. We have shown that reactive ion etching using SF_6 applied to as grown silicon clathrate films is the most promising.

The second part of this thesis was dedicated to the tuning of the sodium content in the silicon cages and the consequences on the structural and optoelectronic properties of the resulting films. We have first demonstrated that it is possible to control the sodium occupation within silicon clathrate using annealing under sodium vapor to insert sodium in the cages. We have also shown that sodium can be extracted from the cages under iodine atmosphere. Thanks to these two different methods, we have obtained type II films that range from the semiconductive $Na_{0.1}Si_{136}$ to the metallic $Na_{23}Si_{136}$ with the semiconductor-metallic transition happening for occupations x around 8 to 10. No variation in sodium content was observed for type I when submitted to similar processes. Thus type II silicon clathrate films with controllable resistivities along four orders of magnitude have been achieved. Our findings were supported by theoretical studies of the electronic structure of the silicon clathrates using DFT calculations that allow to show that the observed evolution is due to the contribution of the electrons donated by the sodium to the silicon framework.

As far as optoelectronic properties are concerned, response of the silicon clathrates films to light has been investigated using both solar simulator and surface photovoltage. We have shown that the type II silicon clathrates are photoactive, but their photovoltaic responses are still very low. Implantation of the silicon clathrate using arsenic ion and subsequent thermal annealing at low temperature resulted in an improvement of the photovoltaic properties but still very limited as the minority carrier transport is dominated by defects within the silicon clathrates.

The preliminary study demonstrates that implantation of silicon clathrate thin films can be performed. This motivates the implantation of the entire layer to better understand how it affects the structure and its properties. This step is a keystone toward the investigation of silicon clathrates for photovoltaics use. On the other hand, sodium can be inserted and removed reversibly from the clathrate structures with hardly any lattice expansion, indicating their potential as batteries.

Furthermore, it seems critical to focus on simultaneously taking advantage of the controllable electrical properties of group IV clathrates which can be modified by changing the guest occupancy as well as using alloyed frameworks such as silicon-germanium framework type II clathrates to modify their gap varying from 0.8 to 1.7 eV depending on the composition. Films with such versatile properties could be tuned to exhibit the optimized properties needed for given photovoltaic use.

Annexes

A.1 Résumé de thèse en français

Grâce à la compréhension de l'effet photovoltaïque et la recherche vers des matériaux toujours plus performant, un véritable marché du solaire s'est développé de manière exponentielle durant ces dernières décennies. Ce marché est dominé par la présence du silicium diamant, majoritairement monocristallin, du fait de son abondance, de son prix en constante chute et de la durabilité du matériau. Pourtant le silicium est loin d'être le candidat optimal : d'une part ses propriétés sont limitées par son gap indirect de 1,12 eV tandis que d'autre part sa purification depuis la silice et sa mise en forme sous lingot mono ou polycristallin sont des procédés très couteux et dont l'impact écologique est considérable. Cette domination du silicium s'explique par un compromis entre les avantages et défauts du matériau et par les avancées spectaculaires permises par la quantité de recherche dont il a été et est l'objet permettant aujourd'hui l'obtention de cellules solaires de silicium monocristallin présentant des rendements allant jusqu'à 26,7%[1], s'approchant de sa valeur maximale d'efficacité de 29%.

Ainsi pour conserver la croissance actuelle du photovoltaïque, il devient urgent de s'orienter vers des concepts ou des matériaux nouveaux permettant des rendements plus élevés. Dans cette optique, et en tenant compte de la quantité de recherches effectuées sur le silicium, la recherche de formes allotropiques présentant un gap direct s'est accélérée.

En effet, de manière similaire aux autres éléments du groupe 14, le silicium présente un profil énergétique sinué de minimum locaux résultant en un riche polymorphisme comme il l'est détaillé sur la **Figure A.1.1**[2]. Il est donc logique de s'intéresser aux possibles allotropes du silicium métastable à conditions ambiantes et présentant un gap direct. Une première exploration de ces phases est faite en soumettant le silicium à des pressions croissantes jusqu'à 248 GPa. Six phases métalliques peuvent être ainsi directement identifiées dont la décompression linéaire mène à quatre phases additionnelles à gap direct ou étroit. Quatre autres phases à gap indirect ou étroit ont également été obtenues par une relaxation brusque de la pression ou en utilisant des lasers nano pulsés sur le silicium diamant. Malgré l'identification de plusieurs phases à bande directe, il n'est pour le moment pas possible de les obtenir en quantités
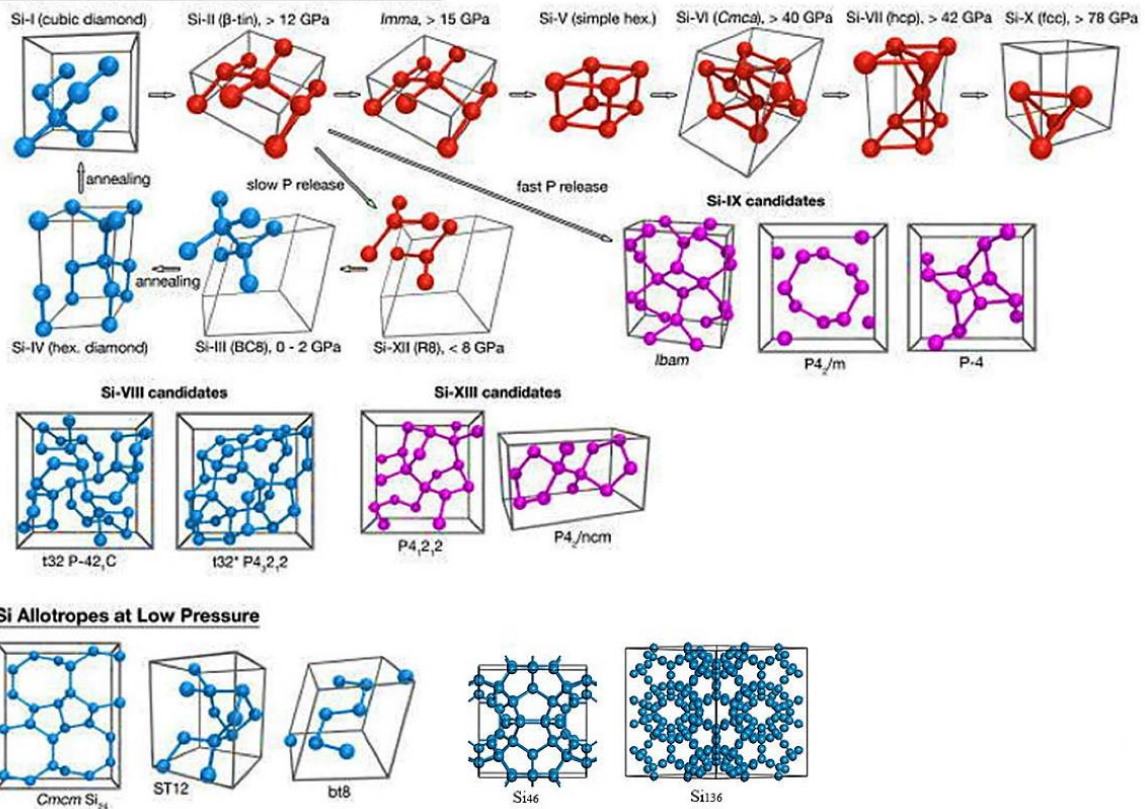
Figure A.1.1 Structures des allotropes connus du silicium. Les structure en bleu sont métastables à conditions ambiantes, les rouges sont stables uniquement à hautes pression tandis que celles en violet sont encore peu connues[2].

suffisantes pour des applications réelles du fait des faibles volumes produits par les systèmes de pressions utilisés (DAC).

Logiquement, une autre partie de l'allotropie à explorer est celle à faible densité. Concernant le silicium, ces phases à faibles densités sont généralement le squelette formé de silicium de composées hôte-invités. Dans ces composés, le silicium forme typiquement des canaux ou des cages dans lesquels des atomes d'espèces chimiques différentes viennent s'insérer en stabilisant la structure. Parmi ces composés à basse densité, les formes dites clathrates du silicium apparaissent intéressantes du fait de leurs bande interdites directes entre 1 et 2 eV une fois les atomes invités extraits.

Le terme « clathrate » a été introduit par Powell[3] pour définir des structures de type hôte-invité particulières du fait d'un réseau tridimensionnel d'une espèce hôte formant des cages qui sont des lacunes idéales afin d'accueillir des atomes ou molécules d'espèces invités. Ces structures sont naturellement présentes dans la nature pour les composés organiques sous la forme molécules de gaz piégées dans des cages formées de molécules d'eau tel les hydrates de méthane.
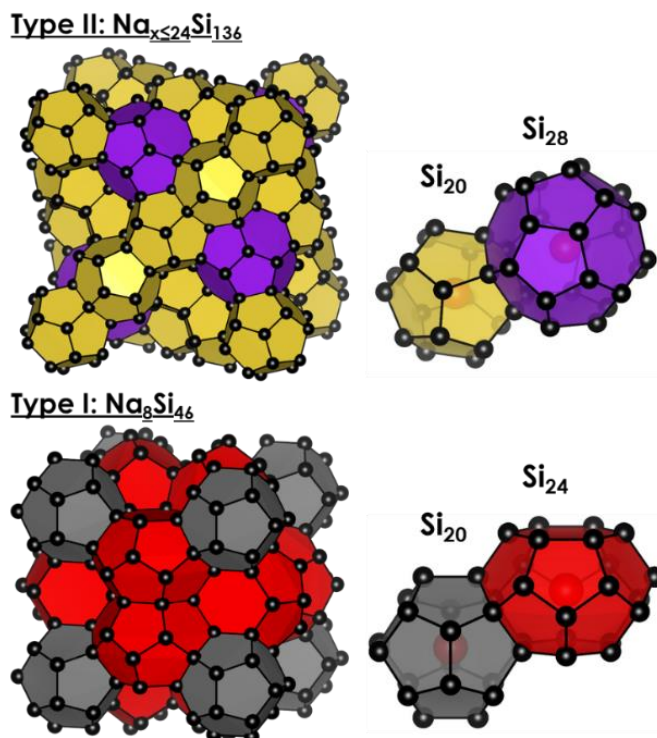
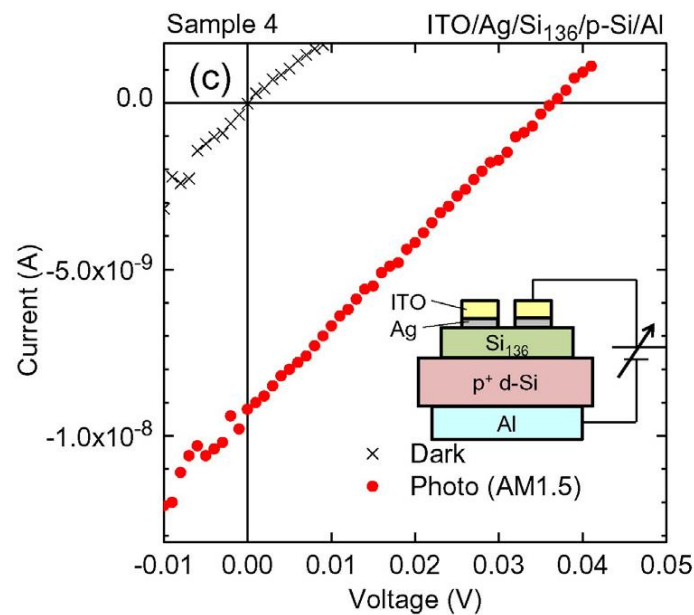**Figure A.1.2** Structure des Clathrates de Silicium de type I et II

Il faudra attendre 1965 pour que les premiers clathrates inorganiques soient synthétisés : ce seront les clathrates de silicium sous leur forme de type I et de type II, voir **Figure A.1.2** suite aux travaux de Hagenmuller et ses associés[4]. Ils suscitent rapidement l'attention du fait de leurs propriétés :

- Les types I, de formule Na_8Si_{46}, pour leur possibles applications en thermoélectricité du fait de l'observation de comportement « phonon-glass electron-crystal » du fait des vibrations ou « rattling » de leurs atomes invités.
- Les types II, de formule $Na_{x\leq24}Si_{136}$, d'une part pour leur analogie avec les plus connus fullerènes, mais aussi par leur capacité unique à pouvoir céder ou recevoir des atomes invités, ce qui pourrait théoriquement permettre d'obtenir de tels clathrates totalement dépourvus d'atomes invités, c'est-à-dire un nouvel allotrope du silicium, qui présente alors des propriétés semi-conductrices.

Du fait de ces caractéristique intéressantes, ces structures ont rapidement été identifiés comme matériaux prometteurs pour des applications optoélectroniques, électrochimiques et de stockage de l'hydrogène.

Les propriétés des clathrates de silicium, simulées puis confirmées par les données recueillies à partir des premiers échantillons synthétisés sous forme de poudre, font de cette phase exotique du Silicium une possible alternative au conventionnel Silicium diamant. En effet, le clathrate de Silicium de type II présente un gap quasi-direct

d'environ 1,8-1,9 eV une fois les atomes invités de sodium extirpés du squelette de Silicium, contrairement au gap indirect du Silicium conventionnel. Motivés par les perspectives qu'offrent les clathrates, deux laboratoires se sont lancés dans la synthèse de clathrates de Silicium sous forme de film dans les années 2010 dans l'objectif de pouvoir intégrer ces clathrates dans des dispositifs optoélectroniques ou/et photovoltaïques fonctionnels : aux Etats-Unis le National Renewable Energy Laboratory[5] en collaboration avec la Colorado School of Mines et au Japon les laboratoires de l'Université de Gifu[6] qui propose la première mesure I-Vdes clathrates de silicium visible sur la **Figure A.1.3**[7].


Figure A.1.3 I-V de la première cellule solaire à base de clathrates de silicium de type-II[7].

D'autre part, du fait de leur nature de composés d'inclusion dont le réseau hôte formé de cages, l'utilisation des clathrates de Silicium dans des applications de stockage d'hydrogène ou en tant qu'anode pour les batteries lithium et sodium est aussi proposée. En effet les cages polyédriques sont propices à des mécanismes d'accueil d'espèces chimiques au sein de la structure suivis de leur évacuation et ce sans conséquente expansion ou contraction de la structure.

L'obtention de films de clathrates de silicium est primordiale afin de permettre leur utilisation dans des dispositifs photovoltaïques mais la synthèse de ces films par de nombreux laboratoires reste limité par la nécessité d'une boite à gant dédiée. Il est donc intéressant de proposer la croissance de films de clathrates en utilisant une

enceinte de recuit sans boîte à gant contrairement. Ceci consiste donc à la détermination des paramètres optimaux (température, durée, pression d'argon, quantité de sodium, géométrie de la tranche de sodium) permettant l'obtention et la caractérisation de films de clathrates de siliciums, sujets centraux du **Chapitre 2**.
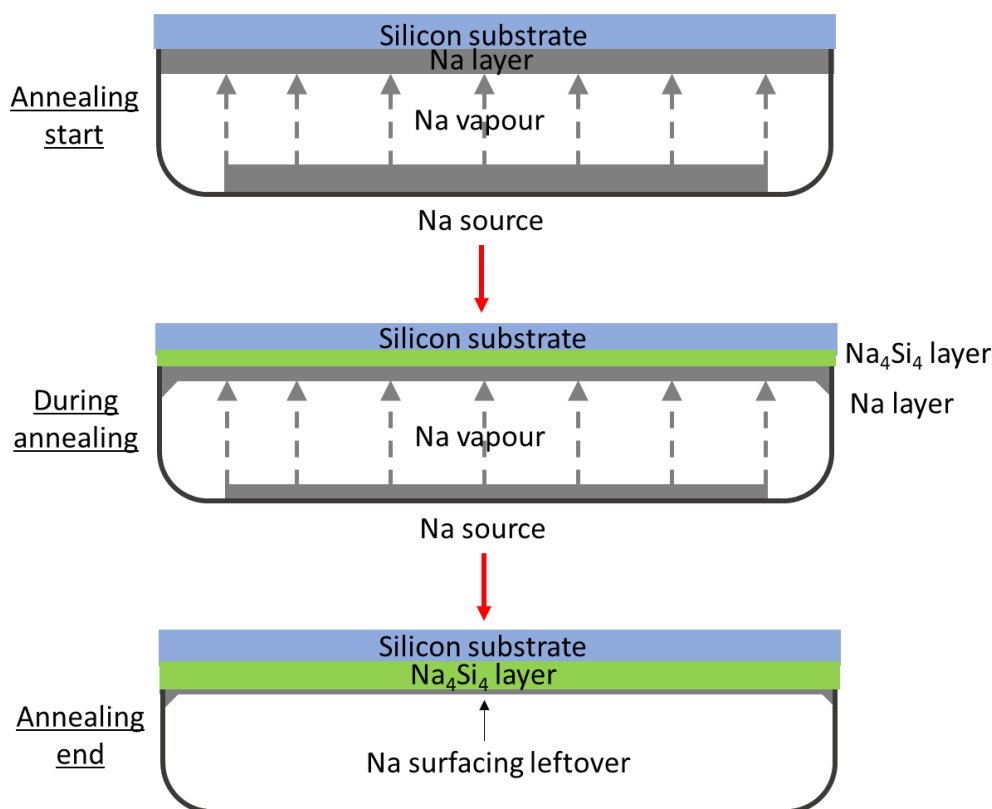
Figure A.1.4 Représentation schématique du mécanisme de formation du

précurseur Na4Si4 par recuit.

La synthèse des films de clathrates de silicium se fait donc de manière similaire à ce qui a été présenté dans la littérature : du sodium est placé proche du substrat de Silicium, qui joue aussi le rôle de réactif, dans une enceinte fermée sous argon. Le tout est ensuite chauffé entre 550 et 650°C afin de faire réagir les vapeurs de Sodium avec le silicium et d'obtenir le réactif intermédiaire qu'est la phase de Zintl de formule Na4Si4, voir **Figure A.1.4**.

Ce précurseur est à son tour placé dans un four sous vide dynamique afin d'extraire le sodium de la structure Na4Si4, induisant de très fortes contraintes locales qui seront compensées par une réorganisation de la structure permettant la création de clathrates
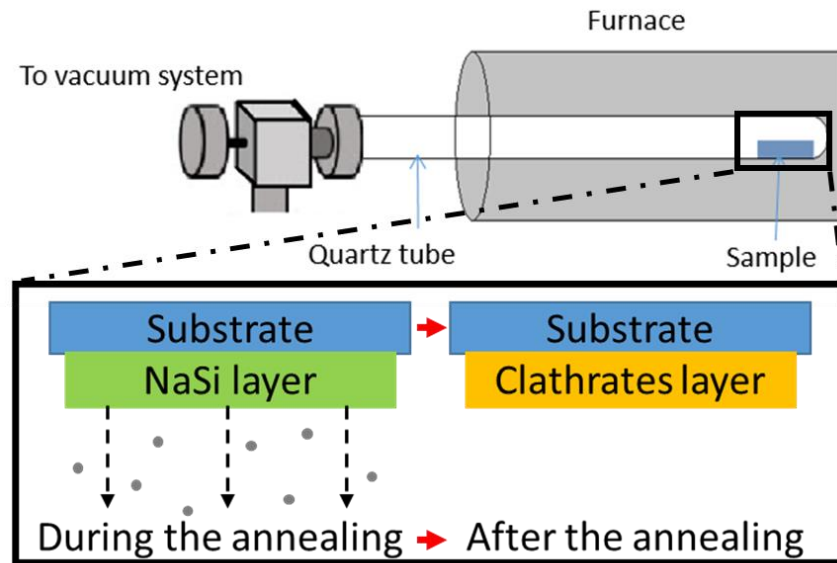
Figure A.1.5 Représentation schématique du mécanisme suspecté de la

décomposition thermique du Na_4Si_4 en clathrates de silicium.

d'un ou plusieurs types selon les conditions et dont le mécanisme est représenté sur la **Figure A.1.5**.

Suite à ces essais et la caractérisation des échantillons par diffraction des rayons X et par spectroscopie Raman, nous démontrons qu'il est possible d'obtenir des films de clathrates de type II sélectivement utilisant la configuration sans boîte à gants, or ce type de clathrates promet de plus grandes perspectives dans l'optoélectronique et la photovoltaïque de par son bandgap quasi direct de 1,9 eV et notamment car les atomes invités de ce type de clathrates peuvent être extraits des cages de silicium. Une exploration plus large de la température du recuit a permis d'obtenir des films purs de type I ou II ou une phase mixte. Les diffractogrammes de chacune des phases sont
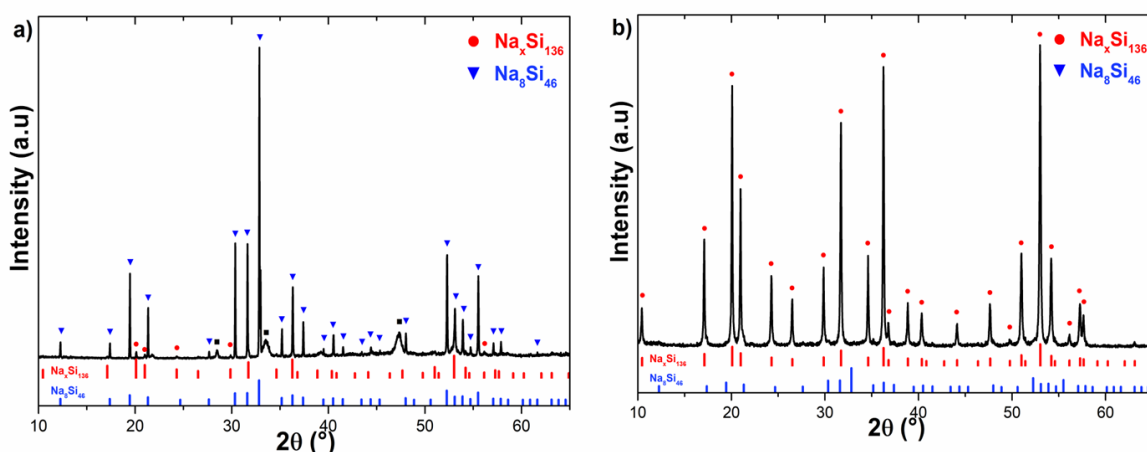

Figure A.1.6 Diffractogrammes des clathrates de silicium de a) Type-I b) Type-II.

disponibles en **Figure A.1.6** Il a également été nécessaire de faire varier certains paramètres afin d'obtenir des films « moins épais » et de meilleure intégrité structurelle.

La détermination du type de clathrates de silicium obtenu et de sa pureté ainsi que l'occupation des cages est rendue possible par Diffraction des Rayons X (Par analyse de Le Bail et Rietveld) et par la Spectroscopie Raman.
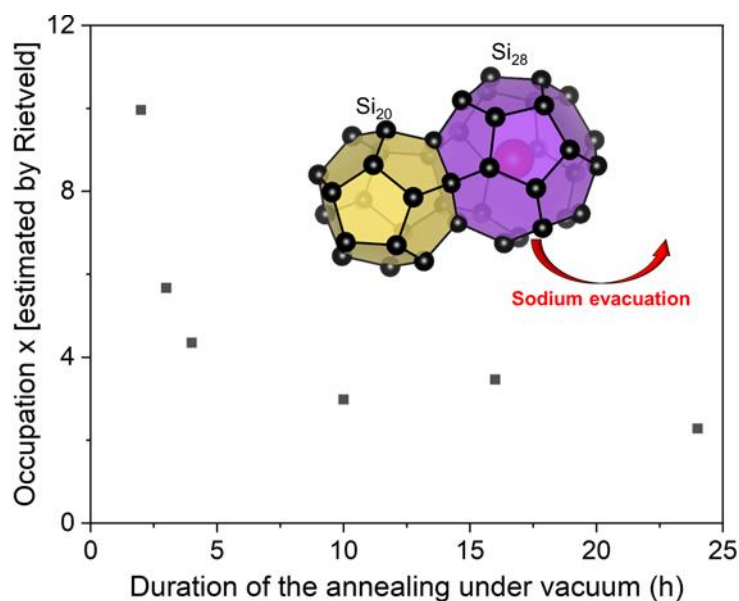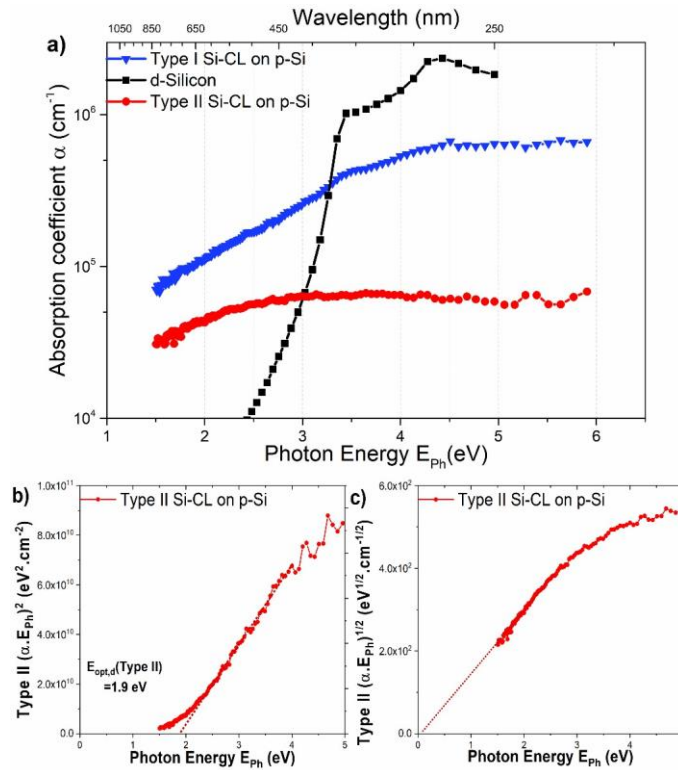

Figure A.1.7 Occupation des films de clathrates de type-II selon le temps de

En appliquant différentes durées de recuit sous vide dynamique des films de clathrate de Silicium de type II, Na_xSi_{136}, avec différentes concentrations de sodium sont obtenus voir **Figure A.1.7**. Ainsi, des occupations entre x = 9 à 2 sont accessibles par cette méthode, résultant en des films semiconducteurs dont la résistivité augmente quand cette occupation est réduite. Par photoluminescence et par la méthode du Tauc plot sur des mesures ellipsométrique, les films de type I sont identifiés comme métallique tandis que les films de type II sont semiconducteur à bande directe de 1,9 eV, voir **Figure A.1.8**.

En complément, des mesures d'effet Hall sur les films de clathrates de Silicium de type-II démontrent que les porteurs de charges sont de type n, confirmé par des mesures de transient Surface Photovoltage (tSPV) et par la méthode de la pointe chaude. Ces porteurs de type n sont cohérents avec la nature de donneurs d'électrons des atomes invités de sodium contenus au réseau hôte de silicium.

Figure A.1.8 a) Valeurs des coefficients d'absorption des différents films de clathrates comparé au silicium diamant. b) Tauc plot pour les films de type II dans le cadre d'un gap direct à gauche et d'un gap indirect à droite.

L'effet Hall a aussi permis de déterminer les propriétés électriques des films, et notamment de confirmer le caractère plus métallique du type-I comparativement aux films de type-II pour les occupations obtenues par décomposition thermique. Les films de Na_8Si_{46} ont une résistivité d'environ $4x10^{-2}$ $\Omega \cdot cm$ avec une mobilité de 40 $cm^2/(V \cdot s)$ pour une densité de porteurs de charge de $-1,5x10^{19}$ cm^{-3}. Concernant les films de type II, la résistivité s'étends de 0,1 $\Omega \cdot cm$ pour les films de Na_9Si_{136} à 10 $\Omega \cdot cm$ pour Na_2Si_{136} pour des mobilités aux alentours de la dizaine de $cm^2/(V.s)$ pour des densités de porteurs de charge entre $5x10^{18}$ à $1x10^{17}$ respectivement.

La surface rugueuse de nos échantillons a été déterminée par microscopie électronique à balayage MEB, technique qui a également permis de déterminer que la concentration de sodium dans les cages était plus élevé à la surface du film que dans le bulk par spectroscopie de rayons X à dispersion d'énergie EDS à différentes épaisseurs. Ce phénomène s'explique par le mécanisme de sublimation du sodium lors de la phase de décomposition thermique.

Du fait des importantes épaisseurs (plusieurs dizaines de micromètres) et rugosités des films obtenus, conjuguées à la faible densité et cohérence du film suite aux

observations en microscopie électronique à balayage, il a été entrepris d'effectuer des recuits sous pression des films obtenus grâce à Céline Chevalier de l'INL-Lyon.

Dans un premier temps, cette étape a permis la compression des films de clathrates de type-I et donc d'obtenir des couches moins épaisse et plus compacte mais a aussi permis d'observer la texturation de ces films qui étaient au départ polycristallin.

Ultérieurement, il a été possible d'effectuer ce recuit sous pression sur des films de type-II, toujours dans l'objectif d'obtenir des films plus compact et moins rugueux [8].

Suite à ces recuits, il a été observé que les deux types de clathrate de silicium n'ont pas le même comportement vis-à-vis de ce traitement : les films de type-II ne présentent pas de texturation et il n'y a pas de réduction significative de l'épaisseur, ce qui peut être expliqué par une meilleure cristallinité des films de type-II obtenus comparativement aux échantillons de type-I. Cependant, la surface des films de type-II montre bien une rugosité réduite (de manière similaire au type-I visible en **Figure A.1.10**) suite au traitement et, de plus, la phase minoritaire de type-I a été réduite grâce à cette étape. Cette réduction de la fraction de type-I est plus marquée quand la température du recuit sous pression augmente.
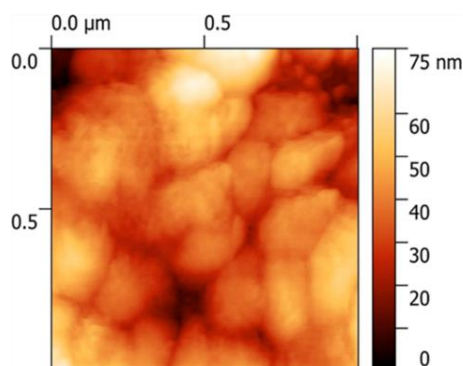
**Figure A.4.10** Cliché AFM d'un film de Clathrate de Silicium après recuit sous pression

Le recuit sous pression permet d'obtenir des films dont les surfaces seraient utilisables pour des applications optoélectroniques malgré l'état de surface (fractures, haute rugosité) des couches obtenues à l'issue de la décomposition thermique.

Enfin, bien que des paramètres de la réaction comme le temps du recuit ou la masse de sodium furent modifiés dans l'espoir d'obtenir des films d'épaisseurs inférieures aumicron, ces essais se sont révélés infructueux.

Une tentative de réduire la quantité de sodium réagissant avec le silicium tout en conservant une pression de vapeur de sodium suffisante à également testée par le

biais de barrières de diffusion sous forme de couche de Si_3N_4. Si des traces de clathrates de Silicium ont pu être détectées par Raman, la formation d'une couche continue n'a pas été obtenue.

Devant ces difficultés, l'utilisation de la décomposition thermique en utilisant des couches de silicium (100) de 400 nm déposés sur des substrats de saphir s'est révélée plus porteuse. Après un changement de paramètre de réaction consistant en une masse de sodium réduite et un temps du premier recuit réduit à environ une heure et un recuit sous vide plus long afin d'éliminer toutes traces de sodium et sa réaction avec
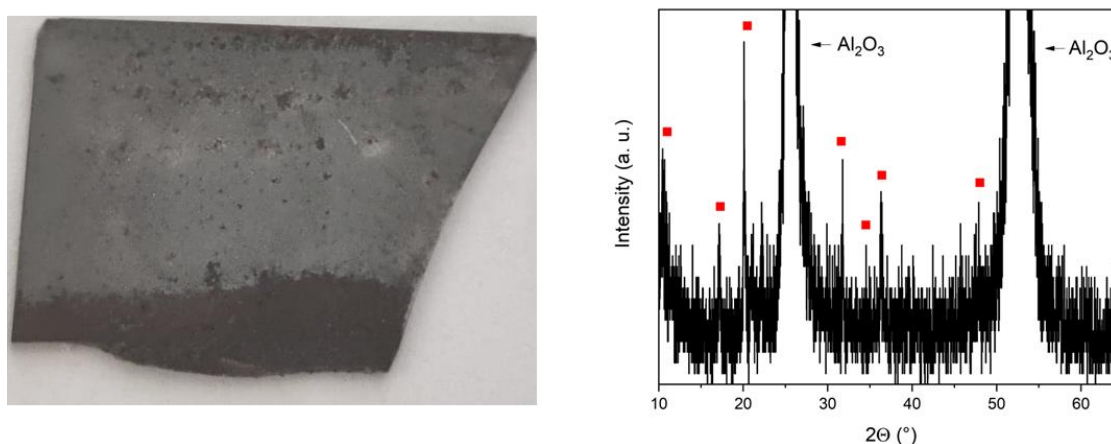
Figure A.1.11 Photographie et diffractogramme du film de clathrates de silicium de type-II obtenus grâce à des substrats SOS.

le film.

Par DRX et Raman les films obtenus sont pour le moment uniquement de type-II, voir **Figure A.1.11** mais il devrait être possible d'obtenir des films de type-I en variant la température du recuit sous vide dynamique. Cependant comme il l'a déjà été mentionné dans la littérature[9], ces films fins de clathrates de silicium présentent une fraction importante d'impureté de surface d'un matériau de silicium désordonné. De plus contrairement aux couches plus épaisses, le transfert d'un four à l'autre doit être d'autant plus rapide sous la peine de permettre la réaction du Na_4Si_4 avec l'air ou avec le sodium restant en surface résultant en des films criblés de trous du fait de sa dégradation.

Une autre manière d'obtenir des films fins serait de graver les couches déjà obtenues sur substrat de silicium.

Initialement, la gravure par voie humide en utilisant un mélange acide de HNO₃/HF avait été utilisée, montrant des vitesses de gravure raisonnables et sans dégrader la phase de type-II. Cependant du fait de l'état de surface fracturé des films, cette gravure n'était que peu homogène et pouvait même causer la délamination complète de la couche si le film était assez perméable pour laisser pénétrer l'acide jusqu'à l'interface clathrates/substrat.

Par la suite, la gravure sèche des clathrates de silicium par Reactive Ion Etching (RIE). Cette gravure est pour le moment estimée à 4 µm.min⁻¹ sur les films de type-II et les RX montrent que la phase est conservée après ce traitement.
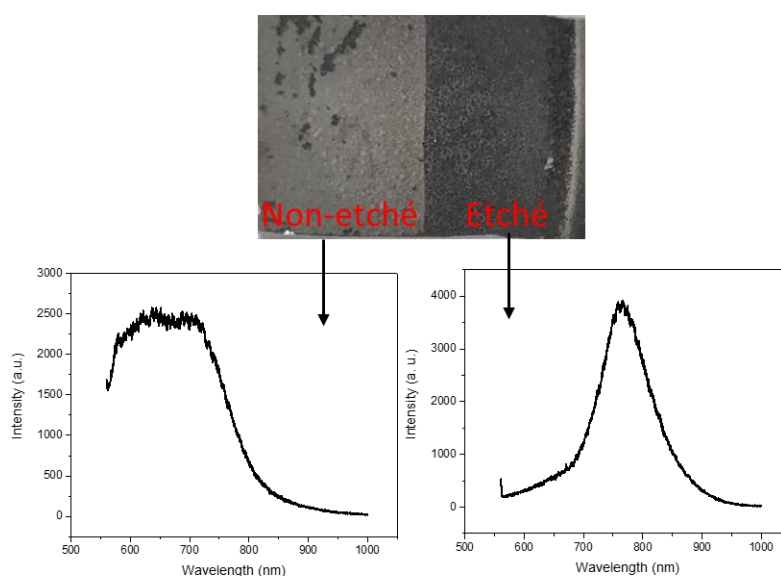

Figure A.1.12 Photographie de l'état du film avant et après gravure par RIE et spectres PL relatifs à chacune de ces zones.

De plus, le matériau révélé par cette gravure par RIE est bien plus pur, comme il l'a été observé par Raman mais également simplement visible par le changement d'apparence, voir **Figure A.1.12**. Cette phase plus pure est aussi identifiable par photoluminescence, ou le pic du matériau gravé est bien plus fin et uniquement dû au clathrates de silicium de type-II.

Une des particularités des clathrates de silicium est la mobilité des atomes invités au sein de ses cages ce qui permet leur extraction du squelette de silicium, changeant la composition de la phase et donc ses propriétés et fait l'objet de la première partie du **Chapitre 3.** L'un des procédés permettant de réduire l'occupation des cages est un cycle de traitements thermiques sous atmosphère de diiode afin d'extraire le sodium

des cages selon la réaction chimique suivante[10] : $Na + \frac{1}{2}I_2 \rightarrow NaI$ dont le fonctionnement a été confirmé par EDX lors des observations MEB.
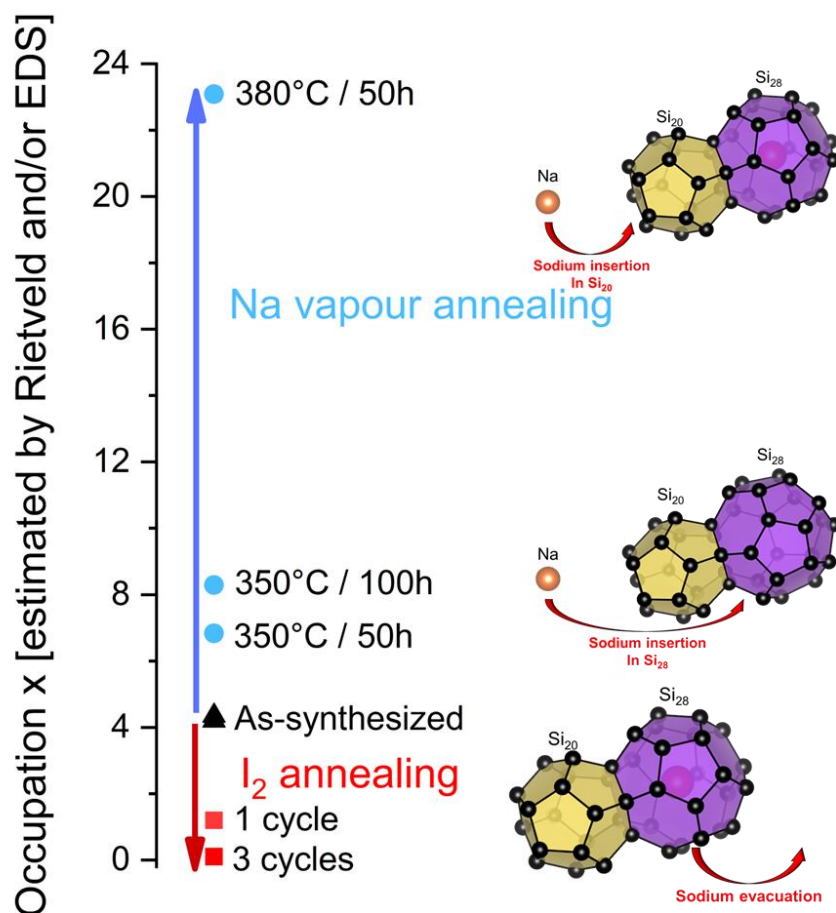
Figure A.1.13 Effet des traitements à l'iode et au sodium sur l'occupation des clathrates de Silicium de type-II

Ce traitement est opéré dans un tube à essai rempli d'iode solide et de l'échantillon qui est mis sous un vide primaire, scellé puis chauffé à 300°C durant 10h. La réaction étant limitée par la quantité d'iode, il est nécessaire d'effectuer plusieurs cycles afin de réduire significativement la quantité d'atomes invités, voir **Figure A.1.13**. Bien qu'il soit aussi théoriquement possible d'obtenir des faibles concentrations d'atomes invités en prolongeant l'étape de décomposition thermique sous vide dynamique, les durées de recuits serait alors extrêmement long (plus de 100h pour atteindre x = 0,5). Cette série de cycles sous atmosphère d'iode représente donc un procédé plus efficient.

D'autre part, il est aussi possible d'insérer des atomes de sodium dans les cages des films de type II. Pour cela, il suffit simplement de recuire les films sous vapeur de sodium à des températures entre 350°C et 380°C pour des durées variables selon

l'occupation désirée. Des analyses Rietveld sur les diffractogrammes RX montrent que les huit larges cages de la structure sont systématiquement remplies avec les seize autres plus étroites. Il est important de préciser que ces modifications du contenu en sodium n'ont qu'un très léger impact sur le paramètre de maille (de 14.6 Å à 14.8 Å).

Les concentrations en sodium obtenues suite à ces traitements ont également été estimées grâce à des mesures EDX et reliées aux mesures Hall ont permis de mettre en évidence la relation entre une occupation décroissante et une plus grande résistivité électrique, disponible dans le **Tableau A.1.1**, qui est dû au fait du rôle de donneur d'électrons des atomes de sodium au sein des cages de la structure clathrates.

Tableau A.1.1 Propriétés des films mesurées par Effet Hall pour différents traitements.

Type de Clathrate	Traitement	Formule	Densité de porteurs de charge (cm^{-3})	Résistivité (Ω.cm)	Mobilité (cm^2/(V.s))
Type-I	Sans traitement	Na_8Si_{46}	-1.5×10^{19}	4.3×10^{-2}	43
Type-II	3 cycles de recuit sous I$_2$	$Na_{\sim 0.1}Si_{136}$	-3.6×10^{16}	110	15
	1 cycle de recuit sous I$_2$	Na_1Si_{136}	-9.2×10^{16}	40.7	21
	Sans traitement	$Na_{4.2}Si_{136}$	-2.1×10^{17}	4.2	7.1
		$Na_{4.35}Si_{136}$	-3.0×10^{17}	2.2	8.0
	Vapeur de Na à 350°C/50h	$Na_{6.9}Si_{136}$	-9.2×10^{17}	6.3×10^{-1}	13.3
	Vapeur de Na à 350°C/100h	Na_8Si_{136}	-6.5×10^{18}	3.3×10^{-1}	6.1
	Vapeur de Na à 380°C/50h	$Na_{23}Si_{136}$	-5.4×10^{20}	1.1×10^{-2}	4.1

L'étude de l'évolution de la résistivité selon la température des films a également été permis grâce aux mesures de Daniele Preziosi à l'IPCMS via un Physical Properties Measurement System (PPMS) DynaCool. Le caractère métallique des clathrates de

silicium de type-I a été confirmé tandis que la dépendance à l'occupation en sodium de la nature du type II a pu être observée.

Pour les concentrations en sodium les plus basses atteintes dans ces travaux, le film se comporte comme un semiconducteur, mais une fois la majorité des cages remplies par des atomes de sodium, le film devient alors métallique, voir **Figure A.1.14**. Cette transition est supposément due par les états de plus en plus isolés des clusters de sodium qui limitent donc le saut des électrons comme il l'a été révélé par des études d'Electron Spin Resonance à basse température[11].
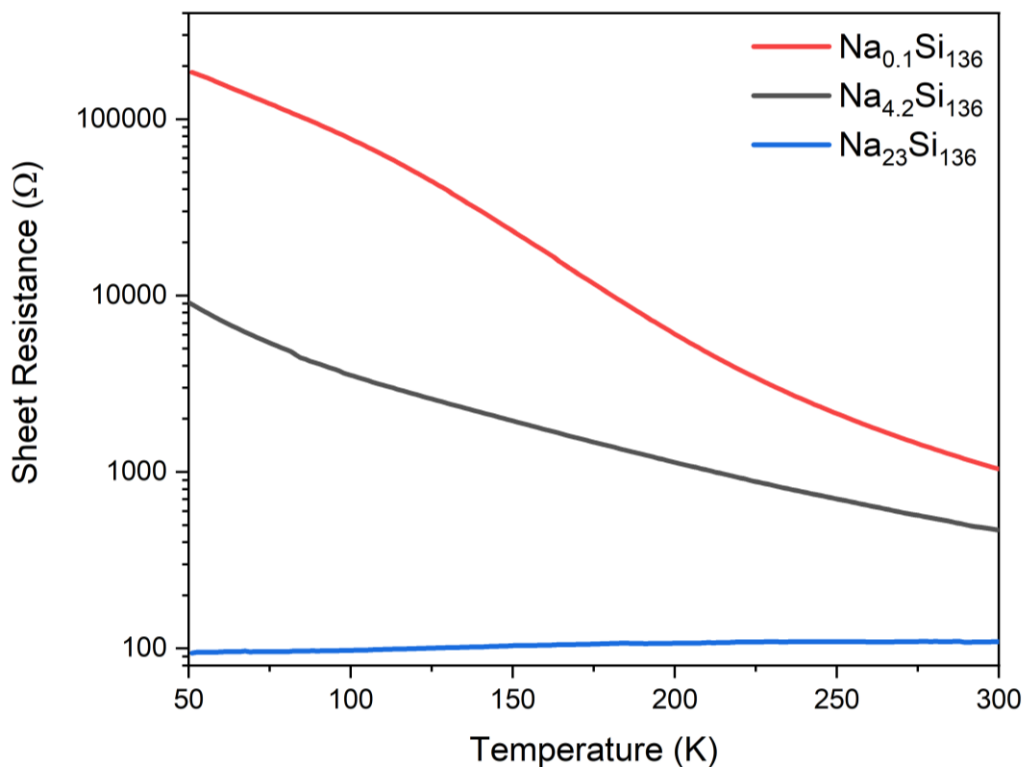
Figure A.1.14 Mesure de Resistance versus température pour des films de type-II avec différentes occupations en sodium

Afin de mieux comprendre l'évolution des propriétés optoélectroniques selon l'occupation du matériau, des calculs de Total Density of States (TDoS) et de Band Structures (BS) ont été réalisés par Daniel Stoeffler sur les deux types de clathrates pour différents niveaux de sodium. Les deux structures présentent des TDoS quasi similaires du fait de leur proximité structurale. Dans les deux cas, la structure libre d'invités à un caractère semiconducteur dont le gap est direct selon les BS calculés. Au fur et à mesure de l'ajout d'atome de sodium, la bande de conduction s'élargit du fait de l'hybridation des états du sodium avec les états des cages de silicium. Du fait de cette bande de conduction de plus en plus large, le « gap » se ferme donc de plus

en plus avec l'ajout d'atome de sodium laissant supposer un matériau de plus en plus métallique.

La variation de la concentration en sodium du clathrates de Silicium de type-II permet donc de faire varier la résistivité des films sur quatre ordres de grandeur. Une transition métal-semiconducteur est observée une fois les cages les plus larges remplies, se faisant donc pour des occupations aux alentours de x = 8 à 10. Les traitements mentionnés ont été tentés sur les films de type-I mais sont restés sans effet sur la composition en sodium.

Une autre voie d'amélioration des propriétés de films de clathrates de silicium pourrait résider dans le dopage en surface : en effet un premier essai avait permis l'amélioration du V_{OC} mais aussi du J_{SC}[8]. La seconde partie du **Chapitre 3** porte donc sur l'étude des propriétés photovoltaïques des clathrates de type II avant et après dopage. Dans un premier temps il est nécessaire de s'assurer que les porteurs de charges photo générés prennent leur origine dans la couche de clathrates de silicium de type-II et non dans le substrat de silicium sur lequel il repose. Pour cela la réponse photovoltaïque des films a été étudié conjointement sous Simulateur Solaire mais également en utilisant la phototension de surface ou surface photovoltage (SPV). Cette réponse est propre au type-II qui présente une valeur maximale de 120 mV tandis que celle du type-I rends en fait compte du substrat de Si (100) dopé p sur laquelle la couche s'est formée. En équipant le système d'un monochromateur d'un réseau de 600 g/mm^{-1}, la réponse à la lumière des matériaux selon l'énergie du photon est mesurée. Ainsi, les films de clathrates de silicium de type II présentent une réponse
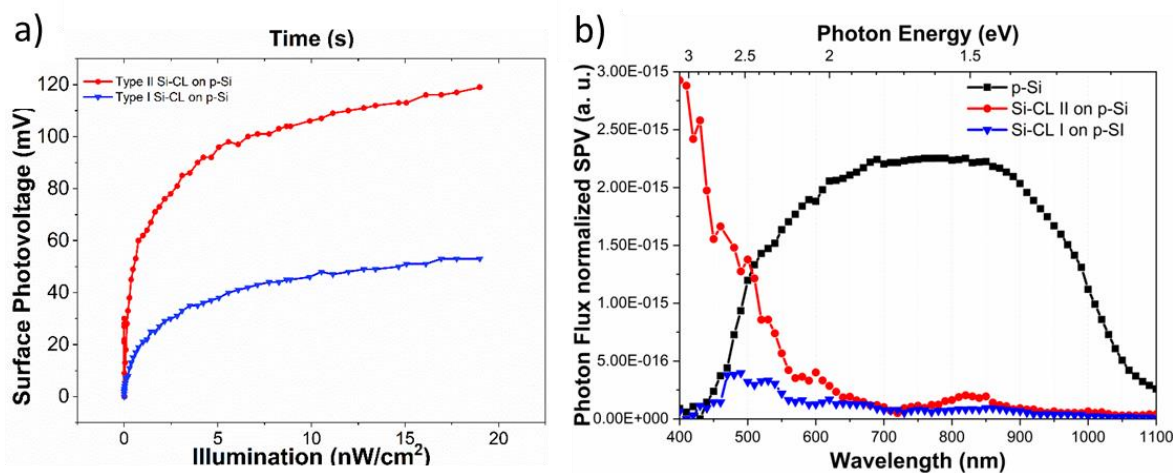
Figure A.1.15 a) Evolution de la phototension de surface des films obtenus sur substrat de silicium dopé p b) Spectroscopie SPV de ces films comparés au substrat de silicium dopé p.

plus élevée que le silicium de type p entre 400 et 500 nm et le band gap direct d'environ 1.9 eV est confirmé comme il l'est montré sur la **Figure A.1.15**.

Suite à ces résultats, il a été entrepris d'étudier différents paramètres d'implantation ionique d'Arsenic sur les propriétés de nos films. Préalablement à ces implantations, une étude de la stabilité de nos films suites à différentes températures de recuit sous atmosphère d'azote suite à la sensibilité de la phase clathrate de silicium à la température (dégradation en silicium diamant dès 650°C). Il en résulte que pour un recuit sous atmosphère d'azote, les films ne sont stables que pour des températures inférieures à 500°C, au-delà : les films sont dégradés, en NaSi$_6$ puis en silicium diamant à plus haute température, comme il l'a été déterminé suite à l'analyse des diffractogramme RX. A la fin du procédé d'implantation suivi d'un RTA à 450°C, il a été confirmé par DRX que la phase de clathrates n'a pas été dégradé. Par RBS, il est apparu que les profondeurs implantées sont légèrement supérieures à celles obtenus pour du silicium diamant mais restent extrêmement faible comparées aux dimensions micrométriques des films de clathrates de silicium.
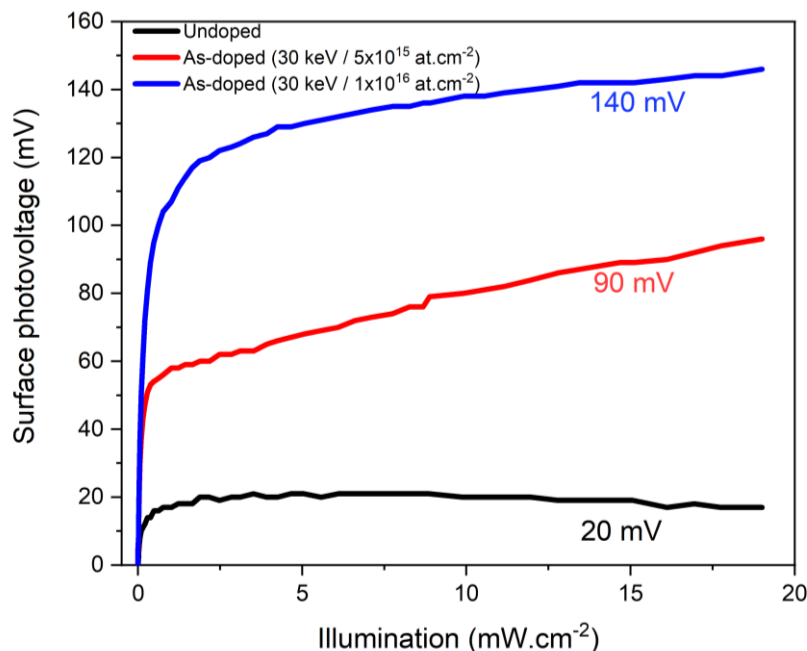
Figure A.1.16 Mesures SPV sur les films de clathrates non-dopé et pour des dopages à différentes doses d'arsenic.

Suites à des mesures de phototension de surface (SPV) par Kelvin Probe mais aussi par des mesures sous Simulateur Solaire, il a été montré que plus la dose est conséquente, plus la tension à circuit ouvert V$_{OC}$ et le SPV est important et permet

donc une amélioration des propriétés photoélectriques du clathrate de Silicium de type-II comme il l'est montré sur la **Figure A.1.16**.

En conclusion, les conditions pour obtenir sélectivement des clathrates de Type I et de Type II sont dorénavant connues et les films ont été caractérisés. Les différentes techniques utilisées pour améliorer les propriétés des films ont montré qu'il était possible d'obtenir des surfaces moins rugueuses et d'améliorer la réponse photovoltaïque des films, qui reste cependant limitée du fait de la mauvaise adhérence des films de Type II sur le substrat de Silicium.

Les propriétés de transport non seulement en température mais aussi en fonction de l'occupation des films de Clathrates ont fait l'objet de mesures d'effet Hall et de mesures électriques en température et comparées à des simulations DFT effectuées sur les cages de clathrates de Silicium et leur comportement selon différentes occupations.

La synthèse de films fins par l'utilisation de wafer SOS est prometteuse bien que les films de 400 nm obtenus soient encore opaques du fait de la fraction élevée de matériau désordonné[9] . La gravure sèche par RIE est aussi un palier important qui une fois contrôlée permettra d'obtenir des couches minces sur silicium qui pourront ensuite être dopées par implantation ionique sur la totalité de leurs épaisseurs.

Dans le domaine des clathrates de silicium et des clathrates inorganiques, il apparaît également intéressant d'étudier la synthèse de films de clathrates dont le réseau hôte est un alliage de silicium et germanium résultant en des films semiconducteurs à bandes directes modulables entre 0,8 et 1,9 eV.

Références du résumé en français

(1) Yoshikawa, K.; Kawasaki, H.; Yoshida, W.; Irie, T.; Konishi, K.; Nakano, K.; Uto, T.; Adachi, D.; Kanematsu, M.; Uzu, H.; Yamamoto, K. Silicon Heterojunction Solar Cell with Interdigitated Back Contacts for a Photoconversion Efficiency over 26%. *Nat Energy* **2017**, *2* (5), 1–8. https://doi.org/10.1038/nenergy.2017.32.

(2) Fan, L.; Yang, D.; Li, D. A Review on Metastable Silicon Allotropes. *Materials* **2021**, *14* (14), 3964. https://doi.org/10.3390/ma14143964.

(3) Powell, H. M. 15. The Structure of Molecular Compounds. Part IV. Clathrate Compounds. *J. Chem. Soc.* **1948**, 61. https://doi.org/10.1039/jr9480000061.

(4) Kasper, J. S.; Hagenmuller, P.; Pouchard, M.; Cros, C. Clathrate Structure of Silicon Na $_8$ Si $_{46}$ and Na $_x$ Si $_{136}$ (x < 11). *Science* **1965**, *150* (3704), 1713–1714. https://doi.org/10.1126/science.150.3704.1713.

(5) Martinez, A.; Krishna, L.; Baranowski, L.; Lusk, M.; Toberer, E.; Tamboli, A. Synthesis of Group IV Clathrates for Photovoltaics. *Photovoltaics, IEEE Journal of* **2013**, *3*, 1305–1310. https://doi.org/10.1109/JPHOTOV.2013.2276478.

(6) Ohashi, F.; Iwai, Y.; Noguchi, A.; Sugiyama, T.; Hattori, M.; Ogura, T.; Himeno, R.; Kume, T.; Ban, T.; Nonomura, S. Thin-Film Formation of Si Clathrates on Si Wafers. *Journal of Physics and Chemistry of Solids* **2014**, *75* (4), 518–522. https://doi.org/10.1016/j.jpcs.2013.12.009.

(7) Kume, T.; Ohashi, F.; Sakai, K.; Fukuyama, A.; Imai, M.; Udono, H.; Ban, T.; Habuchi, H.; Suzuki, H.; Ikari, T.; Sasaki, S.; Nonomura, S. Thin Film of Guest-Free Type-II Silicon Clathrate on Si (111) Wafer. *Thin Solid Films* **2016**, *609*. https://doi.org/10.1016/j.tsf.2016.03.056.

(8) Fix, T.; Vollondat, R.; Ameur, A.; Roques, S.; Rehspringer, J.-L.; Chevalier, C.; Muller, D.; Slaoui, A. Silicon Clathrate Films for Photovoltaic Applications. *J. Phys. Chem. C* **2020**, *124* (28), 14972–14977. https://doi.org/10.1021/acs.jpcc.0c02712.

(9) Liu, Y.; Schenken, W. K.; Krishna, L.; Majid, A. A. A.; Furtak, T. E.; Walker, M.; Koh, C. A.; Taylor, P. C.; Collins, R. T. Synthesis and Characterization of Type II Silicon Clathrate Films with Low Na Concentration. *Applied Physics Reviews* **2021**, *8* (4), 041408. https://doi.org/10.1063/5.0062723.

(10) Ammar, A.; Cros, C.; Pouchard, M.; Jaussaud, N.; Bassat, J.-M.; Villeneuve, G.; Reny, E. Preparation and Characterization of the Silicon Clathrate Na $_x$ Si $_{136}$ (x -> 0). *J. Phys. IV France* **2005**, *123*, 29–34. https://doi.org/10.1051/jp4:2005123004.

(11) Schenken, W. K.; Liu, Y.; Krishna, L.; Majid, A. A. A.; Koh, C. A.; Taylor, P. C.; Collins, R. T. Electron Paramagnetic Resonance Study of Type-II Silicon Clathrate with Low Sodium Guest Concentration. *Phys. Rev. B* **2020**, *101* (24), 245204. https://doi.org/10.1103/PhysRevB.101.245204.

A.2 Annexes of Chapter 2

A.2.1 Atoms positions and occupations refined by Rietveld

Table A.2.1 Atomic position and occupations refined using Jana2006.

	atom	site	x	y	z	Occupation
Na_8Si_{46}	Si1	8a	0.25000	0.50000	0.00000	1
	Si2	32e	0.18412(5)	0.18412(5)	0.18412(5)	1
	Si3	96g	0.00000	0.11719(7)	0.30776(7)	1
	Na1	16e	0.00000	0.00000	0.00000	1
	Na2	8b	0.25000	0.00000	0.50000	1
	atom	**site**	**x**	**y**	**z**	**Occupation**
$Na_{2.283}$ Si_{136}	Si1	8a	0.12500	0.12500	0.12500	1
	Si2	32e	0.03229(14)	0.21770(14)	0.03229(14)	1
	Si3	96g	0.06664(11)	0.37158(17)	0.06664(11)	1
	Na1	16e	-	-	-	-
	Na2	8b	0.37500	0.37500	0.37500	0.285(11)
	atom	**site**	**x**	**y**	**z**	**f**
$Na_{2.982}$ Si_{136}	Si1	8a	0.12500	0.12500	0.12500	1
	Si2	32e	0.03274(11)	0.21726(11)	0.03274(11)	1
	Si3	96g	0.06657(9)	0.37154(13)	0.06657(9)	1
	Na1	16e	-	-	-	-
	Na2	8b	0.37500	0.37500	0.37500	0.373(9)
	atom	**site**	**x**	**y**	**z**	**f**
$Na_{3.466}$ Si_{136}	Si1	8a	0.12500	0.12500	0.12500	1
	Si2	32e	0.0331(4)	0.2169(4)	0.0331(4)	1
	Si3	96g	0.0660(3)	0.3720(5)	0.0660(3)	1
	Na1	16e	-	-	-	-
	Na2	8b	0.37500	0.37500	0.37500	0.43(3)
	atom	**site**	**x**	**y**	**z**	**f**
	Si1	8a	0.12500	0.12500	0.12500	1

Na$_{4.349}$	Si2	32e	0.0322(2)	0.2178(2)	0.0322(2)	1
Si$_{136}$	Si3	96g	0.06580(19)	0.3728 (3)	0.06580(19)	1
	Na1	16e	-	-		-
	Na2	8b	0.37500	0.37500	0.37500	0.544(15)
	atom	**site**	**x**	**y**	**z**	**f**
	Si1	8a	0.12500	0.12500	0.12500	1
Na$_{5.674}$	Si2	32e	0.0323(2)	0.2177(2)	0.0323(2)	1
Si$_{136}$	Si3	96g	0.06656(19)	0.3722(3)	0.06656(19)	1
	Na1	16e	-	-	-	-
	Na2	8b	0.37500	0.37500	0.37500	0.709 (18)
	atom	**site**	**x**	**y**	**z**	**f**
	Si1	8a	0.12500	0.12500	0.12500	1
Na$_{9.961}$	Si2	32e	0.0322(3)	0.2178(3)	0.0322(3)	1
Si$_{136}$	Si3	96g	0.06648(19)	0.3718 (3)	0.06648(19)	1
	Na1	16e	0.00000	0.00000	0.00000	0.123(3)
	Na2	8b	0.37500	0.37500	0.37500	1

A.3 Annexes of Chapter 3

A.3.1 Atoms positions and occupations refined by Rietveld

Table A.3.1 Atomic position and occupations refined using Jana2006.

Na6.834 Si136	atom	site	x	y	z	f	U_{iso}
	Si1	8a	0.125	0.125	0.125	1	0.0113
	Si2	32e	0.0322(3)	0.2178(3)	0.0322(3)	1	0.005(2)
	Si3	96g	0.0663(2)	0.3719(3)	0.0663(2)	1	0.007(2)
	Na1	16e	-	-	-	-	-
	Na2	8b	0.375	0.375	0.375	0.85(2)	0.125

Na8.294 Si136	atom	site	x	y	z	f	U_{iso}
	Si1	8a	0.125	0.125	0.125	1	0.0039
	Si2	32e	0.03271	0.21729	0.03271	1	0.0038
	Si3	96g	0.06734	0.37072	0.06734	1	0.0047
	Na1	16e	0	0	0	0.064(13)	0.02
	Na2	8b	0.375	0.375	0.375	0.91(2)	0.125

Na23.087 Si136	atom	site	x	y	z	f	U_{iso}
	Si1	8a	0.125	0.125	0.125	1	0.0135
	Si2	32e	0.03060(19)	0.21940(19)	0.03060(19)	1	0.0228(9)
	Si3	96g	0.06677(14)	0.3729(2)	0.06677(14)	1	0.0318(9)
	Na1	16e	0	0	0	0.943(10)	0.02
	Na2	8b	0.375	0.375	0.375	1	0.125

A.3.2 Band Structure of the type-II silicon clathrate for x = 0 to x = 8
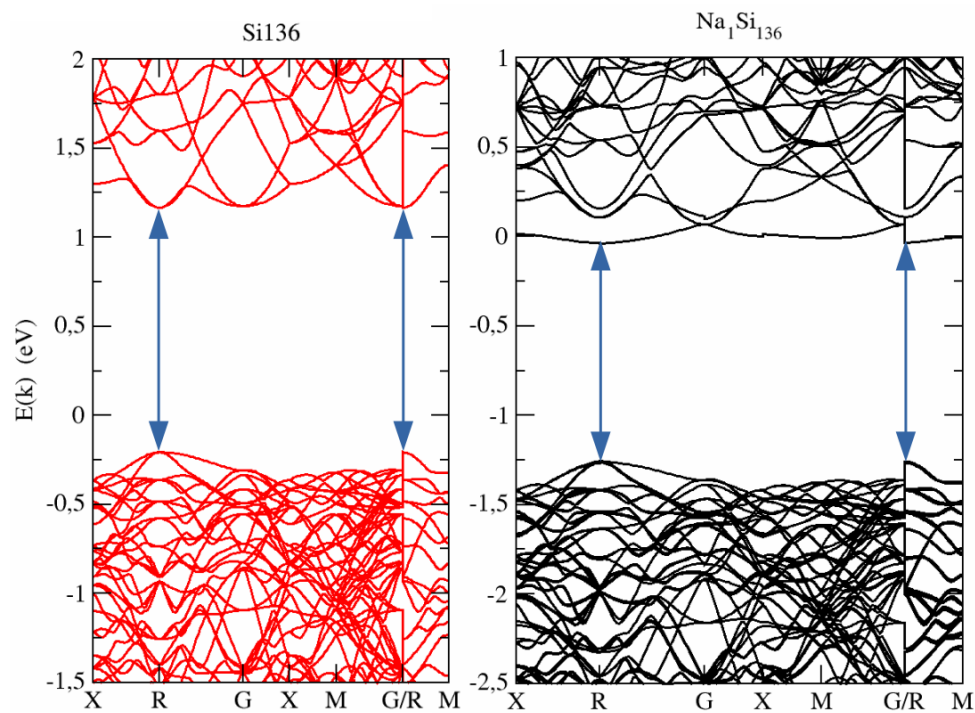
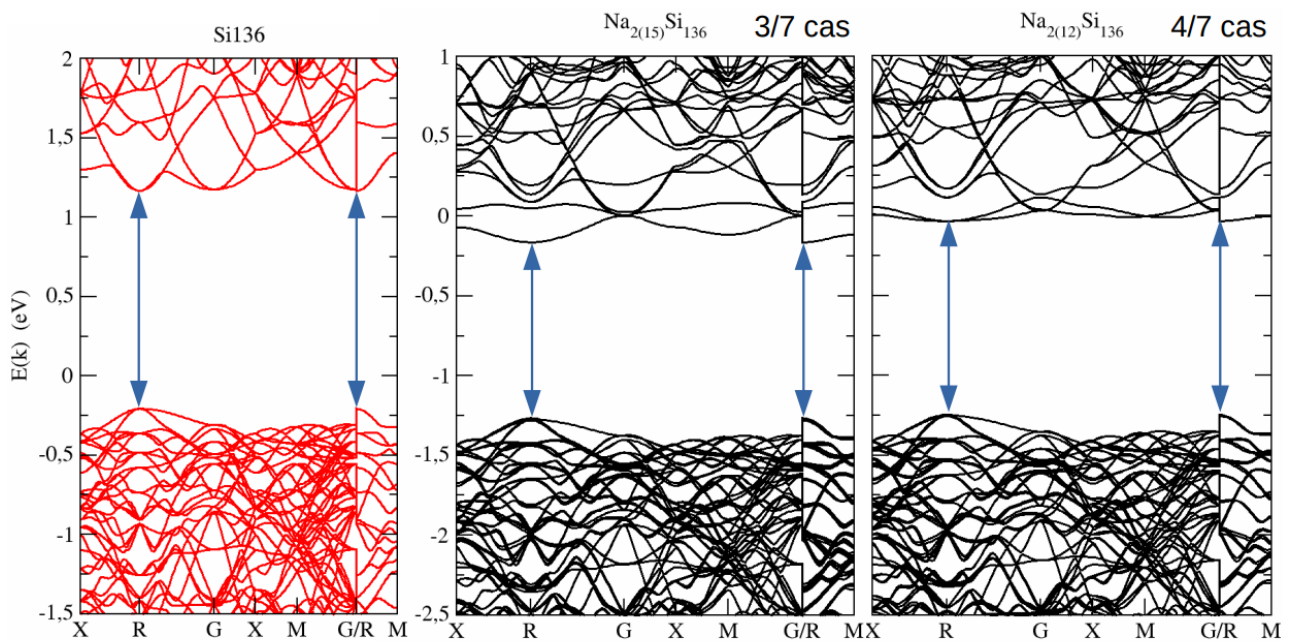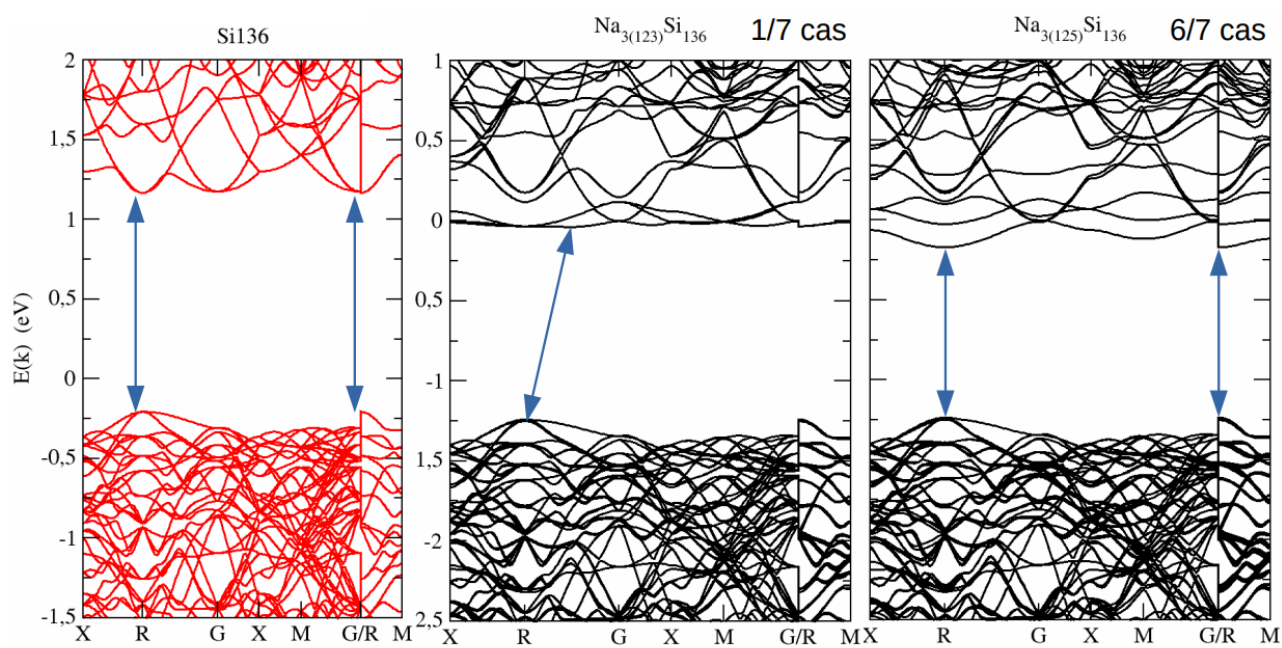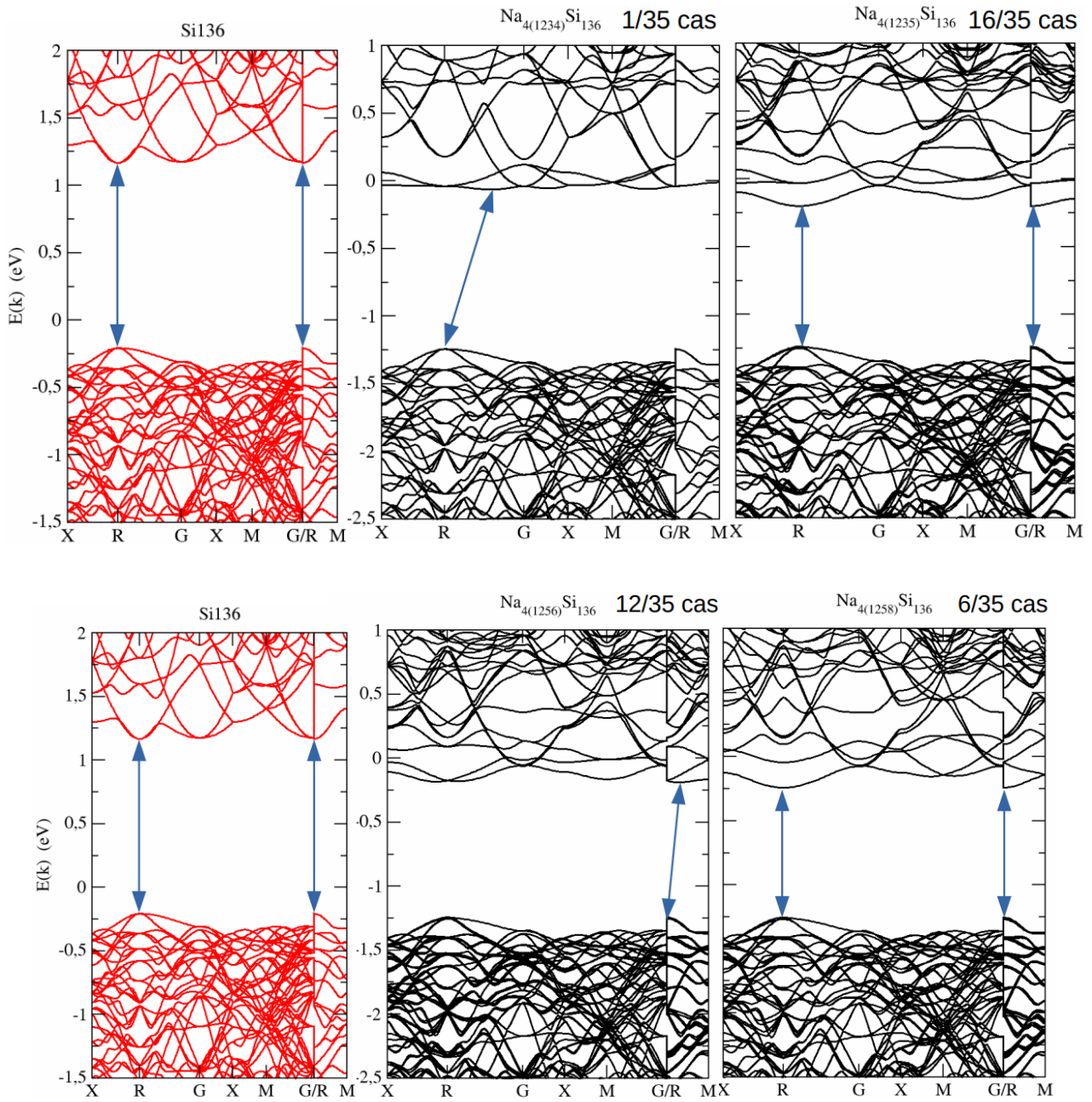**Figure A.3.1** Band Structure of Na_1S_{136} compared to Si_{136}

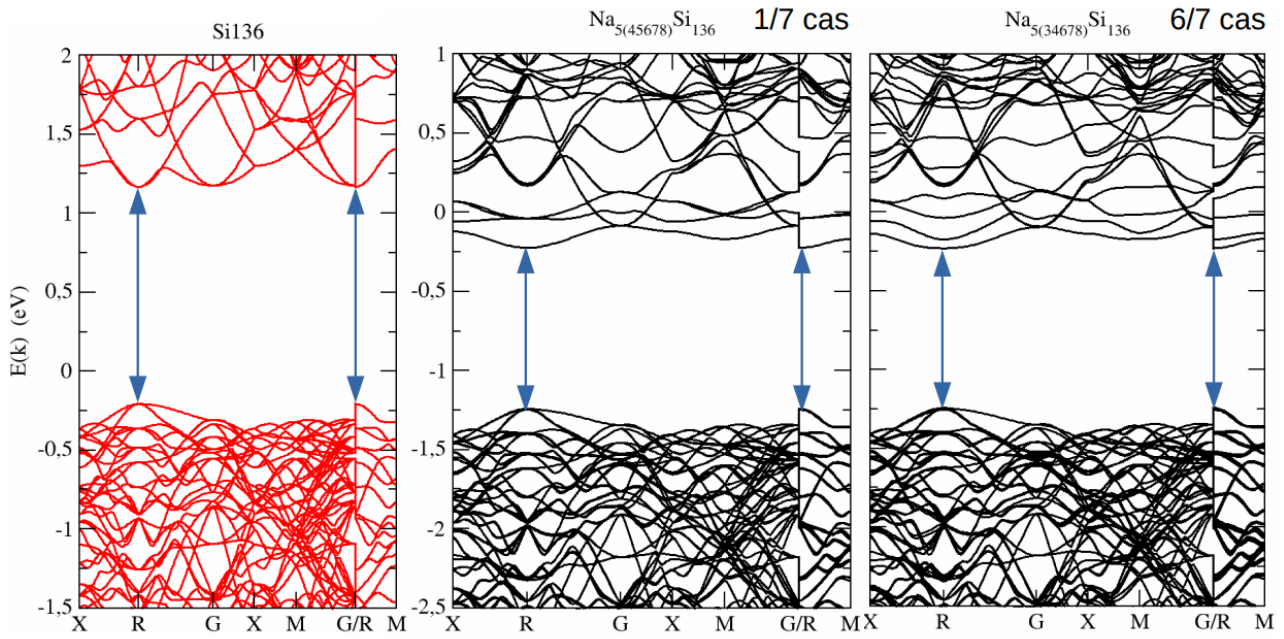**Figure A.3.2** Band Structure of Na_2S_{136} configurations compared to Si_{136}

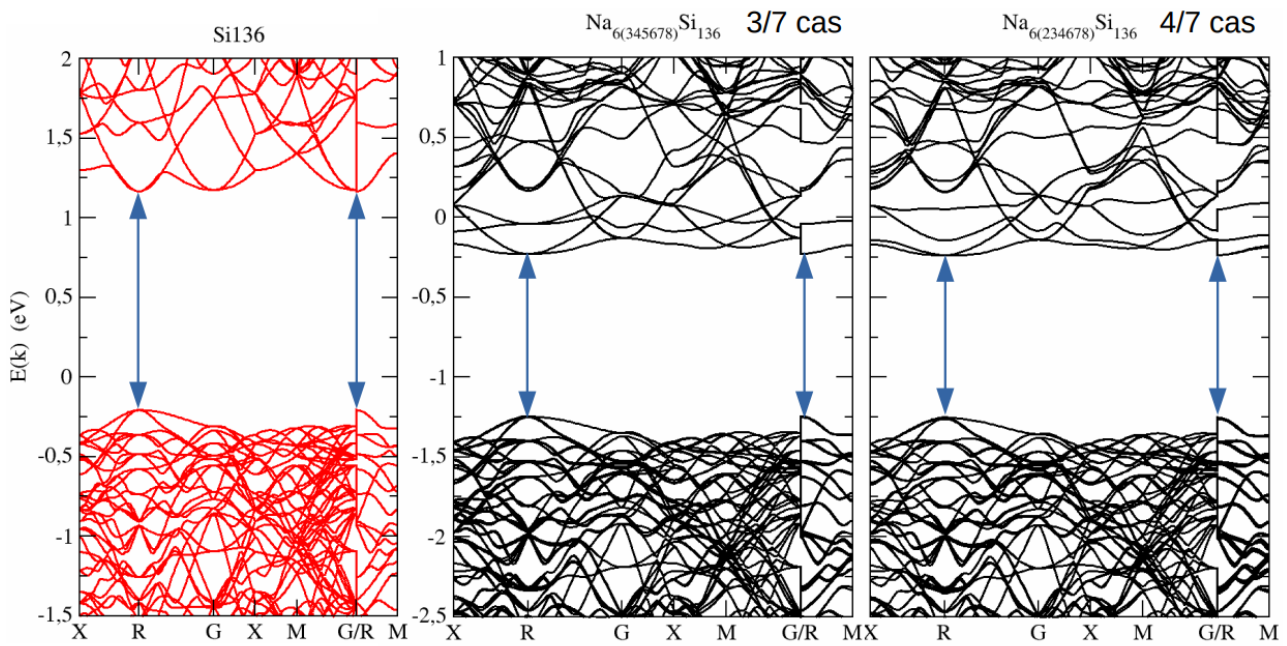**Figure A.3.3** Band Structure of Na_3S_{136} configurations compared to Si_{136}

Figure A.3.4 Band Structure of Na_4S_{136} configurations compared to Si_{136}

.

Figure A.3.5 Band Structure of Na_5S_{136} configurations compared to Si_{136}

Figure A.3.6 Band Structure of Na_6S_{136} configurations compared to Si_{136}

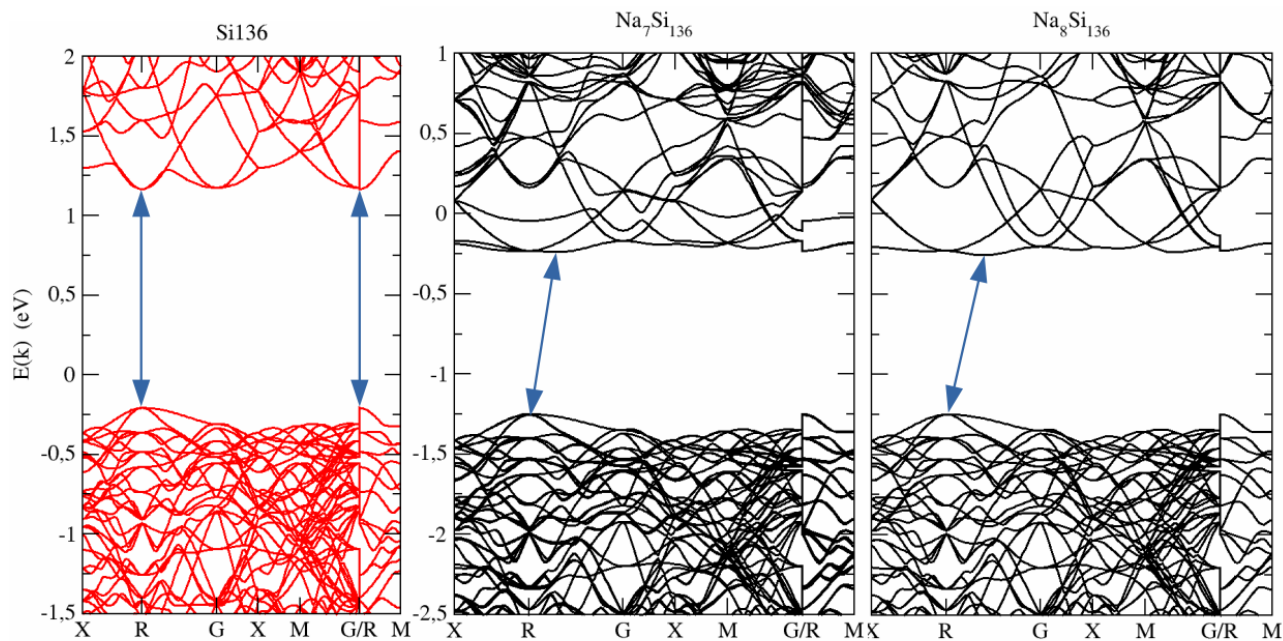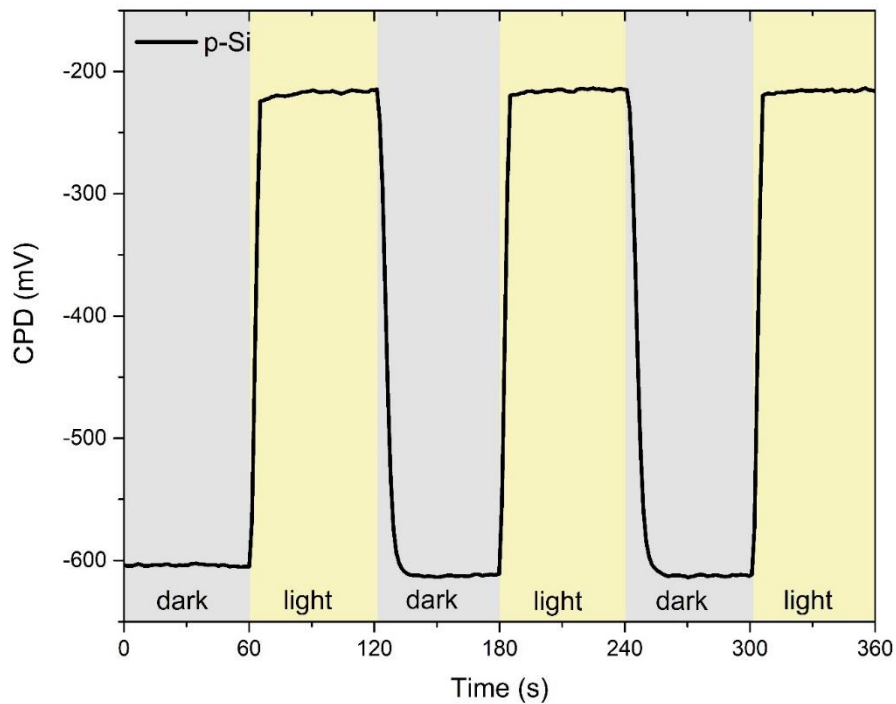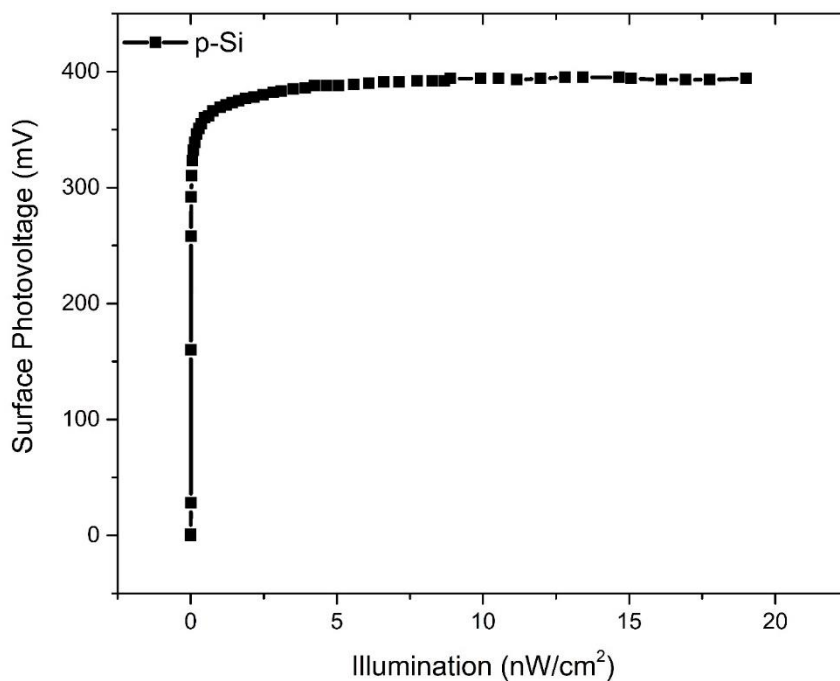**Figure A.3.7** Band Structure of Na_7S_{136} and Na_8Si_{136} compared to Si_{136}

A.3.3 Transient SPV and SPV vs. Illumination measurements of p-doped diamond silicon of 1-5 Ω·cm resistivity
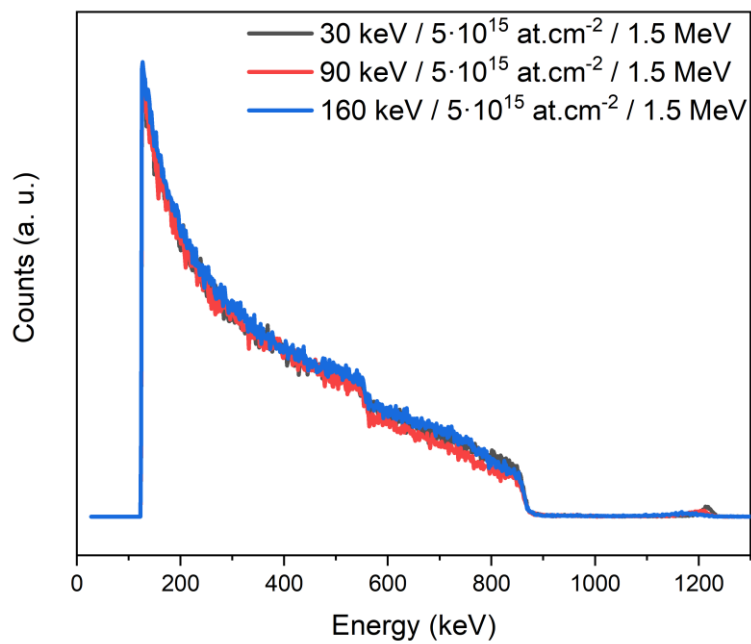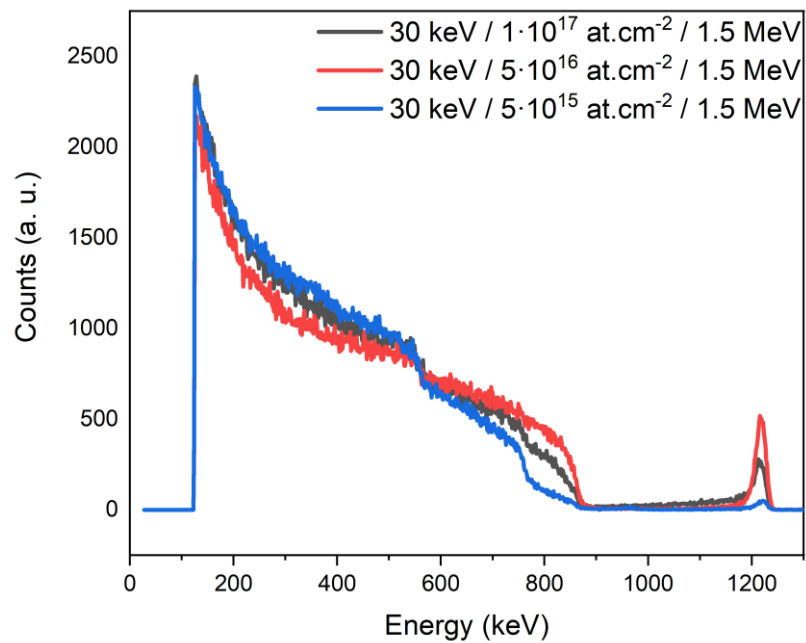

Figure A.3.8 Variation of the Contact Potential Difference (CPD) measured on p-doped Silicon during cycle between illumination by halogen visible light and dark.

Figure A.3.9 Surface Photovoltage (SPV) of p-doped Silicon according to the illumination delivered by the halogen visible light.

A.3.4 RBS measurements of the implanted films

Figure A.3.10 RBS measurements at 1.5 MeV of the type-II implanted films.

Romain VOLLONDAT

Synthesis and Characterization of Silicon Clathrates Films for Photovoltaic Applications

Résumé

Cet ouvrage concerne la synthèse de films de Clathrates de Silicium (SiCL) puis l'investigation et l'optimisation de leurs propriétés optoélectroniques et structurales. Les SiCL sont des composés d'inclusion formés d'un réseau silicié de cages occupées par du sodium. Libres de sodium, ces SiCL sont des allotropes exotiques à bande directe du silicium favorables à des technologies solaires performantes. Une large compréhension des SiCL sous forme de film est donc cruciale. Les films de SiCL de type-I (SiCL-I) et de type-II (SiCL-II) sont obtenus par décomposition thermique et caractérisés (DRX, Raman..). Par analyse des propriétés optoélectroniques (Hall, PL..) les films de SiCL-I sont métalliques tandis que les SiCL-II présentent différentes concentrations en sodium impactant les propriétés optoélectroniques comme prédit par DFT. Le contrôle réversible du niveau de sodium du SiCL-II permet la transition du film de métal à semiconducteur. Les propriétés structurales des films sont améliorées par recuit sous presse. Enfin, l'implantation en surface des couches par de l'arsenic est démontré et les effets sur les propriétés des films de SiCL-II sont étudiés.

Mots clés : Silicium, Clathrates de Silicium, Films, Composés d'inclusion

Résumé en anglais

This study concerns the synthesis of Silicon Clathrates (SiCL) films and the investigation and optimization of their optoelectronic and structural properties. SiCLs are inclusion compounds formed by a host lattice of polyhedral silicon cages stabilized by the presence of guest sodium atoms. The backbone of these SiCLs can be isolated and are then true allotropes with low density and quasi-direct band of silicon which is a stepping stone toward more efficient and less expensive silicon photovoltaic technologies. To obtain efficient applications using SiCL, a better understanding of these materials and their synthesis in the form of films is crucial. Type-I (SiCL-I) and type-II (SiCL-II) SiCL films are obtained by thermal decomposition of a Zintl phase precursor. The synthesis parameters have been refined through characterizations (XRD, Raman, SEM..) allowing the selective synthesis of each of these phases in the form of homogeneous films. By analysis of the optoelectronic properties (Hall, Ellipsometry, PL...) it is shown that the SiCL-I, Na_8Si_{46}, films are metallic and with fixed sodium occupation while the SiCL-II, $Na_{0<x<24}Si_{136}$, films present different sodium concentrations directly impacting their optoelectronic properties and semiconducting character. Press annealing of the films improves their structural qualities by densifying the layers. The insertion and extraction of sodium atoms from SiCL-II films, achieved by annealing under sodium vapour and iodine atmosphere respectively, allows to modulate the resistivity of these films over four orders of magnitude while observing a transition from metal to semiconductor at low sodium concentration. The sodium contribution to this behaviour is explicated thanks to DFT calculations. These reversible modifications of the sodium concentration of SiCL-II do not induce significant expansion/contraction of the structure and are therefore performed without damaging it. Finally, the surface implantation of these films with arsenic has been demonstrated and the impact on the SiCL-II films properties are studied.

Keywords: Silicon, Silicon Clathrates, Films, Inclusion compounds